Pieter Ghekiere

Structure Evolution of Biaxially Aligned Thin Films Deposited by Sputtering

Universiteit Gent
Faculteit Wetenschappen
Vakgroep Vaste Stofwetenschappen

Proefschrift voorgelegd tot het behalen van de graad van
Doctor in de Wetenschappen: Natuurkunde

Promotor:
Prof. Dr. Ir. R. De Gryse
Copromotor:
Prof. Dr. D. Depla

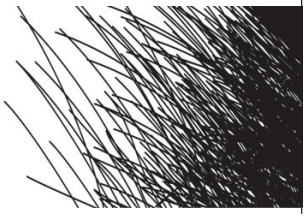

Dankwoord

Dit werk kwam tot stand dankzij een grote groep mensen die mij in meer of mindere mate beïnvloed, geholpen en gesteund hebben. Ik hoop dat deze personen bij het lezen van deze thesis zich zullen realiseren dat ik hun veel dank ben verschuldigd.
In het bijzonder wil ik mijn promotor Prof. Dr. Ir. Roger De Gryse bedanken voor het opvolgen van mijn werk en de ondersteuning van de voorbije jaren. Een andere onmisbare schakel in de sputter groep is Prof. Dr. Diederik Depla. Ik bewonder je drang naar kennis en de wil om alles in detail te willen begrijpen. Bedankt voor de antwoorden op de vele vraagjes, je jarenlange hulp bij allerhande problemen en het grondig nalezen van dit werk.
Als ik één persoon zou moeten bedanken dan is het wel Dr. Stijn Mahieu. De kritische discussies die soms tot grote ergernis leidden, waren een ideale voedingsbodem voor het optimaliseren en het op een goede manier verwoorden van onze modellen. Ik dank je voor de samenwerking. Zonder jou zou dit werk niet de kwaliteit hebben dat het nu heeft. Daarnaast wil ik ook Griet De Winter bedanken. Je was niet enkel een aangename bureau compagnon, maar het was jij die me in het begin stimuleerde om dieper in te gaan op mijn onderzoek. Dankzij jou is dit project gestart, iets wat ik niet snel zal vergeten.
Naast deze mensen, zijn er de vele collega's van S1 die me ondersteund hebben in de experimenten. Voor het lenen of herstellen van vacuümmateriaal, voor het uitvoeren van allerhande metingen, voor het verschaffen van vele nuttige tips of voor de aangename babbel. Dankjewel.
Voor de TEM metingen en de analyse ervan, wil ik speciaal Dr. Oleg Lebedev en Prof. Dr. Staf Van Tendeloo bedanken.
A special 'Thank You' goes to Prof. Dr. Péter Barna. I used to think that impurities were ugly ducklings, but thanks to you, impurities unveiled a part of their mystery and became a bright spot in my work.
Ook wil ik alle leden van de jury bedanken voor het doorworstelen van dit werk.
IWT Vlaanderen wil ik bedanken voor de financiële steun tijdens het GBOU project: "Mechanism of biaxial alignment in thin films grown by unbalanced magnetron sputtering".

Hoe mooi de experimenten ook zijn, het leven buiten het onderzoek is nog veel mooier.
Ontspanning vond ik altijd terug in de chiro. In het bijzonder wil ik iedereen van het JOL bedanken voor de fantastische vriendengroep. Samen zijn we opgegroeid, samen blijven we leute maken. Merci.
Het einde van dit dankwoord brengt me bij de mensen die me het nauwst aan het hart liggen. Mijn ouders wil ik bedanken voor het geven van alle kansen, het jarenlange vertrouwen en de

goede zorgen. De thuis waar ik altijd welkom ben, heeft me werkelijk gesteund. Dank je. Mijn zusje mag ik hierbij ook niet te vergeten. Heidi, merci voor de aangename babbels en de leuke momenten samen.
Tenslotte wil ik mijn vriendin Marjolijn bedanken. Dat voor vele fysici de tijd een raadselachtig begrip is, begrijp ik niet. Het is nogthans eenvoudig: als wij samen zijn, bestaat de tijd even niet. Bedankt voor je liefde, voor je geduld, voor al die mooie dagen en voor je steun op de momenten wanneer het nodig was.

Pieter

Contents

Introduction

Applications in advanced surface engineering will require the most demanding approaches in the near future. New concepts and design methodologies are needed to create and synthesize new thin film devices and to integrate them into architectures for various operations. The application area of thin films situates in the field of protective coatings and buffer layers. In the latter, the functionality of active top layer is connected to the quality and the properties of the thin film.
Thin films can be grown in a wide range of structures. In general, the physical properties of the thin film depend on its intrinsic properties. For example, a porous structure will be advantageous to improve the catalytic properties of the film. Nanocrystalline thin films are another example. These films have a hardness which is higher than the hardness of crystalline thin films.
A key role is reserved for the microstructure and crystallographic texture of the thin film. Therefore, the understanding of the structure evolution is needed and the critical role of surfaces and interfaces must be understood. Knowledge about atomic processes, such as surface diffusion, and their correlation to the deposition process will be essential to describe the growth process and will be treated in this work.
The focus is on a special kind of thin films, namely the biaxially aligned thin films. These are polycrystalline thin films of which the grains are oriented along two crystallographic axes. Biaxially aligned thin films are already used in the superconducting industry. These biaxially aligned thin films can be deposited on all kind of substrates with a low roughness (e.g. electropolished foils, amorphous glass). This is one of the strengths of biaxially aligned thin films. Starting from a non-aligned or amorphous substrate, a thin film is obtained that mimics the properties of a single crystal. Furthermore, the technique which is used to deposited biaxially aligned thin films (Inclined Substrate Deposition (ISD)), can easily be scaled to industrial processes. This offers a growth market for new designs and applications. For example, biaxially aligned MgO thin films serve as a buffer layer between the superconducting film and the substrate, which allows the growth of high temperature superconductors with a high current density on a non-aligned metallic foil. This current density is tightly connected to the angle between the orientation of the grains in the buffer layer and hence to the quality of the biaxially aligned thin film.

In this work, the growth mechanism of the biaxially aligned thin films is emphasized. In seven chapters, the growth of biaxially aligned thin films will be elucidated.
Chapter 1 deals with the fundamental processes that determine the structure evolution of thin films. Because thin film growth can be reduced to these processes, they are discussed into detail in the first chapter. Additionally, the atomic processes which drive the fundamental processes of

structure formation, are discussed.
The thin films are grown by sputter deposition. Chapter 2 summarizes the different aspects of the sputter process and its opportunities to the growth of more multicomponent materials.
The next chapter discusses briefly the various characterization techniques which have been used to analyse the biaxially aligned thin films.
Chapter 4 focuses on the growth mechanism of biaxially aligned thin films. More specific, the growth of biaxially aligned MgO, Cr and InN thin films will be discussed. These materials are not only selected because of their various properties (insulating, metallic and semiconducting respectively) but also for their different crystallographic structure (rocksalt, BCC, wurtzite respectively). With these, the origin of the biaxial alignment is investigated. In this chapter, a model for the growth of biaxially aligned thin films will be suggested.
The model developed in chapter 4 will be elucidated by correlating the deposition parameters to the growth of the biaxially aligned thin films. This will be presented in chapter 5. Both chapter 4 and 5 form the basis of the growth model.
Chapter 6 goes one step further and deals with the texture change in biaxially aligned thin films caused by the codeposition of impurities. It is observed that impurities can modify the fundamental processes of structure evolution and hence the growth of thin films. In this chapter, impurities are added in a controlled way during the growth of biaxially aligned thin films. Their influence on the microstructure and crystallographic texture will be discussed.
In the seventh and last chapter, the growth of biaxially aligned thin films is extrapolated to other materials. Additionally, the material conditions and/or the deposition conditions, that must be fulfilled in order to grow biaxially aligned thin films will be discussed.
I hope I can give you more insight in the domain of thin film growth and you enjoy the reading.

Chapter 1

Aspects of Thin Film Growth

1.1 Introduction

This work deals with biaxially aligned thin films (i.e. thin films with both a preferential out-of-plane and in-plane alignment) that are deposited on a tilted substrate by magnetron sputtering. In order to understand to growth mechanism of biaxially aligned thin films, several concepts have to be introduced and will be used during this work.
The formation of a thin film starts with the condensation of atomic and/or molecular species on the substrate. This chapter discusses how the arriving adspecies are adsorbed on the surface (Section 1.2), how they move around (Section 1.3), how the formation of islands starts (Section 1.4) and how the film growth proceeds in the later stages (Section 1.5). The structure evolution of polycrystalline films can be categorized in a Structure Zone Model (SZM), which gives a correlation between the microstructure and crystallographic orientation of the grains in the polycrystalline thin film as a function of the deposition parameters (Section 1.6).
At the initial stage of the thin film deposition, several atomistic processes are involved such as impingement, diffusion, desorption, adsorption and aggregation as shown in Fig. 1.1. Throughout this work, it will turn out that these processes are fundamental for the structure evolution of the thin films during all stages of the growth and determine the resulting structure. Therefore, these processes will be discussed in detail and will be used as a starting point to describe the structure evolution of thin films.

1.2 Adsorption

In the vicinity of a surface, gas phase species interact with the surface due to the increased reactivity of the surface atoms. The particles are attracted in a potential well by the van der Waals force and get weakly adsorbed on the surface. During this process the electronic state of the adspecies and the surface atoms is almost unaffected. This adsorption process is called physical adsorption or physisorption. Due to the weak bond, adparticles are mobile and can easily desorb. Further, an additional interaction can occur by the formation of a chemical bond between the surface and adsorbate. The formation of chemical bonds between the adsorbate and the surface requires a reordering of one or more of their electronic orbitals, which results in a

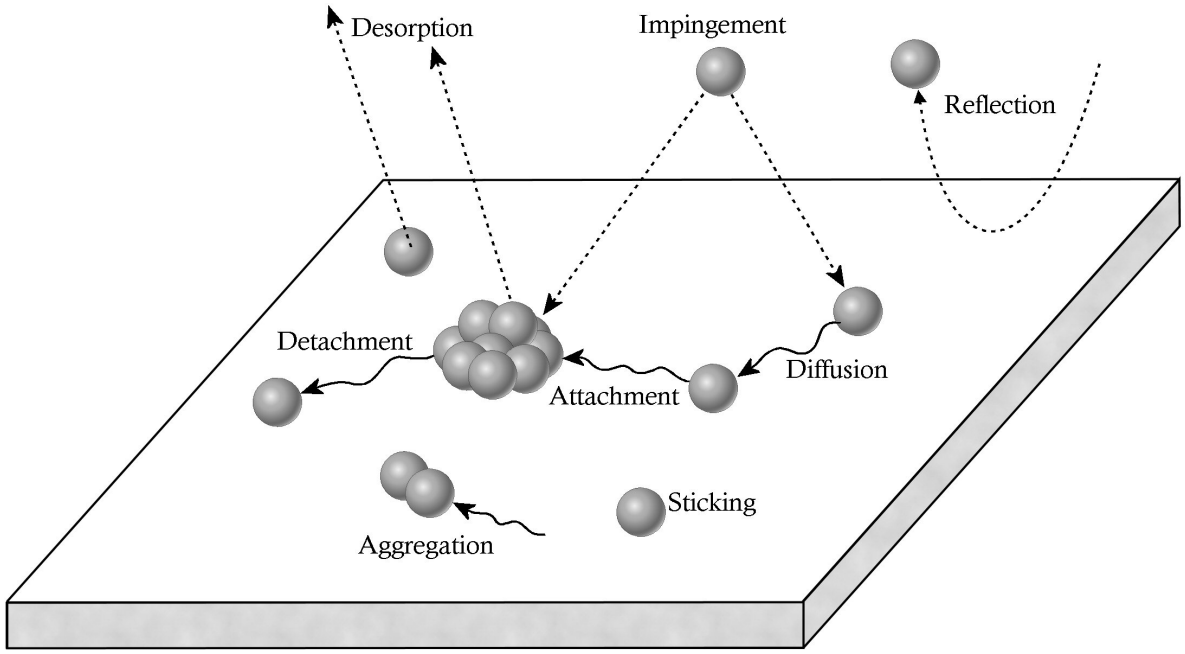

Figure 1.1: Elementary atomic events during the initial stage of thin film growth.

stronger bond. This process is called chemical adsorption or chemisorption.

Physisorption

In case of pure physisorption, the weak van der Waals force is the only attractive force between the adsorbate and the surface. It originates from a mutual induced dipole moment [1, 2]. At shorter distances, there is a strong repulsive force due to the overlapping of negatively charged electron shells. Fig. 1.2 shows the potential energy experienced by an adsorbate in a physisorbed state as a function of the distance to the surface. The shallow minimum arises from the attractive van der Waals force in combination with the strong repulsive force at a short distance. The equilibrium distance is in the order of 3 to 10 Å. There is no activation barrier which prevent the particle to enter the potential well with a depth from 10 to 100 meV [2]. Due to the small depth of the potential well, binding of a particle in a physisorbed state is unlikely at room temperature ($k_BT \approx 25$ meV) and it gets easily desorbed.

Chemisorption

For chemisorption, a chemical bond is formed between the adsorbate and the surface, creating new molecular orbitals by an electron transfer (ionic bond) or by sharing electrons (covalent bond). Chemisorption results in a much stronger bond between the adsorbate and the surface atoms. Hereby, the binding energy is in the order of a few eV. As a result, desorption from a chemisorbed state is unlikely at room temperature.
Two processes in chemisorption are discussed in more detail: non-dissociative chemisorption

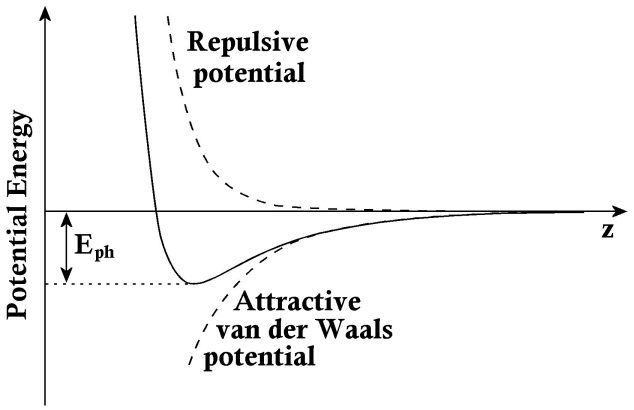

Figure 1.2: The one-dimensional potential energy diagram corresponding to physisorption of a particle on a surface. The physisorption potential arises from the attractive van der Waals force combined with a repulsive intermolecular force. The zero corresponds to the energy of the particle at a large distance. E_{ph} is the depth of the potential well and corresponds to the binding energy of an adsorbate to the surface in a physisorbed state.

and dissociative chemisorption. Non-dissociative chemisorption occurs for a single atom or for a molecule that doesn't break up its intramolecular bonds. However, the axis of the molecule must be well aligned for molecular chemisorption.[1]
Chemical adsorption proceeds mostly in two stages. First, the adparticle is attracted to a physisorbed state, called the precursor state. Additionally, a transition to a chemisorbed state can take place. The potential energy corresponding to the chemisorbed state is shown in Fig. 1.3(a). The chemisorbed state is characterized by a much deeper potential well which is closer to the surface, typically about 1 Å [2]. As can be seen, the potential energy diagram is a combination of the precursor state and the chemisorbed state. Depending on the curve crossing (above or below zero), non-dissociative chemisorption can be activated. This means that an activation barrier has to be overcome to go from the physisorbed state to the chemisorbed state. The process illustrated in Fig. 1.3(a), doesn't need activation because the crossing is below zero.
In the case of dissociative chemisorption, particularly diatomic molecules on metal surfaces, the dissociation of the molecules to atomic species has frequently been observed. The potential energy diagram corresponding to dissociative chemisorption of a diatomic molecule is illustrated in Fig. 1.3(b). The dissociative chemisorption potential is the combination of the potential for a physisorbed molecule and the potential for chemisorption of the corresponding atomic species. A molecule that approaches the surface from a large distance feels an attraction to the surface. Coming too close to the surface would cause a rapid increase in the potential energy due to the repulsive intermolecular potential between the molecule and the surface. If the molecule stays on the surface long enough, the molecule can split up due to a transformation in electronic orbitals caused by an overlap of the orbitals of the molecule with these of the surface atoms. The dissociated atoms can bind to the surface in a chemisorption state which has a much higher binding

[1] Due to the asymmetry of the electronic orbitals of the molecule, the adsorption potential will vary on the orientation of the molecule. In addition to this, the site of impact along the surface will also be important [2].

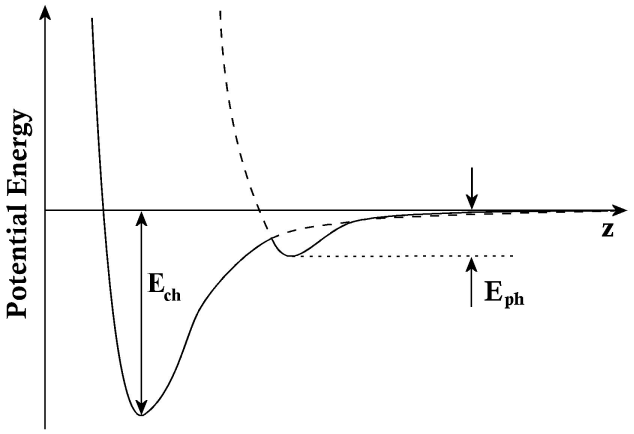

(a) Non-dissociative chemisorption

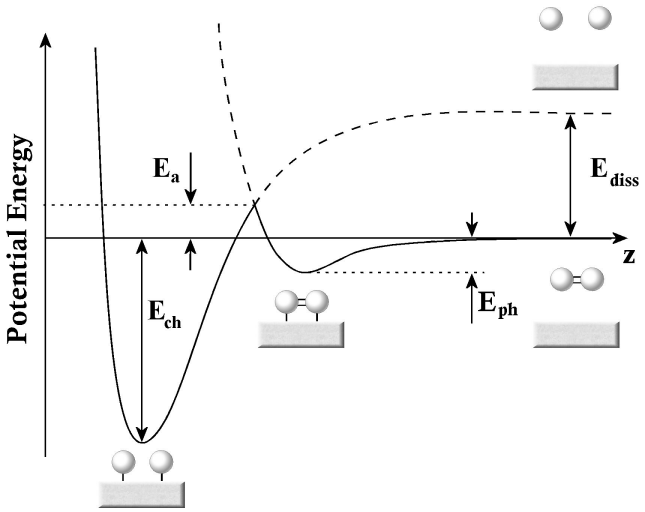

(b) Dissociative chemisorption

Figure 1.3: (a) The one-dimensional potential energy diagram corresponding to non-dissociative chemisorption; (b) The one-dimensional potential energy diagram corresponding to the dissociative chemisorption of a neutral diatomic molecule on a solid surface. Hereby, E_{ch} is the binding energy of chemisorbed state, E_{ph} the depth of the physisorption well, E_a is the activation barrier and E_{diss} is the dissociation energy of the diatomic molecule. The zero in case of dissociative chemisorption corresponds to the potential energy of the diatomic molecule at large distance.

energy.[2] However, the molecule needs sufficient kinetic energy to overcome an activation barrier E_a to follow the chemisorption potential, which can make dissociative chemisorption an activated process. The height of the activation barrier depends strongly on the surface, the orientation of the molecule, the position on the surface plane, etc. Because this activation barrier is lower than the dissociation energy in the gas phase E_{diss}, dissociation of a molecule preferentially occurs on the solid surface. The study of the dissociative activation barrier in the presence of the solid surface is strongly linked to catalytic reactions.

Desorption

If a particle is adsorbed on a surface in a physical or chemical binding state, the adparticle (i.e. adsorbed particle) will oscillate in the potential well. Due to fluctuations, there is a change that the particle is desorbed thermally. During adsorption, the particle must transfer a part of its kinetic energy to the substrate, or it will be desorbed immediately. Once adsorbed, there is a possibility for the adsorbate to desorb again. The rate of desorption depends on the depth of the potential well and is proportional to $\exp(-E_{ph}/kT)$ or $\exp(-E_{ch}/kT)$, which is substantial for physisorption but small for chemisorption.
Desorption is often discussed in terms of the sticking coefficient S_c, which expresses the probability for adsorbates to remain on the surface and become incorporated into the film. S_c varies between unity and zero, depending on the species, deposition conditions, etc. Next to thermal desorption, an adsorbate can desorb by knock-on events caused by energetic arriving particles. This process is likely in PVD processes, like sputter deposition.

1.3 Surface Diffusion

Generally, adatoms or adparticles on the surface usually have sufficient energy to move across the surface. Hereby, the adatoms hop from one well to another. The energy barrier to go from one site to another is smaller than E_{ch} or E_{ph} because some bonds with the surface atoms remain. The motion of adatoms roaming on the surface is called surface diffusion. Mostly, diffusion occurs on an atomic flat surface. At step edges, diffusion is also likely, however the diffusion barriers are higher due to the higher number of surface bonds. Additionally, surface diffusion is sensitive to the chemical state of the surface. Changes in the diffusion barriers, caused by incorporated trace elements, will influence the diffusion properties thoroughly.

1.3.1 Diffusion on a Terrace

The simplest case in describing the dynamic behaviour of adatoms on a surface is diffusion by random walk (Brownian motion) on a flat terrace [3, 4, 5]. A single adatom moving on a flat surface experiences an effective potential caused by the surface atoms (Fig. 1.4). The difference between the saddle point and the minimum is called the activation barrier E_d for the diffusion. The activation barrier is in the order of 5-20% of E_{ch}, in case of a chemisorbed adatom.
The motion of an adatom consists of jumps from one adsorption site to the other. If the diffusion

[2] The potential energy diagram for chemisorption of two atoms differs from that of the corresponding molecule by the dissociation energy of the molecule E_{diss}

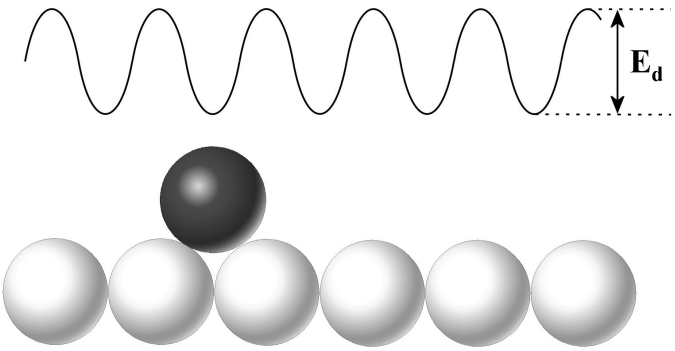

Figure 1.4: One dimensional schematic representation of the effective potential experienced by an adatom moving on a flat surface. E_d is the activation barrier.

is thermally activated, the total jump rate Γ of a single adatom can be written in an Arrhenius form

$$\Gamma = \Gamma_0 e^{-\frac{E_d}{kT}} \tag{1.1}$$

with Γ_0 the prefactor. Although the magnitude is mainly controlled by the activation barrier, the real dynamical information is all contained in the prefactor. Microscopically, the dynamical information comes from the interaction between an adatom and the surface. A rough estimate of the prefactor Γ_0 is

$$\Gamma_0 = n_s \nu_{osc} \tag{1.2}$$

where n_s is the number of hopping directions from a minimum position to an equivalent saddle point (n_s is 4 on square lattices; 6 on triangular lattices (Fig. 1.5)) and ν_{osc} is the vibrational frequency of the adatom in the adsorption site, commonly referred to as the attempt frequency, which is in the order of 10^{12}/s up to 10^{13}/s . In case of a random walk, the surface diffusion coefficient D for a single adatom is

$$D = \frac{1}{4}\Gamma \left\langle l^2 \right\rangle = \frac{n_s \nu_{osc}}{4} \left\langle l^2 \right\rangle e^{-\frac{E_d}{kT}} \tag{1.3}$$

where $\left\langle l^2 \right\rangle$ is the mean square jump length to an adjacent site. This jump length is often comparable to the lattice parameter. The diffusion length Λ in time t is given by the Einstein relation

$$\Lambda = \sqrt{2Dt} \tag{1.4}$$

In some cases, diffusion can also proceed via an exchange mechanism, where a diffusing adatom pushes out a surface atom and takes its position while the former surface atom starts to diffuse. The diffusion by exchange on close-packed planes is rare, because of very high activation energies. However, on less dense packed planes, the activation energy for exchange is often comparable or lower than that for hopping.
The adatom diffusion along different paths will lead to a variety of values for E_d. Furthermore,

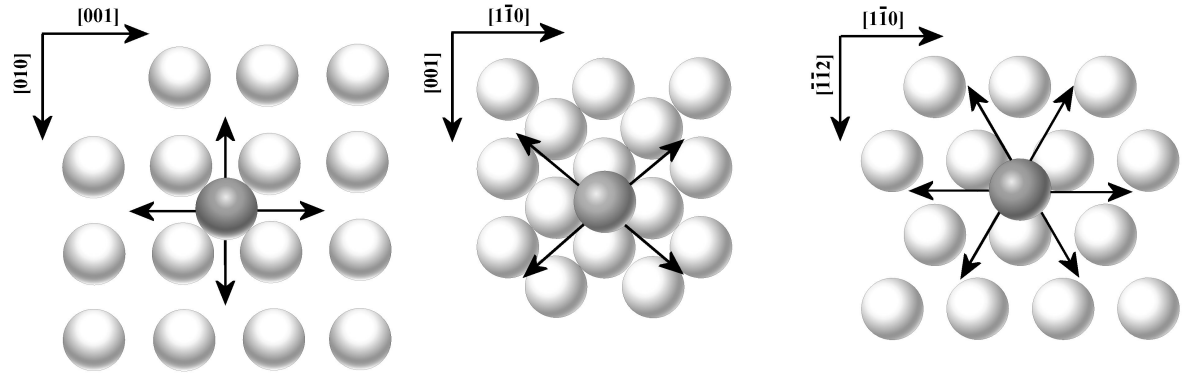

(a) BCC (100) (b) BCC (110) (c) BCC (111)

Figure 1.5: The top layer of BCC low index planes. The directions with the lowest diffusion barrier are indicated. For BCC {100} planes, this is the [001] direction, for BCC {110} planes, the [111] direction and for BCC {111} planes, these are the [001] and [110] directions.

the diffusion barrier varies significantly from one crystallographic surface structure to another. Table 1.1 shows the activation energy for surface diffusion on various crystallographic planes for W on W and Fe on Fe (Body-Centered Cubic (BCC) structure).[3] It is observed that the (110) pla-

Plane	W [eV]	Fe [eV]
(100)	1.34	0.45
(110)	0.86	0.28
(111)	1.78	-

Table 1.1: Activation energies for surface diffusion of W on W(110), W(100) and W(111) and of Fe on Fe(100) and Fe(110) [6, 7, 8].

ne has the lowest diffusion barrier for BCC structured materials. This is a general tendency that the low-index planes have the lowest diffusion barriers. Furthermore, atoms usually jump along close-packed directions. For example, on a BCC(110) surface, diffusion occurs in the [111] direction, as diffusion in the [100] or [110] direction is very unlikely because hopping takes place over an on-top position. The different paths for diffusion on three BCC surfaces are shown in Fig. 1.5.

1.3.2 Step-Edge Diffusion

Adatoms that diffuse on a terrace, can encounter a lattice step, also called a step-edge. Once adatoms reach the step, regardless of whether they reach the step from the upper terrace or from the lower terrace, they can be trapped at step-sites. However, when an adatom arrives from the

[3] Few data about the diffusion barriers can be retrieved for chromium, i.e. one of the material that is examined in this work (chapter 4-5-6). Because similar tendencies are observed for materials of the same isostructural group, it is suggested that Cr will have the same behaviour as iron or tungsten.

upper terrace, an additional energy barrier called the Ehrlich-Schwoebel (ES) barrier, should be taken into account (detailed information is given in section 1.3.3). After being trapped, there is a possibility that the adatom desorbes from the step and diffuses on the terrace (upper or lower) again. If an adatom is incorporated at a step-edge, it has the possibility to diffuse along the step, finding a favourable site. Four different types of edge adatoms can be distinguished, as illustrated in Fig. 1.6: ledge-site atoms A_l, corner-site atoms A_c, kink-site atoms A_k and recessed-site atoms A_r. A general description of the atomistic processes taking place at steps and on terraces, is given in the Terrace-Step-Kink (TSK) model [9, 10]. This model is developed by Burton, Cabrera and Frank and therefore, sometimes it is referred to as the BCF theory.
For kink-site A_k and recessed-site A_r adatoms, the activation energy is high because these adatoms have several bindings with other atoms. Hence, the possibility to be released from its position is very small and the adatom will be trapped.[4]
Adatom diffusion along ledges is not very different from terrace diffusion, however the motion is confined to one dimension. The adatom can move along the ledge until it is trapped in a kink or recessed-site or forms a dimer with another diffusion ledge adatoms and evolves into a stable compound. As mentioned above, ledge-adatoms can detach from the step-edge and diffuse on the terrace. However, the energy to detach is much higher than the energy barriers for diffusion along the step edge, since an additional bond has to be broken. Hence, detachment from a step-edge is more unlikely than diffusion along the step edge. When the adatom diffuses along a

[4] For several materials it has been observed that the kink energy is comparable to cohesive energy (i.e. heat of sublimation). This has been pointed out by Stranski in 1938 that the binding energy of kink site atoms is equal to the cohesive energy of the solid but only in the early nineties, it was possible to confirm this prediction with a high precision time-of-flight kinetic energy measurement of ions in low temperature field evaporation. These experiments have been performed by Liu *et al.* [11].

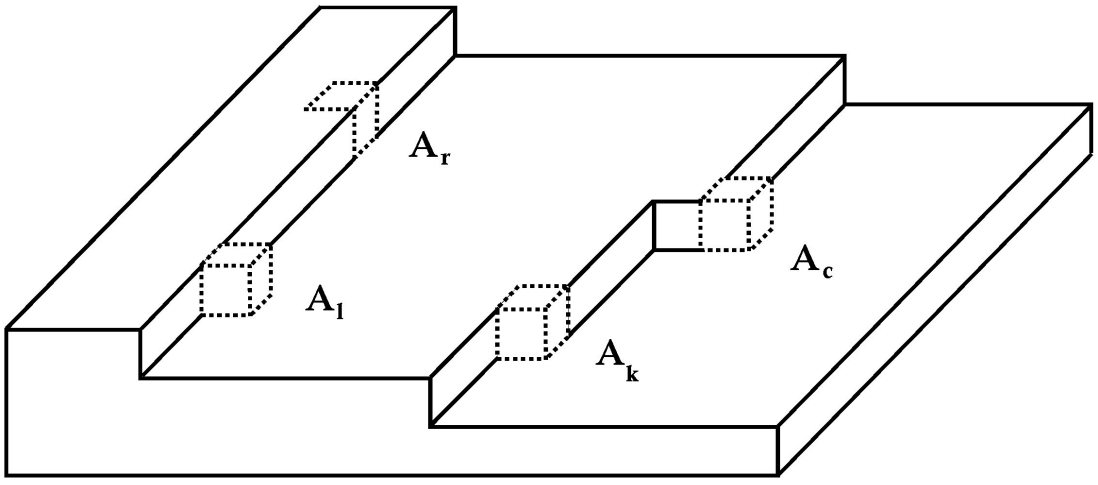

Figure 1.6: Four different types of step-edge adatoms: kink-site atoms A_k, ledge-site atoms A_l, corner-site atoms A_c and recessed-site atoms A_r. The activation energy for diffusion will depend on the numbers of bonds.

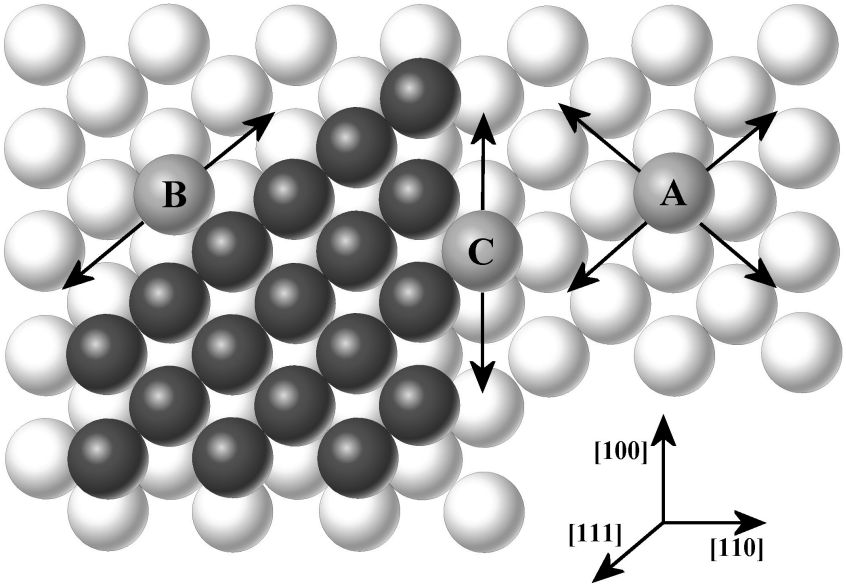

Figure 1.7: Top view of a BCC(110) surface with a single adatom (A), ledge-adatom attached on a (110) island diffusing in the [111] direction (B), ledge-adatom attached on a (110) island diffusing in the [100] direction (C). All diffusion directions on BCC(110) are on-top positions, except for the diffusion in the [111] direction which occurs in a two-fold bridge site.

ledge, it can arrive at a corner site. At the corner site, the adatom will experience an additional reflective barrier, similar to the ES barrier, before crossing the corner [12, 13].
Due to crystal symmetry, diffusion along ledges depends on the crystal symmetry of the terrace and the direction of the ledge. The barriers measured for diffusion of Fe on Fe(110) along two different edges are summarized in Table 1.2. The barrier for diffusion along the ⟨111⟩ direction is much lower than that for diffusion along the ⟨100⟩ direction, because hopping in the ⟨100⟩ direction (and also in the ⟨110⟩ direction) takes place over an on-top position, while an adatom diffuses in a bridge position in the ⟨111⟩ direction (Fig. 1.7 b-c). Hence, an adatom diffuses easily along the ⟨111⟩ direction until it arrives at a kink. This results in smooth edges in the ⟨111⟩ direction and rough edges along the other directions. In conclusion, step-edge diffusion plays a significant role for the shape of the islands in sub-monolayer growth [14]. While a high mobility of adatoms along edges, so low barriers, will lead to the growth of compact island with straight edges, the opposite case will produce rough or dendritic islands.

Edge	Direction	Barrier [eV]
[111]	⟨111⟩	0.34 eV
[100]	⟨100⟩	0.65 eV

Table 1.2: Diffusion barriers of Fe on Fe(110) surface for diffusion along different edges [7].

1.3.3 Step Crossing

If an adatom arrives from the upper terrace, an additional energy barrier should be taken into account when descending the step. Ehrlich and Hudda noticed that the step acts as a reflective boundary for diffusing adatoms [15]. In a series of theoretical papers, Schwoebel attributed this reflection property to the existence of a repulsive potential barrier at the step-edge of the surface [16, 17]. An adatom crossing a step-edge may encounter an additional barrier, known as the Ehrlich-Schwoebel (ES) barrier, caused by a temporary reduced coordination (Fig. 1.8). Hereby, the adatom first has to lower its coordination with the atoms of the lattice before it can be bound in a high coordination site at the step.
Generally, the ES barriers are smaller than adatom diffusion barriers on a flat surface and often amounted to less than 20%. It must be made clear though that not all systems behave similar. Whereas FCC(100) (Face-centered Cubic) surfaces in general exhibit a large reflective barrier, often comparable to the diffusion barrier, FCC(111) surfaces do not show any step barrier.
In conditions far from thermal equilibrium, the growth morphology in vapour deposition can be determined by the relative height of the step barrier and the diffusion barrier. If E_s is comparable or higher than E_d, then all the adatoms arriving at a step-edge will be reflected. The adatoms will diffuse on the terrace, encounter each other and combine into clusters or islands. If all ES barriers are either zero or much smaller than E_d, then the step boundary is ineffective in reflecting adatoms. As a result, layer-by-layer growth will be more pronounced, provided that the atom deposition rate is low, so that the probability of having two adatoms encountering each other is much smaller than that for adatoms to reach a step edge.
Additionally, step crossing may take place by exchange, mostly at kinks where the ES barrier

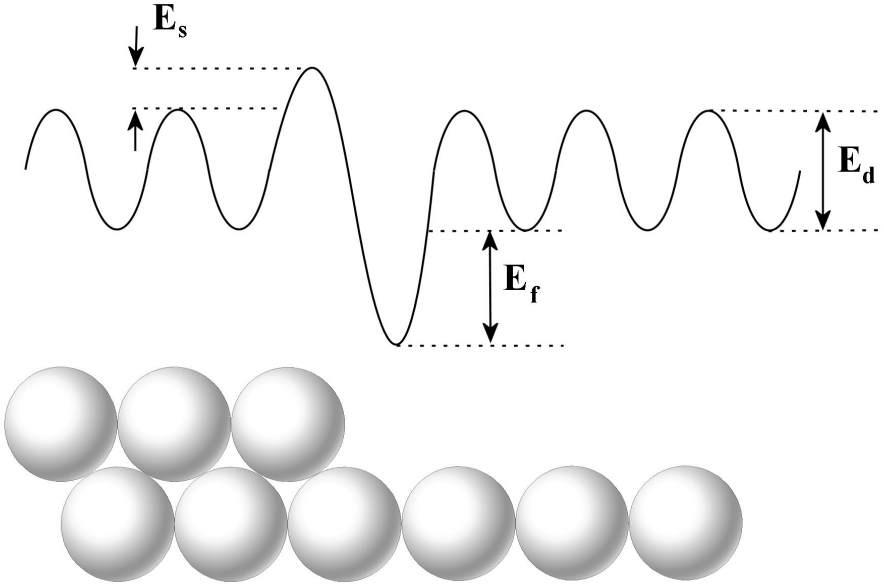

Figure 1.8: One dimensional schematic representation of the effective potential experienced by an adatom moving in the vicinity of a step. E_d is the activation barrier for diffusion, E_s is the Ehrlich-Schwoebel barrier, E_f is the adatom formation energy to the step.

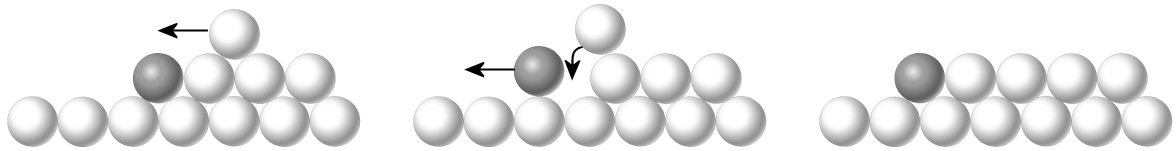

Figure 1.9: One dimensional drawing of the step-down diffusion by the exchange mechanism.

may be reduced [18]. The adatom pushes out an edge atom and takes its position while the edge atom is shifted. The energy barrier for this exchange is often comparable or lower than the ES barrier for hopping. The exchange mechanism is shown in Fig. 1.9.
Table 1.3 summarizes the ES barriers for Fe on Fe(110) at straight step-edges. There is a large difference in additional barrier along different step-edges on similar terraces. Adatoms reaching the [110] edge prefer to descent, while it's more likely to be reflected at a [111] step.[5]

Edge	Mechanism	Barrier [eV]
[111]	Hopping	0.31 eV
	Exchange	0.74 eV
[110]	Hopping	0.25 eV
	Exchange	0.16 eV
[100]	Hopping	0.26 eV
	Exchange	0.26 eV

Table 1.3: Ehrlich-Schwoebel barrier for Fe on Fe(110) when descending at a certain step-edge [7].

1.3.4 Diffusion on Contaminated Surfaces

Impurities incorporated in a surface change the potential energy of the surface. Two limiting cases can be considered [19]. First, the impurities can act as a barrier by changing the saddle point without influencing the binding energy. This is shown in Fig. 1.10(a-b). When the activation barrier for diffusion of the impurity $E_{d,imp}$ is larger than the one on a clean surface E_d, the impurity will act as a reflective barrier, promoting islands growth. A lower barrier enhances the adatom mobility on the surface. Secondly, the impurity can change the chemical reactivity by changing the binding energy for diffusing adatoms. Adatoms reaching an impurity with a higher reactivity than the bare surface, will have a stronger binding (Fig. 1.10(c)) and reduces the adatom mobility. Otherwise, a lower reactivity enhances the adatom mobility (Fig. 1.10(d)).
On real surfaces, incorporated impurities can change both the barrier properties and the trap properties. For instance, oxygen on metal surfaces act as a reflective barrier for diffusing metallic adatoms [20], but also the binding to oxygen is more likely due to the higher reactivity, so a diffusing adatom experiences a deeper well. The real potential energy diagram should be a combination of Fig. 1.10(a) and Fig. 1.10(c). Another example is Ir impurities on a Rh surface

[5] This difference can be visualised in Fig. 1.7

[21]. Here, the Ir will act as an attractive barrier with a higher reactivity (i.e. a combination of Fig. 1.10(b) and Fig. 1.10(c)). Typically, in these cases, the impurity is a pinning site for diffusing adatoms and act as a nucleation center for diffusing adatoms.
Impurities arriving from the vapour flux, will migrate on the surface. It is likely that the impurity binds to a step edge. If an impurity is incorporated at a step edge, the barrier for the step down diffusion can alter. The Ehrlich-Schwoebel barrier will either be lowered or increased. This is shown in Fig. 1.11. If the barrier is lowered, it will be easier for the adatom to reach a lower terrace. So the step down motion will be promoted. In contrast, a higher barrier will force the adatom to remain on the surface. It is likely that a change in magnitude of the ES barrier can change the structure evolution of thin films.

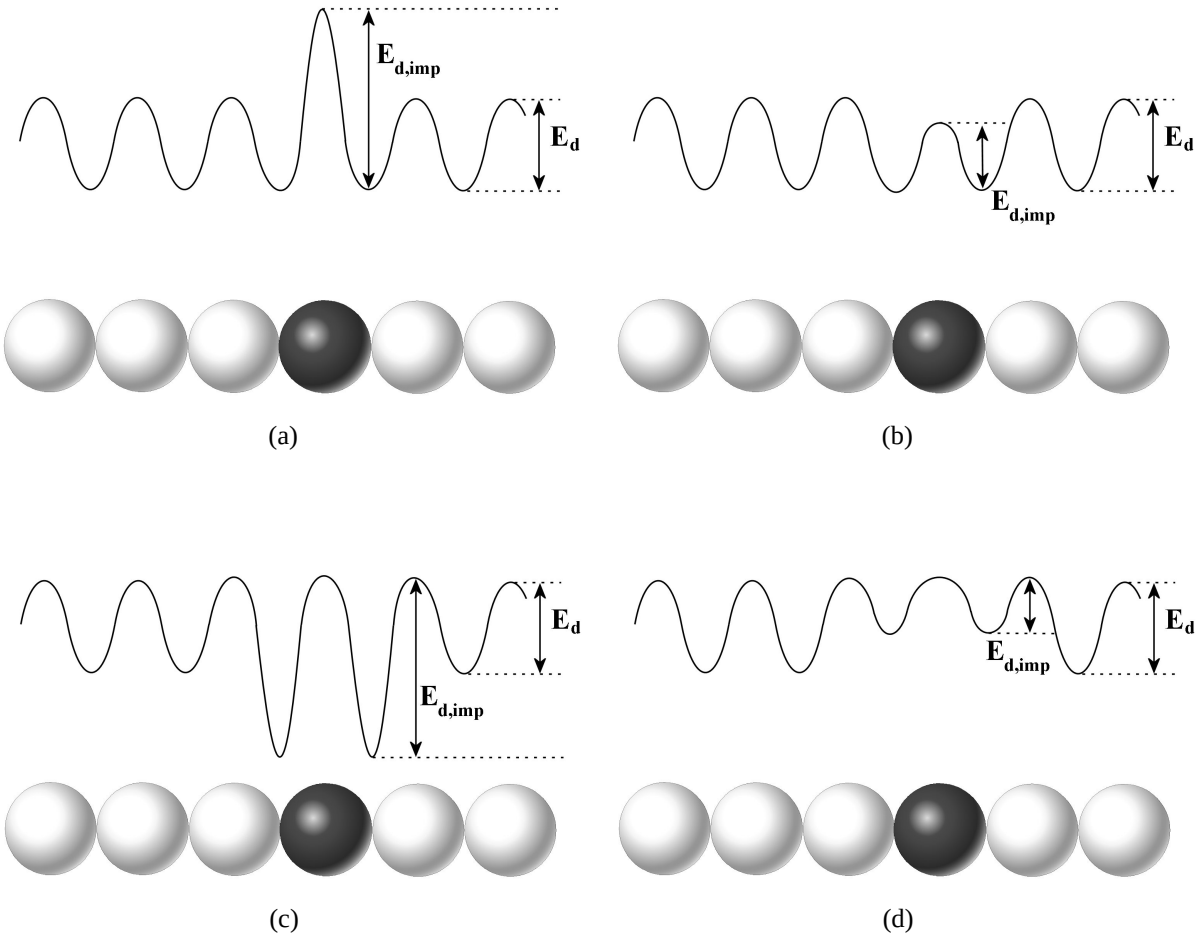

Figure 1.10: One dimensional schematic representation of the effective potential experienced by an adatom moving on a flat surface with an incorporated impurity which can act as a barrier (a-b) or as a trap (c-d).

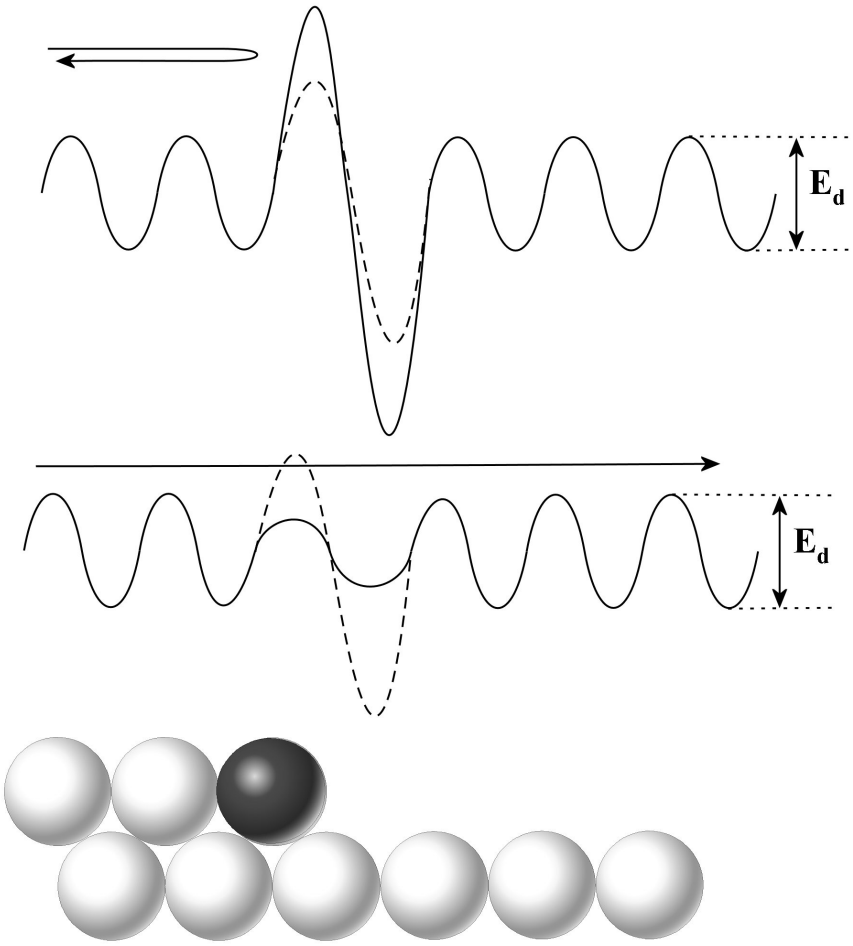

Figure 1.11: The change in ES barrier caused by the incorporation of an impurity at the step edge. The impurity will increase (*top*) or lower (*bottom*) the barrier, enhancing or preventing the step down motion. The dotted lines represent the potential in case the impurity is replaced by a pure atom.

1.4 Nucleation

As the deposition proceeds, the number of diffusing adatoms increases. Besides adsorption at special defect sites like steps, kinks or impurity pinning sites, there is a probability that the adatoms aggregate on a substrate terrace (Fig. 1.1). Adatoms may form pairs with other adatoms or attach to a larger cluster. The process where adatoms assemble and evolve into a stable cluster is known as nucleation.

There are two issues concerning nucleation: can nucleation occur and, if so, how fast. The answer to the question, whether nucleation is possible or not, is given by thermodynamics and is strongly linked to energy minimization. Although nucleation involves a small number of adatoms, the thermodynamical approach which is a macroscopical quantity, is a good approximation to describe nucleation.

The answer to the question how fast nucleation happens, is given by kinetics. Hereby, rate equations are used to determine the nucleation rate and the nucleation density.

1.4.1 Thermodynamical Aspects of Nucleation

For a comprehensive study on the formation of a cluster with size i from individual adatoms, the pairwise interactions between all the adatoms should be calculated. However, because the focus is on this film growth, general knowledge about the nucleation phenomenon is more important than the quantitative treatment. Therefore, thermodynamical approximation is used. Hereby, it is assumed that the total free energy is the sum of the surface free energy and the volume free energy. In the following, heterogeneous nucleation is described on a substrate by the capillary model [22, 23, 10, 24].
Assume that the diffusing adatoms on the substrate aggregate and form a liquid-like nucleus with mean radius r (Fig. 1.12). As the cluster grows, new surfaces and interfaces are created which result in an increase in surface free energy. Conversely, a larger cluster lowers the volume free energy. The change in total free energy to form such a cluster, is the sum of the surface free energy and the volume free energy and can be expressed as

$$\Delta G = \left(a_1 r^2 \gamma_{fv} + a_2 r^2 \gamma_{fs} - a_2 r^2 \gamma_{sv}\right) + a_3 r^3 \Delta G_V \tag{1.5}$$

where $a_1 r^2 \gamma_{fv}$ is the free energy to create a new surface between the nucleus and the vapour phase, $a_2 r^2 \gamma_{fs}$ is the free energy correlated to the substrate-nucleus interface and $a_2 r^2 \gamma_{sv}$ is attributed for the disappearance of the free substrate area. Hereby, f, v and s referring to film, vapour and substrate respectively and the combination of them for the referred interface. With this, a_1, a_2, a_3 are geometric constants defined as $a_1 = 2\pi(1-\cos\theta)$, $a_2 = \pi \sin^2\theta$ and $a_3 = \frac{\pi}{3}(2-3\cos\theta+\cos^3\theta)$ where θ is the contact angle (Fig. 1.12). ΔG_V is the volume free energy. An expression for the volume free energy ΔG_V can be derived from classical thermodynamics and is given by

$$\Delta G_V = \frac{kT}{\Omega} \ln \frac{P}{P_e} \tag{1.6}$$

where T is the substrate temperature, Ω is the volume of an adatom, P is the actual pressure of the species before condensation and P_e is the equilibrium vapour pressure, which depends exponentially on the growth temperature. The ratio P/P_e is known as the supersaturation S and is the driving force for nucleation. A decrease in P_e, e.g. by lowering the growth temperature, or an increase in P, e.g. by increasing the incident flux, results in an increase in S, and also in

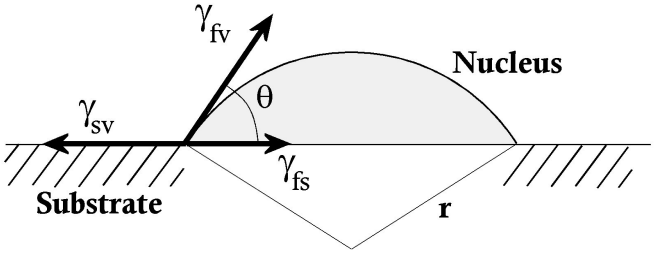

Figure 1.12: Schematic view of a spherical nucleus with radius r, formed on a substrate. The forces originating from the different surface energies γ that act on the nucleus are indicated. The subscript corresponds to the kind of interface with f, v and s stand for film, vapour and substrate, respectively.

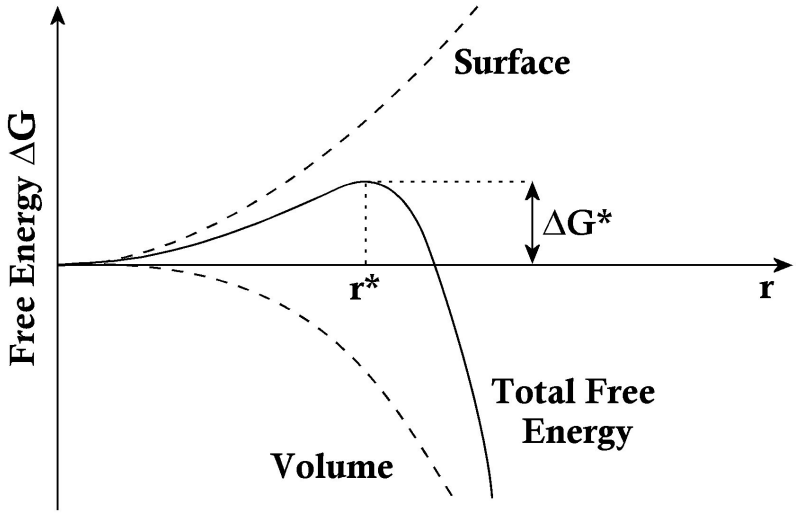

Figure 1.13: The change in free energy ΔG as a function of the cluster radius. ΔG^* is the free energy barrier for nucleation, r^* is the critical nucleus radius.

volume free energy.
The change in total free energy as a function of the cluster size is schematically shown in Fig. 1.13. The condition for thermodynamic equilibrium is obtained by maximization of equation 1.5, so $d\Delta G/dr = 0$. The equilibrium occurs at a critical nucleus size r*

$$r^* = \frac{-2(a_1\gamma_{fv} + a_2\gamma_{fs} - a_2\gamma_{sv})}{3a_3\Delta G_V} \tag{1.7}$$

which has a maximum in total free energy ΔG*

$$\Delta G^* = \frac{4(a_1\gamma_{fv} + a_2\gamma_{fs} - a_2\gamma_{sv})^3}{27a_3^2\Delta G_V^2} \tag{1.8}$$

As can be seen, there is an activation barrier ΔG^* for the nucleation of a stable nuclei. If the cluster radius $r < r^*$ then the cluster will shrink to lower its free energy. Hence, the cluster will disintegrate. On the other hand, if $r > r^*$ then the cluster will grow spontaneously to lower its free energy by capturing more adparticles.
When the substrate temperature increases, the supersaturation decreases exponentially[6], hence the critical radius increases. When the deposition rate increases, the supersaturation increases (on the assumption that the deposition rate is proportional to the pressure P of the species), so the critical radius decreases.
There are several shortcomings to the thermodynamically considerations. Firstly, macroscopical values of the surface energies are used for a few atoms. Also, this model doesn't take into account the dependence of the surface energy on the crystallographic orientation. Furthermore, in PVD

[6] The equilibrium vapour pressure increases exponentially with the deposition temperature.

processes, thin film growth is a kinetical (i.e. non-equilibrium) process, whereas expressions are derivated for an equilibrium process. Moreover, the interaction between neighbouring nuclei is neglected. It is disregarded that a stable nuclei may be absorbed by a larger growing nucleus (Section 1.5).

1.4.2 Kinetic Aspects of Nucleation

Once the nuclei are larger than r^*, they grow continuously by the incorporation of atoms. The atoms can be incorporated by direct capture from the vapour flux or by the capture of diffusing adatoms. The latter is most likely at the initial stage of growth. Nuclei may capture diffusing adatoms within a distance $\bar{x} = \sqrt{2Dt}$ within a given time periode t. As a result, it is unlikely that new nuclei will form within this distance. Omitting the theory for nucleation, the nucleation rate dN can be expressed as:

$$\frac{dN}{dt} = n_s e^{-\Delta G^*/kT} \cdot 4\pi r^{*^2} \cdot R \tag{1.9}$$

where n_s is the number of possible nucleation sites and R is the flux rate. The first term expresses the number density of critical nuclei, the second term accounts for the surface area of the critical nuclei and the last term takes into account the rate of incoming adatoms.
Another possibility to describe the dynamical process is by solving rate equations, which describe the change of cluster density in time. As a result, the island density can be expressed as

$$N \sim \left(\frac{J}{D}\right)^p \tag{1.10}$$

where J is the deposition flux, D is the diffusivity and p is a scaling exponent which depends on the number of adatoms compared to the number of islands.
Detailed information about the kinetical aspects of nucleation is far beyond the scope this thesis, but can be found in the literature [22, 25, 10].

1.4.3 Nucleation at Defects

When an adatom diffuses across a surface, it may encounter surface defects like vacancies, impurities or step-edges. Such defects serve as nucleation centers for diffusing adatoms (e.g. [26]). The nucleation density scales with the surface defect density. In continuous growth, it can happen that epitaxial growth is hindered. On a growing surface new nuclei may form, comparable to initial nucleation. This process is called repeated nucleation.
Codeposition of impurities modify also the nucleation properties, such as the nucleation density and the nuclei size. As a result, different microstructural and crystallographic features may evolve.

1.4.4 Growth Modes

When the nucleus is in equilibrium, the horizontal components of the forces surrounding the nucleus must keep in balance. From Fig. 1.12, Young's Equation can be obtained that

$$\gamma_{sv} = \gamma_{fs} + \gamma_{fv} \cos\theta \tag{1.11}$$

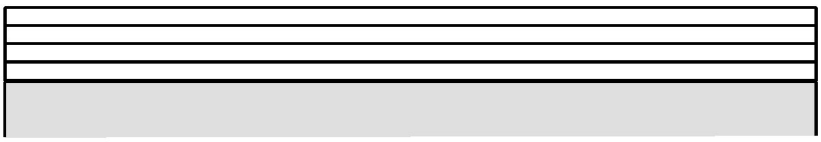

(a) Frank - Van der Merwe (FM)

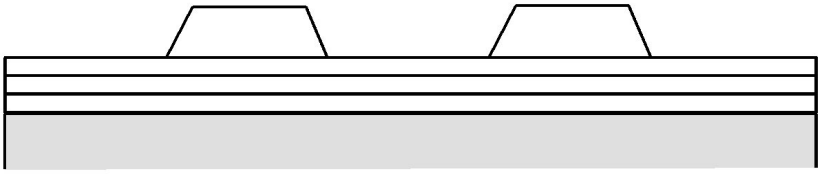

(b) Stranski - Krastanov (SK)

(c) Volmer - Weber (VW)

Figure 1.14: Schematic drawing of the three growth modes.

where θ is the contact angle.
Young's equation provides a way to understand the initial structure evolution, because nucleation on a substrate depends on the free energies. The nucleation process can be devided into three growth modes [22].

- $a_2\gamma_{sv} \geq a_2\gamma_{fs} + a_1\gamma_{fv}$: Frank - Van der Merwe (FM) growth or layer-by-layer growth
- $a_2\gamma_{sv} < a_2\gamma_{fs} + a_1\gamma_{fv}$: Volmer - Weber (VW) growth or island growth
- $a_2\gamma_{sv} = a_2\gamma_{fs} + a_1\gamma_{fv} + \epsilon$: Stranski - Krastanov (SK) growth or layer-by-layer followed by island growth

where ϵ is a parameter which takes into account the strain due to a lattice mismatch.
For layer-by-layer growth, the surface energy of the growing film is lower than the surface energy of the substrate. To reduce the total surface energy, the growing film will try to wet the substrate (Fig. 1.14(a)). As a result, a smooth and flat surface will be observed. Hereby, the contact angle θ will be 0°.
In case of island growth, the surface energy of the growing film is larger than the substrate surface energy. Therefore, it is energetically more favourable to form clusters and islands on the substrate (Fig. 1.14(c)). θ will varies between 0° and 180°. Mostly, the islands aim for a specific growth shape (kinetically or thermodynamically).
Special case is Stranski - Krastanov (SK) growth. At first, the surface is wetted, but after a few monolayers, islands are formed (Fig. 1.14(b)). This is caused by strain in the film that originates

from a mismatch in lattice constants between the film and the substrate. Typically, these are heterogeneous films (e.g. Ge on Si(001)) whereby the growing film has a lower surface energy than the substrate. By forming islands on top of the strained wetting layer, the film relaxes. A textbook case of SK growth with technological prospectives is the formation of quantum dots.

Important to remark is that not only the surface energy plays a role in the growth modes but also the magnitude of the diffusion barriers. For example, the presence of an ES barrier on specific crystallographic planes will promote island growth. Secondly, lattice strain which is present when the film is deposited on an amorphous substrate or a substrate with large lattice mismatch, will promote island growth. A third parameter which encourages VW growth is a high deposition rate. At high deposition rates, adatoms are not able to find the most stable place and nucleation on top of a terrace is more likely because the probability to encounter other adatoms and form a stable nuclei is high.
Another parameter which influences the growth modes are impurities. Incorporated at steps, impurities will lower or raise the barrier for step down diffusion (section 1.3.4), hence promote the FM or VW growth, respectively. In addition, impurities can change the surface energy and hence, the growth mode can change. For example, In is used as surfactant during the growth of GaN because In lowers the surface energy considerably and promotes layer-by-layer growth [27].

In this work, only island growth is observed, as the depositions are carried out on amorphous glass or polycrystalline substrates with a non-matching lattice parameter. Since single crystalline substrates with matching lattice parameters are not used, no epitaxial growth of the thin film on the substrate is expected. Therefore, in the rest of the discussion, island growth is tacitly assumed.

1.4.5 Island - Crystal Shape

Thermodynamical Equilibrium shape - Wulff's construction

At equilibrium, a small island or crystal will have a specific shape. The shape depends on the surface energy $\gamma_{(hkl)}$ of the crystallographic planes. At thermodynamical equilibrium, the total surface energy must be minimized at constant volume or

$$\sum_{(hkl)} \gamma_{(hkl)} A_{(hkl)} = \text{minimum} \tag{1.12}$$

where $A_{(hkl)}$ is the area corresponding to the (hkl) plane.
If $\gamma_{(hkl)}$ is isotropic, the equilibrium shape is a sphere. However, in most cases $\gamma_{(hkl)}$ is anisotropic and depends on the crystallographic orientation (Table 1.4). The crystal shape is constructed by drawing a perpendicular plane with respect to the crystallographic orientation, whereby the distance from the center to the plane is proportional to $\gamma_{(hkl)}$. This leads to the Wulffs theorem:

$$\frac{\gamma_1}{r_1} = \frac{\gamma_2}{r_2} \tag{1.13}$$

where r_1, r_2 are the distances from the center to the respective surfaces.
Fig. 1.15(a) shows the thermodynamical equilibrium shape of Cr, using the values in table 1.4.

(hkl)	γ - Cr [J/m^2]	γ - MgO [J/m^2]
(100)	1.228	1.25
(110)	1.029	3.02
(111)	1.244	3.86

Table 1.4: Surface energy of BCC Chromium [28] and rocksalt structured Magnesium Oxide [29], as determined by computational models.

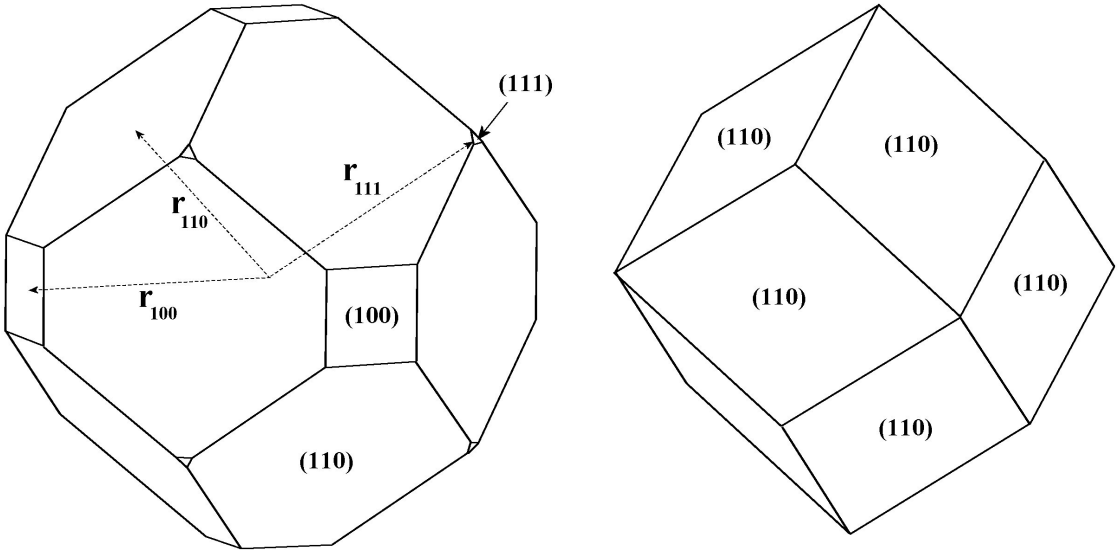

(a) Thermodynamical equilibrium shape (b) Kinetical growth shape

Figure 1.15: (a) Thermodynamical equilibrium shape of BCC Cr, constructed by Wulffs theorem, and (b) kinetical growth shape of BCC Cr.

Both the (100), (110) and (111) planes are present, but the planes with lowest surface energy dominate the equilibrium shape. For MgO, the difference in surface energy is so pronounced, that the equilibrium shape will only be composed of (100) planes. Hence, the thermodynamical equilibrium shape of MgO will be a cube. The planes which confine the island or the crystal, are called facets or faces.

Kinetical growth shape

The shape of a nucleus or island grown from the vapour phase, may deviate from the Wulff's construction because the growth from the vapour phase is a non-equilibrium process. Not only the surface energy plays a role in the island shape, but the normal growth rates of the different planes will determine the final crystal shape, i.e. the growth rate in the direction perpendicular to the crystallographic plane. Hence, kinetics will define the shape of the growing island.
The origin of the kinetical growth shape will be discussed in detail in chapter 4, but is quoted here briefly. The kinetical growth shape depends on the relative normal growth rate of the

different crystallographic planes. In its turn, the normal growth rate of a facet is proportional to the mobility of the corresponding crystallographic plane. With a high mobility, adatoms are able to diffuse towards the edges of the islands and contribute to the lateral growth. In contrast, planes that offer a low mobility to diffusing adatoms, will have a higher normal growth rate. The adatom mobility is determined by the number of nearest neighbours a plane offers to diffusing adatoms [30]. For instance, the adatom mobility will be high if the plane offers a low number of nearest neighbours to diffusing adatoms. Hence, it can be concluded that the normal growth rate of a plane is inversely proportional to the number of nearest neighbours that the plane offers to diffusing adatoms.
Generally, the slowest growing faces become the most prominent faces on the crystal as the fastest growing faces grow themselves out of existence. Initially, it may appear paradoxical, however it is a fundamental property of growing crystals. Fig. 1.15(b) shows the kinetical growth shape of BCC Cr. Because the (110) planes have the lowest normal growth rate, the kinetical growth shape of Cr consists only of (110) planes. (Chapter 4).
In the course of this work, the kinetically preferred growth shape is called the crystal habit. It is important to remark that the normal growth rate, hence the crystal habit can be influenced by several parameters. For example, impurities can modify the crystal habit. If impurities are incorporated on the surface, the chemical composition of the surface will change. Hence, it is possible that the chemical reactivity changes. As a result, the normal growth rate of the crystallographic planes can change and a different growth shape can be observed.

1.4.6 Crystal Growth

After nucleation, numerous discrete islands are dispersed on the substrate. The individual islands (and later on the grains) grow by the incorporation of atoms. These atoms can be incorporated by direct impingement from the vapour flux and/or by adsorption of migrating adatoms on the substrate. This process is referred to as crystal growth [31, 32]. In the early stages of the growth, the adsorption of diffusing adatoms is more significant than direct capture.
If surface diffusion is considerable, growth proceeds by local epitaxy on a crystal face. The mechanism for the epitaxial growth on facets is step flow. Adatoms attach to a step, in stead of nucleation on top of a terrace. As more and more adatoms are incorporated, it gives the impression that the step floats over the surface. As a result of crystal growth, a large number of discrete single crystalline grains with a specific crystal shape[7] are dispersed on the substrate. Hereby, restructurative grain growth is neglected but will be discussed in the next section (section 1.5).
There is no driving force in crystal growth to cause an orientation selection.
It is important to remark that crystal growth occurs also in the subsequent growth stages. Actually, it is the only possibility for the thin film to incorporate new atoms.

[7] In sputter deposition, the kinetical growth shape is obtained as the deposition is carried out far from thermodynamical equilibrium.

1.5 From Nucleation to Film Thickening

During the nucleation stage, a lot of islands are formed on the substrate. Generally, these islands will have a random orientation distribution. As the deposition proceeds, the island density increases until a maximal density is obtained. At a certain point, islands feel a mutual interaction. Depending on the adatom mobility and the energy of the incorporated adatoms, there are two possibilities for the further structure evolution of the thin film. If the energy of the atoms is high enough, restructurative grain growth can occur. Restructurative grain growth will have a specific activation energy. If the energy of atoms in a grain is higher than this activation energy, the atoms are called active.

Formation of an Immobile Grain Boundary

The first case is when the atoms are inactive. This corresponds to a low adatom mobility on the substrate. Hereby, the adatom energy is high enough in order to find the most stable site on a grain. In this case, the islands grow by adsorbing adatoms via crystal growth. At a specific moment, the islands or call them grains make contact. At the point of contact, a grain boundary is formed. Owing to the low energy, the grain boundary is immobile and remains during further growth. These grain boundaries cause a large stress in the film [33]. In case of inactive atoms, the grains retain the orientation of the nucleation stage.

Restructurative Grain Growth

The second possibility is that the atoms are active and restructurative grain growth will occur. Restructurative grain growth is a collective name for processes which modify the initial structure of the islands. The growth stage at which restructurative grain growth occurs, is known as the coalescence stage. Of all the restructurative grain growth process, the three most important processes are discussed.
A first phenomenon is the consumption of small islands by larger ones, referred to as coarsening. The driving force for coarsening is the difference in mean energy per atom of different-sized islands. The energy per atom scales with the surface-to-volume ratio, hence the size of the island. Atoms from a small islands are detached, diffuse towards the larger islands due to a concentration gradient and attach to the larger island. The rate of coarsening increases as the size difference increases. As a result only large islands or grains survive.
A second phenomenon is also based on an energy difference. Here, the driving force of the process is the minimization of surface and interface energy. It is already discussed that the surface energy of the various crystallographic orientations is anisotropic. Therefore, the distribution of islands with random orientation which exists at nucleation, will evolve into an island distribution which favours islands with an orientation with a minimum in surface and interface energy. Hereby, the planes with the lowest surface energy parallel to the substrate will be favoured. Hence, orientation selection will occur. The process where two differently oriented islands or grains evolve into a new single crystal, but also the shrinkage of smaller islands, occurs very fast in a liquid like process. Moveover, it is the most effective process to cause a preferential orientation in thin film growth.
When the grains are consumed, a bare substrate is left behind. Adatoms from the vapour phase

may aggregate in this region and form a new nuclei, which will grow between primary islands. This process is called secondary nucleation.
Remark that the first two restructurative grain growth processes can occur before the various grains make contact. Because the grains continuously incorporated new arriving adatoms from the vapour phase, the grains continue to grow. At a given time, grains of about the same size, will make contact. At the point where two grains make contact, a new surface is created called the grain boundary. This surface has an energy γ_{gb} which is lower than the sum of the surface free energies of both grains. At impingement, the grains are already close to the lowest surface and interface energy and to the preferred orientation. When the atoms in the grain boundary are active, e.g. at a high substrate temperature, atoms from one grain can attach to the other grain by changing their bonding. The driving force is the reduction of the total grain boundary area, which lowers the thin film energy. This process is called grain boundary migration. This process, also known as normal grain growth [34], is much slower and continues even when the film is continuous. A rule of thumb is that grain boundary movement stops when the grain width is three times higher than the film thickness.

It is obvious that all these restructurative grain growth processes will have a specific activation energy. Because for all these processes, adatoms have to detach from a grain and attach to another grain, the activation energy of all restructurative grain growth processes will be in the same order.

1.6 Structure Zone Model

In previous sections, many fundamental phenomena of structure formation have passed in order to understand to structure evolution of polycrystalline thin films. A convenient way to describe the structure evolution of polycrystalline thin films is the use of a so-called Structure Zone Model (SZM), which describes the change of microstructure as a function of some process parameters.
In despite of the regular use of the temperature as a variable, the adparticles mobility is a much better parameter to describe the SZM, taking into account both the energy of the adparticles and the surface diffusion barriers. This is necessary because the adparticle mobility is more than only a thermal activated process. For example, in sputter deposition, low energetic ions reach the growing film and contribute to the adparticle mobility. By changing the ion-to-atom ratio, e.g. by increasing or reducing the deposition rate, the energy provided to migrating adatoms as well as the energy dissipated to the growing film decreases or increases. Mahieu et al. [35] and Petrov et al. [32] reviewed the SZM, emphasizing the adatom mobility. Nevertheless, the homologous temperature T_s/T_m is also used to describe the structure evolution because it's difficult to obtain experimental information about the mobility of adparticles or about the activation barriers for diffusion of a specific material. The substrate temperature T_s is normalized with the melting temperature T_m to include material information like diffusion because the diffusion barriers scales with the binding energy and the melting temperature. In the following discussion, the homologous temperature and adatom mobility are used simultaneously.
Next to the mobility, a lot of other parameters (impurities, energetic bombardment,. . .) influence the structure evolution of thin film. This leads to new or extended structure zone models. Beside the conventional SZM [36, 37, 38, 39, 40, 41], Barna et al. [31] proposed a revised SZM, taking

into account the codeposition of trace elements. Impurities will cause a shift in the different zones and explains the occurrence of zone III.
Generally, it can be summarized that SZM are skilful as guideline and classification system, but one should be careful when using the SZM quantitatively.

1.6.1 Zone I

In zone I, the adatom diffusion is negligible. The adatom energy is too low to overcome the surface diffusion barriers (section 1.3). Consequently, arriving adatoms stick at the site of impingement. This is also called the hit-and-stick regime. This structure can be described by a ballistic model [42].
At nucleation, there is a high island density. These islands are mostly non-crystalline as the adatoms aren't able to find an energetic favourable place. Besides, it is obvious that no restructurative grain growth can occur. Because there is no diffusion, the thin film can only evolve by the direct capture from the vapour flux.
The thin film will consist of fibrous columns with overhanging atomic structures. The overhanging structure, together with the statistical roughened surface, shadows lower parts of the film, causing a porous structure (Fig 1.16). Additionally, if there is a spread on the direction of the incoming material flux, self-shadowing will be more pronounced and more and larger voids between the columns are observed. At oblique incidence, the columns are tilted towards the incoming material flux. The relation between the angle of incidence α and the columnar inclination angle β is given by the tangent rule: $\tan(\beta) = 1/2 \tan(\alpha)$ [43, 44].
In absence of diffusion, the thin film won't have a preferential orientation. The orientation at nucleation, non crystalline or randomly oriented, is conserved in the further film growth as the columns grow independently. Remark that shadowing won't cause an orientation selection, because the growth of the columns is pure statistical and not orientation dependent.

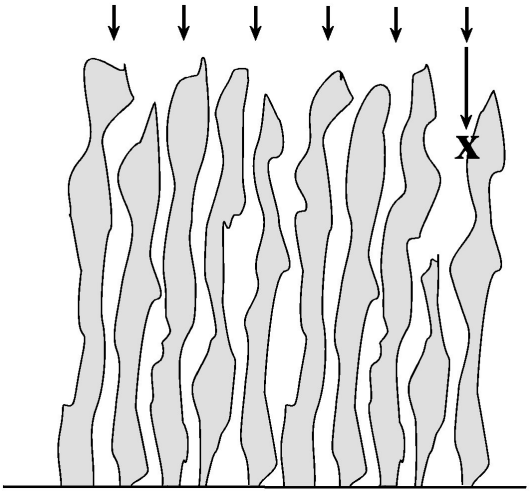

Figure 1.16: Schematic drawing of a thin film deposited with a zone I structure.

It should be mentioned that such a zone I structure can also evolve at conditions when adatom diffusion is possible. This occurs at very high deposition rates when the adatoms are buried very rapidly under other arriving particles and don't have time to move around.
The density of the film can be increased by knock-on events of energetic particles [45]. The energetic particles destroy the overhang structures and the voids fill up. Though, no preferential orientation will be observed. Mahieu assigned another zone to the structure evolution caused by energetic bombardment and called it zone Ib [35].
In sputter deposition the energy of the sputtered particles is typically in the order of a few eV, which is much more than the surface diffusion barriers. Hence, a zone I structure isn't observed in sputter deposited MgO, Cr and InN.

1.6.2 Zone T

By increasing the energy of the incoming adatom or by increasing its energy thermally, adatoms will be able to overcome the surface diffusion barriers and will diffuse on the surface. However, the adatom energy is too low to have restructurative grain growth.
Initially, nucleation of crystalline islands on the substrate occurs. These islands have a random orientation distribution. As the adatoms are able to diffuse on the island, the island will grow according to the kinetically determined growth shape as described in section 1.4.5. As a result the substrate will be covered by grains which have all the same crystal habit but which have a different crystallographic orientation. The grains grow by the capture of diffusing adatoms or by the capture directly from the vapour flux. Growth on the crystal facets continues by local epitaxy because self-diffusion is considerable.[8] At the point of impingement, a grain boundary is formed. Because the activation energy for restructurative grain growth is too high in comparison to the adatom energy, the grain boundary is immobile throughout the complete film thickness.
Although all facets have a similar growth rate, some grains will have a higher perpendicular growth rate with respect to the substrate. As can be seen in Fig. 1.17(a) grains of which the facets have the highest tilt angle with respect to the substrate, will have the highest perpendicular growth rate and will overgrow the others. As a result, a preferential out-of-plane orientation evolves. The anisotropy in perpendicular growth rate is characteristic for zone T growth. The survival of the fastest is also referred to as evolutionary selection [46] and is illustrated in Fig. 1.17(b).
It's important to remark that the crystallographic texture as well as the microstructure changes throughout the film thickness. At the initial stages of the growth, small nuclei with a random orientation will be observed. The grains will be truncated by a crystal habit. Due to the random crystallographic orientation, the crysta habit will be randomly oriented. Later on, specific oriented grains will overgrow the others which result in V-shaped columns with faceted tops. Most columns are overgrown after 300 nm. Hence, the V-shape is most pronounced in this region. A typical zone T structure is shown in Fig. 1.18.
If there is oblique material incidence, also V-shaped columns are observed. However, in contrast with zone I, the tilt angle of the columns doesn't obey the tangent rule because the adatoms are able to diffuse. Through this, the columns will be less tilted towards the flux.

[8] Self-diffusion is the diffusion of an adatom on a surface consisting of the same adatoms. For example, diffusion of Cr on Cr(110).

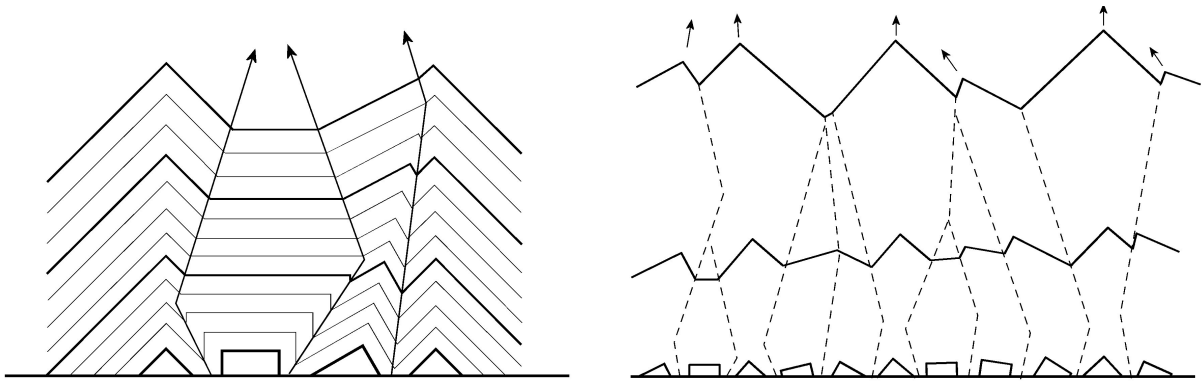

(a) (b)

Figure 1.17: (a) Overgrowth mechanism of different oriented grains truncated by planes with lowest normal growth rate [35], (b) van der Drift construction for zone T growth, illustrating the V-shaped columnar growth [46].

The growth rate anisotropy as well as the columnar faceting play a key role in the structure evolution of some biaxially aligned thin films. This will be illustrated in more detail in chapter 4, which clarifies and models the out-of-plane and in-plane alignment in zone T conditions.
It is not mentioned before but it is important that adatoms can move from one grain to another. Mahieu et al. [35] discussed that when the diffusion of adatoms is restricted to a single grain, faceted grains will grow, but no preferential out-of-plane orientation evolves as the grains grow independent and overgrowth is not possible. This growth is subdivided in another zone, called Zone Ic. However, in this work, the thin films which exhibit a zone Ic structure are not observed.

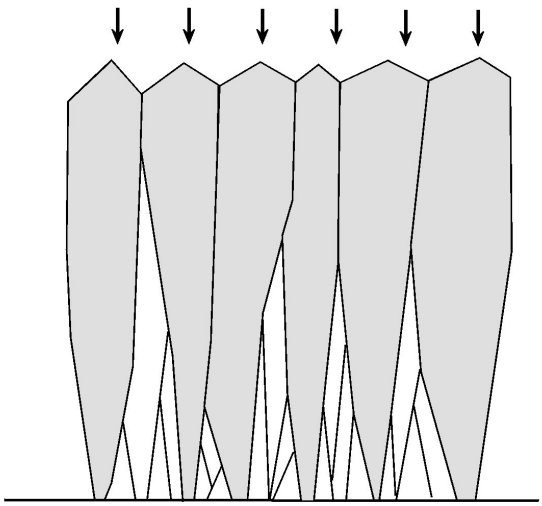

Figure 1.18: Schematic drawing of a thin film deposited with a zone T structure.

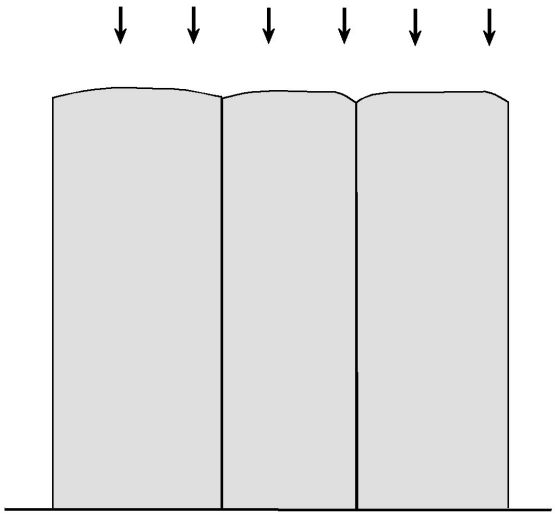

Figure 1.19: Schematic drawing of a thin film deposited with a zone II structure.

1.6.3 Zone II

Further increasing the adatom energy, restructurative grain growth will occur. At nucleation small islands are formed on the substrate which are randomly oriented. At the coalescence stage, restructurative grain growth is pronounced in order to reduce the surface and interface energy. As mentioned in section 1.5, larger grains grow at the expense of smaller grains or unfavourably oriented grains are consumed by "good" oriented grains. This reduces the number of islands that were formed during nucleation. Because the thin film aims for the lowest surface and interface energy, only grains which have a plane with the lowest surface energy parallel to the substrate, will be stable. The crystallographic orientation perpendicular to the plane with lowest surface energy will be the preferential orientation.
At impingement, a grain boundary is formed, however, this grain boundary is mobile. To reduce the interface and grain boundary energy, the grain boundaries will be straight and perpendicular to the substrate. As a result broad equiaxed columns evolve in the film (Fig. 1.19). The width of the columns increases with increasing mobility. Increasing the energy even more, will never cause a change to another zone, although a lot of people discussed the existence of a zone III in terms of bulk diffusion. A zone III structure is characterized by a globular bulk structure with grain boundaries that are not perpendicular to the substrate. However, the structure grown in zone II is the most stable growth structure. A globular structure cannot occur in pure films during deposition. Only in post-deposition processes, like annealing, such a globular bulk structure can evolve by recrystallization if the ratio in diameter versus column length is less than 0.1. In non-pure conditions, a globular structure can be obtained in the deposition process.

1.6.4 And what about impurities?

The codeposition of impurities is inevitable in every deposition system. The main source of impurities is the residual gas after pumping down the deposition system. Even in small concentrations, the influence of impurities on the growth is pronounced. The impurities will act on the atomistic processes during all growth stages (detailed information is given in previous sections) and therefore change the growth process. A change in the SZM is expected. Barna et al. studied the influence of impurities on the fundamental processes of structure formation and examined the change in the SZM with codeposition of impurities, resulting in a revised structure zone model [31, 32, 47, 48, 49].
Impurities that are soluble into the crystal lattice, have no effect on the morphology nor the crystallographic texture because they are dissolved into the crystal lattice without building up their own phase. These impurities won't change the structure zone model. For the insoluble impurities, two types can be distinguished. Promoters enhance the diffusion on a surface by lowering the ES barriers, which results in larger grains or an improvement in layer-by-layer growth during epitaxial growth. Inhibitors form an own phase, limiting the surface diffusion. This minority phase builds up on the surface as a tissue phase or in the grain boundary. This leads to smaller grains and a strong variation in the structure evolution. Therefore the effect of an inhibitor on the SZM will be discussed.[9]

In zone I, the adatoms don't have any mobility. Impurities that are codeposited, are also fixed at the site of impingement and the ballistic model holds. A similar microstructure as described in pure conditions will be observed. Also, no preferred orientation will develop.
In zone T, the boundary with zone I shifts to higher energies with increasing impurity concentration because the impurities limit the adatom mobility. Typical for zone T growth, is the growth according to a specific crystal habit. This results from a difference in normal growth rate of the crystallographic planes. It is known that impurities behave differently on the various crystallographic planes due to a difference in chemical interaction [50]. Owing to this anisotropy, certain crystal faces can be blocked, while other can grow unhindered. Therefore, the normal growth rate of the various faces will be different from the pure conditions, through which another crystal habit and microstructure evolves. Together with a change in crystal habit, a change in preferential orientation can occur. A comprehensive discussion about this effect is given in Chapter 6, which is completely dedicated to the influence of codeposited impurities on the structure evolution of biaxially aligned thin films grown in zone T. At high impurity concentration, the growth on all faces is blocked and growth proceeds by repeated nucleation. A nanocrystalline structure with 3D nuclei will evolve.
With the presence of impurities, restructurative grain growth in zone II will be incomplete because impurities prevent coarsening. The islands will be decorated with impurities, they stop the step flow and pin the island motion. Also in the grain boundaries impurities accumulate, which make the grain boundaries immobile. A bimodal structure evolves at low impurity concentrations. Therefore, a shift of the boundary between zone T and zone II to higher energies will be observed. Additionally, impurities will act differently on the various faces, similar to in zone T.

[9] Barna's SZM is mainly based on experimental observations of the growth of Al with various concentrations of oxygen. At room temperature, pure Al grows in Zone II because of the low diffusion barriers. With increasing oxygen concentrations, a change from zone II to zone T to zone I is observed [31, 48, 49].

Because in zone II the film tends to minimize the surface and interface energy, a change in texture may occur, if the planes with lowest surface energy cannot grow freely or if the chemical state, hence the surface energy, has increased due to the impurities. At high impurity concentration, zone II disappears completely.
Special about thin film growth with a minority phase, is the appearance of an additional zone III. Zone III is characterized by globular grains present throughout the complete film thickness, and a random crystallographic orientation. Depending on the impurity concentration, the globular grains range from microcrystalline to nanocrystalline. In pure conditions, there is no cause for the existence of zone III. At low impurity concentrations, a surface covering layer develops faster at the highest mobilities (i.e. far in zone II). This impurity layer stops the growth of the equiaxed crystals and growth proceeds by repeated nucleation. As a consequence, the thin film is composed of three dimensional grains with a random orientation. With increasing impurity concentration, the boundary for zone III shifts to lower energies, until at very high concentration zone I is reached.
Fig. 1.20 shows the revised Structure Zone Model as described above and as proposed by Barna [31, 49]. Depending on the impurity concentration, different zones at different substrate temperature or mobility appear.

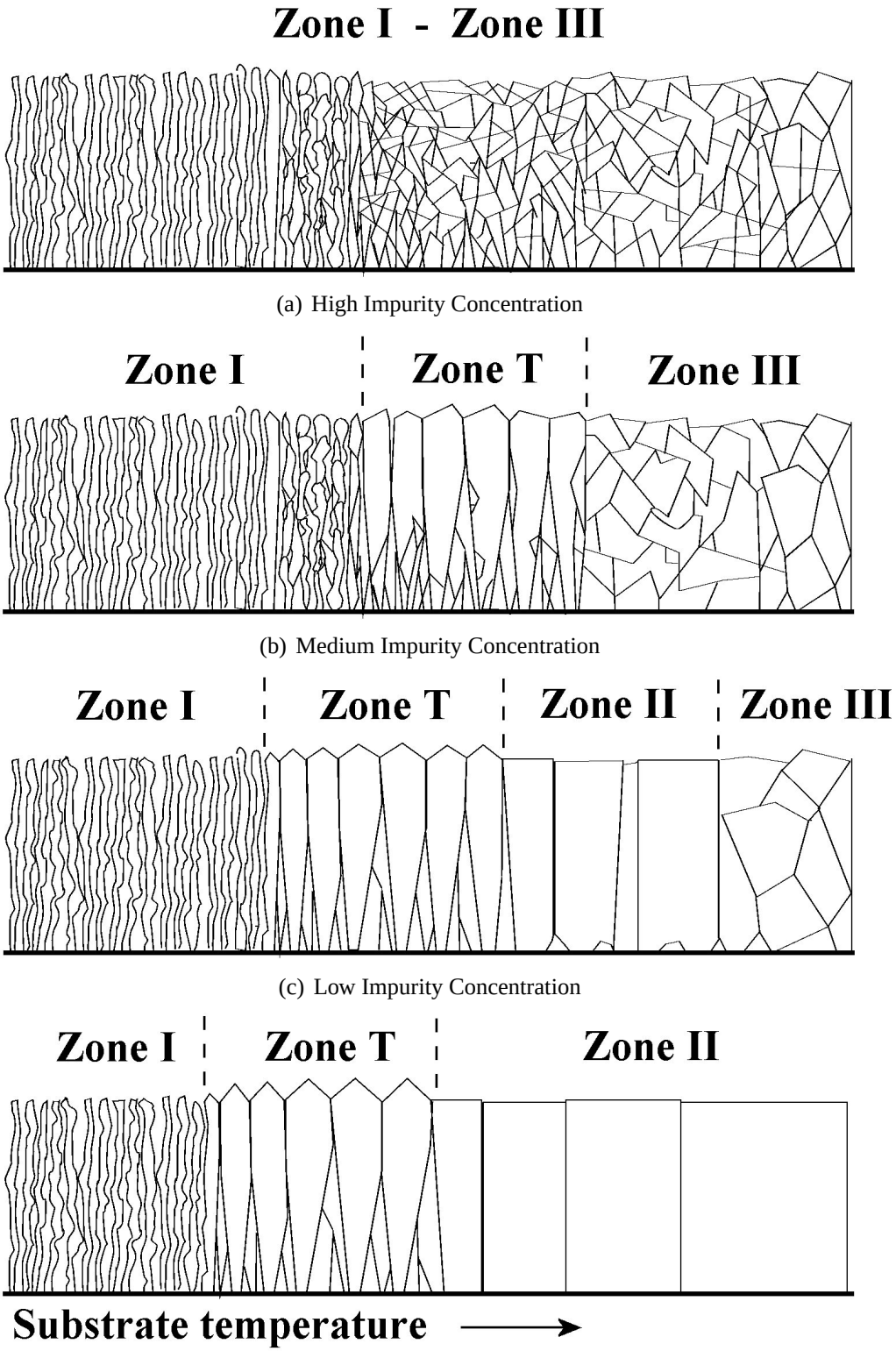

(a) High Impurity Concentration

(b) Medium Impurity Concentration

(c) Low Impurity Concentration

(d) Pure Conditions

Figure 1.20: The revised SZM as proposed by Barna for different impurity concentrations [31, 49].

Bibliography

[1] A. Zangwill, Physics at Surfaces, forth Edition, Cambridge University Press, 1988.

[2] H. Lüth, Solid Surfaces, Interfaces and Thin Film, forth Edition, Springer-Verlag Berlin Heidelberg New York, 2001.

[3] M. C. Tringides, Surface Diffusion - Atomistic and Collective Processes, Plenum Press, New York, 1997.

[4] T. Ala-Nissila, R. Ferrando, S. C. Ying, Collective and single particle diffusion on surfaces, Advances in physics 51 (3) (2002) 949–1078.

[5] P. Nikunen, I. Vattulainen, T. Ala-Nissila, Effects of quenched impurities on surface diffusion, spreading, and ordering of O/W(110), J. Chem. Phys. 117 (14) (2002) 6757–6765.

[6] E. G. Seebauer, C. E. Allen, Estimating surface diffusion coefficients, Prog. Surf. Sci. 49 (3) (1995) 265–330.

[7] A. C. Schindler, Theoretical aspects of growth on one and two dimensional strained crystal surfaces, Ph.D. thesis, University of Duisenberg - Essen (1999).

[8] J. A. Stroscio, D. T. Pierce, R. A. Dragoset, Homoepitaxial growth of iron and a real space view of reflection-high-energy-electron diffraction, Phys. Rev. Lett. 70 (23) (1993) 3615–3618.

[9] Z. Zhang, M. G. Lagally, Atomistic processes in the early stages of thin-film growth, Science 276 (1997) 377–383.

[10] J. A. Venables, Surface and Thin Film Processes, 1st Edition, Cambridge University Press, 2000.

[11] J. Liu, C. W. Wu, T. T. Tsong, Measurement of the binding energy of kink-site atoms of metals and alloys, Phys. Rev. B 43 (14-15) (1991) 11595–11604.

[12] O. Pierre-Louis, M. R. DOrsogna, T. L. Einstein, Edge diffusion during growth: The kink Ehrlich-Schwoebel effect and resulting instabilities, Phys. Rev. Lett. 82 (18) (1999) 3661–3664.

[13] M. G. Lagally, Z. Zhang, Thin-film cliffhanger, Nature 417 (2002) 907–910.

[14] U. Köhler, C. Jensen, C. Wolf, A. C. Schindler, L. Brendel, D. E. Wolf, Investigation of homoepitaxial growth on bcc surfaces with stm and kinetic monte carlo simulation, Surf. Sci. 454 (2000) 676–680.

[15] G. Ehrlich, F. G. Hudda, Atomic view of surface self-diffusion: Tungsten on tungsten, J. Chem. Phys. 44 (3) (1966) 1039–1049.

[16] R. L. Schwoebel, E. J. Shipsey, Step motion on crystal surfaces, J. Appl. Phys. 37 (10) (1966) 3682–3686.

[17] R. L. Schwoebel, Step motion on crystal surfaces II, J. Appl. Phys. 40 (2) (1969) 614–618.

[18] J. Merikoski, I. Vattulainen, J. Heinonen, T. Ala-Nissila, Effect of kinks and concerted diffusion mechanisms on mass transport and growth on stepped metal surfaces, Surf. Sci. 387 (1997) 167–182.

[19] J. Krug, New mechanism for impurity-induced step bunching, Europhys. Lett. 60 (5) (2002) 788–794.

[20] H. Over, Crystallographic study of interaction between adspecies on metal surfaces, Prog. Surf. Sci. 58 (4) (1998) 249–376.

[21] G. L. Kellogg, Direct observation of substitutional-atom trapping on a metal surface, Phys. Rev. Lett. 72 (11) (1994) 1662–1665.

[22] J. A. Venables, G. D. T. Spiller, M. Hanbucken, Nucleation and growth of thin-films, Rep. Prog. Phys. 47 (4) (1984) 399–459.

[23] J. B. Hudson, Surface Science, 1st Edition, John Wiley & Sons, Inc., New York, 1998.

[24] M. Ohring, Materials Science of Thin Films, 2nd Edition, Academic Press, San Diego, 2002.

[25] H. Brune, Microscopic view of epitaxial metal growth: Nucleation and aggregation, Surf. Sci. Rep. 31 (3-4) (1999) 125–229.

[26] J. Krug, P. Politi, T. Michely, Island nucleation in the presence of step-edge barriers: Theory and applications, Phys. Rev. B 61 (20) (2000) 14037–14046.

[27] F. Widmann, B. Daudin, G. Feuillet, N. Pelekanos, J. L. Rouvire, Improved quality GaN grown by molecular beam epitaxy using in as a surfactant, Appl. Phys. Lett. 73 (18) (1998) 2642–2644.

[28] J. M. Zhang, F. Ma, K. W. Xu, Calculation of the surface energy of BCC metals by using the modified embedded-atom method, Surf. Interface Anal. 35 (8) (2003) 662–666.

[29] G. W. Watson, E. T. Kelsey, N. H. de Leeuw, D. J. Harris, S. C. Parker, Atomistic simulation of dislocations, surfaces and interfaces in MgO, J. Chem. Soc., Faraday Trans. 92 (3) (1996) 433–438.

[30] H. C. Huang, G. H. Gilmer, T. D. de la Rubia, An atomistic simulator for thin film deposition in three dimensions, J. Appl. Phys. 84 (7) (1998) 3636–3649.

[31] P. B. Barna, M. Adamik, Fundamental structure forming phenomena of polycrystalline films and the structure zone models, Thin Solid Films 317 (1998) 27–33.

[32] I. Petrov, P. B. Barna, L. Hultman, J. E. Greene, Microstructural evolution during film growth, J. Vac. Sci. Technol. A 21 (5) (2003) S117–S128.

[33] H. Windischmann, Intrinsic stress in sputter-deposited thin films, Crit. Rev. Solid State Mater. Sci. 17 (6) (1992) 547–596.

[34] C. V. Thompson, Structure evolution during processing of polycrystalline films, Annu. Rev. Mater. Sci. 30 (2000) 159–190.

[35] S. Mahieu, P. Ghekiere, D. Depla, R. De Gryse, Biaxial alignment in sputter deposited thin films, Thin Solid Films 515 (4) (2006) 1229–1249.

[36] B. A. Movchan, A. V. Demchishin, Investigations of the structure and properties of thick Ni, Ti, W, Al_2O_3 and ZrO_2 vacuum condensates, Phys. Met. Metallogr. 28 (1969) 83–89.

[37] J. A. Thornton, Influence of apparatus geometry and deposition conditions on structure and topography of thick sputtered coatings, J. Vac. Sci. Technol. 11 (4) (1974) 666–670.

[38] J. A. Thornton, High rate thick film growth, Ann. Rev. Mater. Sci. 7 (1977) 239–260.

[39] C. R. M. Grovenor, H. T. G. Hentzell, D. A. Smith, The development of grain-structure during growth of metallic-films, Acta Metall. 32 (5) (1984) 773–781.

[40] R. Messier, A. P. Giri, R. A. Roy, Revised structure zone model for thin film physical structure, J. Vac. Sci. Technol. A 2 (2) (1984) 500–503.

[41] J. A. Thornton, The microstructure of sputter-deposited coatings, J. Vac. Sci. Technol. A 4 (6) (1986) 3059–3065.

[42] A. G. Dirks, H. J. Leamy, Columnar microstructure in vapor-deposited thin films, Thin Solid Films 47 (3) (1977) 219–233.

[43] L. Abelmann, C. Lodder, Oblique evaporation and surface diffusion, Thin Solid Films 305 (1997) 1–21.

[44] Paritosh, D. J. Srolovitz, Shadowing effects on the microstructure of obliquely deposited films, J. Appl. Phys. 91 (4) (2002) 1963–1972.

[45] K. H. Müller, Ion-beam-induced epitaxial vapor-phase growth: A molecular-dynamics study, Phys. Rev. B 35 (15) (1985) 7906–7913.

[46] A. Van der Drift, Evolutionary selection, a principle governing growth orientation in vapor-deposited layers, Philips Res. Rep. 22 (1967) 267–288.

[47] P. B. Barna, Impurity effects in the structural development of vacuum deposited thin films, Proc. IX IVC-V ICSS, Madrid (1983) 382–396.

[48] P. B. Barna, M. Adamik, Science and Technology of Thin Films, 1st Edition, World Scientific, 1995, *Chapter: Growth Mechanism of Polycrystalline Thin Films*.

[49] P. B. Barna, Protective Coatings and Thin Films: Synthesis, Characterization and Applications, 1st Edition, Kluwer Academic Publishers, 1997, *Chapter: Formation and Characterisation of the Structure of Surface Coatings*.

[50] P. B. Barna, Proc. Diagnostics and Application of Thin Films, Inst. Phys. Publ., Bristol, 1992, *Chapter: Crystal growth and recrystallization during structure evolution of thin films*.

Chapter 2

Sputter Deposition of Thin Films

2.1 Introduction

In sputter deposition, a cathode which contains the source material, also referred to as the target, is kept at negative potential with respect to the chamber walls and the substrate. In the presence of a gas, usually a rare gas like Ar, a glow discharge is created. In this glow discharge, Ar^+ ions are accelerated towards the cathode in an electric field. Upon impingement, the energetic ions provokes several interactions of which some are illustrated in Fig. 2.1. For example, the energetic Ar^+ ions can cause a collision cascade in the target material. Atoms are displaced and

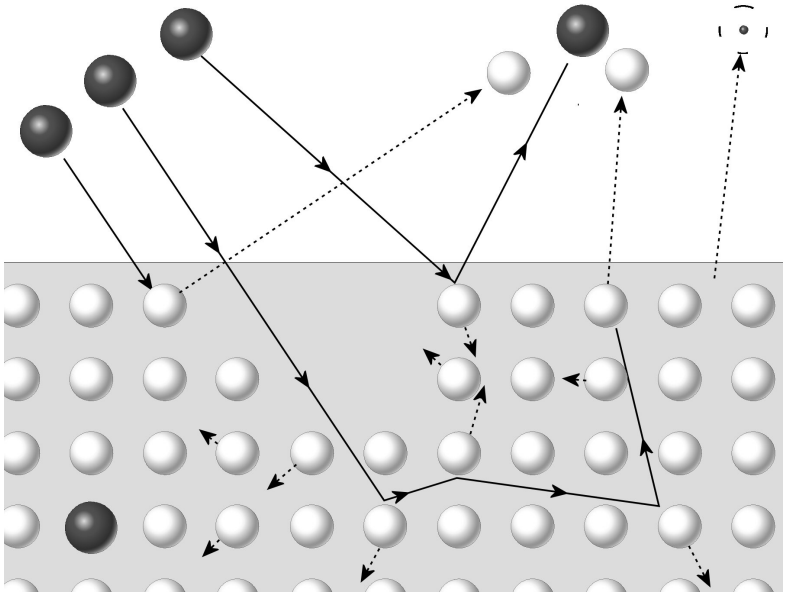

Figure 2.1: Schematic drawing of several ion-solid interaction processes: energetic Ar^+ ions (black) bombard a surface, which can result in a collision cascade. Hereby, atoms are displaced and some of them can leave the solid. Other processes that can occur, are the creation of secondary electrons, ion implantation, reflection, etc.

some of them can escape from the surface to the vapour phase. The process that generates atoms and clusters by an ion-solid interaction, is called sputtering.
Statistically, each ion generates a number of sputtered particles. These particles leave the target with a specific energy and spatial distribution. Furthermore, confining the discharge closer to the target by using magnets and the use of reactive gases during deposition make sputter deposition a very useful technique to grow all kind of thin films with specific crystallographic orientation and microstructure.

2.2 Energetic Ion Solid Interactions

2.2.1 Interaction Processes

Collision Cascade Ar^+ ions cause a range of collisions when penetrating the target. The scattering process can be described by the elastic collisions between the nuclei of the energetic ion and target atoms and by the inelastic scattering of the ions with the electrons in the solid. Although the inelastic collision causes a continuous deceleration of the energetic Ar^+ ions, it is not substantial for sputtering as the energy of the Ar^+ ions is transferred to a lot of atoms. In contrast, during an elastic collision, the ion transfers a fraction of its kinetic energy to a single target atom. For low energy Ar^+ ions ($\sim$ 100 eV), there is only a single knock-on. At higher energies ($\sim$ 300 eV, i.e. typical sputter range), the Ar^+ ion has multiple collisions, before settling or leaving the target. If a target atom receives enough energy, the atom will be knocked out of its position and will be displaced. On its turn, the target atom is able to collide with other target atoms and displace them. The series of collisions due to particle collisions is known as a collision cascade. Most the recoils are scattered forward (i.e. deeper into the target), however a fraction of the target atoms are backscattered. If the momentum is high enough, atoms or clusters[1] will be able to leave the target surface towards the vapour phase. The number of ejected particles per incident ion is called the sputter yield and depends on the energy of the ions, the angle of incidence and the target material.

Ion Implantation There is a probability for the Ar ion to be entrapped in the target (a few percent). As the sputter process proceeds, the rare gas atom will be resputtered. The fraction of implanted Ar-ions increases with increasing energy. It has been reported that trapped Ar gas, can influence the sputter yield, however, this occurs only for ion energies above the normal sputter conditions. In reactive sputtering (Sect. 2.5) the reactive gas can also be ionized, accelerated towards the target and cause a collision cascade. It goes without saying that there is a possibility for the reactive gas ions to be implanted. As this influences the chemical composition and the reactivity of the target, an effect on the sputter characteristics is expected.

Reflection Ar^+ ions may be reflected by the target surface and be neutralized by picking up an Auger electron. The number of reflected ions depends on the target material (the fraction of reflected ions increases for higher masses) and the angle of incidence (higher angle, higher reflection probability).

[1] Atomic clusters may be ejected by the target. The size-distribution $Y(E)$ of the atomic clusters obeys a power law: $Y(E) \sim n^{-\delta}$ with n the number of atoms in the cluster and δ an exponent that depends on the ion energy and the target material, ranging between 4 and 8 for small clusters [1].

Secondary Electron Emission By bombarding the surface, an electron can be ejected from the target surface to the vapour phase [2]. For typical sputter processes, the probability of creating an electron is in the order of 0.1, a quantity known as the secondary electron emission coefficient γ_e. The secondary electrons are necessary to ionize the Ar-atoms in the plasma. Electrons transfer their energy to the Ar-atoms inelastically by exciting internal electrons of the Ar-atom. This is more likely than contributing to the kinetic energy of Ar, because of the mass difference between the electrons and the Ar atoms.
More information about the role of the secondary electrons in the sputter process is given in section 2.3.

2.2.2 Sputter Yield

The sputter yield $S(E_i)$ gives the number of ejected particles per incident ion and largely determines the deposition rate. It depends on several parameters such as the target material, ion mass, ion energy, crystal orientation, ... Sigmund derived an analytical formula for the sputter yield using a linear cascade model based on binary collisions [3]. In this model, the number of defects per recoil is proportional to the kinetic energy. This is not longer the case for high energy ion bombardment (> 1 keV) which generates thermal spikes. Omitting the theoretical details for sputtering, the sputter yield $S(E_i)$ at normal incidence can be expressed as

$$S(E_i) = \frac{3}{4\pi^2}\alpha\frac{4M_iM_t}{(M_i + M_t)^2}\frac{E_i}{E_{bind}} \tag{2.1}$$

where E_i is the energy of the incident ion, E_{bind} is the binding energy of atoms to the surface, comparable to the heat of sublimation [4], M_i, M_t are the atomic masses of the incident ion and the target atom, respectively and α is a monotonic increasing function depending on M_t/M_i. The formula is valid for amorphous or polycrystalline target materials and ion energies below 1 keV, which is reasonable for the depositions carried out in this work.
The sputter yield depends also on the impact angle of the ions. With increasing angles, the ions remain closer to the surface through which the possibility for sputtering increases. The dependency of the impact angle has roughly an inverse cosine distribution. However, at to high angles, the ions are reflected, hence the sputter yield drops.

2.2.3 Energy and Spatial Distribution of the Sputtered Atoms

In the collision cascade, the incoming ions dissipate most of their energy to the target, which causes heating. Only a small fraction of the initial energy is passed on to the kinetic energy of the sputtered particles. An expression for the energy distribution of nascent sputter flux is of the form:

$$N(E) \sim \frac{E}{(E + E_{bind})^3} \tag{2.2}$$

with E the energy of a sputtered particle. The analytical expression for the energy distribution is derived by Thompson [5, 6] for a planar surface and is valid for the linear cascade model.[2] The

[2] The formula is derived in the assumption of hard sphere collisions and for low energy ions. For higher ion energies, an energy dependent parameter m is added to the exponential. The formula yields $N(E) \sim E/(E + E_{bind})^{(3-m)}$

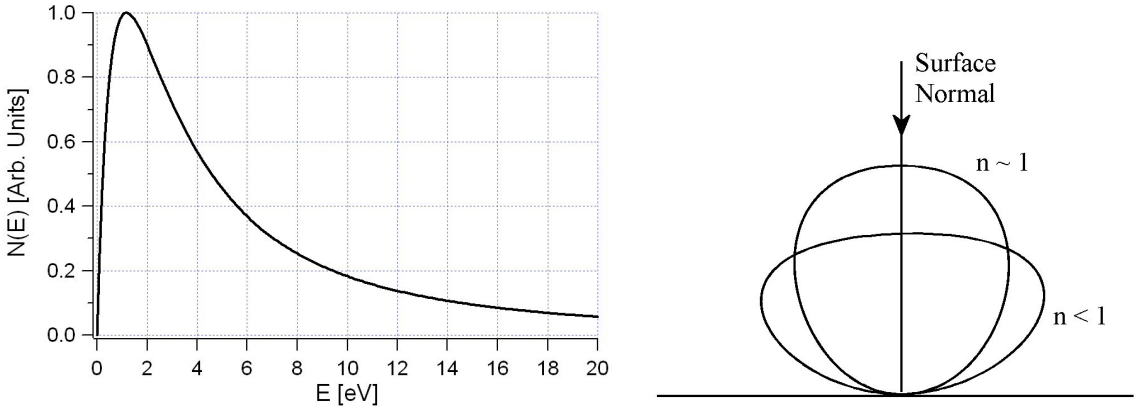

(a) Energy distribution (b) Spatial distribution

Figure 2.2: (a) Energy distribution of sputtered In by Ar^+ bombardment with an incident energy of 400 eV, with $E_{bind} \approx \Delta H = 2.49$ eV, (b) Spatial distribution of the sputtered particle at normal incidence. For low energy bombardment, n<1, an under-cosine distribution is observed.

energy distribution for sputtering of In in Ar with an energy of 400 eV is shown in Fig. 2.2(a). The particles are sputtered in a large range of energies, most of them in the order of a few eV. The function has a maximum for $E = E_{bind}/2$ and has a large tail at higher energies.
Fig. 2.2(b) shows the spatial distribution of the sputtered particles, which is proportional to $\cos^n \theta$ where *n* depends on the energy of the incident ions and the masses of the ion and target atoms. The cosine-distribution originates from the isotropic distribution of moving recoils just below the surface. The distribution is off-normal for oblique incident ions. Additionally, for polycrystalline targets with a preferential orientation, the ejection occurs preferentially along the close-packed directions of the grains. Note that the energy of the sputtered particles depends on the ejection angle.
There are several computational programs which model the ion-solid interaction, including the sputter process. SRIM and TRIM [7] deal with amorphous targets, MARLOWE [8] takes account for the crystal structure and TRIDYN [9] considers the target modification during bombardment.

2.3 Glow Discharge and Plasma

Essential for sputtering is the bombardment of the cathode with energetic particles. The easiest way to create energetic particles is to ionize gas atoms by means of a gas discharge and accelerate them towards the cathode by an electric field. Such gas discharges can be categorized in different modes [10]. Sputtering operates in the abnormal glow discharge, where the glow covers the cathode completely. In this mode, the discharge voltage increases with increasing current. At too high currents, thermionic electrons can be emitted which causes arcing.

The ionization process goes as follows. Energetic primary electrons near the cathode which are typically generated by ionization of a gas atom by a cosmic ray, are accelerated by the electric field between anode and cathode. If the energy gained by the electron is sufficient, an inelastic

collision with a gas atom may result in the ionization of the gas atom ($Ar + e^- \rightarrow Ar^+ + 2e^-$). Electrons can also excite a gas atom by inelastic collision. Returning to its ground state, characteristic photons are ejected. Also recombination of an ion and an electron causes the emission of a photon.[3] If ionization takes place a second electron is released into the gas. Subsequently both electrons will be accelerated again, creating a condition known as gas breakdown. The positive charged ions bombard the cathode and secondary electrons are emitted next to sputtered particles. These secondary electrons increase the ionization of the gas and sustain the discharge. Only the high energy electrons can ionize atoms. Although 15.76 eV is enough for an electron to create an Ar^+ ion, a rule of thumb is that only the electrons with an energy two or three times larger, are able to ionize the rare gas. These secondary electrons can maintain the discharge [11].

The DC glow discharge is usually a low density plasma with a degree of ionization in the order of 10^{-4}. Within the bulk plasma, the number of electrons in the plasma equals the number of positively charged ions. However, due to the mass difference, the electrons in the plasma travel at a much higher velocity than the ions. Assume that the plasma is at a certain potential V_p. When an electrically isolated object is immerged in the plasma, a space charge layer with negative potential with respect to the plasma potential builds up. This is due to the mass difference between ion and electron which causes a much higher electron current than ion current towards the object. The potential energy distribution is shown in Fig. 2.3. An electric field builds up, which repels the electrons. This electric field prevents the electrons from leaving the plasma. In steady state, the object is at floating potential V_f, a potential for which the electron and ion current towards the object are equal. The space charge layer is called the sheath. At each boundary to the plasma, a sheath is formed. Within the sheath the potential drops from V_p to more negative V_f. The

[3] By analysing the optical spectrum of the glow discharge, the plasma composition can be determined. This technique is called Optical Emission Spectroscopy (OES).

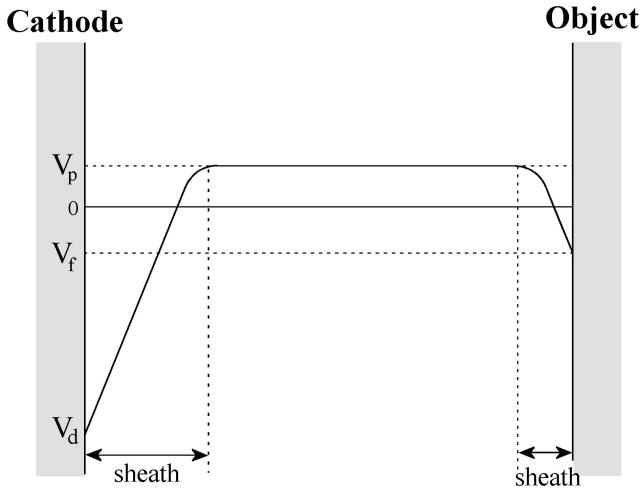

Figure 2.3: Distribution of the potential energy in a glow discharge in presence of a negatively charged cathode and an electrical isolated object.

voltage drop V_f-V_p is about -10 V. In the deposition chamber, the walls are at zero potential.[4] In order to confine the electrons in the plasma and maintain the plasma, the plasma potential must be positive. Moreover, the plasma potential is the most positive potential in the system.
At the cathode the situation is different, since the cathode potential is largely negative. Also a sheath develops (Fig. 2.3), repelling all the electrons but it contains the much heavier ions, which are accelerated towards the cathode. Secondary electrons are generated at the cathode and accelerated through the sheath,[5] gaining sufficient energy to ionize the Ar atoms. The energy of the electrons ejected by the Ar atom, however, is mostly too low to ionize other Ar atoms.[6] As it cannot be accelerated by the sheath (very strong repulsion), it has no contribution to maintain the plasma. Within the plasma, these thermalized electrons are the majority.

Once the sputtered particles are ejected from the target, they travel through the plasma towards the substrate. During the transport, collisions with other particles, primarily with rare gas atoms, are possible. Each collision, elastic or inelastic, causes a change in energy and direction. After interaction, the atom proceeds until it's scattered again, or it's adsorbed on a surface.
The mean free path λ is the average distance between two collisions. An expression for the mean free path is

$$\frac{1}{\lambda} = 4\sqrt{2}\pi\frac{p_s}{kT}r_s^2 + \pi\frac{p_s}{kT}\left(r_s + r_g\right)^2\left(1 + \frac{M_s}{M_g}\right)^{1/2} \tag{2.3}$$

where p_s is the pressure, r_s and r_g are the radia of the sputtered particle and the gas atom, respectively and M_s and M_g are their respective masses. Typically, a sputtered particle in our experimental setup collides 2 or 3 times during its transport. Since both the energy and the direction of the deposited species have a major influence on the growing film, it is important to know how the mass transport in the plasma occurs. Mahieu et al, modeled the transport through the vapour phase using a Monte Carlo simulation code [12] based on binary collisions.

2.4 Magnetron Sputtering

Magnetron sputtering utilizes a magnetic field parallel to the target surface, which constrains the motion of the electrons to the vicinity of the target. Electrons that are accelerated away from the cathode by the negative potential, are forced to follow the magnetic field lines. In first approximation, the much heavier ions are not influenced by the magnetic field and follow a straight line within the cathode sheath. The electrons, which executes a cycloidal motion around the magnetic field lines, are bent back towards the target by the Lorentz force.[7] As a result, the electrons travel a much larger distance in front of the target as compared to the situation without magnets, which give rise to an increase in inelastic collisions with a rare gas atom. The degree of ionization, hence the plasma density, is a factor of 100 times higher than without the support of a magnetic field (on the condition that all sputter parameters are the same). This means that the ion

[4] We assume that the walls are not coated with an insulating coating.

[5] The number of secondary electrons in the sheath is much lower than the number of ions.

[6] When an electron ejected by an Ar atom is generated in the sheath, the electron will accelerate due to the electrical field. If the electron is generated close to the cathode, it may gain enough energy to ionize Ar.

[7] The radius of gyration depends on the mass and velocity of the charge particle and is approximately 300 times larger for ions than for electrons.

bombardment increases. As the ion bombardment increases, the number of emitted secondary electrons increases. In combination with the longer travel distance, it allows the glow discharge to be maintained at lower operating voltages and at lower working pressures. Due to the lower working pressure, the sputtered particles have less collisions in the plasma and will arrive more directly at the growing film.
Fig. 2.4(a) shows a diagram form of a conventional planar magnetron. The magnet configuration at the back of the target is made up of an inner and an outer magnet. The cycloidal motion of the electrons, following the magnetic field lines is indicated. For conventional magnetrons, the magnet strength of both magnets is equal, resulting in a strongly confined plasma to the target region. Few charged particles reach the substrate, which is useful in cases where low energetic bombardment is required (e.g. when using a plastic substrate). However, it is known that the bombardment with ions or electrons, modify the thin film growth, as they act on the atomistic processes taking place at the growing surface. The bombardment of the substrate with energetic particles can be achieved by unbalancing the magnet configuration. For unbalanced magnetron sputtering the magnet strength of both magnets is different [13]. The difference in magnet strength can be obtained by using permanent magnets with a different total area. The ratio in area of both magnets corresponds to the magnet strength ratio. As a result the magnetic field lines can intersect with the substrate (Fig. 2.4(b)). The electrons will follow the magnetic field lines as well as the ions by ambipolar diffusion. Hence, the electron and ion density near the substrate increases. Additionally, an external potential known as a substrate bias can be applied to the substrate. A positive substrate bias causes the electrons to be attracted and the ions to be repelled, a negative bias acts oppositely.
Due to the magnet configuration, the magnetic field across the target varies in magnitude and direction. A higher plasma density, hence a higher ion bombardment is observed between the magnetic poles. The non-uniform ion bombardment across the target surface leads to the formation of an erosion profile or a racetrack. This leads to an inefficient target usage where only 30% of the target material is sputtered.

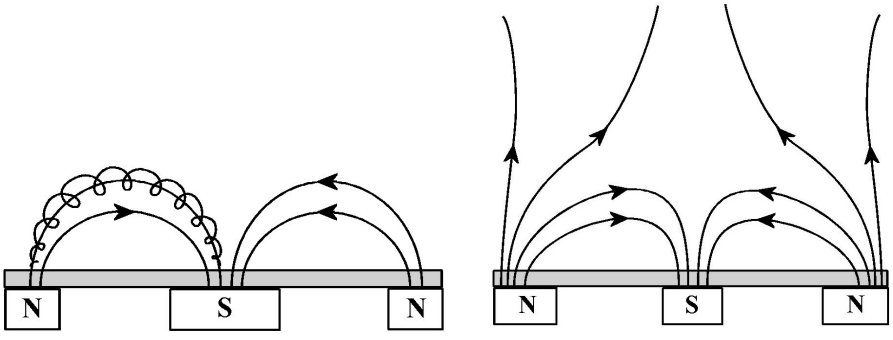

(a) Balanced Magnetron (b) Unbalanced Magnetron

Figure 2.4: (a) Balanced and (b) Unbalanced Magnetron configuration. The outer magnetic field of the unbalanced magnetron is stronger than the inner one. Owing to this, the magnetic field lines may intersect with the substrate. Next to the magnetic field lines, the cycloidal motion of one electron is indicated.

2.5 Reactive Sputter Deposition

Reactive sputter deposition is a method to deposit films which have a different composition from the target. This method is used to deposit ceramic materials because sputtering from a ceramic target is not preferred due to the electrical insulating nature of the target. With RF sputtering it is possible to use a ceramic target, but due to the low deposition rates, reactive sputtering is preferred. To deposit the thin film with reactive sputtering, in most cases, a pure metallic target is used. By adding a reactive gas to the sputtering system a compound is deposited at solid surfaces by reaction of the gas with the sputtered target material. Through this, a high deposition rate and a stoichiometric film can be obtained. Reactive sputtering is also used to dope films with the desired percentage of the gas (e.g. nitrogen doped Ta films). Important to remark is that in the vapour phase at normal sputter pressures, reaction between two particles (e.g. O + Mg) cannot occur during a collision because it is impossible to conserve both the energy and the momumtum in a two-body reaction. Mostly a surface acts as a third body for reaction. Essentially, chemical reaction only takes place at surfaces in the system.
The reactive gas plays a role in the entire sputter process. Assume sputtering from a metallic Mg target in Ar-O_2 atmosphere. In the plasma it may occur that O_2 ionizes. In the vicinity of the target O_2^+ is accelerated towards the target. At the target surface O_2^+ may dissociate upon impact and be reflected. Also, O_2 may be chemisorbed, dissociative or not. If O_2^+ gains enough energy, it may sputter target material and can be implanted. During sputtering oxygen or MgO will be resputtered from the target. At the substrate (and other surfaces, like the chamber walls) O_2 or ionic O_2^+ can (dissociative) chemisorb and create a MgO compound. Also atomic O can arrive at the substrate (and the target) and take part in the growth. The fraction of atomic O in a sputter plasma is about 4%, which is rather low.
Mostly, the reactive sputter process is discussed in terms of the partial pressure of the reactive gas. Without sputtering, the partial pressure (e.g. O_2) increases linearly with increasing reactive gas flow, as the pumping speed is constant. During sputtering, initially all O_2 that is added, reacts with the sputtered Mg at all surfaces to form MgO. At the target, there is a balance between the sputter proces and the compound formation. However, at a given gas flow, the compound formation will dominate at the target surface. As a result, the sputter rate decreases because the surface binding energy of MgO is much higher than the metallic Mg. As the sputter rate decreases, more O_2 is available, which leads to the formation of larger compound area on the target, hence a lower sputter rate, so more O_2,... The cascade continues until the complete target is covered. A swift increase in partial pressure is observed as well as a drop in deposition rate. The formation of an oxide-covered target is called poisoning. When the target isn't covered with an oxide or compound, the process is called sputtering in metallic mode. Now, when the O_2 flow rate is reduced, a reverse cascade is observed, since at a given pressure, MgO is removed from the target. However, as the sputter rate for the compound is much lower, the cascade occurs at much lower flows.
This hysteresis effect is also observed in the discharge voltage (Fig. 2.5) because of the difference in secondary emission coefficient between the ceramic compound and the metal.
Theoretically the hysteresis effect is described by Berg et al. for chemisorption of the reactive gas at the surfaces [14].[8] As discussed above, the reactive gas doesn't only chemisorb at the

[8]Three elements consume the reactive gas: the target, other surfaces and the pumping of the gas.

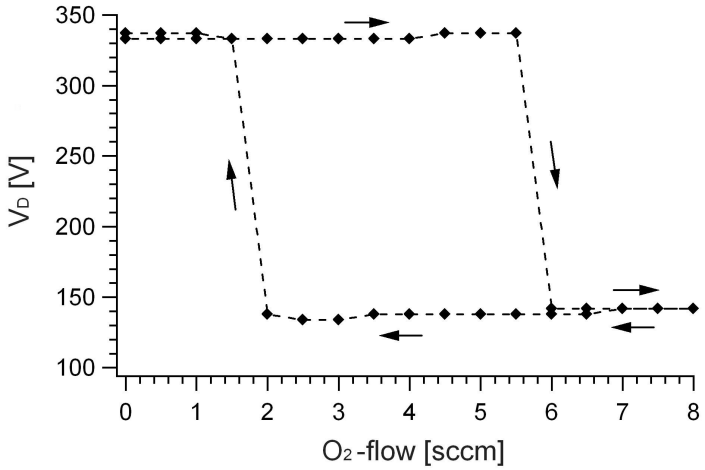

Figure 2.5: Influence of the oxygen flow on the discharge voltage V_d during DC sputtering of a metallic Mg target.

target, but due to its acceleration through the cathode sheath, a considerable fraction is implanted in the target. Depla et al. argued that, although chemisorption may explain the general hysteresis effect, the implementation of implantation is necessary to describe various phenomena [15]. More detailed information on reactive sputtering can be found in [16] or [17].

In this work, MgO and InN are sputtered from a metallic Mg or In target with the addition of oxygen and nitrogen, respectively. For the growth of MgO thin films, Ar is used as a sputter gas. For the growth of InN thin films, Ne is used as a sputter gas, to obtain a high atomic fraction of nitrogen in the plasma. This is beneficiary for the growth of stoichiometric InN. Detailed information for the use of Ne as sputter gas is given later on in Section 5.5.3.

2.6 Experimental Setup

In this work Magnesium Oxide (MgO), Chromium (Cr) and Indium Nitride (InN) thin films are grown by unbalanced magnetron sputter deposition using a 5 cm circular metallic Mg, Cr or In target with 4N purity. An unbalanced magnetron type II, i.e. with the outer magnets stronger than the inner ones, is used to increase the plasma density near the substrate. For the various materials, depositions have been carried out with a magnetic field ratio of 1:3 or 1:9.
Fig. 2.6 is a schematic drawing of the used sputter deposition system. Before deposition, the chamber is pumped down to a pressure of 10^{-4} Pa by a turbo-molecular pump. The pressure is measured by a dual gauge, i.e. combination Penning-Pirani, and during deposition by a capitance gauge. The typical operation pressure, later referred to as the working pressure, ranged between 0.1 to 1 Pa. The flow rate of the sputter gas is controlled by a mass flow controller which ranged between 1 and 150 sccm. Argon is used as a sputter gas. However, to enhance the degree of ionization of nitrogen, Neon is used as sputter gas during the deposition of InN. For the growth of MgO and InN, oxygen and nitrogen is used as reactive gas, respectively, with a flow rate ranging between 1 and 50 sccm.

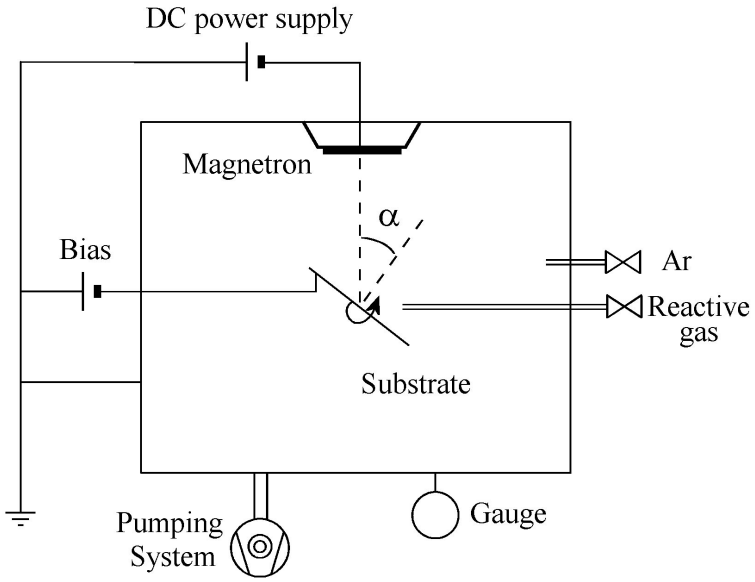

Figure 2.6: Experimental setup - deposition chamber.

In Chapter 6 the influence of contaminants on the growth of biaxially aligned layers is examined. The contamination is introduced by the inlet of a small amount of reactive gas before and during deposition. N_2, O_2 and CH_4 is introduced into the deposition chamber by using a needle valve . Before deposition, the needle valve is opened until a given pressure is reached. During deposition, the corresponding flow is kept constant.
A tiltable substrate is placed in front of the magnetron. The distance between the substrate and the magnetron ranged from 7 cm to 13 cm. The tilting angle α of the substrate is the angle between the substrate normal and the normal on the target. A negative or positive bias can be applied to the substrate to repel or attract charged particles.
The depositions are carried out on different substrates. Rolled metallic substrates without alignation or amorphous glass is used since the subject of this thesis was not concentrating on epitaxial growth. The thin films grown on glass are used to obtain cross sectional images. MgO is deposited on non-aligned stainless steel (ferrite) and glass. Chromium is grown on Hastelloy, Austenite[9] and glass. Finally, InN is deposited on stainless steel and glass.

[9] Cr isn't deposited on ferrite-stainless steel because both materials have the same lattice parameters, which makes XRD analysis unsuitable for determining the preferred orientation.

Bibliography

[1] L. E. Rehn, R. C. Birtcher, S. E. Donnelly, P. M. Baldo, L. Funk, Origin of atomic clusters during ion sputtering, Phys. Rev. Lett. 87 (20) (2001) 207601.

[2] C. E. Carlston, G. D. Magnuson, P. Mahadevan, D. E. Harrison, Electron ejection from single crystals due to 1- to 10-keV noble-gas ion bombardment, Phys. Rev. 139 (3A) (1965) A729–A736.

[3] P. Sigmund, Theory of sputtering. I. sputtering yield of amorphous and polycrystalline targets, Phys. Rev. 184 (2) (1969) 383–416.

[4] J. Liu, C. W. Wu, T. T. Tsong, Measurement of the binding energy of kink-site atoms of metals and alloys, Phys. Rev. B 43 (14-15) (1991) 11595–11604.

[5] M. W. Thompson, Atomic collision cascades in solids, Vacuum 66 (2002) 99–114.

[6] M. W. Thompson, The contribution of collision cascades to sputtering and radiation damage, Phys. Trans. R. Soc. Lond. A 362 (1814) (2004) 5–28.

[7] W. Eckstein, Quantitative predictions of sputtering phenomena, Surf. Interface Anal. 14 (2) (1989) 383–416.

[8] M. T. Robinson, I. M. Torrens, Computer simulation of atomic-displacement cascades in solids in the binary-collision approximation, Phys. Rev. B 9 (12) (1974) 5008–5024.

[9] W. Möller, W. Eckstein, J. P. Biersack, Tridyn-binary collision simulation of atomic collisions and dynamic composition changes in solids, Comp. Phys. Comm. 51 (3) (1988) 355–368.

[10] B. Chapman, Glow Discharge Processes, 1st Edition, Wiley, New York, 1980.

[11] G. Buyle, Simplified model for the d.c. planar magnetron discharge, Ph.D. thesis, Ghent University (2005).

[12] S. Mahieu, G. Buyle, D. Depla, S. Heirwegh, P. Ghekiere, R. De Gryse, Monte Carlo simulation of the transport of atoms in DC magnetron sputtering, Nucl. Instr. and Meth. in Phys. Res. B 243 (2) (2006) 313–319.

[13] B. Window, N. Savvides, Charged particle fluxes from planar magnetron sputtering sources, J. Vac. Sci. Technol. A 4 (2) (1986) 196–202.

[14] S. Berg, H. O. Blom, T. Larsson, C. Nender, Modeling of reactive sputtering of compound materials, J. Vac. Sci. Technol. A 5 (2) (1986) 202–207.

[15] D. Depla, R. De Gryse, Target poisoning during reactive magnetron sputtering: Part i: the influence of ion implantation, Surf. Coat. Technol. 183 (2-3) (2004) 184–189.

[16] S. Berg, T. Nyberg, Fundamental understanding and modeling of reactive sputtering processes, Thin Solid Films 476 (2) (2005) 215–230.

[17] W. D. Sproul, D. J. Christie, D. C. Carter, Control of reactive sputtering process, Thin Solid Films 491 (1) (2005) 1–17.

Chapter 3

Thin Film Analysis

3.1 X-ray Diffraction

X-rays interact primarily with the electrons of an atom. A single atom will scatter these X-rays spherically. When atoms are arranged in a periodic lattice, the scattered waves of the different atoms will interfere resulting in a diffraction pattern where few directions will have constructive interference. The geometry of the lattice determines the angles at which diffraction peaks are present. The intensity of the diffraction peaks is caused by the charge distribution in the unit cell and is expressed in the structure factor.
To deal with the interference problem, different approaches are developed among them Bragg diffraction, which is considered here. Bragg started from the idea that a lattice is composed of a series of parallel planes separated by an interplanar distance d_{hkl} as indicated in Fig. 3.1. The X-rays are reflected at these planes. The path difference between X-rays scattered at two adjacent planes is $2d_{hkl}\sin\theta$ with θ the angle between the incoming (and outcoming) wave and the plane (Fig. 3.1). To have constructive interference, the path difference from successive planes has to

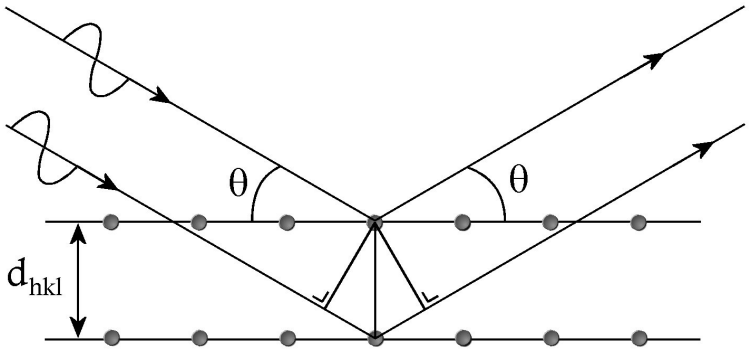

Figure 3.1: Bragg's law - Condition for diffraction of X-rays.

be a multiple n of the wavelength λ. This results in Bragg's law:

$$n\lambda = 2d_{hkl}\sin\theta \tag{3.1}$$

Since monochromatic x-rays are used,[1] it is possible to calculated the interplanar spacing by measuring the angle θ.

3.1.1 Angular Scan

The most common diffraction measurement is an angular scan, also called a $\theta - 2\theta$ scan. In this setup, monochromatic X-rays are directed towards the substrate with an angle θ to the substrate plane. The detector is positioned in the direction of the reflected beam at the same angle θ to the substrate plane, so an angle 2θ to the incident X-rays. By varying the angle θ, diffraction peaks will appear at Bragg conditions. Hereby, the source and detector move simultaneously. The diffraction spectrum will indicate which crystallographic planes are parallel to the substrate and hence the preferential out-of-plane orientation can be determined. The fraction of grains with a [hkl] out-of-plane orientation is calculated by measuring the area under the (hkl) diffraction peak. Since the intensity of the diffraction peak depends on the structure factor, the measured peak area must be corrected with the relative peak intensity of the corresponding powder as reported in the Joint Committee for Powder Diffraction Standard card (JCPDS). The formula to calculate the fraction of grains with a [hkl] out-of-plane orientation is

$$\frac{A_{(hkl)}}{i_{(hkl)}} \Big/ \sum_{(hkl)} \frac{A_{(hkl)}}{i_{(hkl)}} \tag{3.2}$$

with $A_{(hkl)}$ the area under the (hkl) peak and $i_{(hkl)}$ the relative peak intensity in comparison with the most intens peak, ranging from 0 to 1 with 1 for the most intens peak.[2]

3.1.2 Texture Analysis

A texture measurement is used to determine the orientation distribution of crystalline grains in a polycrystalline thin film.[3] This is also referred to as a pole figure as it is plotted in polar coordinates consisting of the tilt and rotation angles, with respect to a given crystallographic orientation.
A pole figure is measured at a fixed Bragg diffraction angle to examine the distribution of that specific orientation. The measurement consists of a series of ϕ-scans, which analyses the in-plane orientation around the center of the sample, at different tilt angles χ, also called the azimuthal angle. These angles are indicated in Fig. 3.2. The angle ϕ can be varied between 0° and 360°, while χ can be varied between 0° and 90°.
The diffraction intensity at a given ϕ and χ is proportional to the number of (hkl) planes in Bragg

[1] Cu-radiation is used as X-ray source. By using a Göbelmirror and a series of slits, monochromatic K_α radiation with parallel beam optics is selected. The wavelength λ is 1.54Å.

[2] Not shown here, is a correction applied to take into account a different illumination area at various angles. This includes also the use of variable or fixed slits.

[3] Texture is used as a synonym for the preferred out-of-plane and in-plane crystallographic orientation in the polycrystalline material.

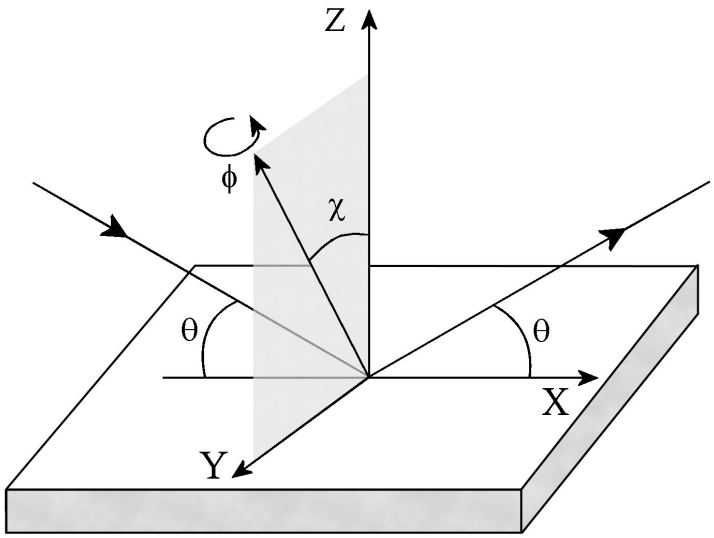

Figure 3.2: Conditions for a texture measurement.

condition. The pole figure data is displayed as a contour plot with the zero in the center.[4] Hence, the pole figure gives the probability of finding a given (hkl) plane normal as a function of the thin film orientation.
If the grains in the polycrystalline film are randomly oriented, the pole figure will have an uniform intensity distribution. When the thin film has a [uvw] out-of-plane orientation, but a random in-plane orientation, then the (hkl) pole figure will exhibit a ring pattern at a tilt angle χ which corresponds to the angle between the [uvw] direction and the normal of the (hkl) planes. If the film is biaxially aligned, so with a preferential out-of-plane and in-plane orientation, the ring pattern is transformed into intensity spots, which indicates that a second crystallographic orientation of the grains is aligned to certain direction. A measure for the orientation distribution of grains which are aligned according to a certain direction, is the Full Width at Half Maximum (FWHM) of the pole in the ϕ direction. These three issues are illustrated in Fig. 3.3.

3.2 Transmission Electron Microscopy

In Transmission Electron Microscopy (TEM), high-energy electrons pass through the specimen. After entering, most of the electrons are elastically scattered in the specimen. Compared to X-rays, the interaction of electrons with the specimen is huge and multiple scattering events are common, therefore thin specimens and specific preparation techniques are required. The inelastic scattered electrons contribute mostly to the background of the image. However, the energy loss spectrum of the inelastic scattered electrons contains valuable information of the

[4] Most common, pole figures are represented in a stereographic projection. In such a representation, an area measured at ϕ=90° would have the same area if measured at 0°.

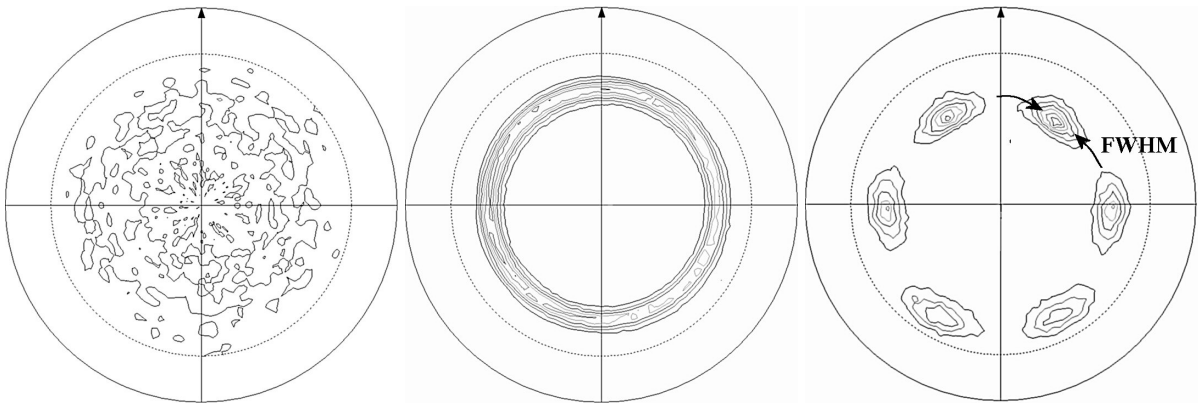

Figure 3.3: $(10\bar{1}1)$ XRD pole figures of InN thin film with different crystallographic orientation. (a) random orientation, (b) preferential [0001] out-of-plane orientation but no in-plane alignment, (c) biaxial alignment with [0001] out-of-plane and strong in-plane alignment.

chemical composition of the specimen and can be extracted by energy filtering. This technique is called Electron Energy Loss Spectroscopy (EELS), but is not discussed here.
TEM enables local analysis, as the electron beam can be focused easily. The unique combination of imaging and diffraction as well as the atomic resolution, are the main advantages of TEM.

3.2.1 Structure of the Microscope

In this section, the basic components of a TEM are discussed. The electrons are generated by a LaB_6 filament by means of thermoionic emission. Electrons that gain sufficient energy by heating to overcome the work function will be emitted from the surface.[5] After emission, the electrons are accelerated to an energy of a few hundred keV. The electron beam is focused and directed to the specimen by condenser lenses[6], which also control the illumination of the specimen.
After interaction with the specimen, the electrons are scattered in a particular direction. The objective lens focuses these electrons in the back focal plane. Hence, the back focal plane contains information about the diffraction pattern of the specimen.
To obtain a higher magnification, a intermediate and projector lens system is used.[7] The intermediate lenses also determines whether a diffraction pattern or an image is formed. By changing the current in the lenses, and so the magnetic field strength, the focal length can be adjusted to change from image mode to diffraction mode. A diffraction aperture can be used at the image plane of the objective lens to confine the diffraction pattern to a selected area of the specimen. Both modes are illustrated in Fig. 3.4.

[5] A field emission gun is also frequently used to generate electrons. By applying a strong electrical field, the work function is lowered for electrons to escape, which increases the emission, hence the current density considerably.
[6] Note that all lenses are electro-magnetic and are subjected to aberrations.
[7] Depending on the type, an additional lens, called the diffraction lens can be used.

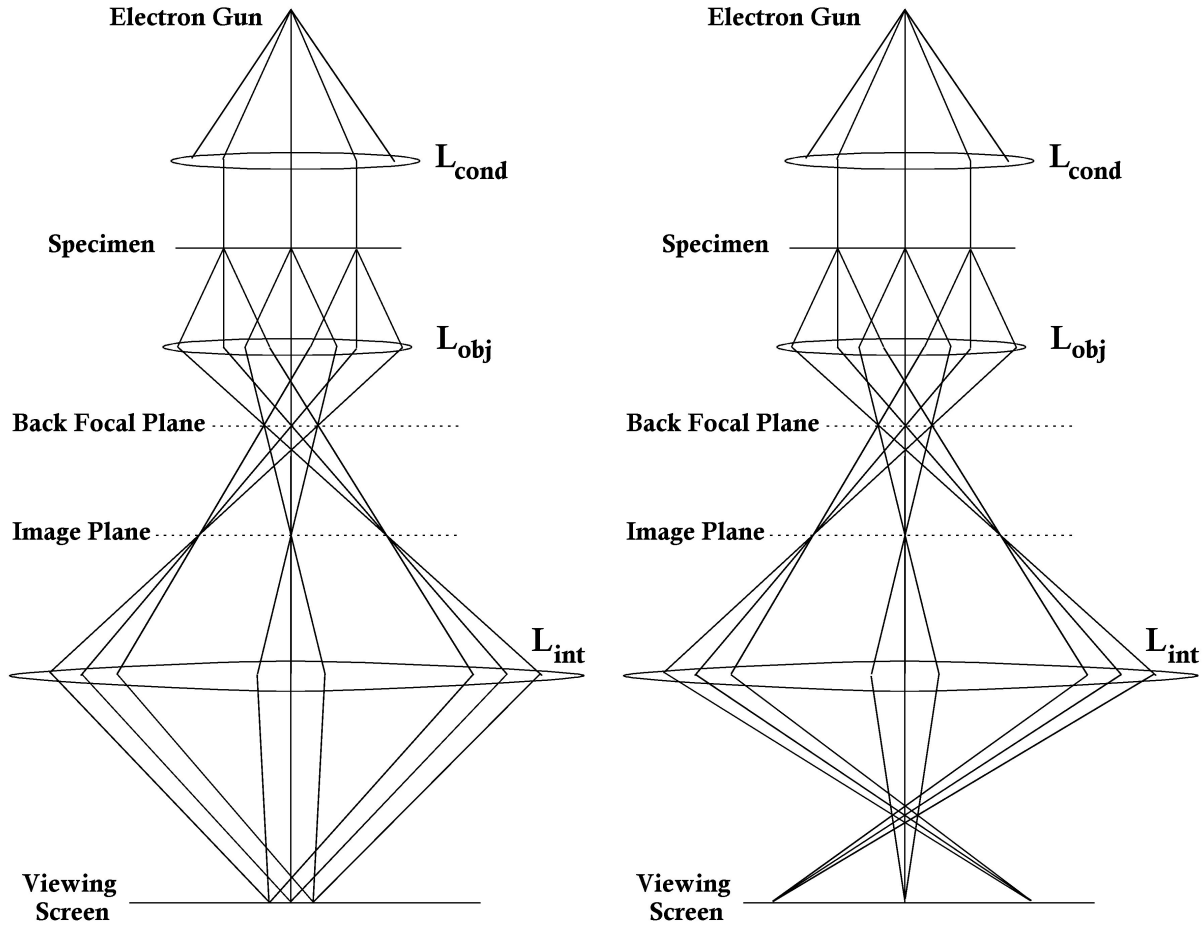

(a) Diffraction Mode (b) Image Mode

Figure 3.4: Electron beam paths in a TEM. The different sets of lenses are indicated: condenser lenses L_{cond}, objective lens L_{obj}, intermediate lenses L_{int}. The projector lens, located between the intermediate lenses and viewing screen, is not shown here. Distance and angles are not to proportion. At the position of the back focal plane an aperture can be used in image mode to obtain the image of electrons that are diffracted at a specific angle. In diffraction mode, an aperture can be used at the image plane to obtain the diffraction pattern of a selected area on the specimen.

3.2.2 Diffraction Pattern

If a zone axis is aligned with the optical axis of the microscopy than the Bragg condition is fulfilled.[8] So $2d\sin\theta = \lambda$. Now $\theta < 1^o$ so,

$$2\sin\theta \sim 2\tan\theta \sim \tan(2\theta) = \frac{R}{L}$$

where R is the distance between the optical axis and the diffraction spot and L is the camera-length. This yields

$$Rd = \lambda L \tag{3.3}$$

A typical electron diffraction pattern (ED) of a single crystalline phase is shown in Fig. 3.5. From the separation of the diffraction spots in the diffraction pattern, the interplanar spacing can be determined. Also structural information can be obtained. For polycrystalline films with only a preferential [uvw] out-of-plane orientation, the diffraction pattern consists of diffraction rings.[9] The ED pattern of biaxially aligned polycrystalline films exhibit diffraction spots which are broadened, as it is a superposition of ED patterns of single crystalline grains with a slight variation in orientation. Hence the peak width is an indication for the alignment in the polycrystalline film.

[8] In literature, the Ewald construction is often used to describe the diffraction pattern, as the diffraction spot corresponds to the intersection of the Ewald sphere with a point in the reciprocal space.

[9] The specimen has to be oriented according to the [uvw] zone axis.

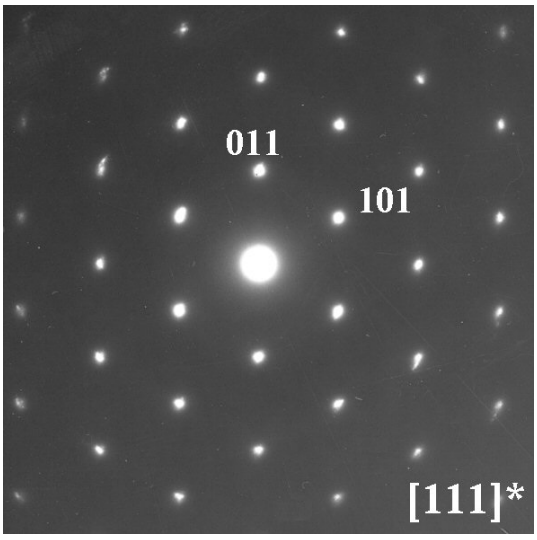

Figure 3.5: The ED pattern of a single crystalline grain Cr with a BCC structure. By measuring the distances an the angles between the diffraction spots, the diffraction pattern can be indexed. In this example, the grain is oriented parallel to the [111] zone axis (or the symmetry variants). The index of a few diffraction spots is indicated.

3.2.3 High Resolution Electron Microscopy

A High-Resolution Electron Microscopy (HREM) image is an interference pattern between forward-scattered and diffracted electron waves and is best understood in terms of the Fourier transform of the distribution of the atoms in the specimen. A detailed description, however, is far beyond the scope this work, but we refer to [1, 2].
Nevertheless, some remarks should be made. Firstly, an electron wave contains information about the amplitude and the phase. Yet, an HREM image only displays the intensity $I = |\Psi|^2$ and the phase information is lost. You do not see atoms but a configuration. Secondly, the resolution of a HREM image depends on quality of the objective lens. An ideal microscope should have a perfect point resolution. However, due to aberrations, a point is defocused and spreads out (Fig. 3.6). The resolution of the microscope is the FWHM of this spread.

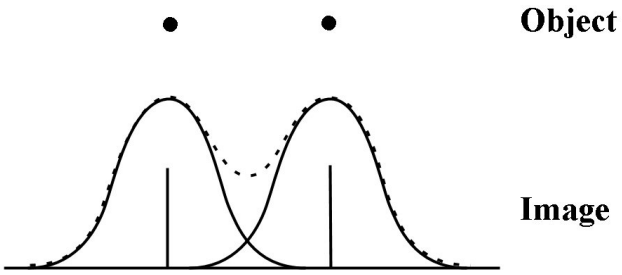

Figure 3.6: Spread of a point of the image due to aberrations in the lenses. The image, indicated with the dotted line, is the superposition of these point spreads. Without aberrations, the image of a point object is a Dirac function.

3.3 Scanning Electron Microscopy

Scanning Electron Microscopy (SEM) is a technique used for imaging the surface. In contrast with conventional TEM, only imaging is possible, where TEM has the strength of obtaining both an image and diffraction information. In SEM, the image builds up by scanning the surface.[10] Electrons, generated by a field emission gun, are focused and accelerated towards the specimen by several electromagnetic lenses. The energy of the electrons ranges from a few keV to 30 keV. Coils located at the objective lens deflect the beam systematically to scan the surface point by point. The typical spot size of the electron beam is about 10 Å [3]. Upon impingement, the primary electrons will interact with the specimen causing numerous electronic excitations including secondary electrons and backscattered electrons, and the emission of characteristic X-rays within a droplet-shaped interaction volume (Fig 3.7).
Secondary electrons originate from outer shell electrons that are weakly bound to the atoms in the specimen. By inelastic scattering of the primary electrons they receive sufficient energy to be

[10] In Scanning Transmission Electron Microscopy (STEM) a focused electron beam scans also the surface.

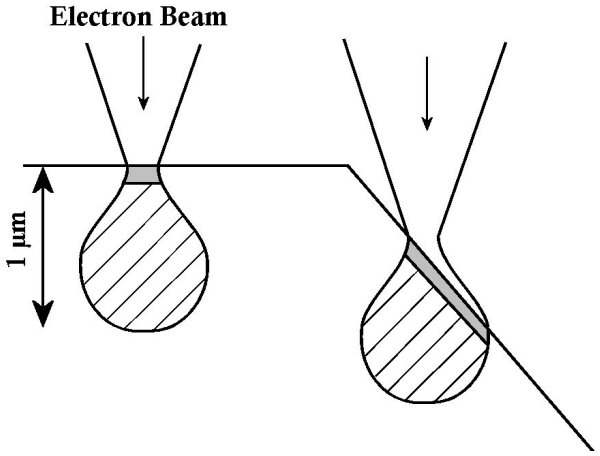

Figure 3.7: Droplet-shaped interaction volume during the impact of primary electrons on the specimen. The volume strongly depends on the energy of the electron beam and the specimen composition. The depth from which secondary electrons are emitted, is gray coloured. The effect of the surface topography on the emission of secondary electrons is also shown.

ejected from the atom and some will escape from the surface. The energy of secondary electrons is less than 50 eV. Due to the strong interaction with matter, the secondary electrons are emitted from the surface region, as indicated on Fig. 3.7. The contrast in a SEM image is directly connected to the surface topography. Inclined surfaces produce more secondary electrons as the section of the interaction volume is larger than for horizontal surfaces (Fig. 3.7). Since the emission of secondary electrons is confined by a small volume near the primary beam impact, the resolution is about the size of the electron beam. SEM is also used to verify the microstructural evolution of the thin film. A cross-sectional view is obtained by cleaving the sample.
Backscattered electrons are primary electrons which are elastically scattered and re-escape from the surface after several collisions. Their energy is close to the energy of the primary electrons. Since the interaction volume is larger and the escape depth is high (about 200 nm), SEM images built up only by these electrons contain less topographical contrast. Important to remark is that on the trajectory, secondary electrons are generated by exiting backscattered electrons which may contribute to the total amount of secondary electrons. The fraction of these secondary electrons is significant for specimens with a high atomic number Z, since the probability for backscattering increases with Z.[11] Backscattered electrons are mostly used in Electron Backscatter Diffraction (EBSD), where Kikuchi patterns give information about the local crystallographic orientation of the grain [3].
When primary electrons knocks out a core-shell electron, a vacancy is created. When that vacancy is filled by another shell electron, characteristic X-ray are emitted. By analysing the energy of these X-rays, the chemical composition of the specimen can be obtained and compositional maps can be constructed. This technique is known as Energy Dispersive X-ray analysis (EDX).

[11] For Au, the fraction secondary electrons originating from backscattered electron is 1.5 times higher than those originating from the primary beam [3].

3.4 X-ray Photoelectron Spectroscopy

X-ray Photoelectron Spectroscopy (XPS) is used to investigate the chemical composition of the surface of the thin film. Incident X-rays, generated by a X-ray tube with Al-anode, ionize an atom. The emitted core-shell electron is bound to the atom with an energy E_{bind}. If the energy of the photon is transferred to the electron, the electron leave the film with an energy of $h\nu - E_{bind}$.[12] By using monochromatic X-rays radiation and by measuring the electron energy, the binding energy can be obtained. Since the binding energy of the electrons is characteristic for each element, XPS spectra contain information about the chemical composition of the thin film. The observed spectrum of a specific element is labeled with 1s, 2s, 2p ... depending on the ionized electron shell. Fig. 3.8(a) shows a typical XPS spectrum of a Cr thin film surface. Next to Cr peaks, also an O 1s peak arises due to surface oxidation and a C 1s peak is present due to organic contaminants.
Because the atoms are bounded, an electron fine structure can be observed in the XPS spectrum. For example a peak shift can be observed for binding to a specific atom with a certain binding state. A typical multiplex for Cr 2p is shown in Fig. 3.8(b). Both the Cr $2p_{3/2}$ and the Cr $2p_{1/2}$ are visible with an in-between energy difference of 9.3 eV. As can be seen, the Cr $2p_{3/2}$ (and Cr $2p_{1/2}$) peak is composed of three peaks, located at different binding energies. The different components can be attributed to Cr^0, Cr^{2+} and Cr^{3+} [4]. The first comes from the metallic Chromium, while the other components represent two oxidation states.[13] A direct method to quantify the chemical composition, is to measure the area under the different peaks. A background, which originates from inelastic scattering of the electrons, is subtracted from the spectrum. It's important to remark that only information of the first few nm is obtained, as the escape depth of the electrons is small.

[12] Al K_α X-rays have an energy of $h\nu$ = 1487eV, which set the upper bound to the kinetic energy of the detected electrons.

[13] The binding energy of Cr-O is higher than the Cr-Cr bond because of the higher electro-negativity of oxygen.

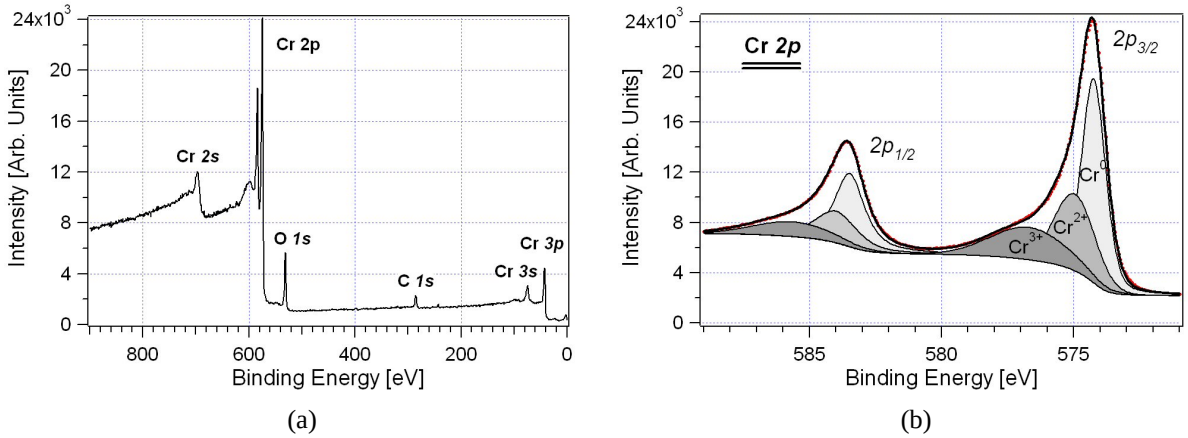

Figure 3.8: (a) XPS Survey spectrum of Cr thin film surface, (b) Multiplex of Cr 2p.

Bibliography

[1] B. Fultz, J. M. Howe, Transmission Electron Microscopy and Diffractometry of Materials, 2nd Edition, Springer-Verlag Berlin Heidelberg New York, 2002.

[2] D. B. Williams, C. B. Carter, Transmission electron microscopy : a textbook for materials science, Plenum Press, New York, 1996.

[3] J. I. Goldstein, D. E. Newbury, P. Echlin, D. C. Joy, C. E. Lyman, E. Lifshin, L. Sawyer, J. R. Michael, Scanning Electron Microscopy and X-Ray Microanalysis, 3rd Edition, Kluwer Academic/Plenum Publishers, New York, 2003.

[4] M. Eriksson, J. Sainio, J. Lahtinen, Chromium deposition on ordered alumina films: An x-ray photoelectron spectroscopy study of the interaction with oxygen, J. Chem. Phys. 116 (9) (2002) 3870–3874.

Chapter 4

Growth of Biaxially Aligned Thin Films

4.1 Introduction

This chapter is dedicated to the growth mechanism of biaxially aligned thin films. During this work, biaxially aligned layers with various crystal structure are deposited by unbalanced magnetron sputtering. MgO (rocksalt structure) and InN (wurtzite structure) are grown from a metallic target in a reactive ambient; Cr (BCC structure) is also deposited from a metallic target but in an inert atmosphere. First, the experimental observations will be discussed for the various materials. Afterwards, a mechanism for the development of a preferential out-of-plane alignment is discussed. Also a mechanism for the in-plane alignment is proposed and discussed.

4.2 Biaxial Alignment

A polycrystalline thin film is composed of individual crystalline grains for which each grain is characterized by its crystallographic orientation. Roughly speaking, there is no correlation between the crystallographic orientation of the grains. Therefore, if the individual grains are randomly oriented, there is no alignment (Fig. 4.1(a)).
If a crystallographic axis of all grains is aligned according to a specific direction, one has an

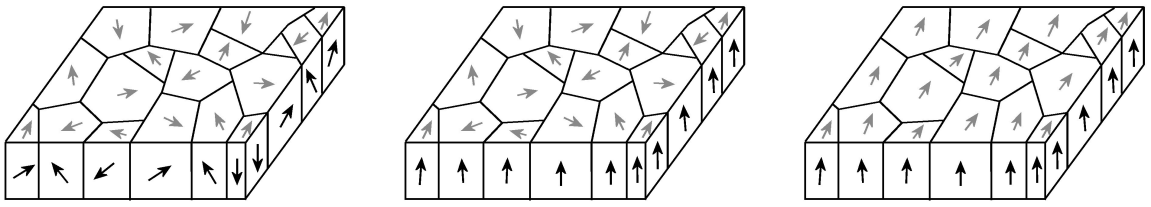

(a) Non Aligned (b) Uniaxial Alignment (c) Biaxial Alignment

Figure 4.1: Schematic drawings of the alignment in polycrystalline thin films: (a) non aligned, (b) uniaxially aligned, (c) biaxially aligned thin film.

uniaxially aligned thin film. If the crystallographic axis is parallel to the substrate normal, the film has a preferential out-of-plane orientation. The orientation of the grains perpendicular to the aligned axis, i.e. the in-plane orientation, is random (Fig. 4.1(b)).
If the crystallographic axis of the grains which is parallel to the substrate, is also aligned, there is an in-plane alignment. Biaxially aligned thin films are polycrystalline thin films with both a preferential out-of-plane and a preferential in-plane alignment (Fig. 4.1(c)). In the limit, all grains are perfectly aligned along the two axes and the thin film resembles to a single crystalline thin film.
In this work, the preferential out-of-plane alignment is determined by XRD angular scan (section 3.1.1). The in-plane alignment is investigated by XRD pole figures (section 3.1.2), whereby the FWHM of the pole is a measure for the spread of the in-plane orientation of the grains with respect to a specific axis. When it is mentioned that the in-plane alignment improves, this means that the in-plane orientation of the grains is closer to the preferred axis. Consequently, a smaller FWHM will be observed.

4.3 Experimental Observations of Biaxially Aligned Thin Films

4.3.1 Experimental Observations of MgO

MgO has a rocksalt structure with the space group $Fm\bar{3}m$. The cubic structure is composed of two Face-Centered Cubic (FCC) sublattices, one for Mg and one for O, which are shifted over distance $a/2$ along the [100] direction, with a the lattice parameter. The lattice parameter for MgO is 4.211 Å.
Biaxially aligned MgO thin films are grown by unbalanced magnetron sputter deposition with an 1 : 9 magnet configuration. A 5 cm circular metallic Mg target is sputtered in an Ar/O_2 ambient. A working pressure of 0.45 Pa is used with a flow rate of 60 sccm Ar and 3 sccm O_2. An O_2 local inlet, close to and pointing to the substrate, is used to grow stoichiometric MgO thin films without poisoning the target.[1,2] The target substrate distance is fixed at 10 cm and the discharge current was 0.70 A. The MgO thin film is deposited on non-aligned Stainless Steel at floating potential. Using these deposition parameters, a deposition rate of about 100 nm/min is obtained. The layer thickness was about 1.5 μm.
On a non-tilted substrate, a strong (111) diffraction peak in the XRD angular scan is observed (Fig. 4.2(a)). Next to the (111) diffraction peak, small (200) and (220) peaks are visible. The fraction of grains with a [hkl] out-of-plane orientation is calculated by equation 3.2 (Sect. 3.1.1). Because the relative peak intensity of the (200), (220) and (111) reflections measured for a MgO powder scales with 100 : 46 : 3.7 respectively, the fraction of [100] or [110] out-of-plane oriented grains is negligible. This indicates that the MgO thin film exhibits a preferential [111] out-of-plane orientation. It should be mentioned that the relative peak intensity deviates from the values giving in the JCPDS cards. This is due to different optics of our XRD equipment. The equipment

[1] Because the O_2 inlet is close to the substrate, the oxygen first hits the growing surface where it forms a stoichiometric MgO film, before it's spread into the chamber. At the target, the oxygen partial pressure is too low to cover completely the race track with a MgO compound. As a result, a stoichiometric MgO film is deposited while sputtering in metallic mode.

[2] Stoichiometric MgO thin films are completely transparent in the visual light range. If the oxygen concentration in the MgO thin film is too low, the film is opaque.

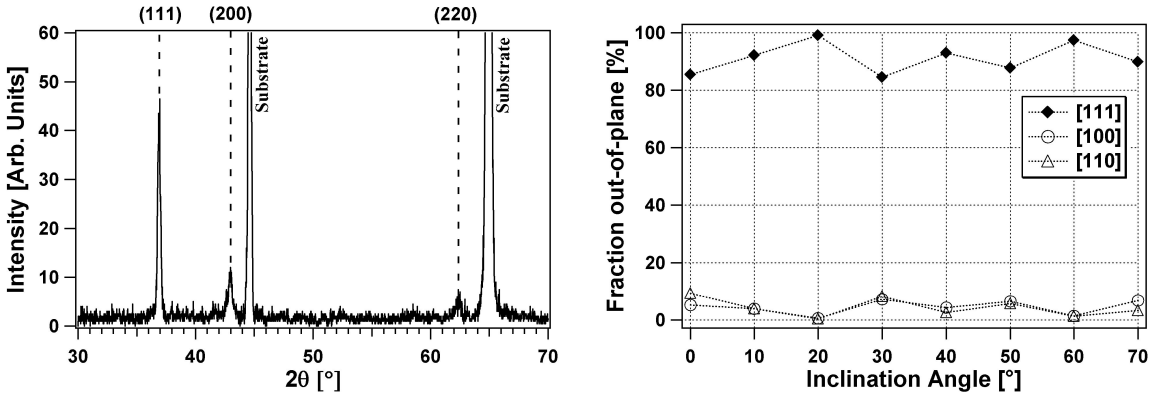

(a) XRD Angular Scan (b) Influence of the inclination angle

Figure 4.2: (a) XRD angular scan of a MgO thin film deposited on a non-tilted substrate, indicating a preferential [111] out-of-plane orientation. (b) The out-of-plane alignment of MgO thin films as a function of the substrate inclination angle α.

is calibrated by the diffraction peaks of corundum [1].
Fig. 4.2(b) shows the fraction of grains with a specific out-of-plane orientation as a function of the substrate inclination angle α. All the MgO thin films exhibit a preferential [111] out-of-plane orientation, in despite of some small variations. Moreover, in this thesis work, MgO thin films with another out-of-plane orientation aren't observed. Depending on the used deposition parameters, the fraction of [111] out-of-plane oriented grains could decrease but it did not result in another preferred orientation. In stead, the fraction of randomly oriented grains increased.
When depositing on an inclined substrate, the MgO thin films exhibit a preferential in-plane orientation. Fig. 4.3(a) shows the (200) pole figure of a biaxially aligned MgO thin film deposited on a tilted substrate (α = 70°). Three distinct poles are observed which indicates a strong in-plane alignment. One of the poles is observed at an angle χ close to 45°. Because the angle between the (100) and (111) planes is 55°, it is suggested that the [111] direction is slightly tilted away from the substrate normal. Nevertheless, a [111] out-of-plane alignment is considered. The poles are located at ϕ=0°±n·120° with respect to the incoming material flux. Hence, one of the poles is oriented towards the incoming material flux.
As can be seen in Fig. 4.3(b), the degree of the in-plane alignment depends on the inclination angle of the substrate. On a non-tilted substrate (α = 0°), the MgO thin film has a random in-plane orientation. Similar to Fig. 3.3(b), the (200) pole figure of an uniaxially aligned MgO thin film consists of a ring pattern situated at 55°(not shown here). With increasing inclination angle, the in-plane alignment improves. However, at a larger inclination angle, the improvement of the in-plane alignment is less pronounced. The position of the (200) poles does not change by changing the inclination angle.
The surface of an uniaxially aligned MgO thin film, grown on a non-tilted substrate, is shown in Fig. 4.4(a). The grains are truncated by a clear crystal habit with a threefold symmetry. Knowing the [111] out-of-plane orientation, it is suggested that the facets of the crystal habit corresponds to the {100} planes. This crystal habit is schematically shown in Fig. 4.4(c). Also the biaxially aligned thin films exhibit an {100} crystal habit (Fig. 4.4(b)). Hereby, one of the {100} facets

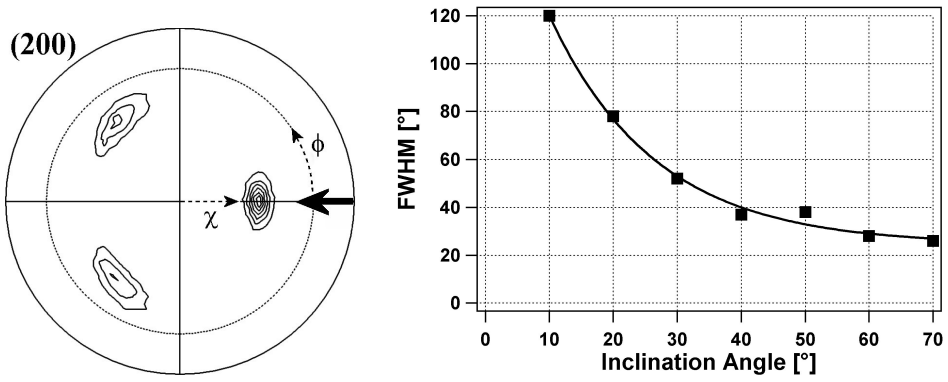

(a) (200) pole figure (b) Influence of the inclination angle

Figure 4.3: (a) (200) pole figure of a MgO thin film deposited on a tilted substrate ($\alpha = 70°$). The direction of the incoming material flux is projected on the pole figure and is indicated by an arrow; (b) The influence of substrate inclination angle on the in-plane alignment of MgO thin films. The FHWM of the (200) pole is used to obtain information about the in-plane orientation distribution of the grains.

is oriented towards the incoming material flux. This result can be correlated to the XRD pole figure, where the (200) pole is oriented towards the flux. Because one of {100} facets is always oriented towards the incoming material flux, the MgO thin film exhibit a high degree of in-plane alignment.

Fig. 4.5(a) shows a SEM cross section of a biaxially aligned MgO thin film. At the substrate/thin film interface, a large number of small grains are observed. During the growth, some of the grains are overgrown by the others. During this overgrowth, the grains expand laterally, which results in a typical V-shaped columnar structure. Because the MgO thin film is [111] out-of-plane oriented, it's suggested that the [111] out-of-plane oriented grains overgrow differently

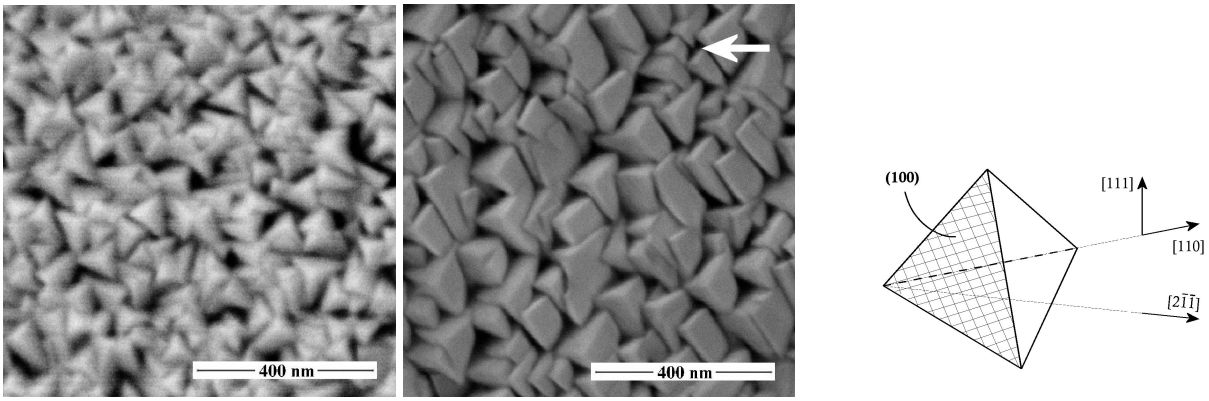

(a) Uniaxially Aligned MgO (b) Biaxially Aligned MgO (c) {100} crystal habit

Figure 4.4: Plan View SEM image of (a) uniaxially aligned MgO thin film; (b) biaxially aligned MgO thin film. The arrow indicates the direction of the incoming material flux. The observed {100} crystal habit is shown in (c).

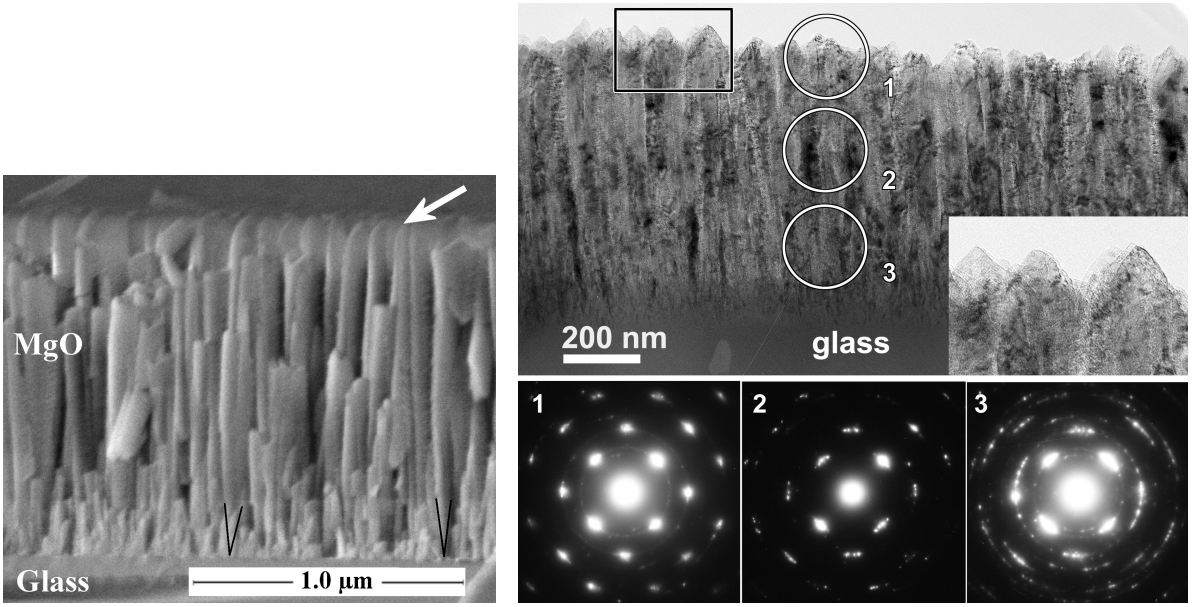

(a) SEM Cross Section (b) TEM Cross Section

Figure 4.5: (a) SEM and (b) TEM Cross Section of a biaxially aligned MgO thin film deposited on a tilted glass substrate. The inset shows the faceting on top of the columns. The ED pattern is taken at various film thicknesses.

oriented grains. The TEM cross section of a similar MgO thin film indicates that the overgrowth is almost completed after a few 100 nm (Fig. 4.5(b)). This can be deduced from the Electron Diffraction (ED) patterns, where only a few diffraction spots are observed. Less intens spots are also visible on ED pattern 3. This indicates that there are grains with an orientation different from the [111] out-of-plane orientation present at the film/substrate interface. At a higher thickness, only diffraction spots of [111] out-of-plane oriented grains are observed. In the inset of Fig. 4.5(b), the upper part of the MgO thin film is enlarged. It is observed that the columns are truncated by a clear crystal habit.
Although the thin film is grown on a tilted substrate, the columns grow perpendicular to the substrate. This is in contrast to the empirical tangent rule, which is only valid during ballistic depositions (section 1.6.1). This suggests a high mobility of the adatoms during the growth.
Finally, it can be concluded from the observations of a crystal habit, the V-shaped columnar growth, the evolutionary overgrowth and the preferred crystallographic out-of-plane orientation that the MgO thin films are deposited in Zone T conditions (see section 1.6.2).

4.3.2 Experimental Observations of Cr

Cr has a Body-Centered Cubic (BCC) crystal structure which has an $Im\bar{3}m$ space group with a lattice parameter *a* of 2.884 Å.
Both uniaxially and biaxially aligned Cr thin films are deposited by unbalanced magnetron sputtering. Therefore, a 5 cm circular metallic Cr target is sputtered in a pure Ar atmosphere at a working pressure of 0.38 Pa. The target-substrate distance was 10 cm and the discharge current

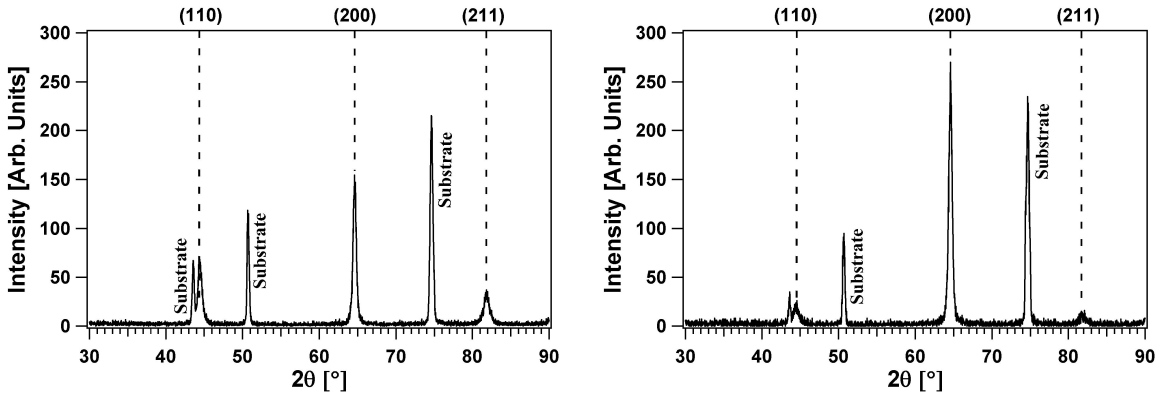

(a) Non tilted substrate (b) Tilted substrate

Figure 4.6: XRD Angular scan of a Cr thin film deposited on a non-tilted substrate (a) and a tilted substrate (b).

is fixed at 0.65 A. An 1 : 3 magnet configuration is used which is slightly unbalanced (Sect. 2.4). The Cr thin films were deposited on non-aligned Hastelloy at floating potential. With these parameters, a deposition rate of about 30 nm/min is obtained. The film thickness was about 1.0 μm. Both depositions on a non-tilted ($\alpha = 0°$) and tilted ($\alpha = 60°$) substrate are performed.
Fig. 4.6 shows the XRD angular scan of a Cr thin film deposited on a non-tilted substrate (a) and tilted substrate (b). For the Cr thin film deposited on a non-tilted substrate, several diffraction peaks are observed. Because the relative peak intensity of the (110), (200) and (211) peaks from a powder diffraction pattern scales with 100 : 19 : 39 (following the JCPDS cards, corrected for the used optics), the (200) peak is dominant. Hence, it can be concluded that the Cr thin film exhibits a preferential [100] out-of-plane orientation. As can be seen in Fig. 4.6(b), the Cr thin film deposited on a tilted substrate also exhibits a preferential [100] out-of-plane orientation. In this case, the contribution of differently oriented grains is much smaller than for the Cr thin film grown on a non-tilted substrate.
Fig. 4.7 shows the (110) XRD pole figures of the Cr thin film deposited on a non-tilted (a) and a tilted substrate (b). On a non-tilted substrate, a typical ring pattern is observed at $\chi = 45°$. This angle corresponds to the angle between the (100) and (110) planes and confirms the [100] out-of-plane alignment. The ring pattern points at a random in-plane alignment. Hence, uniaxially aligned Cr thin films are obtained when the substrate is not tilted. When depositing on an inclined substrate, four distinct poles are observed which indicates an in-plane alignment. These poles are located at ϕ=45°±n·90° with respect to the incoming material flux. It can be concluded that Cr thin films exhibit a biaxial alignment when deposited on an inclined substrate.
Fig. 4.8 displays the SEM image of a Cr thin film grown on a non-tilted substrate having an uniaxial alignment (a), and on a tilted substrate having a biaxial alignment (b). The grains of the uniaxially aligned Cr thin film are truncated by a clear crystal habit with a fourfold symmetry. Because of the fourfold symmetry and the [100] out-of-plane orientation, the facets of the crystal habit correspond to the {110} planes. This crystal habit is schematically shown in Fig. 4.8(c). Remark that the top of the {110} pyramid, not always points upwards. This corresponds to a minority of differently oriented grains and explains the appearance of (110) and (211) diffractions

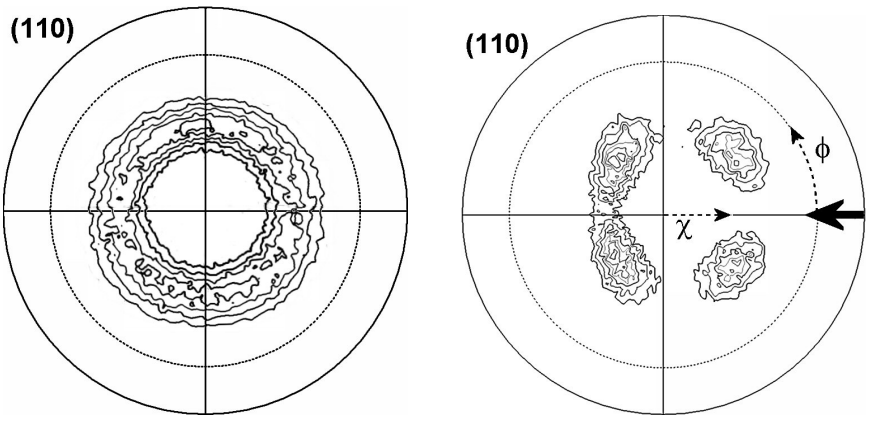

(a) Non tilted substrate (b) Tilted substrate

Figure 4.7: (110) pole figure of a Cr thin film deposited on a non-tilted substrate (a) and a tilted substrate (b). The direction of the incoming material flux is projected on the pole figure and is indicated by an arrow.

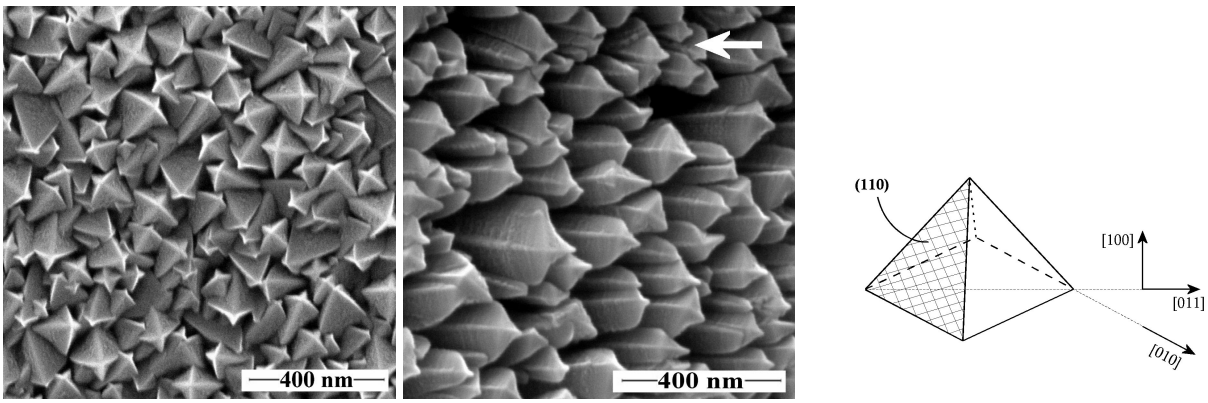

(a) Uniaxially Aligned Cr thin film (b) Biaxially Aligned Cr thin film (c) {110} crystal habit

Figure 4.8: Plan View SEM image of an uniaxially aligned Cr thin film (a) and a biaxially aligned Cr thin film (b). The arrow indicates the direction of the incoming material flux. The observed {110} crystal habit is shown in (c).

peaks in XRD.
The grains of the biaxially aligned Cr thin film are also truncated by an {110} crystal habit. In addition, the edge of the {110} crystal habit points towards the incoming material flux, which confirms the in-plane alignment.
Fig. 4.9 shows a TEM cross section of a biaxially aligned Cr thin film deposited on an inclined substrate ($\alpha = 60°$). A clear columnar structure can be observed where the columns are inclined towards the incoming material flux. The tilt angle of the columns is about 30°, which deviates from the tangent rule (an angle of 41°is expected). On the substrate/film interface, a lot of small columns are observed. Throughout the film thickness, some of the columns are overgrown by others, resulting in a typical V-shaped columnar structure. The top of the columns are clearly

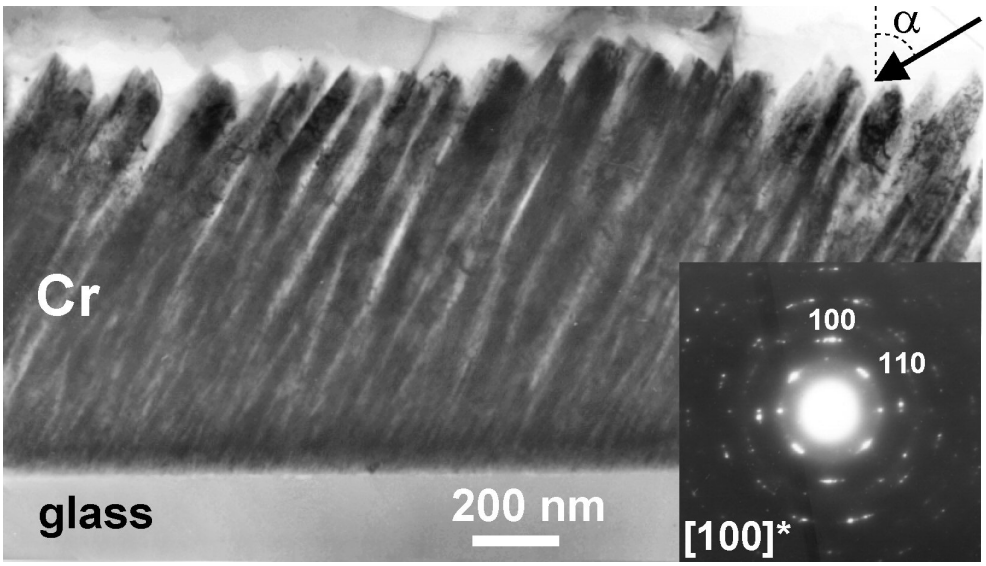

Figure 4.9: TEM Cross Section of a biaxially aligned Cr thin film deposited on a tilted glass substrate (α = 60°).

faceted. The ED pattern, taken at the upper most part of the Cr thin film, confirms the [100] out-of-plane orientation.
To confirm the evolutionary overgrowth, Cr thin films are deposited on an inclined substrate with various thicknesses. Fig. 4.10(a) shows the out-of-plane orientation as a function of the layer thickness. At a layer thickness of 500 nm, a small fraction of randomly oriented grains is present. With increasing thickness, the Cr thin film becomes fully [100] out-of-plane oriented. This indicates that [100] out-of-plane oriented grains overgrow differently oriented grains.

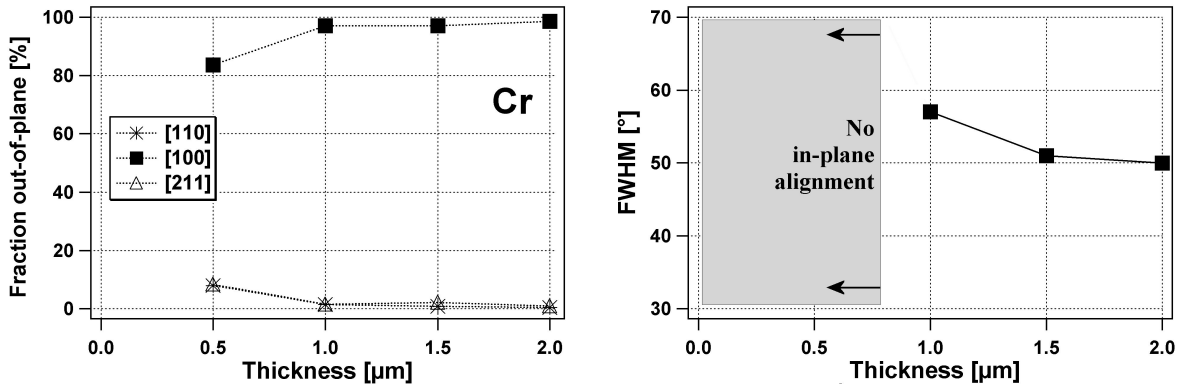

(a) Out-of-plane Alignment (b) In-plane Alignment

Figure 4.10: Influence of the layer thickness on the out-of-plane alignment (a) and the in-plane alignment (b) of biaxially aligned Cr thin films. The fraction of preferentially out-of-plane oriented grains is determined by measuring the peak area of the various diffraction peaks in the XRD angular scans. The FWHM is obtained from the (110) XRD pole figures.

Also the in-plane alignment improves with increasing thickness (Fig. 4.10(b)). No in-plane alignment is observed for a layer thickness below 1.0 μm. This suggests that also the mechanism for the evolution of the in-plane alignment should be based on an overgrowth of different grains.

It can be concluded that the growth of biaxially aligned Cr thin films is characterized by an evolutionary overgrowth of [100] out-of-plane oriented grains. Also the in-plane alignment is established by the overgrowth of differently in-plane oriented grains. Together with a clear {110} crystal habit and a V-shaped columnar growth, it can be concluded that biaxially aligned Cr thin films are grown in Zone T conditions.

4.3.3 Experimental Observations of InN

The crystal structure of the III-V semiconductor InN is the hexagonal wurtzite structure (space group: $P6_3mc$) having the lattice parameters a = 3.536 Å and c = 5.704 Å [2]. Wurtzite consists of two HCP sublattices, for which the HCP sublattice of N is shifted over a distance $\frac{5}{8}$c in the c direction.
InN thin films are deposited by unbalanced magnetron sputtering using an 1 : 3 magnet configuration. A water cooled[3] metallic In target is sputtered in a Ne-N_2 ambient. Ne is used as sputter gas to increase the atomic fraction of nitrogen in the discharge to enhance the stoichiometry [3] (Detailed information is given in next chapter in section 5.5.3). In addition, an excessive amount N_2 gas is used to deposit InN. This has been done in accordance to the observations of Guo et al. [4]. They examined the effect of nitrogen to argon ratio on the growth of InN thin film deposited by RF magnetron sputtering and reported stoichiometric InN thin films at the highest N_2-Ar ratio. In the experiments here under discussion, a flow rate of 8 sccm Ne and 36 sccm N_2 is used, giving a working pressure of 0.25 Pa. A deposition rate of about 90 nm/min is obtained with a target-substrate distance of 9 cm, a discharge current of 0.55 A and a substrate bias of −40 V. The InN thin films have a thickness of 1.5 μm. Non-aligned stainless steel is used as substrate. InN thin films are also deposited on Si, however with the only purpose of TEM measurements. No difference in experimental results is observed between the two substrates.

Before discussing the results, a short comment on the angles between directions and planes in a hexagonal system must be made. In a hexagonal system, a = b ≠ c and the angle γ between the lattice vectors $\vec{a}$ and $\vec{b}$ is 120°. As a result, planes and directions with the same indexing aren't orthogonal in a hexagonal system. Calculations of the angle between the different planes and directions in a hexagonal system are given in Appendix B. This has consequences for interpreting the results and could lead to confusion. More specific, XRD angular scans in a θ-2θ setup, give the number of (uvw) planes that are parallel to the substrate. However, the normal to the plane and the [uvw] direction aren't always parallel.[4] (For instance, the angle between the $[20\bar{2}3]$ direction and the $(20\bar{2}3)$ plane is 33.02°.) During this work, the term *preferred orientation* refers to the normal of the plane which is parallel to the substrate. With this, if the $(20\bar{2}3)$ planes are parallel to the substrate, the thin film has a preferential $[20\bar{2}3]_\perp$ out-of-plane orientation (Remark the $\perp$ sign).

[3] Although the low melting temperature of In (156.6°C) and the high power density on the target (30 W/cm^2), the water cooling at the back of the target was sufficient to prevent the melting of the target.

[4] Moreover, the <0001> directions are the only set of directions which are perpendicular to the corresponding {0001} planes.

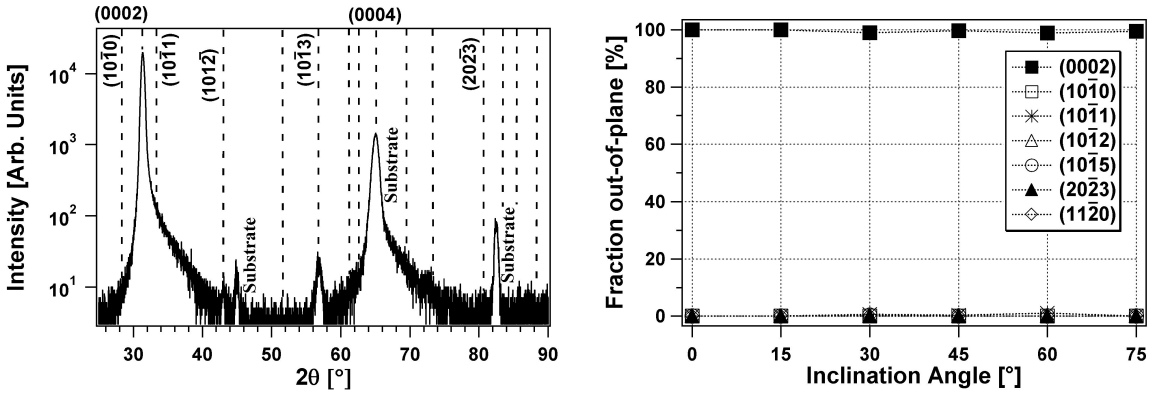

(a) XRD Angular Scan (b) Influence of the inclination angle

Figure 4.11: (a) XRD Angular scan of an InN thin film deposited on a non-tilted substrate, indicating a preferential [0001] out-of-plane orientation. Some of the diffraction peaks are indexed. The (0004) coincides with a substrate peak, however, this peak is negligible in comparison to the (0004) peak. The intensity is plotted in a logaritmic scale. (b) The out-of-plane alignment of InN thin films as a function of the substrate inclination angle α.

On a non-tilted substrate, both the (0002) and (0004) diffraction peaks are observed in the XRD angular scan (Fig. 4.11(a)). The extended tail originates from the used XRD optics. The (10$\bar{1}$2) and (10$\bar{1}$3) peaks which are also observed, are negligible because the relative peak intensity of the (0002), (10$\bar{1}$2) and (10$\bar{1}$3) reflection in a powder diffraction scales with 40 : 20 : 28 (according to the JCPDS cards, corrected with the used optics). Therefore, the InN thin film exhibits a preferential [0001] out-of-plane orientation. By tilting the substrate, similar XRD angular scans are observed. Therefore, there is no influence on the out-of-plane plane alignment by tilting the substrate (Fig. 4.11(b)).

Fig. 4.12(a) shows a XRD (10$\bar{1}$1) pole figure of an InN thin film deposited on an inclined substrate (α = 60°). The six distinct poles, confirming the hexagonal symmetry, indicate a strong in-plane alignment, hence a biaxial alignment. The poles are located at an angle ϕ=30° ± n·60° with respect to the incoming material flux. Additionally, the preferential [0001] out-of-plane alignment is confirmed by the position of the poles at χ = 60°, which corresponds to the angle between the (0001) planes and the (10$\bar{1}$1) planes (61.70°). The InN thin films deposited on a non-tilted substrate exhibit a ring pattern at χ = 60° (not shown). This indicates that the grains in the thin films have a preferential [0001] out-of-plane orientation and a random in-plane orientation.

Fig. 4.12(b) shows the FWHM of the (10$\bar{1}$1) pole as a function of the substrate inclination angle. Without inclination, no in-plane alignment is observed. By increasing inclination angle, the in-plane alignment improves.[5] For the highest inclination angles, the improvement of the in-plane alignment saturates. No change in the position of the poles is observed for the InN thin films deposited with a different inclination angle.

[5] At 15°, no uniform ring pattern nor distinct poles are observed. This is due to the overlap of broad (10$\bar{1}$1) poles. It wasn't possible to obtain qualitative data about the FWHM of the poles.

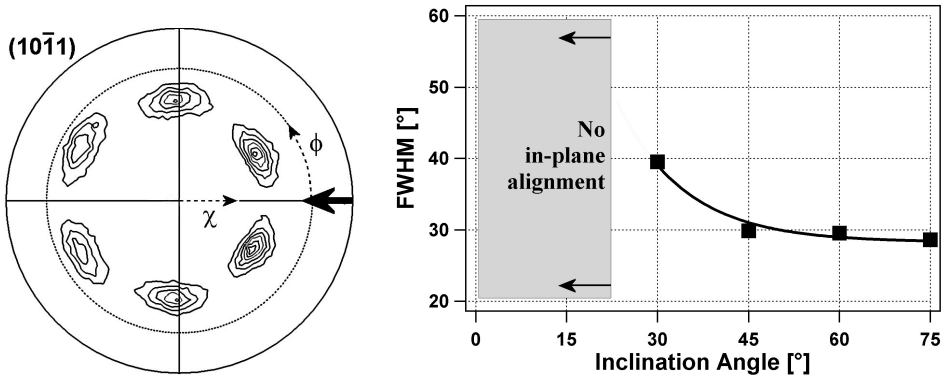

(a) (200) pole figure (b) Influence of the inclination angle

Figure 4.12: (a) (10$\bar{1}$1) pole figure of an InN thin film deposited on a tilted substrate (α = 60°). The direction of the incoming material flux is projected on the pole figure and is indicated by an arrow; (b) influence of substrate inclination angle on the in-plane alignment of InN thin films. The FWHM of the (10$\bar{1}$1) pole is used to obtain information about the in-plane orientation distribution of the grains.

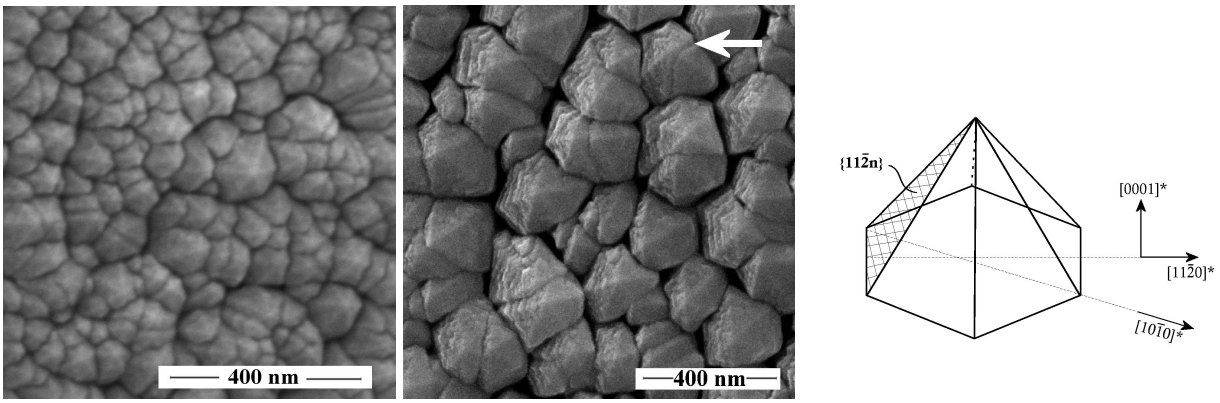

(a) Uniaxially Aligned InN thin film (b) Biaxially Aligned InN thin film (c) {11$\bar{2}n$} crystal habit

Figure 4.13: (a) Plan View SEM image of an uniaxially aligned InN thin film grown on a non tilted substrate (0°); (b) Plan View SEM image of a biaxially aligned InN thin film grown on a tilted substrate (60°). The arrow in (b) indicates the direction of the incoming material flux. The observed {11$\bar{2}$3} crystal habit is shown in (c).

Fig. 4.13 shows the SEM plan view images of an uniaxially aligned (a) and biaxially aligned (b) InN thin film deposited on a non-tilted and a tilted substrate respectively. Both the InN thin film grown on a non-tilted and tilted substrate have a clear faceted grain structure with a sixfold symmetry. For the uniaxially aligned InN thin film, it wasn't possible to identify the crystal shape univocally. Because there is no preferential in-plane orientation, no distinction between {11$\bar{2}n$} and {10$\bar{1}n$} grains could be made. Hereby is n an integer. In comparison with the biaxially aligned thin films (grown on a tilted substrate), the grains are much smaller. Roughly, the grains of the InN thin film grown on a non-tilted substrate have a width of 50 nm, while the InN thin

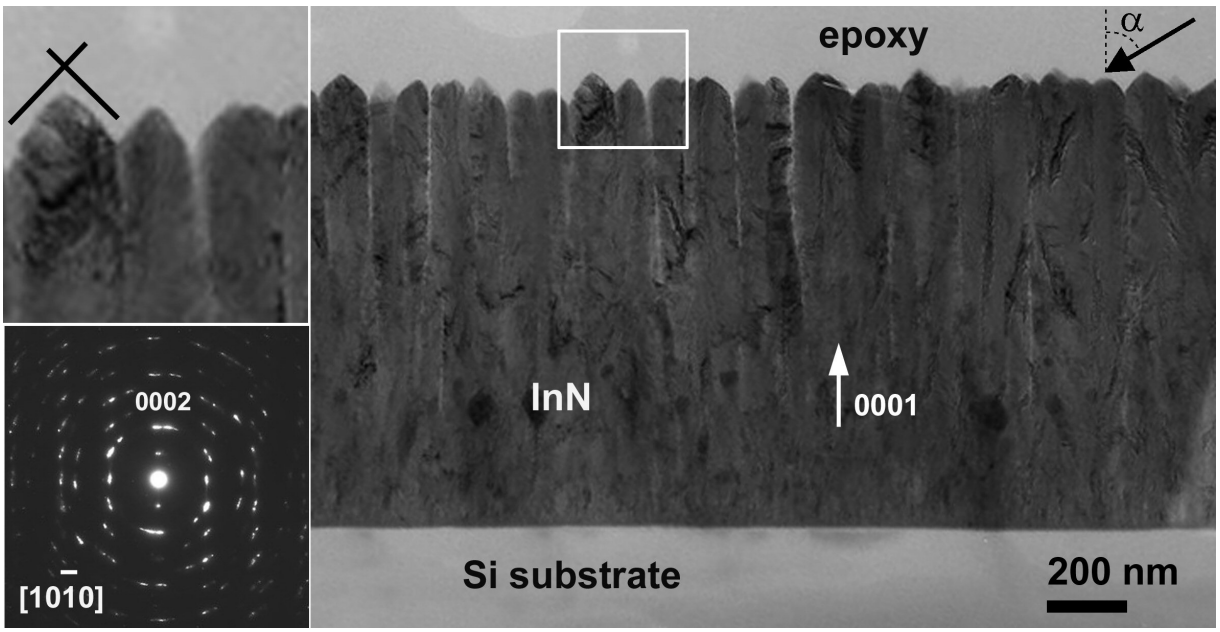

Figure 4.14: TEM Cross Section of a biaxially aligned InN thin film deposited on a tilted Si substrate. The ED pattern indicates a preferential [0001] out-of-plane alignment. The inset shows the faceting on top of the columns. The cross section is taken along the direction of the incoming material flux, which is indicated with an arrow.

film deposited on a tilted substrate has a grain size of 200 nm.
For the biaxially aligned InN thin film, the side of the crystal shape is oriented towards the incoming material flux, which confirms the in-plane alignment. Because the InN thin film has a preferential [0001] out-of-plane orientation and the $(10\bar{1}1)$ pole is located at 30°, it is suggested that the crystal shape is composed of $\{11\bar{2}n\}$ planes, where n is an integer. This is reasonable because in the stereographic projection, the angle between the center and the $(10\bar{1}1)$ plane and the center and an $\{11\bar{2}n\}$ plane is always 30°. A schematic drawing of an $\{11\bar{2}n\}$ faceted grain with a preferential [0001] out-of-plane orientation is shown in Fig. 4.13(c). The integer n can be determined by measuring the enclosed angle of the pyramid. This angle can be determined by using a TEM cross section of such a thin film. Fig. 4.14 shows a TEM cross section of a biaxially aligned InN thin film. The enclosed angle is 88°±3°, which is the closest to the enclosed angle between the $\{11\bar{2}3\}$ planes (Table 4.1). Therefore, it can be concluded that the grains of InN thin films are truncated by an $\{11\bar{2}3\}$ crystal shape.
On the TEM cross section (Fig. 4.14) a clear columnar structure is observed. The columns grow perpendicular to the substrate. No tilt towards the incoming material flux is observed. The ED pattern confirms the [0001] out-of-plane plane alignment.

Fig. 4.15 shows a high resolution TEM image of the substrate/film interface. On the TEM image, four different grains can be distinguished. The grain boundaries at the substrate/film interface are indicated. The grains have a size of 30 to 40 nm. It can be seen that one of the grains is overgrown by the two neighbouring grains. The overgrowth is completed after 60 nm. It was not possible to determine the crystallographic orientation of the grains, because of the degradation

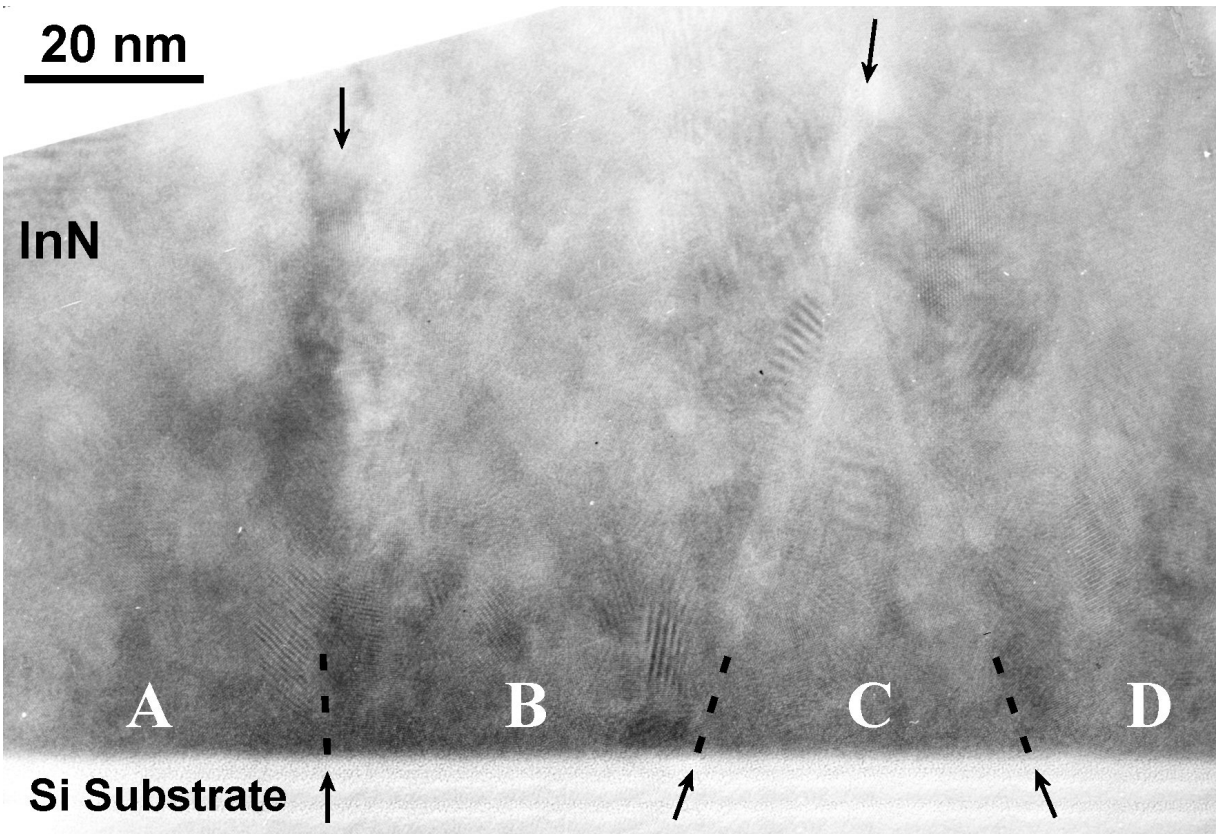

Figure 4.15: HREM image of the TEM Cross Section at the substrate/film interface of a biaxially aligned InN thin film deposited on a tilted Si substrate. Four different grains can be observed. The grain boundaries are indicated.

of the sample probably caused by oxidation. To verify this hypothesis, the surface oxidation of an InN thin film is measured by XPS. Fig. 4.16 shows the ratio between the O and In signal as a function exposure time to the air of a biaxially aligned InN thin film. A clear increase in oxygen concentration is observed with increasing exposition time. This suggests that the InN thin film is sensitive to surface oxidation. Because the time between the sample preparation and the HREM measurement is in the order of a few weeks, it suggested that the sample was degraded by the

Habit	Enclosed Angle	Habit	Enclosed Angle
$\{10\bar{1}0\}$	n/a	$\{11\bar{2}0\}$	n/a
$\{10\bar{1}1\}$	56.61°	$\{11\bar{2}1\}$	34.54°
$\{10\bar{1}2\}$	94.25°	$\{11\bar{2}2\}$	63.75°
$\{10\bar{1}3\}$	116.48°	$\{11\bar{2}3\}$	86.01°
$\{10\bar{1}4\}$	130.19°	$\{11\bar{2}4\}$	102.39°

Table 4.1: The enclosed angle of the crystal shape truncated by various crystallographic planes. The angle is calculated by making use of the equations in Appendix B.

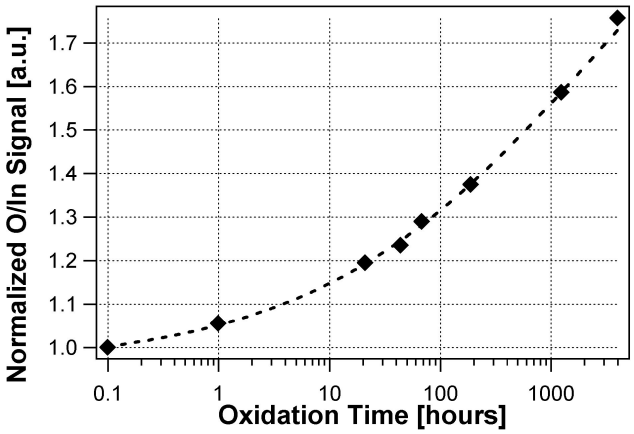

Figure 4.16: O/In ratio as determined by XPS as a function of the exposition time to air of a biaxially aligned InN thin film.

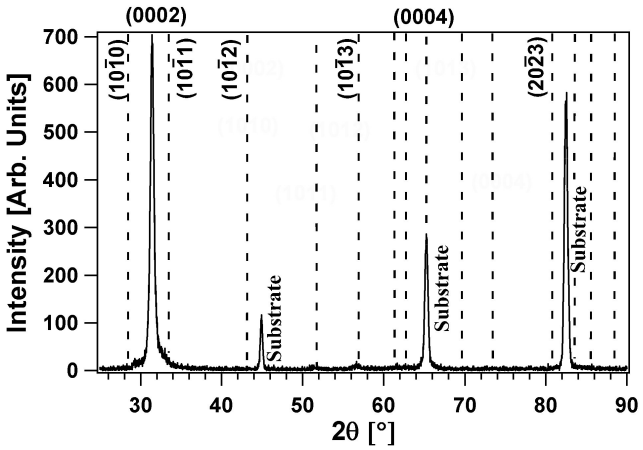

Figure 4.17: XRD Angular scan of an InN thin film deposited on a non-tilted substrate with a layer thickness of 50 nm. The (0004) peak coincides with the substrate peak. However, this peak is not important to determine the out-of-plane orientation because it scales with the (0002) peak.

formation of an oxide.[6]

In order to know the orientation of the grains at the substrate/film interface, an other approach is followed. An InN thin film is deposited on a tilted substrate with a layer thickness of 50 nm. Fig. 4.17 displays this XRD angular scans. Only the (0002) peak is visible. If differently out-of-plane oriented grains would nucleate, these grains would have a contribution in the XRD angular scan. Since no other XRD peaks are observed, it can be concluded that the grains which nucleate on the substrate have an [0001] out-of-plane orientation. Hence, the grains observed at the substrate/film interface in the HREM (Fig. 4.15), have an [0001] out-of-plane orientation. So, the overgrowth of the grain isn't caused by the overgrowth of differently oriented grains. This is different from the observations of the MgO and Cr thin films.

[6] Also, traces of a cubic compound are found in HREM, probably originating from the cubic In_2O_3

4.3.4 Summary of the Experimental Results

Crystallographic Orientation

The thin films deposited on a non-tilted substrate exhibit a preferential out-of-plane orientation but a random in-plane orientation. The MgO, Cr and InN thin film exhibit an [111], [100] and [0001] out-of-plane orientation, respectively. Tilting the substrate has no influence on the out-of-plane orientation. For MgO and Cr thin films, there is an overgrowth of differently out-of-plane oriented grains, while for InN thin films the grains have already an [0001] out-of-plane orientation at the substrate/film interface.
When depositing on a tilted substrate, an in-plane alignment is observed for the various thin films in addition to a preferential out-of-plane alignment. The in-plane alignment improves with increasing inclination angle.

Microstructure

All thin films have a clear columnar structure. On a non-tilted substrate, the columns grow perpendicular to the substrate. On a tilted substrate, the columns of the MgO and InN thin film grow perpendicular to the substrate, while the columns in the Cr thin film are tilted towards the incoming material flux.
For the cubic materials Cr and MgO, a large number of small grains are formed at the substrate/film interface. During the growth, grains with another crystallographic orientation are overgrown by other grains. This results in a typical V-shaped columnar growth. For InN thin films deposited on a tilted substrate, also an overgrowth is observed, however this overgrowth is less pronounced than for MgO or Cr thin films.
The columnar tops are truncated by a crystal habit, as well for the uniaxially aligned thin films as for the biaxially aligned thin films. For the biaxially aligned thin films, the egdes and planes of the crystal habit have a specific orientation with respect to the incoming material flux due to the in-plane orientation.

The experimental results are summarized in table 4.2.

	MgO	Cr	InN
Out-of-plane Orientation	[111]	[100]	[0001]
In-plane Orientation	ϕ at 0°	ϕ at 45°	ϕ at 0°
Crystal Habit	{100}	{110}	$\{11\bar{2}3\}$

Table 4.2: Summary Experimental Results

Summary

By comparing the experimental results of the three different materials, the observations for MgO and Cr are very similar. The growth of the thin films is characterized by an evolutionary overgrowth of grains with a specific out-of-plane orientation. Together with a clear crystal habit and

the V-shaped columnar structures, it can be concluded that the MgO and Cr thin films are deposited in Zone T. Therefore, the growth model to elucidate the growth mechanism of the biaxial aligned thin films will be based on zone T characteristics. Due to the similarities between MgO and Cr thin films, the growth mechanism for these cubic materials will be treated simultaneously (Sect. 4.4).
The experimental results of InN deviate from those of the cubic materials. For InN thin films, all grains have already the same [0001] out-of-plane orientation at the substrate/film interface. This suggest an orientation selection at the early stages of the growth. This observation disagrees with the characteristics of zone T, at which the grains have a random crystallographic orientation at nucleation. Therefore, the structure evolution, particularly the preferential out-of-plane alignment, of InN thin films will be different from the cubic materials and will be discussed in a separate section (Sect. 4.5).
For the three materials, an in-plane alignment evolves when depositing on a tilted substrate. Concerning the in-plane alignment, similar results are observed for the different materials, which suggests the same growth mechanism. This evolution of the in-plane alignment will be discussed in section 4.6.

4.4 Evolution of the Out-of-plane Alignment of a Cubic Structure

In section 1.6.2 it has been discussed that the out-of-plane alignment in zone T evolves by the competitive growth of neighbouring grains. This competitive growth results from an anisotropy in perpendicular growth rate of differently oriented grains. As a result, there will be an anisotropy in microstructure and crystallographic orientation throughout the complete film thickness. Therefore the structure evolution will be discussed progressively throughout all stages of growth. The proposed model will be discussed for the various crystallographic structures. The mechanism of the out-of-plane alignment however is slightly different for a cubic and a hexagonal crystal system and will be treated separately.
As discussed in section 1.4.4 islands will nucleate on the substrate (VW growth). Because the adatoms can diffuse on the surface, they are able to find a stable place on the island. Therefore the islands will be crystalline but they will have a random crystallographic orientation. In zone T, there is no orientation selection during the island growth because the energy of the atoms is too low. If orientation selection occurs through restructurative grain growth, a typical zone II structure would be observed. Since the adatoms can find a stable place on the grain, the grain will grow according to a specific crystal habit. This crystal habit will correspond to the kinetical preferred growth shape of the various materials. The growth according to a specific crystal habit is a first fundamental property of zone T, which is used to explain the biaxial alignment.

4.4.1 Kinetical Growth Shape

Because the adatom mobility is considerable, the adatoms are able to find the energetic favourable place on the grain. As a result, the islands which are dispersed on the substrate during nucleation, will be limited by a certain crystallographic plane.

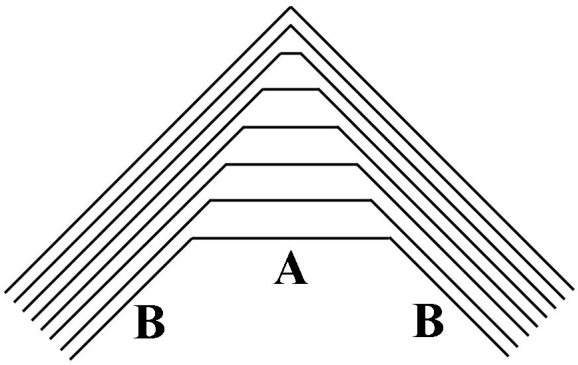

Figure 4.18: Evolution of the grain shape. The A facets which have a larger growth rate, grow themselves out of existence and the crystal habit will consist of the slower growing B facets.

From the crystallography and mineralogy it is known that the kinetical growth shape of a crystal is determined by the facets with the lowest normal growth rate. The planes with a higher normal growth rate grow themselves out of existence. This will also be applicable for the growth of individual grains on the substrate. The grains of the thin film will be truncated by planes with the lowest normal growth rate. Fig. 4.18 shows the mechanism of the facet formation. Initially, the grain can be limited by various crystallographic planes with a different normal growth rate. In this example, the grain is limited by A and B facets for which the B facet has a lower normal growth rate than the A facet. Purely based on geometrical aspects, it can be observed that the B facets will envelop the A facets. As a result, the grain will consist of the slower growing B facets. Because the kinetical growth shape is determined by the planes with the lowest normal growth rate, the normal growth rate of the various crystallographic planes $R_{(hkl)}$ should be calculated. In despite of it importance, it isn't straightforward to obtain information of the normal growth rate of the crystal facets. Throughout the history, different approaches are used to obtain the normal growth rate of the various crystallographic planes [5].

- In the early years, the normal growth rate R of the crystal facets was expected to be proportional to the surface free energy γ [5]. In contrast to the thermodynamical equilibrium shape, this approach doesn't require the minimization of the total surface energy. However, the constructed crystal shape often deviates from the experimentally observed growth shape.

$$R_{(hkl)} \sim \gamma_{(hkl)}$$

- According to Bravais-Friedel and Donnay-Harker, the normal growth rate of the various faces is inversely proportional to the interplanar spacing d_{hkl} [5]. The theory is corrected for the extinction conditions of the space group. Planes with the highest d-value, will have the lowest normal growth rate because the density will be higher. Also, this theory has a lot of discrepancies with experimental results and there are some shortcomings. For instance, this model is purely based on geometry and doesn't account for the energetics of the system.

$$R_{(hkl)} \sim (d_{(hkl)})^{-1}$$

- Another approach by Docherty [6] and Berkovitch [7] includes the energetics of the system. They stated that the relative growth rate of a flat crystallographic plane is proportional to its attachment energy. Planes with a lower attachment energy will have a lower normal growth rate. The attachment energy is determined by calculating the energy release to attach a (hkl) slice to the crystal surface.

$$R_{(hkl)} \sim E^{att}_{(hkl)}$$

- The Hartman-Perdok theory is another model to determine the growth shape of a crystal [8, 9]. Without going into the details of the theory, the attachment energy for all the connected nets must be calculated. Such a connected net[7], is a two dimensional surface which is constructed from a combination of Periodic Bond Chains (PBC). Hereby, a PBC represents a chains of bonds which are periodically repeated in the crystal system. In order to obtain information about the PBC, the bond energy between the growth units (ions or molecules) should be calculated, taking into account the crystal structure. Nets with the strongest PBC will have the lowest attachment energy, hence the lowest normal growth rate.
  This model is mostly used to construct the growth shapes of organic compounds. Although the Hartman-Perdok theory provides a good understanding, it's a tedious job to calculate the pair potentials between the growth units and to determine the PBC.

Mahieu et al. suggested a new approach to obtain the relative growth rate of the crystallographic planes with a cubic structure in an easy way [10]. It has been discussed that the normal growth rate of the various crystallographic planes depends on the number of nearest neighbours a plane offers to incoming adparticles.
This can be explained as follows. If a plane offers a low number of binding possibilities, the diffusion barrier will be small (section 1.3.1). Because the diffusivity scales with $\exp\left(-\frac{E_d}{kT}\right)$, the mobility of an adparticle on a plane which offers a low number of nearest neighbours will be high [11]. With a high mobility, the adparticles are able to reach the edges of the facet and contribute to the lateral growth of the plane.
In contrast, planes which offer a high number of nearest neighbours, will offer a low mobility to an incoming adparticle. Those planes will contribute to the normal growth rate. Hence, the normal growth rate of the plane will be inversely proportional to the number of nearest neighbours.

$$R_{(hkl)} \sim (\#\text{ Nearest Neighbours (hkl)})^{-1}$$

In a short summary, it can be concluded that the number of nearest neighbours for the various crystal planes should be calculated to obtain the crystal habit.

In order to calculate the number of nearest neighbours that a plane offers to incoming adparticles, two aspects play a key role, especially in the deposition of a multicomponent system, like MgO or InN. At first, the termination of the crystallographic plane is of importance. The termination of the plane will be different if the state of the reactive gas changes from molecular (N_2 or O_2)

[7] In a rather simple inorganic compound, the connected nets with a low attachment energy, correspond in most cases with the low index planes.

to atomic gas (N or O) [10]. This is due to the higher reactivity of the atomic gas.[8] In a single component system, like Cr, there is no change in termination of the crystallographic plane.
Secondly, the state of the incoming adparticle is of importance. The number of offered nearest neighbours will change if the particle is an adatom (Mg, In or Cr) or an adparticle. As a result, the adparticle mobility and the growth rate will change.
For the different cubic materials, the formation of the crystal habit will discussed using this model.

Kinetical Growth Shape of BCC Chromium

Because the growth of pure Chromium is a single component system, the termination of the different crystallographic planes doesn't change. Fig 4.19 shows the termination of the low index planes of Cr. It is often observed that only low index planes are present in a cubic growth shape. Therefore, only these planes are taken into account.
Next to the termination of the various crystallographic planes, the state of the arriving particle

[8] Atomic gas binds to the surface as soon there is one nearest neighbours. In contrast, molecular gas only dissociatively chemisorbs if it finds the half of its maximum number of nearest neighbours [1].

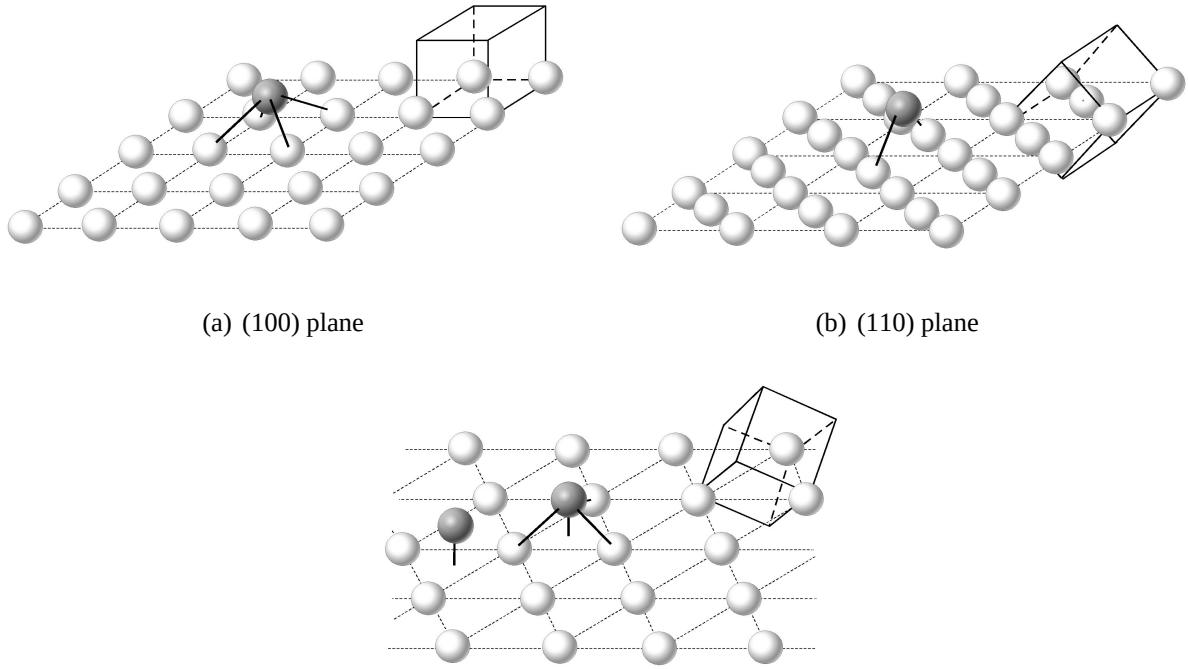

(a) (100) plane

(b) (110) plane

(c) (111) plane

Figure 4.19: Number of nearest neighbours offered by the various low index crystallographic planes of BCC Cr structure (a) (100) plane; (b) (110) plane; (c) (111) plane. Hereby, the bond length is 2.50 Å. Also the unit cell of Cr is shown. The raster network is used as a guide for the eye to identify the plane, but it has no physical meaning.

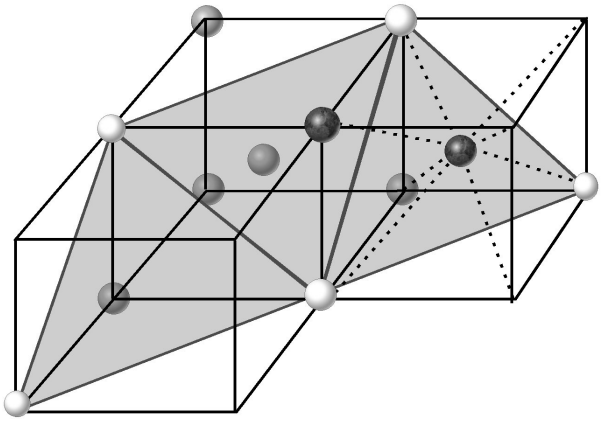

Figure 4.20: Three BCC unit cells on which an (111) plane is indicated. The white atoms correspond to the top layer and are situated in the (111) plane. The grey atoms are located in the second and third layer. The black atoms correspond to the arriving atoms. The solid lines are the boundaries of the unit cell, while the dashed lines show the binding possibilities.

must be known. In magnetron sputtering, mostly atoms are sputtered from the target (Sect. 2.2.1) [12]. Additionally, no dimer formation can occur in the plasma in a two body reaction (Sect. 2.5). Hence, it is suggested that Cr arrives as an adatom to the growing surface.
As can be seen in Fig. 4.19(a), the (100) plane offers 4 nearest neighbours to incoming Cr adatoms. In contrast, the (110) plane offers only 2 binding possibilities to the adatom (Fig. 4.19(b)). The (111) plane offers or 1 or 4 nearest neighbours, depending on the position on the plane (Fig. 4.19(c) and Fig. 4.20). It offers four nearest neighbours if the Cr adatoms is located in the center of the unit cell, while it can only make one binding if it's located at a corner site (Fig. 4.20). On average, an (111) plane offers 2.5 nearest neighbours to incoming adatoms.
Because the (110) plane offers the lowest number of nearest neighbours to incoming Cr adatoms, this plane will have the lowest normal growth rate. As a result, an {110} crystal habit will evolve. If the {110} crystal habit would be free standing, it corresponds to a rhombic dodecahedron (Fig. 1.15). When depositing thin films, only a section of the crystal habit parallel to the substrate will be visible.

Remark that some of the other approaches to determine the growth rate of the various facets also yield to the same {110} crystal habit. This can be deduced from Table 4.3.

	(100)	(110)	(111)
Number of nearest neighbours	4	2	2.5
Surface Energy γ [J/m^2]	1.228	1.029	1.244
d_{hkl} [Å]	1.442	2.039	0.832

Table 4.3: Overview of the parameters which could determine the slowest growing plane. The d value is corrected for the extinction conditions of the space group: $h + k + l = 2n$.

Kinetical growth shape of a Rocksalt Structure - MgO

To determine the number of nearest neighbours involved in the interaction of the plasma with the various planes of MgO, first the state of the reactive gas should be known. Therefore, plasma measurements with a mass spectrometer have been performed during the reactive sputter process. It has been observed that the fraction atomic oxygen is about 3 á 4%,[9] when deposting the MgO thin film in metallic mode. From the flow rate of 3 sccm O_2, the oxygen partial pressure can be obtained, hence, the impingement rate of atomic O and molecular O_2 can be calculated by using the kinetic theory of gases [14]. An impingement rate of $3.8{\cdot}10^{15}$ atoms O/cm^{2}s and $6.5{\cdot}10^{16}$ molecules O_2/cm^{2}s is obtained for atomic O and molecular O_2 respectively. From the deposition rate of 100 nm/min, the flux of metallic Mg adatoms is determined and is $9.0{\cdot}10^{16}$ atoms Mg/cm^{2}s. Because the impingement rate of atomic O is much smaller that the flux of metallic Mg adatoms, it can be concluded that in first assumption, molecular O_2 is decisive for the termination of the planes.
Not only the state of the reactive gas is of importance, one should know also the state of the incoming adparticle. Because the deposition is carried out in a metallic sputtering mode, mostly metallic Mg particles are sputtered. Because the probability for a two body reaction in the plasma is small, it can be concluded that mainly atomic Mg arrives at the growing surface.
With this, the number of nearest neighbours a plane offers to incoming Mg adatoms can be calculated, similar to Cr. Fig. 4.21 shows the low index planes of the MgO rocksalt structure. As can be seen, the (100) plane offers 1 nearest neighbour to an arriving Mg adatom.[10] The (110) plane offers 2 nearest neighbours and the (111) plane offers 3 nearest neighbours. Remark that the (111) plane is polar and is expected that (111) plane reconstructs to reduce the dipole moment [15].
Because the (100) plane offers the lowest number of nearest neighbours, it is expected the (100) planes will have the lowest growth rate and a {100} crystal habit will evolve (This is a cube). This is in agreement with the experimental observations.
From Table 4.4, it can be concluded that not all the approaches will result in a {100} crystal habit.

	(100)	(110)	(111)
Number of nearest neighbours	1	2	3
Surface Energy γ [J/m^2]	1.25	3.02	3.86
d_{hkl} [Å]	2.106	1.489	2.432

Table 4.4: Overview of the parameters which could determine the slowest growing plane. The *d* value is corrected for the extinction conditions of the space group: h, k, l = all even or odd.

[9] Hereby, the ionization cross section of O_2 and O has been taken into account [13].
[10] In case of atomic gas regime, there would be 5 binding possibilities.

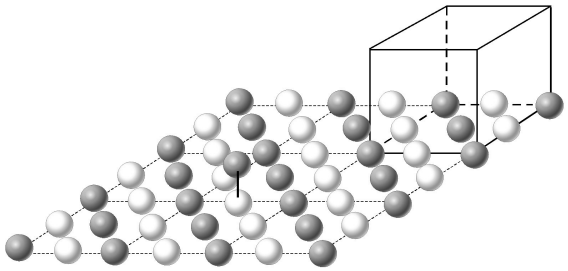

(a) (100) plane

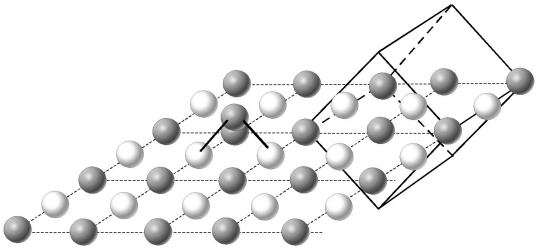

(b) (110) plane

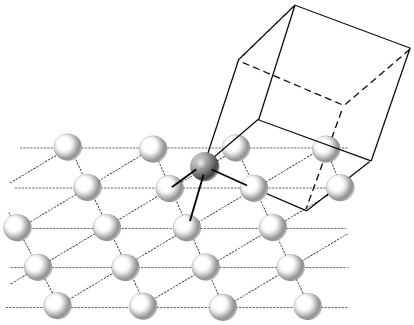

(c) (111) plane

Figure 4.21: Number of nearest neighbours offered by the various low index crystallographic planes of rocksalt MgO structure (a) (100) plane; (b) (110) plane; (c) (111) plane. Hereby, the dark atoms represent Mg atoms, while the light atoms correspond to oxygen.The bond length is 2.10 Å. Also the unit cell of MgO is shown. The raster network is used as a guide for the eye to identify the plane, but it has no physical meaning.

4.4.2 Geometric Fastest Growth Direction

As discussed in the previous part, small grains truncated by a specific crystal habit, will be dispersed on the substrate. The orientation of the grains is random because there is no restructurative grain growth. The grains grow by the incorporation of diffusing adatoms and/or by direct capture from the flux. At the point where the grains make contact, a grain boundary is formed, which is immobile throughout the film thickness.
Although all facets of the crystal habit have the same growth rate, some grains will have a higher perpendicular growth rate, i.e. the growth rate of the grain perpendicular to the substrate. This was illustrated in Fig. 1.17 when discussing the SZM (section 1.6.2). The anisotropy in perpendicular growth rate is purely based on geometrical considerations. There is no difference in energetics because the grains are faceted by identical crystallographic planes. Therefore, the perpendicular growth rate depends on the geometrical orientation of the crystal habit, and hence the crystallographic orientation of the grain. Grains with the fastest perpendicular growth rate, will overgrow the other grains, through which a preferential out-of-plane alignment evolves. This

idea has been formulated by van der Drift and is known as evolutionary selection or survival of the fastest [16].
To obtain the geometric fastest growth direction, the growth rate of the grain should be calculated in all directions. These calculations have been performed for MgO and Cr.

Perpendicular Growth Rate of {100} faceted grains - MgO

Consider an {100} crystal habit, which agrees with a cube (Fig. 4.22(a)). The geometrical fastest growth direction of the crystal habit corresponds to the orientation of the crystal habit for which the increase in height is at its maximum. Therefore the increase in height of differently oriented {100} crystal habits is calculated. The orientation of the crystal habit is defined by the angles θ and ω as illustrated in Fig. 4.22(b) and Fig. 4.22(c). The substrate corresponds to the XY-plane. The increase in height is calculated from the projection of the crystal habit onto the Z-axis and is given by:

$$R_{\{100\}} = \cos(\theta)\cos(\omega) + \sin(\theta)\cos(\omega) + \sin(\omega)$$

and is plotted in Fig. 4.23. The perpendicular growth rate is at its maximum for $\omega = 45°$ and $\theta = 35.26°$. This orientation of the crystal habit corresponds exactly with an [111] out-of-plane orientation of the grain. The {100} crystal habit of an [111] out-of-plane oriented grain is shown in Fig. 4.4(c). Hereby, only the top part is shown because the substrate has to be taken into account, hence, only the top part will be visible.
It can be summarized that grains with an [111] out-of-plane orientation will overgrow the differently oriented grains and determine the out-of-plane orientation of the thin film.

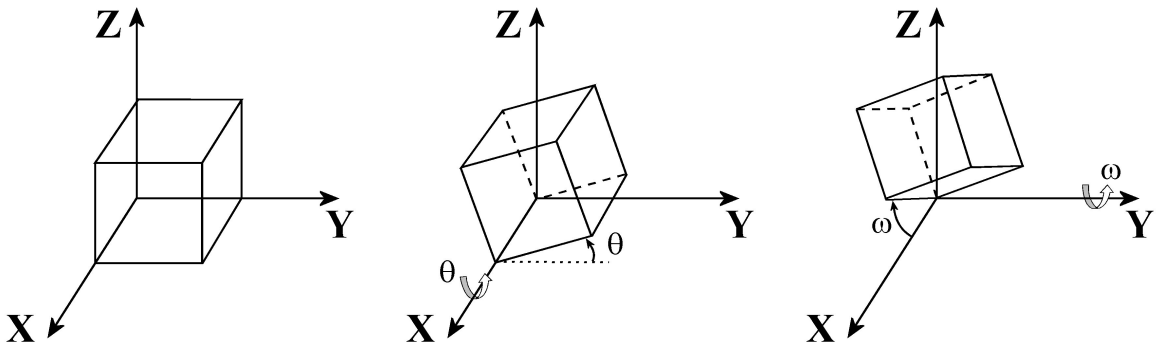

(a) (b) (c)

Figure 4.22: Schematic drawing of a cube in a XYZ coordination system. θ is the rotation angle around the X-axis. ω corresponds to the rotation around the Y-axis. The substrate is parallel to the XY plane.

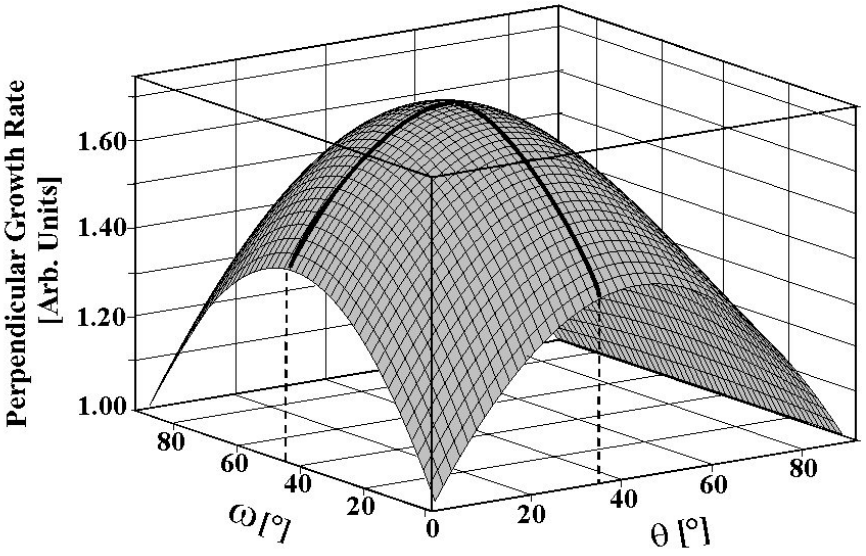

Figure 4.23: Perpendicular growth rate of an {100} crystal habit defined by the angle θ and ω

Perpendicular Growth Rate of {110} faceted grains - Cr

Also for a {110} faceted grain, the increase in height is calculated for different orientations. A free standing {110} faceted grain corresponds to a rhombic dodecahedron, and is defined in a XYZ coordination system, as illustrated in Fig. 4.24. The orientation of the {110} crystal habit is expressed with the angles θ and ω which tilt the habit around the X-axis and Y-axis respectively. The substrate plane corresponds to the XY-plane. The perpendicular growth rate is determined

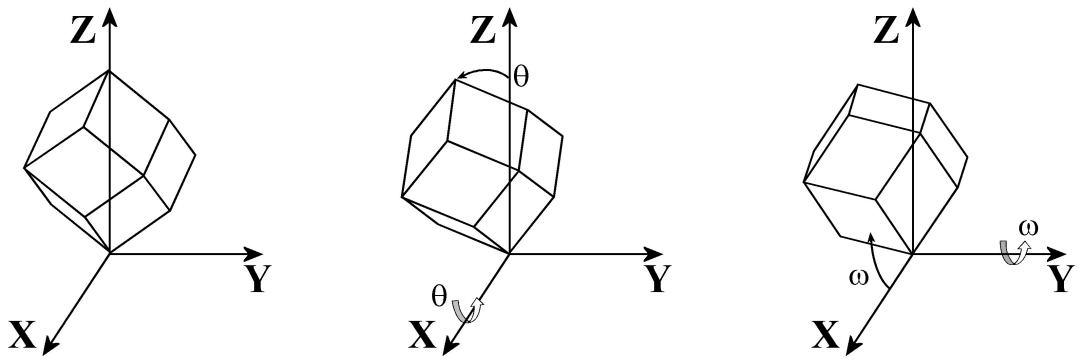

Figure 4.24: Schematic drawing of a rhomic dodecahedron in a XYZ coordination system. θ is the rotation angle around the X-axis. ω corresponds to the rotation around the Y-axis. The substrate is parallel to the XY plane.

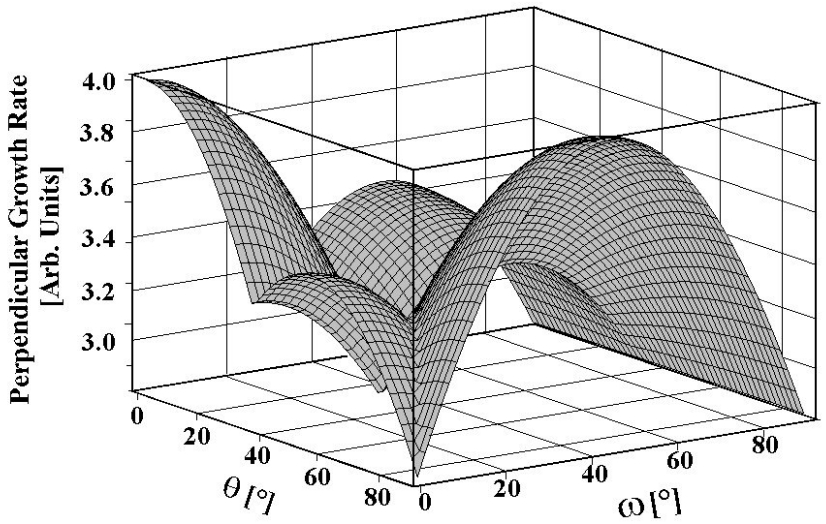

Figure 4.25: Perpendicular growth rate of an {110} crystal habit defined by the angle θ and ω. Due to the crystal symmetry, the calculations were limited both for θ and ω in the range [0°,90°]

by the projection of the crystal habit onto the Z-axis.
The increase in height along the Z-axis for the different orientations is plotted in Fig. 4.25. The increase in height is at its maximum for $\omega = 0°$; $\theta = 0°$ and $\omega = 45°$; $\theta = 90°$. For both orientation of the crystal habit, the [100] out-of-plane orientation of the grain is parallel to the Z-axis.[11] Two minor maxima are observed at $\omega = 0°$; $\theta = 54.74°$and $\omega = 54.74°$; $\theta = 0°$. These orientations correspond to the [111] orientation of the grain.[12]
However, the grains with an [100] out-of-plane orientation will have the fastest increase in height. They will overgrow the differently oriented grains and determine the out-of-plane orientation of the thin film. Indeed, for this orientation, the planes of the crystal habit have the highest tilt angle.
The {110} crystal habit of an [100] out-of-plane oriented grain, taking into account the substrate, is shown in Fig. 4.8(c).

Rule of Thumb

These calculations can be very hard for a complex crystal habit. To avoid these calculations, a simple rule can be used to determine that geometric fastest growth direction of the grains: The grains for which the facets of the crystal habit have the highest tilt angle with respect to the substrate, will have the highest perpendicular growth rate. This can clearly be seen in Fig. 1.17. For MgO, the grains are truncated by an {100} crystal habit. If the crystal habit is [111] out-

[11] For these orientation the fourfold symmetry axis of the rhombic dodecahedron is parallel to the Z-axis.
[12] For these orientation the threefold symmetry axis of the rhombic dodecahedron is parallel to the Z-axis.

of-plane oriented, the angle between the {100} planes and the substrate is 54.74°. For all other orientations, there is always a plane which makes a smaller angle. Owing to this, the [111] out-of-plane orientated grains will have the highest perpendicular growth rate and overgrowth the differently out-of-plane oriented grains.
The same reasoning can be applied to the {110} crystal habit of Cr. If the crystal habit is [100] out-of-plane oriented, the angle between the {110} planes and the substrate is 45°. For all other orientations, there is always a plane which makes a smaller angle. As a result, a [100] out-of-plane orientation will evolve.

4.5 Evolution of the out-of-plane Alignment of a Wurtzite Structure

The experimental observation of wurtzite InN clearly differs from those of a cubic crystal structure. At first, the preferential [0001] out-of-plane orientation corresponds to the normal to the plane with lowest surface free energy, being the (0001) plane.[13] Secondly, the InN thin film is completely [0001] out-of-plane oriented at a film thickness of 50 nm. The grains which are formed on the substrate/film interface, all have an [0001] out-of-plane orientation. This disagrees with the zone T characteristics, which states that islands with a random crystallographic orientation nucleate on the substrate (Sect. 1.6). The only possibility to have only [0001] out-of-plane oriented grains at the substrate/film interface is that there is orientation selection at initial stages of the growth. This is a typical zone II characteristic (Sect. 1.6).
Although the crystallographic observations indicate a zone II structure, some observations doesn't seem to fit at first glance with zone II growth. Firstly, when depositing on a tilted substrate, no broad equiaxed columns are observed but rather small grains in comparison to other zone II structures. Although some grains are equiaxed, some grains are overgrown by other grains. There are only few grains which overgrow. Secondly, it can be seen in plan view that the grains are truncated by a specific shape (Fig. 4.13). Both the overgrowth and the growth according to a specific shape are pointing out to a zone T structure.
Due to these experimental results, it isn't obvious if the InN thin film is deposited in Zone T or Zone II. Because of the orientation selection, we propose that the InN thin film is deposited in zone II, however, with some additional, limiting conditions. In this respect, the grain faceting will be explained.

Initially, small islands nucleate on the substrate. Because restructurative grain growth occurs, islands with the (0001) plane parallel to the substrate will be favoured in order to reduce the total free energy of the thin film. If all the islands are truncated by $(000\bar{1})$ planes, the surface will be very flat. In MBE, a lot of papers deal with the formation of three dimensional structures on initially flat high-symmetry surfaces [17, 18, 19, 20]. It is generally believed that these structures, mostly pyramids, originate from the Ehrlich-Schwoebel (ES) barrier at the step edges which hinders the adatoms to reach a lower terrace [17]. As a result, the initially flat surfaces become rougher and a mound or pyramid forms.
The slope of this pyramid will depend on the crystal symmetry and the mobility of the arriving

[13] A lot of authors report contradictory values for the surface free energies of the various planes of a wurtzite structure. Here, we follow the most accepted assumption that the (0001) plane has to lowest surface free energy.

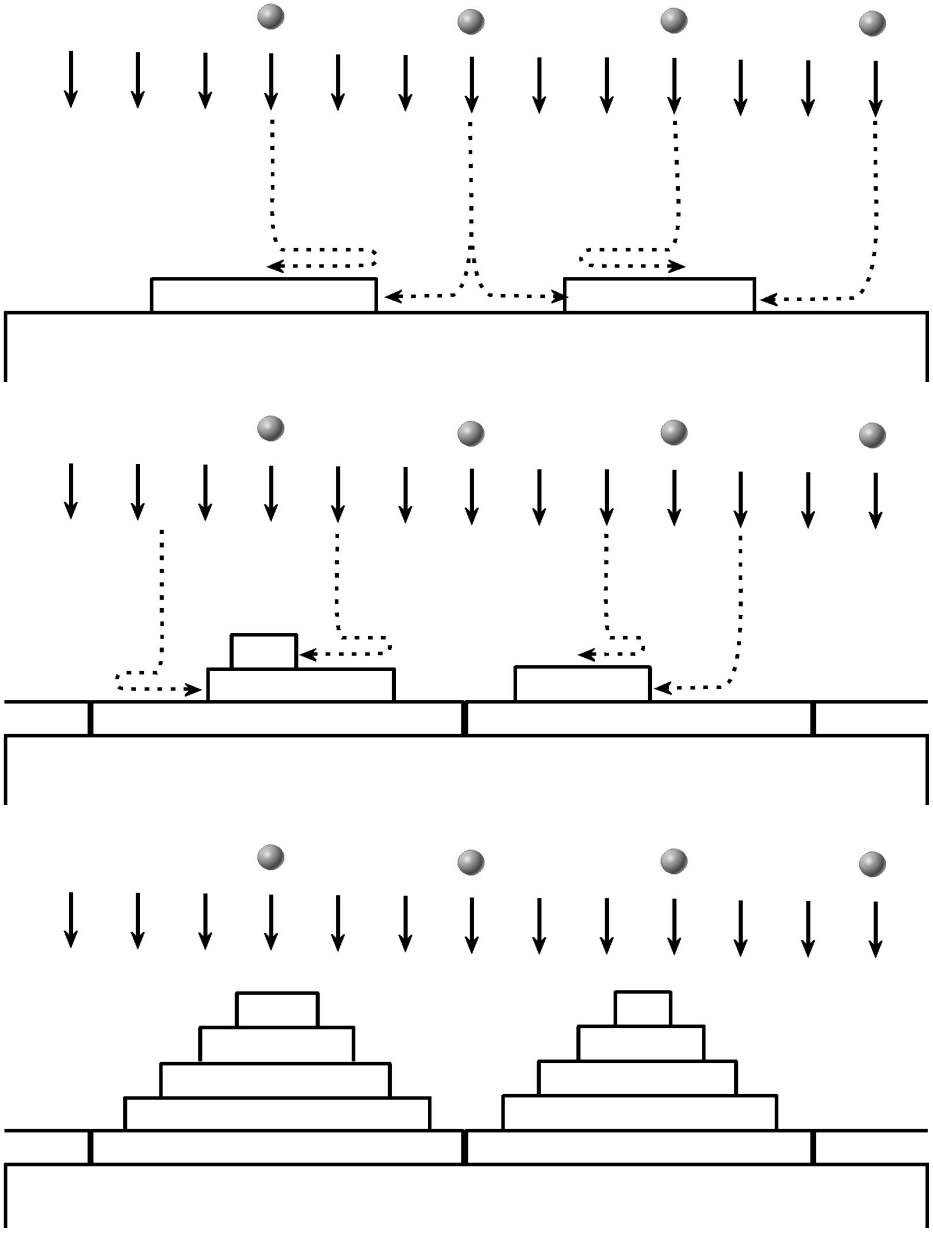

Figure 4.26: Mound formation during the growth of InN

adatoms [18]. This effect counterbalances the effect of the ES barrier. With a higher mobility, the adatoms are able to reach to lower terrace. As a result the pyramids become flatter. Another effect which opposes the ES barrier is known as downward funneling [20]. In this process, adparticles deposited at the side of such a pyramid, glides downwards until they reach an adsorption site at a lower terrace. The driven force is the downward vertical component of the momentum of the arriving adparticle.
All these processes will balance and a characteristic slope will evolve for which the corresponding surface is stable. As soon as these pyramids have developed, the slope of this pyramid

remains constant. This complete process of mound formation, also known as kinetic roughening, is illustrated in Fig. 4.26.
In our depositions, a $\{11\bar{2}3\}$ crystal habit is observed for InN. It is reasonable that the crystal habit is formed by the process of mound formation. However, to our knowledge, no data about the step edge barriers of InN or other material with a wurtzite structure is found in literature.
Similar to our results, Baxter et al. [21] is the only group who observed an $\{11\bar{2}3\}$ mound formation on ZnO. More often, flat needle like structures are observed with flat (0001) surfaces. This agrees with the proposed model. In all these experiments, the substrate was heated. This causes an increased adatom mobility. Owing to this, it's easier for the adatoms to cross the ES barrier and reach the lower terraces. This results in a flat surface.
There are a lot other models which tries to explain the structure evolution of polycrystalline thin films with a wurtzite structure. However, all these models have some shortcomings [22].

Because all the grains have an [0001] out-of-plane orientation, even at nucleation, the InN thin film will have a preferential [0001] out-of-plane alignment. Because the out-of-plane alignment doesn't evolve by a growth competition of differently out-of-plane oriented grains, no overgrowth should be observed. However, on the TEM image of Fig. 4.15, it is observed that a specific grain is overgrown by the neighbouring grains. However, this overgrowth isn't caused by a growth competition between differently out-of-plane oriented grains because all grains have the same [0001] out-of-plane orientation. The TEM image which is shown, is taken from an InN thin film deposited on a tilted substrate. As will be discussed in section 4.6, the overgrowth is due to a growth competition between differently in-plane oriented grains but is quoted here in order to explain the experimental observations.
On a non-tilted substrate, no overgrowth is expected. The grains that are formed during nucleation, survive throughout the complete film thickness. As a result, there will be no lateral expansion and small grains at the surface should be observed. This is confirmed experimentally. At the substrate-film interface, the grain size is about 40 nm. The grain size on at the thin film surface is about 50 nm, which indicates that there is no lateral expension, hence no overgrowth. On a tilted substrate however, there is an overgrowth of differently in-plane oriented grains through which the grains are much larger.

4.6 In-plane Alignment

As observed for the three materials, an in-plane alignment develops when depositing on a tilted substrate. Because in sputter deposition, adatoms arrive from a specific direction, it is suggested that the direction of the incoming particles with respect to the substrate normal is of importance to elucidate the evolution of the in-plane alignment.
In section 1.5, it is discussed that the grains can grow by the capture of particles directly from the vapour flux, and/or by the incorporation of diffusing adparticles. Both processes will contribute to the development of the in-plane alignment. Mahieu [23] called the direct capture from the vapour flux the 3D growth, while he referred to the incorporation of diffusing particles as 2D growth.
The faceted grains will capture directly from the vapour flux during all stages of the growth, while 2D growth only occurs until the out-of-plane alignment is completed (Fig. 4.27). To know whether 2D or 3D growth contributes the most to the development of the in-plane alignment, a two-stepped deposition has been carried out for cubic materials [23]. Therefore, a thin film is deposited on a non-tilted substrate and half-way the deposition the substrate is tilted. Also the opposite deposition is performed: a thin film is deposited on a tilted substrate and half-way the orientation of the substrate is changed in such a way that there was no tilt with respect to the direction of the incoming material flux. By comparing both depositions, it was concluded that 2D growth or the incorporation of diffusion adparticles contributes the most to the development of an in-plane alignment [23].
However, a remark should be made. Once the overgrowth of differently out-of-plane oriented grains is completed, diffusion between the various grains is still possible. Therefore, the incorporation of diffusing adparticles (2D) will contribute to the evolution of the in-plane alignment in the growth stages after the completion of the out-of-plane alignment. Both the 2D growth and

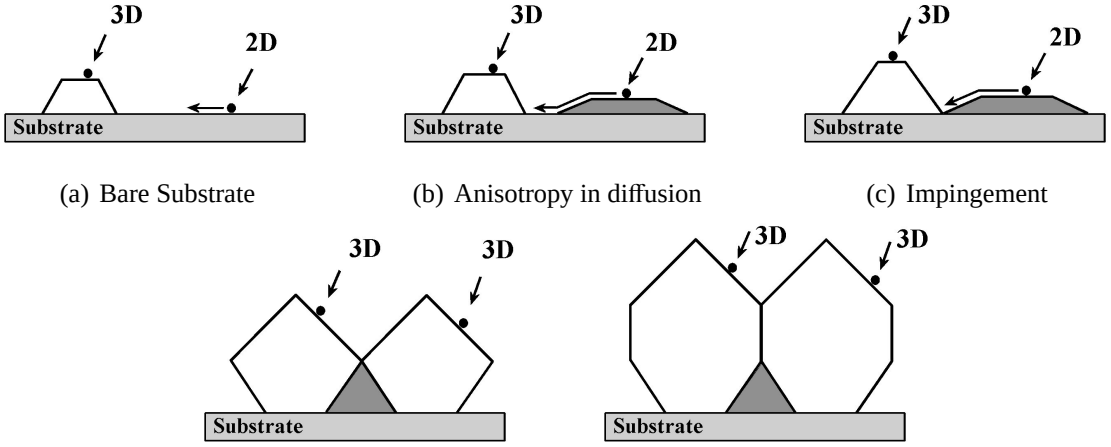

(a) Bare Substrate (b) Anisotropy in diffusion (c) Impingement

(d) Completion out-of-plane alignment (e) Film Thickening

Figure 4.27: The growth of the grains in zone T by the capture directly from the flux (3D) or by the incorporation of diffusion adatoms (2D) [23].

3D growth occurs during all growth stages (this is different from Fig. 4.27). Even more, for InN, there is no growth competition between differently out-of-plane oriented grains, because all grains have an [0001] out-of-plane orientation. Here also, both 2D as 3D growth will occur.
In this respect, it should be remarked that as the grain size increases with increasing thin film thickness, the distance to diffuse towards another grain increases. As such, the contribution of 2D growth diminishes, but cannot be neglected.
In order to elucidate the mechanism of the in-plane alignment, both the contribution of diffusing adatoms (Sect. 4.6.1) and the contribution by direct capture from the flux (Sect. 4.6.2) should be taken into account.

4.6.1 2D growth - Directional Diffusion

As already mentioned, the adatoms arrive from a specific direction. On a non-tilted substrate, the adatoms arrive according to the substrate normal. After impingement, the diffusion direction is random. When depositing on a tilted substrate, the adatoms arrive with an angle with respect to the substrate normal. Because of the conservation of the momuntum, the adatoms will diffuse in the projected direction of the incoming material flux (Fig. 4.28). This diffusion is called directional or biased diffusion [24, 25, 26].
For cubic materials, grains grow according to a specific growth shape which is determined by the facets with lowest growth rate in a cubic structure (Zone T). For InN, $\{11\bar{2}3\}$ mounds will be observed due to a balance between the ES barrier and the adatom mobility. Because of the directional diffusion of the adatoms, the in-plane orientation of these crystal habits become important. Depending on the in-plane orientation, some grains will capture more diffusing adatoms. As a results, these grains will have a higher growth rate and overgrow the other grains, through which an in-plane alignment evolves. Therefore, the proposed model will be based on an anisotropy in amount of captured adatoms by differently in-plane oriented grains.

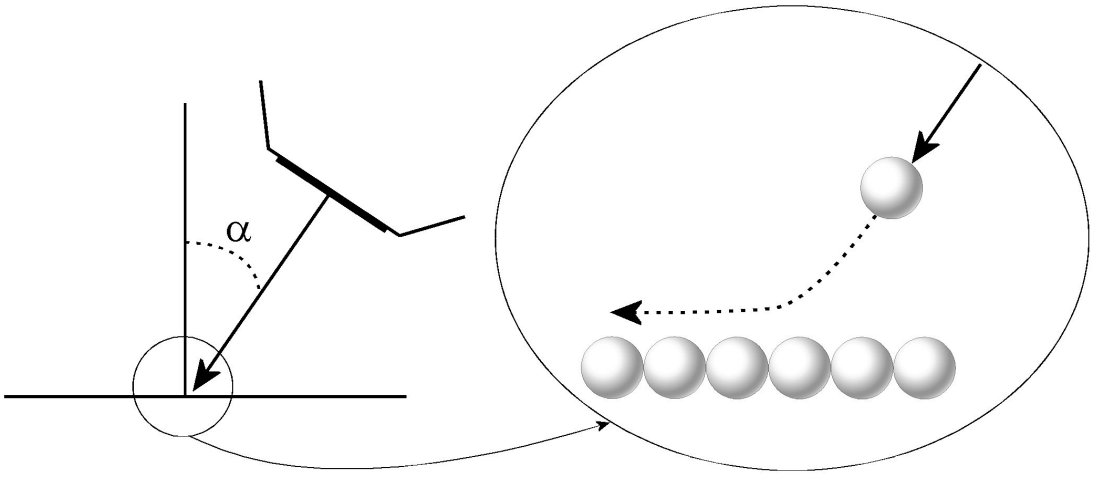

Figure 4.28: Directional diffusion. A component of the momentum is conserved when the atoms arrive with an angle to the substrate normal on the substrate. Consequently, the adatoms will diffuse in the direction of the incoming material flux.

In this thesis work, materials with different crystal structure are deposited. Since the crystal habit depends on the crystal structure, the in-plane alignment for MgO, Cr and InN will be different. For the different materials, the influence of the directional diffusion is examined. The reasoning is elucidated in case of a MgO thin film.

In-plane alignment of MgO caused by directional diffusion

During nucleation, crystalline grains are dispersed over the substrate. For MgO, these grains are truncated an {100} crystal habit. As discussed in section 4.4.2, only the grains with a preferential [111] out-of-plane orientation will survive during the growth because they have the highest perpendicular growth rate. The grains which are not [111] out-of-plane oriented have a lower perpendicular growth rate and will be overgrown. Therefore, consider a surface which is covered with [111] out-of-plane oriented grains and differently oriented grains (or a bare substrate) (Fig. 4.29). In projection, the [111] out-of-plane oriented grains with an {100} crystal habit are represented by triangles. Because the differently oriented grains are not of importance, these grains are represented by a grey surface. Adatoms landing on differently oriented grains are able to diffuse towards the [111] out-of-plane oriented grains and contribute to the growth.
Since the adatoms diffuse in a specific direction, the number of adparticles a grain incorporates, will depend on the in-plane orientation of the grain. Therefore, the number of incorporated adparticles must be calculated as a function of the in-plane orientation of the grain. It is reasoned that the number of incorporated adparticles is proportional to the capture length. Hereby, the capture length is defined as the projection of the crystal shape on the direction perpendicular to the diffusion direction. The grains with the highest capture length, will incorporate the highest amount of adparticles. Hence, these grains will have the highest growth rate and overgrow the other grains, through which an in-plane alignment evolves.

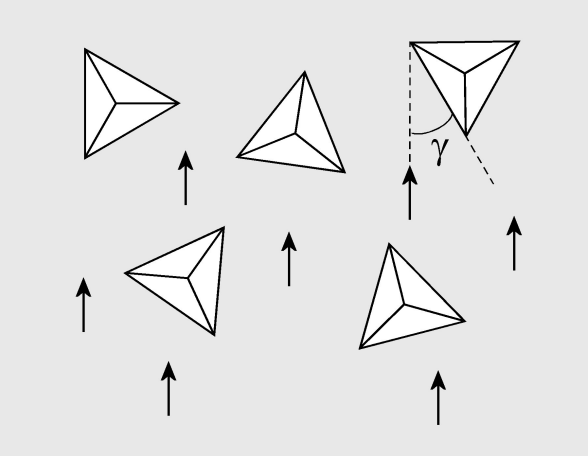

Figure 4.29: Representation of the MgO surface after nucleation in Zone T. {100} faceted grains are dispersed on the substrate. The [111] out-of-plane oriented grains are shown in projection as triangles. The grey area represents the other oriented grains, which will be overgrown due to their lower perpendicular growth rate, or the bare substrate. The diffusion direction is indicated by the arrows. γ is the angle between the side of the triangle and the diffusion direction.

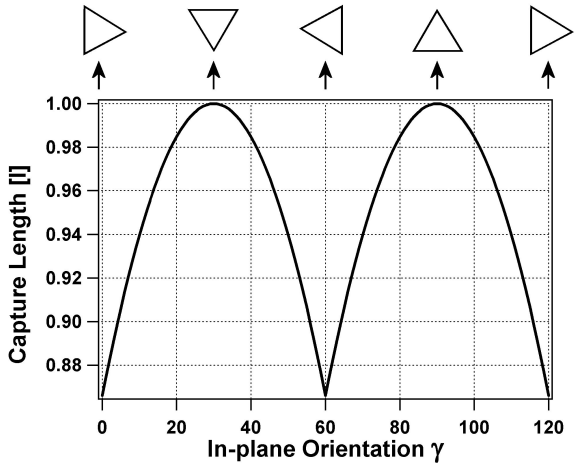

Figure 4.30: Capture length of an [111] out-of-plane oriented grain with an {100} crystal habit. The capture length is given in terms of l, which is the length of the side of the triangular projection. The arrow indicates the diffusion direction

The calculations to obtain the capture length as a function of the in-plane orientation are summarized in Appendix C. The capture length is given by:

$$\sigma_{\mathrm{2D,MgO}} = \begin{cases} \frac{\sqrt{3}}{2}\cos(\gamma)\cdot l + \frac{1}{2}\sin(\gamma)\cdot l & \text{if} \quad \gamma \in [0^o, 60^o] \\ \sin(\gamma)\cdot l & \text{if} \quad \gamma \in [60^o, 120^o] \end{cases} \tag{4.1}$$

where l is the length of the side of the triangle and γ is the angle between the side of the triangle and the direction of the incoming adparticles. The capture length as a function of the in-plane orientation is plotted in Fig. 4.30.
The capture length has its maximum when γ equals 30° and 90°. These in-plane orientations correspond to the situations where the edge of the {100} habit (30°) and the side of the {100} habit (90°) are oriented to the flux (Fig. 4.30). However, in the experiments, only the case where the side is oriented towards the flux is observed (Fig. 4.4). There is no evidence that the directional diffusion of adparticles favours the growth of the grains with the side oriented towards the flux.

Overview of the in-plane alignment caused by direction diffusion for the various materials

The same reasoning can be applied to calculate the contribution of directional diffusion to the in-plane alignment of Cr and InN. For Cr, only the [100] out-of-plane oriented grains with an {110} crystal habit are of importance, while for InN, these are the [0001] out-of-plane oriented grains truncated by an $\{11\bar{2}3\}$ mound. In projection, the crystal habit corresponds to a square and a hexagon for Cr and InN respectively. Due to the crystal symmetry, the calculations are restricted to [0°,90°] for Cr and to [0°,60°] for InN. Table 4.5 summarizes the different steps in the reasoning.

MgO	Cr	InN
Surface covered with good out-of-plane oriented grains with a specific crystal habit and differently out-of-plane oriented grains (grey)		
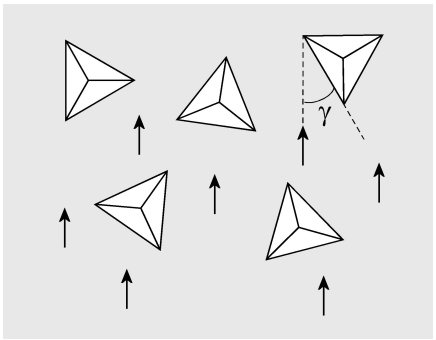	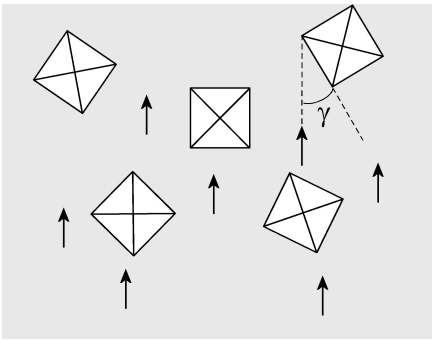	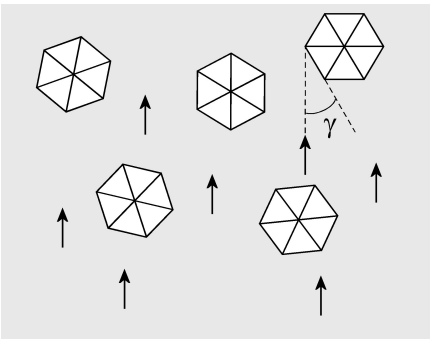
Plot and formula of the Capture Length σ_{2D} as a function in-plane orientation γ of the faceted grains		
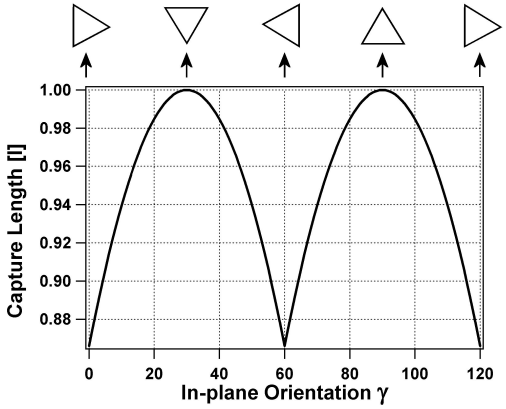	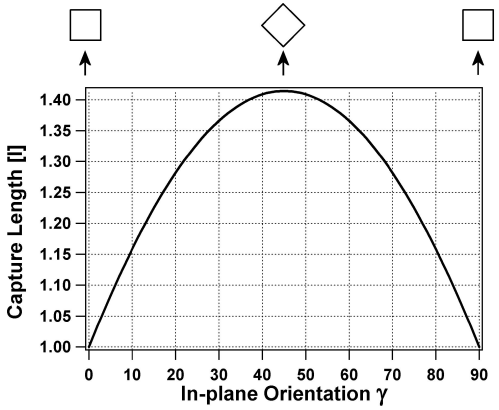	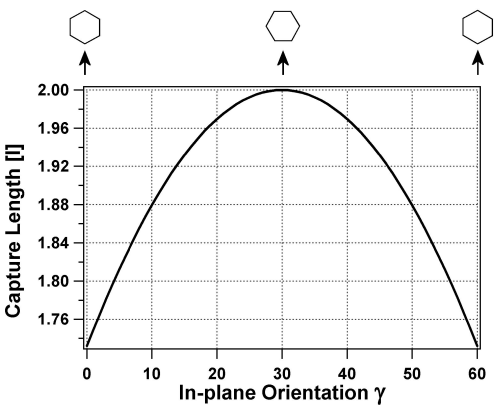
$\begin{cases} \frac{\sqrt{3}}{2}\cos(\gamma)\cdot l + \frac{1}{2}\sin(\gamma)\cdot l & \text{if} \quad \gamma \in [0^o, 60^o] \\ \sin(\gamma)\cdot l & \text{if} \quad \gamma \in [60^o, 120^o] \end{cases}$	$\sin(\gamma)\cdot l + \cos(\gamma)\cdot l$	$\sin(\gamma) + \sqrt{3}\cos(\gamma)$

Table 4.5: Schematic overview of the influence of directional diffusion on the in-plane alignment of MgO, Cr and InN. (*top*) Starting point of the reasoning; (*bottom*) Calculated capture length as a function of the in-plane orientation of the grain.

For Cr, the capture length is at its maximum if $\gamma = 45°$. This corresponds to the in-plane orientation for which the edge of the square is oriented towards the flux. Therefore, grains which are oriented with the side towards the flux will capture the highest amount of diffusing adparticles and overgrow the others. Only these grains will survive and an in-plane alignment evolves. This is agrees with the experimental observations (Fig. 4.8).

For InN, the capture length is at its maximum if the side of the hexagon is oriented towards the flux ($\gamma = 30°$). These grains will capture the most adparticles and overgrow the others. The overgrowth of differently in-plane oriented grains is experimentally observed (Fig. 4.15). Because grains with a side of the hexagon oriented towards the flux will overgrow its neighbouring grains, an in-plane alignment will evolve. This corresponds to the experimental observations, where mainly grains with the side of the $\{11\bar{2}3\}$ mound are visible on the InN thin film surface (Fig. 4.13).

4.6.2 3D growth - Direct Capture

During deposition, the grains can grow by direct capture from the vapour flux. When depositing on an inclined substrate, the area for an adatom to imping on a specific grain will depend on the direction of incidence and the orientation of the grain. The adparticle will *see* the crystal habit differently for different in-plane orientations and inclination angles. This is illustrated in Fig. 4.31. Grains which offer the largest impingement area, will capture the highest number of incoming particles. If the probability to incorporate the particles scales with the number of

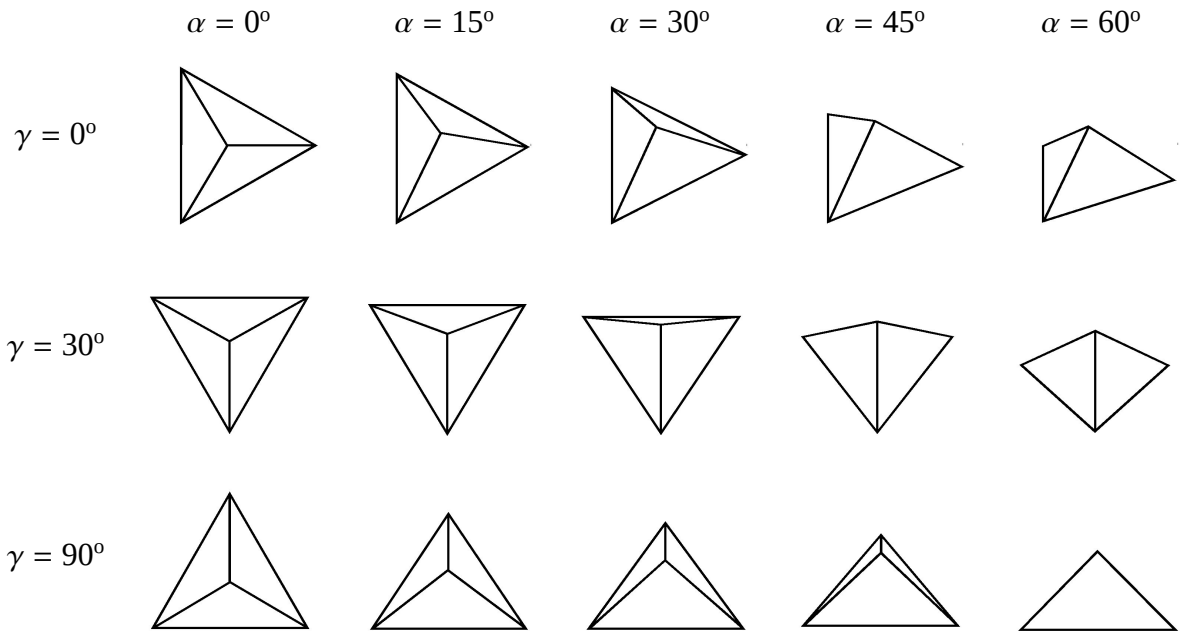

Figure 4.31: The {100} crystal habit of an [111] out-of-plane oriented grain seen by incoming adatoms for three different in-plane orientations: $\gamma = 0°, 30°, 90°$. For each in-plane orientation, the projected crystal habit is shown for five different inclination angles of the substrate: $\alpha = 0°, 15°, 30°, 45°, 60°$.

impinging adparticles, the growth rate of the grain will be proportional to that area. Hereby, in agreement with zone T growth, it is assumed that the adparticles spread out over the grain completely. Grains with the highest perpendicular growth rate will overgrow the other grains and determine the in-plane orientation.
To determine the contribution of the direct capture to the in-plane alignment, the impingement area of differently oriented grains has to be calculated for different inclination angles. This area which we call the capture area, is calculated by projecting the crystal habit on the normal plane of the direction of the material incidence.
For the calculation of the cubic materials, only the grains for which the out-of-plane orientation corresponds to the geometric fastest growth direction are taken into account because these grains will survive during the evolutionary selection. These are the [111] out-of-plane oriented grains with an {100} faceting for MgO and the [100] out-of-plane oriented grains with an {110} faceting for Cr (Sect. 4.4). For wurtzite InN, the [0001] out-of-plane oriented grains with an $\{11\bar{2}3\}$ mound are taken into account (Sect. 4.5).
The calculations of the capture area as a function of the in-plane alignment and the substrate inclination angle are given in Appendix D for the various materials. The results will be discussed for the three materials.

In-plane alignment of MgO caused by direct capture

Fig. 4.32(a) shows the total capture area of an {100} faceted grain with an [111] out-of-plane orientation as a function of the in-plane orientation γ and the substrate inclination angle α. These angles γ and α correspond to those in Fig. 4.31. For an inclination angle below 35°, there is no difference in capture area of differently in-plane oriented grains. With this, no in-plane alignment could evolve. At a higher inclination angle, some facets of the crystal habit will be shadowed through which less adparticles can be captured.[14] Because the shadowing depends on the in-plane orientation of the grain, there is an anisotropy in capture area.
Fig. 4.32(b) shows the capture area as a function of the in-plane orientation at an inclination angle of 55°.[15] The capture area is at its maximum for $\gamma = 30°$. For this in-plane orientation the edge of the crystal habit is oriented towards the incoming material flux. In contrast, if the side of the crystal habit is oriented towards the incoming vapour flux ($\gamma = 90°$), then the capture area is minimal. Because the in-plane orientation with the edge oriented towards the flux has the largest capture area, it is expected that the grains with this orientation will have the largest growth rate and overgrow the other in-plane oriented grains. However, this is inconsistent with the experimental results. The SEM image of the MgO thin film deposited on a tilted substrate (Fig. 4.4(b)) clearly shows that the side of the {100} crystal habit is oriented towards the flux. This tendency is similar at the other inclination angles. Always the grains of which the edge of the {100} crystal habit is oriented to the flux, will have the largest capture area. Additionally, for an inclination angle of 30°, a minor in-plane alignment is experimentally observed (Fig. 4.3(b)) which doesn't agrees to the model of direct capture.
Because the results for MgO of the model for in-plane alignment caused by the direct capture are incompatible with the experimental results, it can be concluded that the contribution of direct

[14] After impingement , the adparticles can move around on the grains and can reach the shadowed facet. As a result, the facets will have the same growth rate and the crystal habit is conserved.
[15] This angle is preferred because most of the MgO thin film are deposited with an angle of 55°.

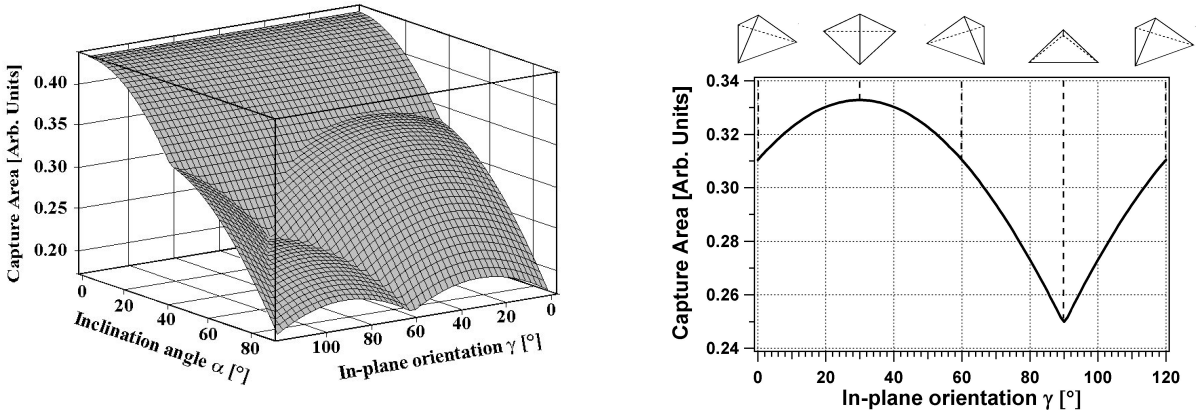

(a) (b)

Figure 4.32: (a) Capture area of the [111] out-of-plane oriented grains truncated an {100} crystal habit as a function of the substrate inclination angle α and the in-plane orientation of the grain γ. A section of this surface plot for α=55° is shown in (b). The projection of the crystal habit of some in-plane orientation is shown above the graph.

capture to the evolution of the in-plane alignment is much less than the contribution of directional diffusion.

In-plane alignment of Cr caused by direct capture

Fig. 4.33(a) shows the total capture area of an {110} faceted grain with an [111] out-of-plane orientation as a function of the in-plane orientation γ and the substrate inclination angle α. For a substrate inclination angle α below 45°, grains with a different in-plane orientation will capture the same number of adparticles. Hence, no in-plane alignment can evolve. For a higher α, an anisotropy in capture area is observed. For instance, for α = 60°,[16] the capture area is at its maximum for γ = 0° ± n·90°(Fig. 4.33(b)). This angle corresponds to the orientation where the side of the {110} crystal habit is oriented towards the incoming material flux. This suggests that those grains will have the highest growth rate and survive during the growth. However, this is in contrast to the experimental observation for which the edge of the crystal habit is oriented towards the flux (Fig. 4.8(b)). Only at the highest inclination angles (α > 68°), the grains with the side oriented towards the flux will have the highest capture area. Remark that for α = 60°, the difference in capture area between the orientation with the highest and lowest capture area is only 7%, which is probably too low to obtain an evolutionary selection for thin film with a thickness of 1 μm.
Again, the results for Cr of the model for in-plane alignment caused by the direct capture do not corresponds with the experimental results. As such, it can be concluded the contribution of direct capture to the evolution of the in-plane alignment is much less than the contribution by directional diffusion.

[16] The depositions of Cr on a tilted substrate are carried out with a 60° inclination angle.

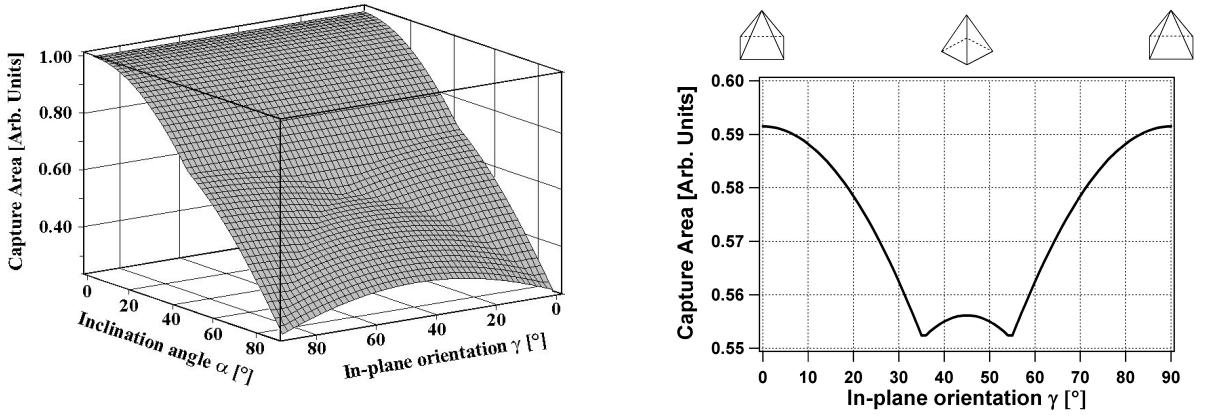

(a) (b)

Figure 4.33: (a) Capture area of the [100] out-of-plane oriented grains truncated an {110} crystal habit as a function of the substrate inclination angle α and the in-plane orientation of the grain γ. A section of this surface plot for α=60° is shown in (b). The projection of the crystal habit of some in-plane orientation is shown above the graph.

In-plane alignment of InN caused by direct capture

Fig. 4.34(a) shows the total capture area of an $\{11\bar{2}3\}$ faceted grain with an [0001] out-of-plane orientation as a function of the in-plane orientation γ and the substrate inclination angle α. Analogous results as for MgO and Cr are obtained. For $\alpha < 39°$ no difference in capture area of differently in-plane oriented grains is observed. So no overgrowth and in-plane alignment is expected. However, an in-plane alignment is observed experimentally for $\alpha = 30°$.
For larger substrate inclination angles a difference in capture area is observed. Fig. 4.34(b) shows the capture area of differently in-plane oriented grains for $\alpha = 60°$. A maximum is observed for $\gamma = 0° \pm n{\cdot}60°$. At this angle, the crystal habit is oriented with the edge towards the flux. It is expected that only these grains will survive during the growth. Again, this is inconsistent with the experimental results for which the side of the crystal habit is oriented towards the flux. Only at the highest inclination angles ($\alpha > 68°$), this orientation will be favoured. It should be noted that the difference in capture area between the two limiting cases, is only 5%, which is rather low to cause an overgrowth.

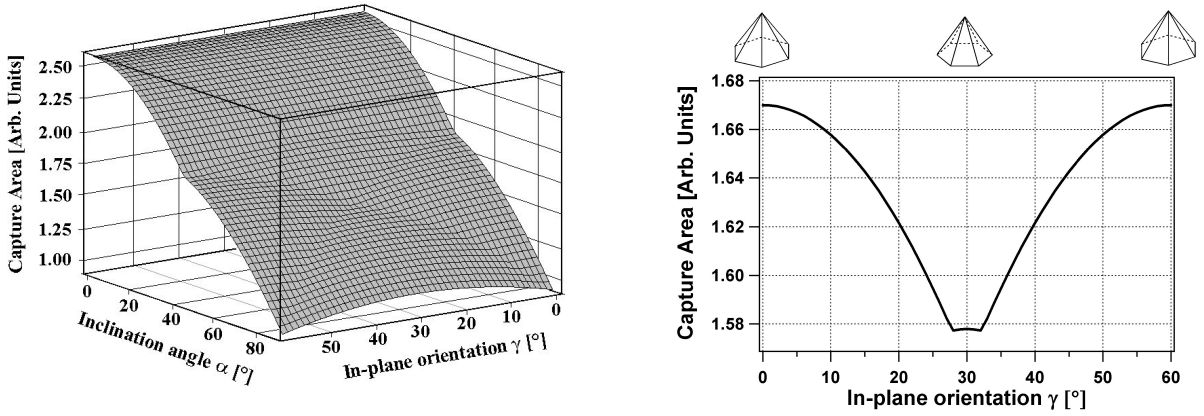

(a) (b)

Figure 4.34: (a) Capture area of the [0001] out-of-plane oriented grains truncated an $\{11\bar{2}3\}$ crystal habit as a function of the substrate inclination angle α and the in-plane orientation of the grain γ. A section of this surface plot for α=60° is shown in (b). The projection of the crystal habit of some in-plane orientation is shown above the graph.

4.7 Conclusions

Out-of-plane Alignment

The thin films with a cubic structure exhibit a clear zone T structure. The evolution of the out-of-plane alignment can be understood as an overgrowth mechanism of neighbouring grains with a different perpendicular growth rate. The anisotropy in growth rate is a consequence of a difference in crystallographic orientation. Because all grains grow according to a specific crystal habit, one can conclude, purely on geometrical considerations, that the grains whereby the facets of the crystal habit have the largest tilt angle, will have the largest perpendicular growth rate and will determine the preferential out-of-plane orientation.
Important to notice is that for a cubic structure, the crystal habit is decisive for the evolution of the out-of-plane alignment. This crystal habit is built up of facets with the lowest growth rate. If one way or another it could be possible, to change the crystal habit, hence change the growth rate of the various crystallographic planes, than it could be possible to tailor the preferential out-of-plane orientation and the topography of the thin films. This aspect is treaded in more detail in chapter 6.
Hexagonal InN thin films exhibit a preferential [0001] out-of-plane alignment. The out-of-plane alignment results from an orientation selection during nucleation, through which only [0001] oriented grains are observed at the substrate/film interface. The grains are truncated by mounds which originate from the existence of a high ES barrier. In the remaining of the text, these mounds will also be called crystal habits, although they are not formed by planes with the lowest growth rate.

In-plane Alignment

The same tendency is observed for the three cases: the model which describes the influence of direct capture on the evolution of the in-plane alignment is incompatible with the experimental results. Therefore, it can be concluded that the in-plane alignment is caused by directional diffusion. Due to this directional diffusion, there is an anisotropy in the number of incorporated adatoms of differently in-plane oriented grains. These grains will grow faster and determine the in-plane orientation.
It is important to remark that the inclination angle is important for the degree of in-plane alignment. The larger the inclination angle, the larger the component of the momentum in a specific direction. As such, the diffusion is more directed and the anisotropy in number of incorporated adparticles will be larger. As a result, the difference in growth rate will be larger and the in-plane alignment evolves faster.

Bibliography

[1] S. Mahieu, Biaxial alignment in sputter deposited thin films, Ph.D. thesis, Ghent University (2006).

[2] A. G. Bhuiyan, A. Hashimoto, A. Yamamoto, Indium nitride (inn): A review on growth, characterization and properties, J. Appl. Phys. 94 (5) (2003) 2779–2808.

[3] A. D. Wilson, J. C. Avelar-Batista, S. J. Dowey, J. Robson, A. Leyland, A. Matthews, K. S. Fancey, Investigation into nitrogen-inert gas interactions in d.c. diode glow discharges, Surf. Coat. Technol. 142-144 (2001) 540–545.

[4] Q. Guo, N. Shingai, Y. Mitsuishi, M. Nishio, H. Ogawa, Effects of nitrogen/argon ratio on composition and structure of InN films prepared by r.f. magnetron sputtering, Thin Solid Films 343-344 (1999) 524–527.

[5] D. T. J. Hurle, Handbook of Crystal Growth. 1a Fundamental, 1st Edition, Elsevier Science, 1993.

[6] R. Docherty, G. Clydesdale, K. J. Roberts, P. Bennema, Application of bravais-friedel-donnay-harker, attachment energy and ising models to predicting and understanding the morphology of molecular crystals, J. Phys. D 24 (2) (1991) 89–99.

[7] Z. Berkovitch-Yellin, Toward an ab initio derivation of crystal morphology, J. Am. Chem. Soc. 107 (26) (1985) 8239–8253.

[8] P. Hartman, W. Perdok, On the relations between structure and morphology of crystals, Acta Cryst. 8 (1955) 49–52, 521–524, 525–529.

[9] P. Hartman, P. Bennema, The attachment energy as a habit controlling factor 1. theoretical considerations, J. Cryst. Growth 49 (1) (1980) 145–156.

[10] S. Mahieu, P. Ghekiere, G. De Winter, R. De Gryse, D. Depla, G. Van Tendeloo, O. I. Lebedev, Mechanism of preferential orientation in sputter deposited titanium nitride and yttria stabilized zirconia layers, J. Cryst. Growth 279 (1-2) (2005) 100–109.

[11] H. C. Huang, G. H. Gilmer, T. D. de la Rubia, An atomistic simulator for thin film deposition in three dimensions, J. Appl. Phys. 84 (7) (1998) 3636–3649.

[12] L. E. Rehn, R. C. Birtcher, S. E. Donnelly, P. M. Baldo, L. Funk, Origin of atomic clusters during ion sputtering, Phys. Rev. Lett. 87 (20) (2001) 207601.

[13] A. Ershov, L. Pekker, Model of d.c. magnetron reactive sputtering in Ar-O_2 gas mixtures, Thin Solid Films 289 (1-2) (1996) 140–146.

[14] M. Ohring, Materials Science of Thin Films, 2nd Edition, Academic Press, San Diego, 2002.

[15] V. E. Henrich, P. A. Cox, The Surface Science of Metal Oxides, 1st Edition, Cambridge University Press, 1994.

[16] A. Van der Drift, Evolutionary selection, a principle governing growth orientation in vapor-deposited layers, Philips Res. Rep. 22 (1967) 267–288.

[17] J. Villain, Continuum models of crystal growth from atomic beams with and without desorption, J. Phys. I 1 (1991) 19–42.

[18] M. Siegert, M. Plischke, Slope selection and coarsening in molecular beam epitaxy, Phys. Rev. Lett. 73 (11) (1994) 1517–1520.

[19] M. Siegert, M. Plischke, Formation of pyramids and mounds in molecular beam epitaxy, Phys. Rev. E 53 (1) (1996) 307–318.

[20] J. W. Evans, P. A. Thiel, M. C. Bartelt, Morphological evolution during epitaxial thin film growth: Formation of 2D islands and 3D mounds, Surf. Sci. Rep. 61 (1) (2006) 1–128.

[21] J. B. Baxter, F. Wu, E. S. Aydil, Growth mechanism and characterization of zinc oxide hexagonal columns, Appl. Phys. Lett. 83 (18) (2003) 3797–3799.

[22] Y. Kajikawa, Texture development of non-epitaxial polycrystalline ZnO films, J. Cryst. Growth 289 (2006) 387–394.

[23] S. Mahieu, P. Ghekiere, D. Depla, R. De Gryse, Biaxial alignment in sputter deposited thin films, Thin Solid Films 515 (4) (2006) 1229–1249.

[24] L. Abelmann, C. Lodder, Oblique evaporation and surface diffusion, Thin Solid Films 305 (1997) 1–21.

[25] X. W. Zhou, H. N. G. Wadley, Hyperthermal vapor deposition of copper: athermal and biased diffusion effects, Surf. Sci. 431 (1999) 42–57.

[26] J. C. S. Kools, Suppression of nanoscopic shadowing during physical vapor deposition by biased diffusion, J. Vac. Sci. Technol. A 23 (1) (2005) 85–89.

Chapter 5

Influence of the Deposition Parameters on the Growth of Biaxially Aligned Thin Films

5.1 Introduction

Thin film growth depends strongly on the deposition or process parameters. Changing the deposition conditions affects elementary processes like diffusion, directly. For example, modifying a specific deposition parameter could decrease the energy of a sputtered particle. After impingement, the adatom mobility will be reduced through which the adatom won't be able to find the energetically most favourable site on the grain or the diffusion towards another grain will be restricted. A possible change in the structure evolution can be expected.
In this work, the influence of the different deposition parameters on the growth of biaxially aligned thin films is investigated in order to understand the growth mechanism [1]. Looking at the influence of the deposition parameters on both the structure evolution of the thin films and the elementary processes involved, will give more insight in the relation between these elementary processes and the structure evolution of biaxially aligned thin films. As a result of this research, the optimal conditions to deposit biaxially aligned thin films are obtained.
Table 5.1 gives an overview of the deposition parameters that have been investigated for the various biaxially aligned thin films. Both the preferential out-of-plane alignment and the in-plane alignment are investigated for all these deposition series. The results are presented below. The error on the XRD measurement is negligible for the angular scans and is about 5% for the XRD pole figures. The error on the out-of-plane alignment and in-plane alignment, when repeating the same deposition series is in the order of 5%. However, because performing the same deposition series once more is time consuming and doesn't yield new results, this has only be done for a few series. Therefore, no error bars are indicated on the figures.
Appendix E summarizes the values of the deposition parameters which has been kept constant during the various deposition series in order to examine the influence of one specific parameter. The parameters that are not mentioned in the overview, are the same for all deposition series.

Deposition Parameter	MgO	Cr	InN
Substrate Inclination Angle α	X	X	X
Target-Substrate Distance $d(T-S)$	X	X	X
Working pressure p	X	X	X
Substrate Bias V_{bias}	X	X	X
Discharge Current I_d	X	X	X
Film thickness t	X	X	X
Magnet Configuration	X		X
Reactive gas flow	X		
Sputter Gas			X
Substrate Temperature T_{subst}	X	X	
Substrate		X	

Table 5.1: Overview of the deposition parameter for which their influence on the growth of the biaxially aligned thin film have been examined. The 'X' indicates if the parameter is verified for the specific material.

5.2 Experimental Observations

5.2.1 Influence of the Target-Substrate Distance

Fig. 5.1 shows the change in out-of-plane (left) and the in-plane alignment (right) as a function of the target-substrate distance for MgO, Cr and InN thin films. Closer to the target, the fraction of [111] out-of-plane oriented grains decreases for MgO. Similar for Cr, a decrease in the fraction of [100] out-of-plane oriented grains is observed when the thin film is grown closer to the target. For InN, the opposite tendency is observed. Here, the fraction of [0001] out-of-plane oriented grains decreases with increasing target-substrate distance. When the preferential out-of-plane alignment diminishes, the fraction of randomly oriented grains increases.
Concerning the in-plane alignment, an optimum is observed for the three materials. For InN, the in-plane alignment gradually diminishes when moving away from the optimum located at 9 cm. For MgO, the in-plane suddenly disappears at a target-substrate distance of 9 cm, while a slow decrease is observed when depositing at a larger target substate distance. To deposit biaxially aligned Cr, the target-substrate distance had to be 10 or 11 cm. No in-plane alignment is observed with a lower or higher target-substrate distance.

5.2.2 Influence of the Working Pressure

Fig. 5.2 displays the out-of-plane (left) and in-plane alignment (right) of MgO, Cr and InN thin films as a function of the total pressure during deposition. For the deposition of MgO and InN thin films, the working pressure is the sum of the Ar partial pressure and reactive gas partial pressure.
There is no change in preferential out-of-plane alignment by changing the total pressure during deposition. However, a minor increase of randomly oriented grains is observed with decreasing working pressure for the deposition of MgO and Cr thin films (Fig. 5.2).

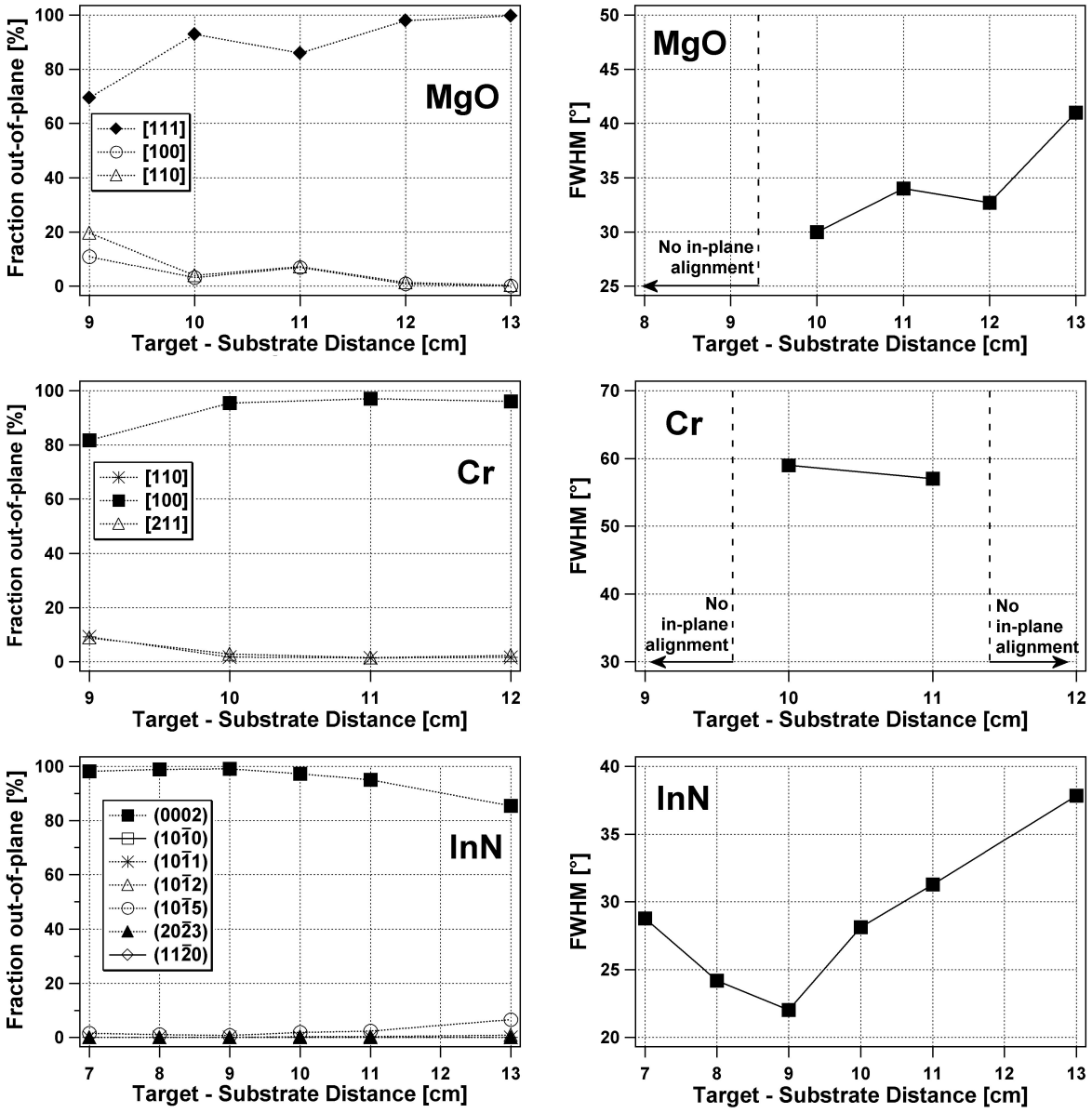

Figure 5.1: Influence of the target-substrate distance d(T-S) on the out-of-plane alignment (*left*) and the in-plane alignment (*right*) of biaxially aligned MgO, Cr and InN thin films. The FWHM is obtained from the (200), (110) and (1011) XRD pole figures for MgO, Cr and InN respectively.

An optimum in in-plane alignment is observed for the three deposited materials. With decreasing pressure, the in-plane alignment improves until the optimum is reached. Depositing at an even lower pressure is disadvantageous for the in-plane alignment. Below the 0.40 Pa, 0.30 Pa and 0.20 Pa for MgO, Cr and InN respectively, the glow discharge is unstable and no crystalline thin films could be deposited.

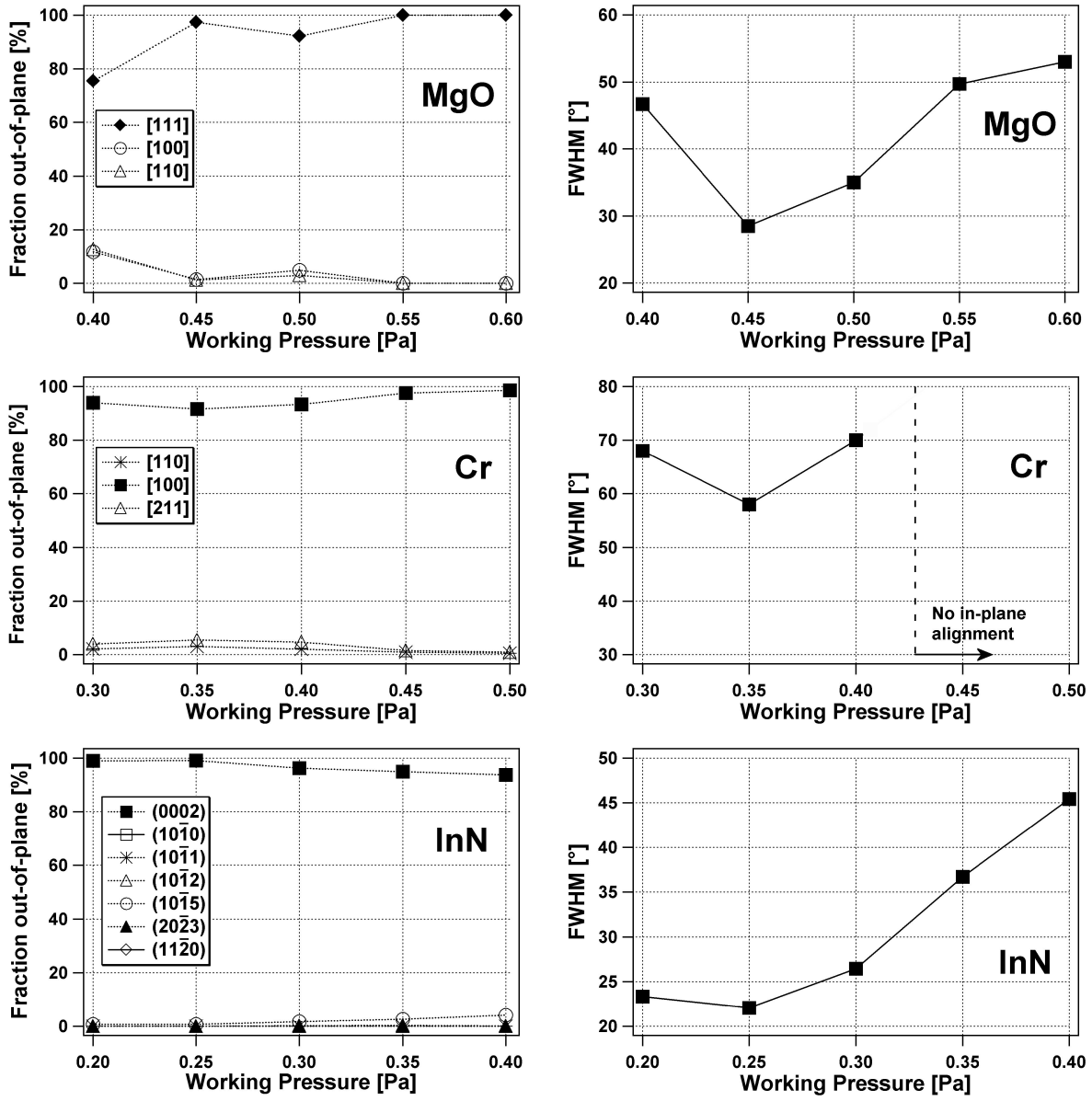

Figure 5.2: Influence of the working pressure p on the out-of-plane alignment (*left*) and the in-plane alignment (*right*) of biaxially aligned MgO, Cr and InN thin films. The FWHM is obtained from the (200), (110) and (10$\bar{1}$1) XRD pole figures for MgO, Cr and InN respectively.

5.2.3 Influence of the Substrate Bias

Fig. 5.3 shows the influence of the substrate bias on the out-of-plane (left) and in-plane alignment (right) of MgO, Cr and InN thin films. MgO is preferentially [111] out-of-plane oriented if a negative bias is applied to the substrate. If a positive bias is applied, the fraction of randomly oriented grains increases. Also if the substrate bias is too negative, the fraction of randomly oriented grains increases. However, this is due to a charging effect of the non-conducting MgO

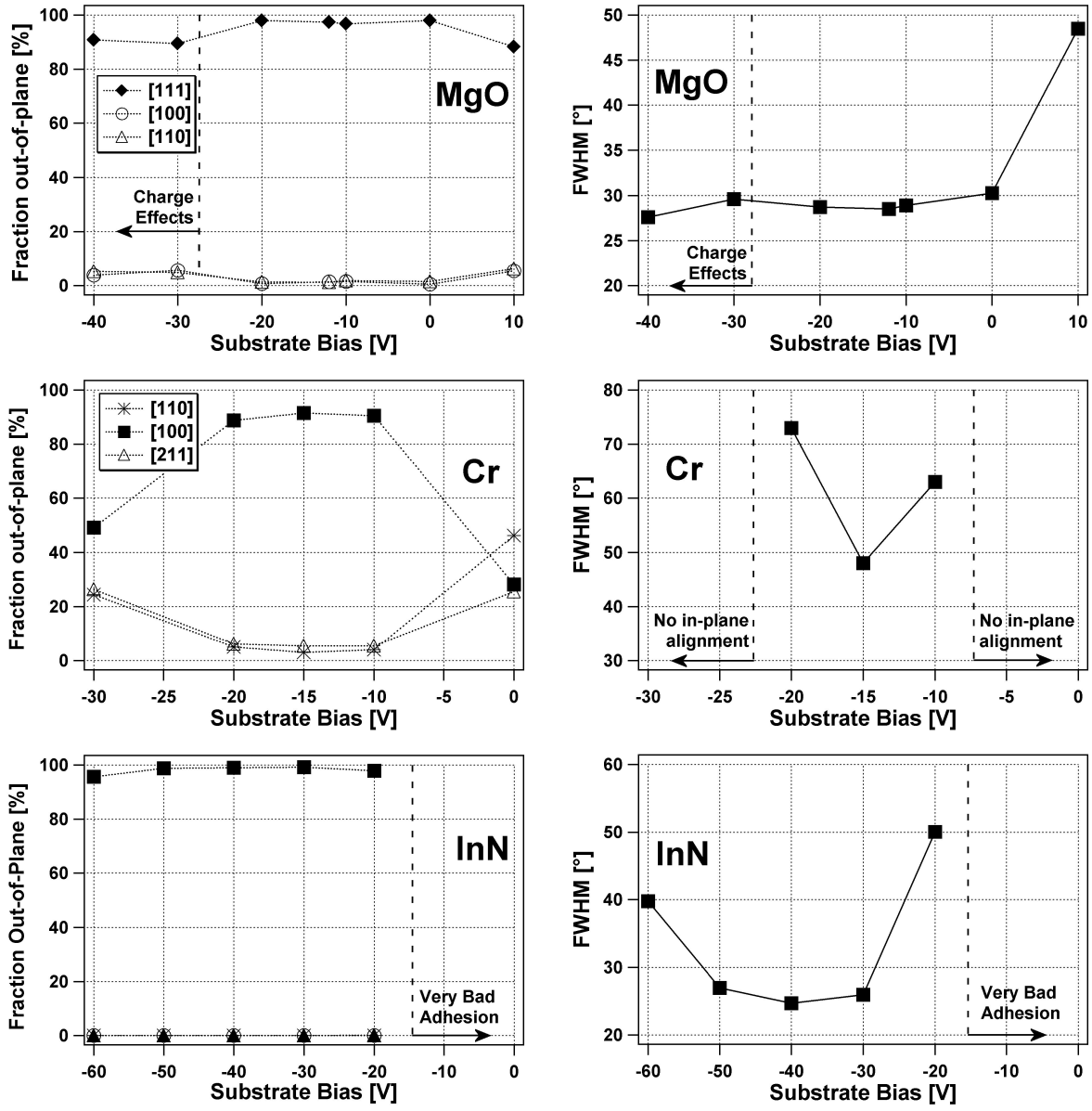

Figure 5.3: Influence of the substrate bias V_{bias} on the out-of-plane alignment (*left*) and the in-plane alignment (*right*) of biaxially aligned MgO, Cr and InN thin films. The FWHM is obtained from the (200), (110) and (1011) XRD pole figures for MgO, Cr and InN respectively.

thin film on a metallic substrate, which reduces the film quality.[1] Due to its strong electrical insulating properties, the substrate bias is only effective in the early stage of the thin film growth. Thereafter, the surface of the growing MgO film is at floating potential.

[1] At the start of the deposition, a high amount of charged particles are attracted to the substrate. As the deposition proceeds, an electrical insulating MgO layer grows which prevents the charged particles to pass their charge to the conducting substrate. As a result, a charge layer builds up on top of the growing MgO film. At a particular charge, one can expect a breakdown. This sudden breakdown is also characterized by the ejection of macroparticles out of the growing surface. This disruptes the thin film growth [2].

With a negative bias, the Cr thin film is [100] out-of-plane oriented. The fraction of out-of-plane oriented grains increases at a high negative bias. When the substrate is grounded or positive bias is applied, the Cr thin film is randomly out-of-plane oriented. InN is preferentially [0001] out-of-plane oriented. No change is preferential out-of-plane orientation is observed. However, when the substrate bias is more positive than −10V, there is a very poor adhesion of the InN thin film to the substrate and no useful information could be obtained.

The in-plane alignment has an optimum for all three materials. This optimum is close to the floating potential which is −12 V for MgO, −15 V for Cr and −35 V for InN. In comparison to the floating potential, a more negative or more positive bias is disadvantageous for the in-plane alignment.

5.2.4 Influence of the Discharge Current

The influence of the discharge current on the out-of-plane and in-plane alignment of MgO, Cr and InN thin films is shown in Fig. 5.4. By changing the discharge current, no change in out-of-plane alignment is observed for MgO and InN. The MgO and InN thin film exhibit a preferential [111] and [0001] out-of-plane orientation. At low discharges currents, the Cr thin film has a preferential [100] out-of-plane alignment. The preferential orientation changes to a random out-of-plane orientation at 0.80 A.
For the three deposited materials, an optimum in the discharge current is observed. The Cr thin film deposited at 0.80 A has a random in-plane alignment.

5.3 Degree of Out-of-plane Alignment

5.3.1 Out-of-plane Alignment of Cubic Materials

In the previous chapter, the evolution of the preferential out-of-plane alignment during the growth of biaxially aligned thin films on an inclined substrate has been discussed (Chapter 4). The cubic materials are typically deposited in zone T. Initially, crystalline islands with a random crystallographic orientation nucleate on the substrate. Because of an anisotropy in normal growth rate of the various crystallographic planes, a crystal habit develops. The facets of this crystal habit corresponds to the crystallographic plane with the lowest normal growth rate. The grains increase in size by crystal growth (Section 1.4.6). Depending on their orientations, grains with a specific orientation will have a larger perpendicular growth rate than the neighbouring grains. Grains with the geometric fastest growth direction perpendicular to the substrate will overgrow the other grains and determine the out-of-plane orientation.
The evolution of the out-of-plane alignment is controlled by one fundamental parameter: the mobility of the adparticles on the surface. Since the Zone T growth is crucial for the biaxial alignment of cubic materials, the adparticle mobility has to be sufficient so the adparticles are able to diffuse on the grain in order to find its energetically most favourable place. However, the mobility cannot be too high or restructurative grain growth processes occur and a zone II structure will evolve. An optimal mobility of the adparticle will be necessary.
Firstly, the adparticle mobility is controlled by the energy at which the particle arrives at the surface. This energy will depend on the energy of the particle that the particle has when it leaves

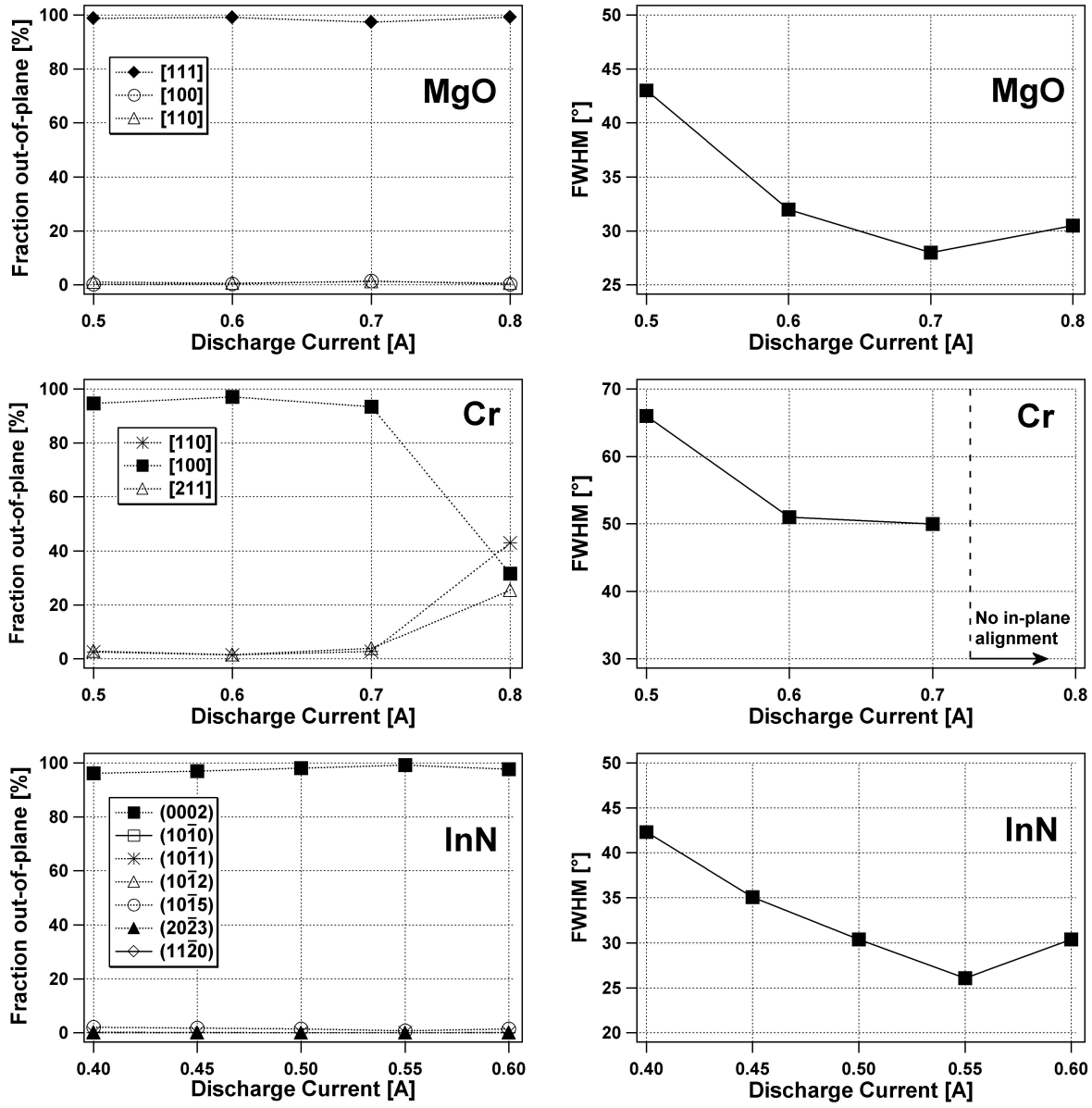

Figure 5.4: Influence of the discharge current I_d on the out-of-plane alignment (*left*) and the in-plane alignment (*right*) of biaxially aligned MgO, Cr and InN thin films. The FWHM is obtained from the (200), (110) and (10$\bar{1}$1) XRD pole figures for MgO, Cr and InN respectively.

the target (Sect. 2.2.3) and will depend on the interaction with the sputter gas during the transport through the plasma (Sect. 2.3). Secondly, the adparticle mobility is controlled by the energy transfer between the particle and the growing film surface. At a high bombardment rate with energetic particles, a high power will be dissipated to the growing film, through which the adparticle mobility will increase. A third parameter which influences the mobility is the magnitude of the diffusion barriers. These barriers are material dependent. Because the diffusion barriers are invariant, they will not change the adparticle mobility when changing a deposition parameter.

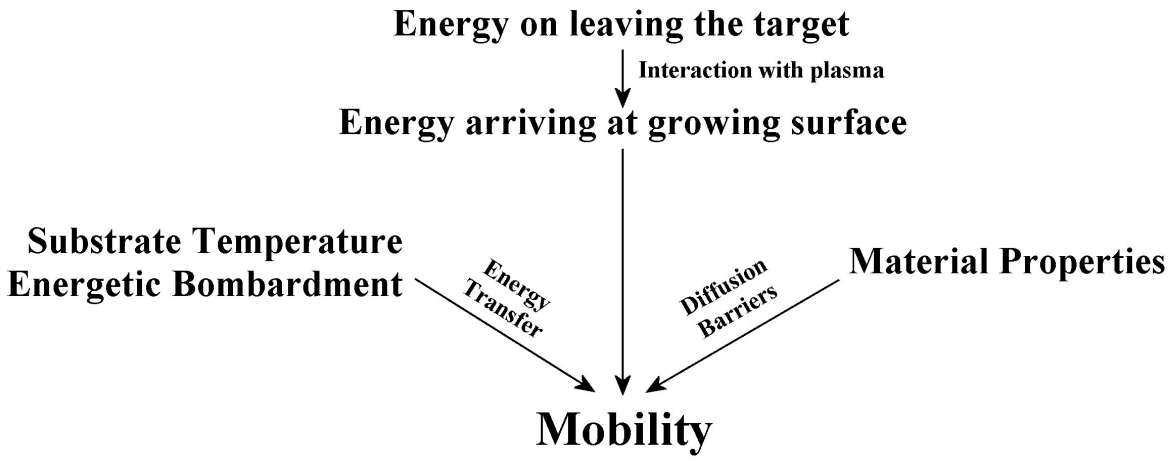

Figure 5.5: Schematic overview of the three parameters which influence the adparticle mobility

The influence of these three parameters on the mobility is schematically shown in Fig. 5.5.
By changing the deposition parameters, it is possible to change and tune the adparticle energy in such a way that the optimized zone T conditions are obtained. For each deposition series, the influence of the deposition parameter on the adparticle mobility will be discussed.

By reducing the *target-substrate distance*, the sputtered particles collide less during the transport through the plasma and arrive on the substrate with more kinetic energy. However, at these pressure, the particles have typically a mean free path of several cm. By reducing the target-substrate distance a few cm, only a minority of the sputtered particles will have fewer collision. Hence, the energy change will be minimal. Also the bombardment with energetic particles can be different at various target-substrate distances. Fig. 5.6(a) shows the electron and ion density during sputtering of Cr at various distances. As can be seen, both the electron density and ion density decrease with a larger target-substrate distance. Hence less energy is delivered to the total growing film. However, not the total power should be taken into account. To have an idea of the adparticle mobility, the energy per deposited particle is of importance. Therefore, the energy delivered to the growing film should be averaged over the number of deposited particles. A third consequence of reducing the target-substrate distance is that the deposition rate increases. Fig. 5.6(b) shows the deposition rate of Cr thin films as a function of the target-substrate distance. It is observed that the deposition rate increases with decreasing target-substrate distance. Because the increase in deposition rate is more pronounced than the increase in energy supply when the substrate is placed close to the target, the energy per deposited particle will decrease closer to the target. This conclusion is in accordance with the results of Ekpe et al. [3] who measured the energy per deposited particle as a function of the target-substrate distance. As a result of the lower energy per deposited particle, the adparticle mobility will decrease closer to the target. If the mobility is too low, zone T growth will be difficult and consequently, the preferential out-of-plane orientation will decrease and result in an increase of randomly oriented grains. This is experimentally observed for MgO and Cr (Fig. 5.1).
By examening the influence of the *working pressure* on the out-of-plane alignment, an increase in the fraction of randomly oriented grains is observed with decreasing pressure (Fig. 5.2). Also

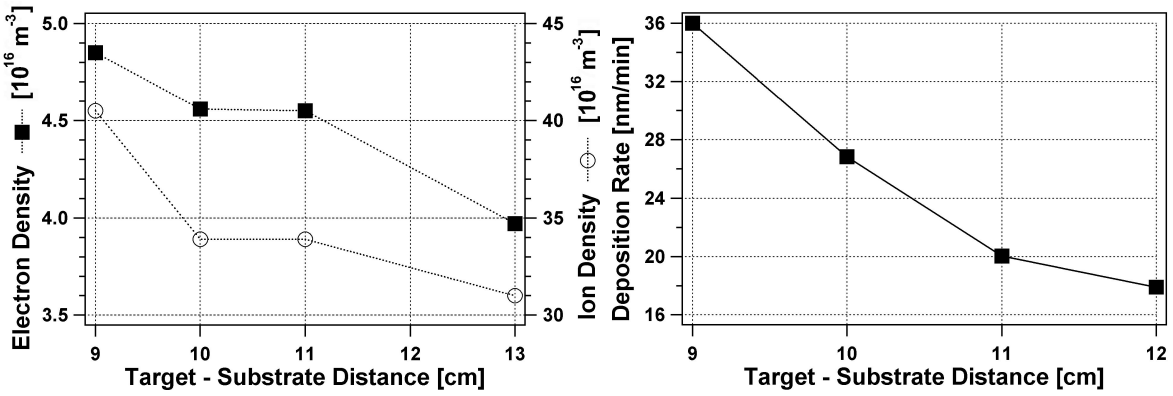

Figure 5.6: (a) The electron density (■) and the ion density (◯) as a function of the target substrate distance for sputtering from Cr target. The used parameters correspond to those for Fig. 5.1 (App. E). The densities are obtained from Langmuir probe measurements. The high ion density number is probably due to the weak signal which makes the calculations of the ion density less reliable and results in an overestimation. (b) The deposition rate of Cr as a function of the target-substrate distance. For both graphs, the used deposition parameters are listed in App. E

this expermental result can be linked to a reduction in adparticle mobility. Drüsedau et al. [4] measured and simulated the energy per atom as a function of the sputter pressure. They observed a decrease in adatom energy with decreasing sputter pressure.
Concerning the *substrate bias*, a more positive bias with respect to the floating potential is disadvantageous for the preferential out-of-plane alignment (Fig. 5.3). In literature, it has been reasoned that, in first approximation, the electrons are responsible for the power delivered to the growing film [5]. Now, a more positive bias attracts the electrons towards the substrate, which leads to an increase in energy flux. Making the substrate potential more negative, the energy flux towards the substrate decreases. Hence, the substrate bias will influence the energy (and so the mobility) of the diffusing adparticles. Because an optimum energy is needed to deposit the thin film in zone T, an optimum in preferential out-of-plane orientation is observed.
Finally, at the highest *discharge current* for the growth of Cr, an increase in randomly oriented grains is observed. Again, this can be explained considering the energy of the adparticles. Drüsedau et al. [4] observed a decrease in total energy per atom with increasing power. As the power scales with the discharge current[2], an increase in discharge current will cause a decrease in adparticle energy. If the energy is too low, the conditions for zone T growth aren't satisfied and the preferential out-of-plane alignment diminishes.
It should be remarked that these parameters are varied in a specific region. Hence, an optimum is not always observed. However, when broadening the range of all parameters sufficiently, an optimum must appear.

[2] The power is defined as $P = I \cdot V$. In sputter deposition, there is a relation between the discharge current and the discharge voltage and is given by $I = kV^n$, where k and n are constants [6]. Consequently, $P \sim I^{(n+1)/n}$

5.3.2 Out-of-plane Alignment of InN

InN thin films are grown in zone II conditions and exhibit a biaxial alignment, if a high ES barrier is present (chapter 4). It was discussed that the ES barrier causes the mound formation. The preferential out-of-plane alignment evolves by orientation selection during island growth. Grains of which the plane with lowest surface energy is parallel to the substrate will be favoured. Because the (0001) plane is the plane with probably the lowest surface energy, all grains will have a preferential [0001] out-of-plane alignment.
The only conditions to have orientation selection is that the energy of the deposited adparticles is high. Hence, increasing the energy per deposited adparticle will be advantageous for the growth of [0001] out-of-plane oriented InN thin film.
However, in the various deposition series, no change in preferential [0001] out-of-plane alignment is observed. Therefore, it can be concluded that the energy per deposited adparticle is high enough.
Only for the deposition series, where the substrate bias has been varied, one remark should be made. It is observed that the adhesion is worse with a positive bias. A possible explaination goes as follows. With a positive bias, electrons are attracted to the substrate which causes an increase in energy flux. As a result, the energy per deposited adparticle will increase. Owing to this, the ES barrier will become ineffective in reflecting the adparticles and restructurative grain growth will be more pronounced. This will result in much broader columns. Because there is no epitaxial relationship between the substrate and the InN thin film, stress accumulates at the substrate/film interface. If the grains become broader, the stress at the interface increases and the adhesion reduces.

5.4 Degree of In-plane Alignment

As discussed in section 4.6.1, the directional diffusion is the decisive parameter which controls the in-plane alignment. Grains with an out-of-plane alignment which corresponds to the geometric fastest growth direction, will capture a different amount of diffusing adparticles depending on their in-plane alignment. The grains which capture the highest number of adparticles will have the highest perpendicular growth rate, overgrow the others and determine the in-plane alignment. The directional diffusion arises from retaining a component of the momentum of the incoming particle when it arrives with an angle with respect to the substrate normal. The larger this contribution, the more directed the diffusion. As a result, the anisotropy in amount of captured particles will be more pronounced and the in-plane alignment evolves faster. A good example of this, is that the in-plane alignment improves with increasing substrate inclination angle (Fig. 4.12(b)). At a larger inclination angle, the component of the momentum is larger, hence the in-plane alignment will improve.
In the description of the model (see chapter 4), it has tacitly been assumed that the particles arrive always from one specific direction. However, in sputtering, the particles are ejected from the target according to a cosine distribution (Sect. 2.2.3). Additionally, the particles undergo several collisions during the transport through the plasma. As a result, there will also be a spread on the incoming direction of sputtered particles. Due to the momentum conservation, there will be a spread on the diffusion direction of the particles (Fig. 5.7(a)). Because of this spread, grains

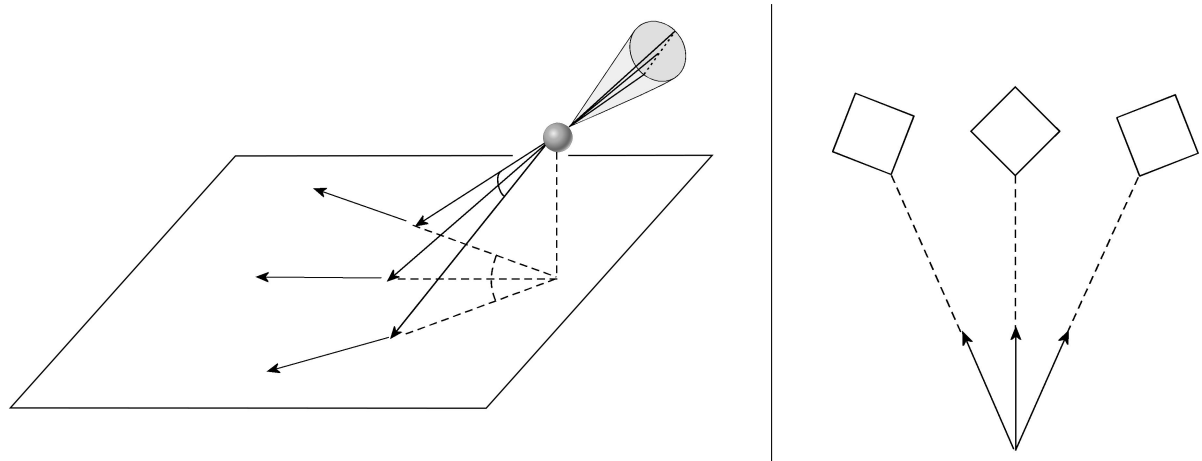

(a) 3D (b) Plan View

Figure 5.7: (a) A spread on the incoming direction of the sputtered particles, causes a spread on the diffusion direction of the adparticles. The spread on the incoming direction will be cone-shaped. However, only the spread on the direction parallel to the substrate has to be taken into account because only this contributes to the spread of the diffusion direction. The other component of the spread on the incoming direction causes a change in diffusion length, but it's contribution is small if the deposition is carried out on a tilted substrate with a high inclination angle. (b) Due to a spread on the adparticle diffusion direction, grains with another in-plane orientation could capture a comparable amount of diffusing adparticles.

with an in-plane orientation which deviates from the optimal in-plane alignment, will incorporate a comparable amount of diffusing adparticles (Fig. 5.7(b)). As a result, these grains will also survive during the growth. Consequently, a spread on the in-plane alignment will be observed. Therefore, it can be concluded that the degree of in-plane alignment is directly connected to the angular spread on the incoming direction of the particles. Furthermore, the angular spread will be a lower limit for the degree of in-plane alignment. For example, if the angular spread is about 15°, the FWHM of a pole in a XRD pole figure should be about 15°.

To obtain the best in-plane alignment, the spread on the material incoming direction must be minimized. This can be obtained by optimizing the deposition parameters. However, a lot of deposition parameters have the disadvantage (or advantage) not only to change the angular spread but also the total energy per adparticle. If the adparticle energy is reduced, the diffusion distance will be smaller through which the capture rate anisotropy of differently in-plane oriented grains is less pronounced. Additionally, if the adparticle mobility is reduced even more for a cubic material, it is likely that the conditions for zone T growth are no longer satisfied. Also for InN, the adparticle mobility should be high enough so orientation selection can occur. It can be concluded that the adparticle energy should be as high as possible so the directional diffusion is pronounced.

However, both for the cubic materials and for InN, there is an upper limit to the energy of the adparticles. For the cubic materials, the energy cannot be too high, since no restructurative grain growth may occur (zone T). For InN, the mobility should also be restricted, because at high mobilities, the ES barrier will be ineffective in reflecting the adparticles and no mound formation will occur. Additionally, the restructurative grain growth will be more pronounced and the InN

thin film will minimize both the surface and interface energy. As a result, no specific grain shape is expected and there will be no anisotropy in amount of captured adparticles. Hence, no in-plane alignment will occur.
It can be concluded that the degree of in-plane alignment will depend on two intrinsic parameters: the angular spread of the incoming particles and the energy of the diffusing adparticles.

By changing the *target-substrate distance*, the angular spread of the particles will alter. Closer to the target, the particles collide less with the sputter gas which reduces the angular spread. Because of the smaller spread, the in-plane alignment will improve. This has been observed for the various materials (Fig. 5.1). However, not only the angular spread changes, also the energy of the diffusing adparticles changes. In paragraph 5.3.1 it has been discussed that the energy per atom decrease closer to the target. In this way, the adparticles mobility is reduced. When the substrate is placed too close to the target, the adparticle mobility is reduced so much that the growth conditions aren't satisfied. Owing to this, the degree of in-plane alignment get worse. For MgO and Cr, the in-plane alignment entirely disappears. Remark that for these materials, the disappearance of the in-plane alignment is coupled with a reduction in preferential out-of-plane alignment, which confirms the reasoning of a kinetic limited growth.
Changing the *working pressure* has also an influence on both the angular spread of the incoming particles and on the adparticle mobility. Lowering the working pressure causes an increase in mean free path λ of the sputtered particles, through which the particles collide less with the sputter gas. As a result, the angular spread diminishes and the in-plane alignment improves. However, the particle energy reduces at a lower working pressure (see paragraph 5.3.1), ending up in the case of kinetically limited growth. If the working pressure is too low, the in-plane alignment will deteriorate. In conclusion, the influence of the working pressure on the in-plane alignment will exhibit an optimum, which is confirmed experimentally for the three biaxially aligned materials (Fig 5.2).
The *substrate bias* essentially influences the adparticle mobility. By making the substrate bias more positive (with respect to the floating potential), mainly electrons are attracted towards to substrate. Because the electrons contribute significantly to the deposited power and the contribution of ions is minimal [5], an increase in electron bombardment will cause an increase in adparticle mobility. As mentioned in the beginning of this section, there is an upper limit in the energy of diffusing adparticles. Hence, a strong positive bias will result in a decrease in in-plane alignment. Conversely, a strong negative bias repels the electrons, which reduces the adparticle mobility. If the mobility becomes too limited, the degree of in-plane alignment gets worse. In conclusion, an optimum in in-plane alignment should be observed, which is experimentally confirmed for Cr and InN (Fig. 5.3). Because MgO is electrical insulating, charge effects play a role at high potentials.
The *discharge current* mainly influences the adparticle energy and much less the angular spread. With increasing discharge current, the adparticle mobility reduces (Paragraph 5.3.1). Since optimizing the adparticle mobility will result in an optimized in-plane alignment, also the discharge current will exhibit an optimum. This is experimentally observed (Fig. 5.4)

5.5 Other Parameters

The target-substrate distance, the working pressure, the substrate bias and the discharge current influence both the energy and the angular spread of the particles. These key parameters are well examined and easily controllable. But these are not the only parameters with influence the growth of biaxially aligned thin films. Hereafter, the results of the other deposition parameters are presented. For some of them, peculiar observations are obtained for which, at first glance, the growth mechanism should be revised. Therefore, these parameters are described in more detail in following section.

5.5.1 Influence of the Film Thickness on the growth of MgO

The influence of the layer thickness on the growth of biaxially aligned Cr and InN has been already discussed in chapter 4. For Cr, an improvement of both the out-of-plane alignment and the in-plane alignment with increasing film thickness is observed (Sect. 4.3.2). Because both growth mechanisms are based on an overgrowth mechanism, the results of Cr are consistent with the proposed models (see chapter 4). The best biaxially aligned Cr thin films were obtained at the highest thicknesses. For InN, an improvement of the in-plane alignment with increasing thickness is observed. Also this can be explained in terms of an overgrowth mechanism.
Because MgO is a cubic material, an analogous behaviour like for Cr is expected, as the evolution of the biaxial alignment of MgO is also based on an overgrowth mechanism.
Fig. 5.8(a) shows the fraction of out-of-plane oriented grains as a function the MgO film thickness. Already at 0.25 μm, the MgO thin film exhibits a preferential [111] out-of-plane orientation. This out-of-plane orientation is maintained until a layer thickness of 1.5 μm. For a larger film thickness, the fraction of [111] out-of-plane oriented grains decreases and the MgO thin film is more randomly out-of-plane oriented.
Fig. 5.8(b) shows the degree of in-plane orientation as a function the MgO film thickness. Between 0.25 μm and 1.5 μm, the degree of in-plane alignment improves with increasing layer

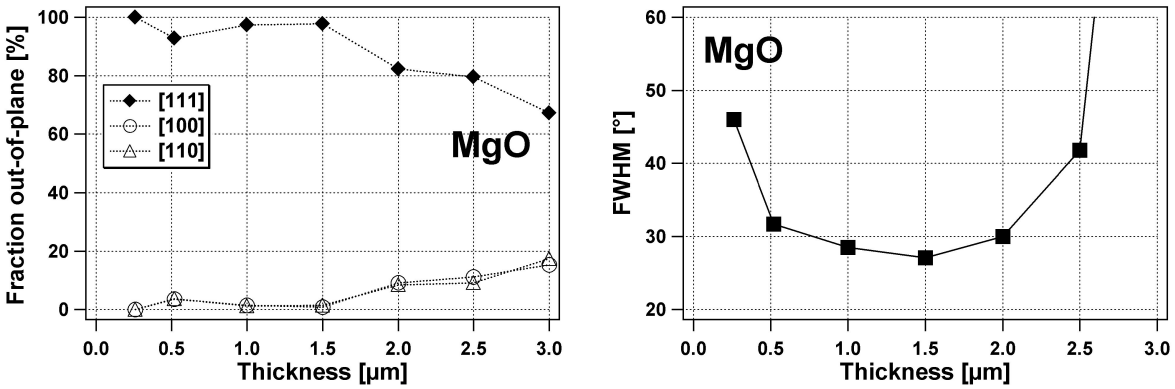

(a) Out-of-plane Alignment (b) In-plane Alignment

Figure 5.8: Influence of the layer thickness on the out-of-plane alignment (*left*) and the in-plane alignment (*right*) of biaxially aligned MgO thin films. The FWHM is obtained from the (200) XRD pole figures.

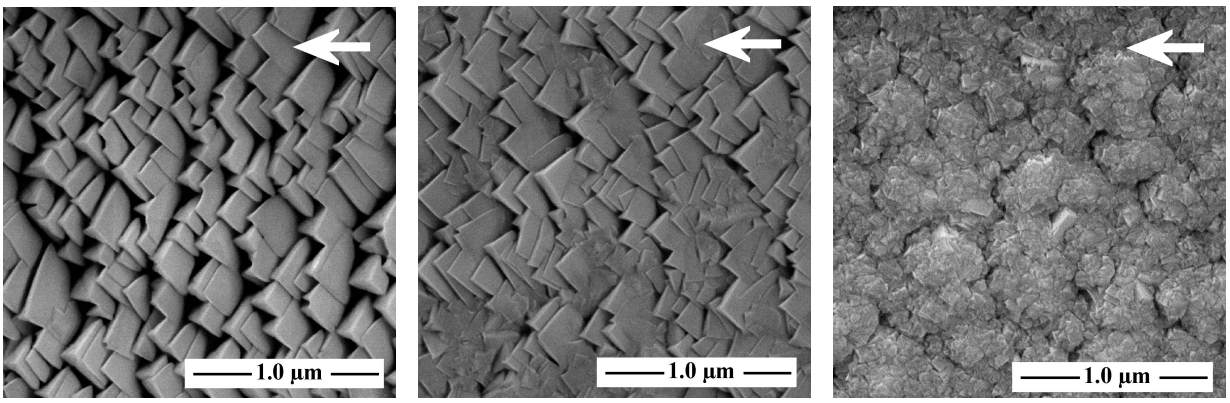

(a) 1500 nm (b) 2000 nm (c) 3000 nm

Figure 5.9: SEM plan view image of biaxially aligned MgO thin films deposited at three different thicknesses: 1500 nm, 2000 nm and 3000 nm.

thickness. At a larger film thickness, the in-plane alignment gets worse. With a film thickness of 3.0 μm, no in-plane alignment is observed.
In the region between 0.25 μm and 1.5 μm, the change in biaxial alignment can be explained by the proposed model. The preferential [111] out-of-plane orientation is due to the overgrowth of differently oriented grains. The grains with the geometric fastest growth direction parallel to the substrate normal, will have the highest perpendicular growth rate and overgrow the others (Sect. 4.4.2). Remark that the overgrowth process of the differently out-of-plane oriented grains, is already completed after 0.25 μm. Also the improvement of the in-plane alignment can be explained by the model for in-plane alignment. Because the grains are truncated by a specific crystal habit (Fig. 5.9(a)), there will be an anisotropy in incorporated diffusing adatoms. As a result, some grains will grow faster and overgrowth the others. Due to the overgrowth, the in-plane alignment will improve throughout the film thickness.
However, at 2.0 μm layer thickness, the growth of the MgO thin film changes. This is in contrast to the observations for Cr and InN thin films. Fig. 5.9(b) shows the surface of such a MgO thin film. At this thickness, disrupted regions without a clear crystal shape appear on the surface of the growing film. These regions extend during further growth and overgrow the {100} faceted grains (Fig. 5.9(c)). Because the XRD angular scans indicate that the film is randomly out-of-plane oriented at 3.0 μm, it is likely that these disrupted regions have a random orientation. Because of the random orientation, also the in-plane alignment will disappear gradually.
Because all parameters are kept constant during the growth, it is not obvious why the MgO thin film doesn't continue to grow by local epitaxy on the {100} facets. Most probably, the mobility of the particles changed during the deposition [7]. By the continuous bombardement with energetic particles, the temperature of the growing surface will increase. As a result, the adparticle mobility will increase. It is reasonable that there is a transition temperature at which the atoms at the surface become active and restructurative grain growth should occur. However, because the layer is about 1.5 μm, the single crystalline grains have a lateral size of about 200 nm, the surface and interface minimization will not be so obvious. Several regions on the surface will have another energy minimization, depending on the surface and the interface, hence special features

will evolve. In despite of this, it expected at larger thicknesses a zone II structure should evolve, however, this is not investigated.

5.5.2 Influence of the Reactive Gas Flow on the Growth of Biaxially Aligned MgO

The MgO thin films are deposited by reactive magnetron sputtering in an Ar/O_2 atmosphere. To examine the influence of oxygen on the growth of MgO thin films, MgO thin films were deposited at various O_2 flows (1 sccm → 5 sccm). The total pressure in the deposition chamber is kept constant.
Fig. 5.10(a) shows the preferential out-of-plane orientation as a function of the O_2 flow. Below the 2 sccm O_2, the MgO thin films were non stoichiometric and the films were opaque. Between the 2 sccm and 4 sccm, the fraction of [111] out-of-plane oriented grains increases slightly with increasing O_2 flow. At 5 sccm O_2, the target was poisoned. In poisoning mode no MgO thin films with a thickness of about 1 μm could be deposited. A deposition time of about 7 hours was required to deposit a MgO thin film of 1 μm, because the deposition rate dropped from 100 nm/min to 2-3 nm/min. However, the glow discharge in poisoning mode was unstable due to the strong electrical insulating properties of MgO. The maximum thickness of a MgO film deposited in poisoning mode was about 150 nm, and not usefull for further research.
Also the degree of in-plane alignment changes by changing the O_2 flow. As can be seen in Fig. 5.10(b), the degree of in-plane alignment improves with increasing O2 flow.
A possible explanation could be a change in deposition rate with increasing O_2 flow. However, no change in deposition is observed. Moreover, no explanation is found for this result up to now.

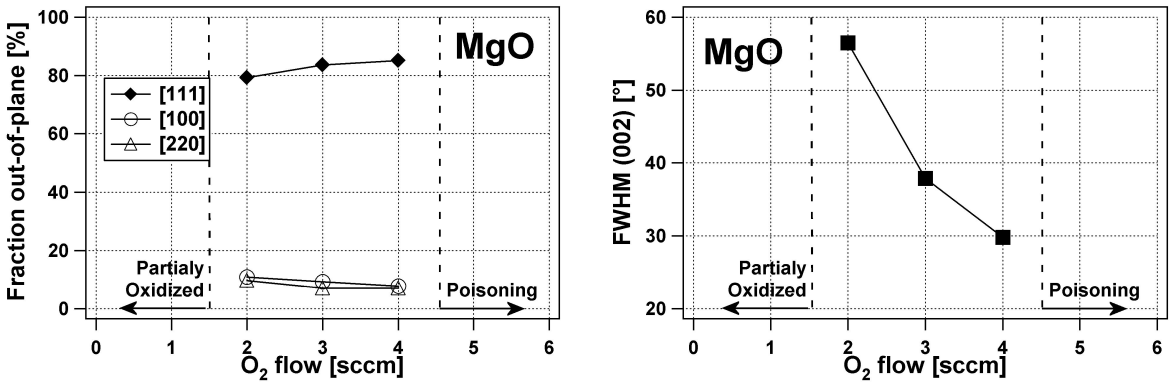

Figure 5.10: Influence of the reactive gas flow on the in-plane alignment of biaxially aligned MgO thin films. The FWHM is obtained from the (200) XRD pole figures.

5.5.3 Influence of the Sputter Gas on the growth of InN thin films

InN thin films were deposited by sputtering from an In target in a Neon/Nitrogen ambient. Because it's hard to obtain stoichiometric InN thin films in an Argon/Nitrogen plasma. The growth of InN thin films in an Ar/N_2 atmosphere has been investigated by depositing several thin films in an ambient with different Ar and N_2 concentrations. For this, the gas flow of the Ar sputter gas and the reactive N_2 gas has been varied (Ar: 90 sccm → 0 sccm; N_2: 10 sccm → 100 sccm;). The total gas flow is kept constant. The thin films were deposited on a non-tilted substrate, so only the influence on the out-of-plane alignment could be examined.
Fig. 5.11 shows the out-of-plane orientation of the uniaxially aligned InN as a function of the N_2/Ar flow ratio. Below a flow ratio of 2.5, only XRD peaks of pure Indium were observed. This indicates that the fraction of InN in the film is very low and the thin film is mainly composed of pure In. The In thin films have a random out-of-plane orientation. For clarity, the fraction of the various peaks of In is not shown in Fig. 5.11.
For a flow ratio between 2.5 and 4, both In and InN peaks are observed. With increasing N_2/Ar flow ratio, the InN peaks become more dominant. At a ratio 2.5, the InN grains are randomly out-of-plane oriented. As the fraction of InN in the thin film increases, also the fraction of [0001] out-of-plane oriented grains increases. Fig. 5.12 shows the surface of an In/InN thin film deposited with a N_2/Ar flow ratio of 2.5. It can clearly be seen that large clots have formed on the surface. EDX showed that these droplets contain a high concentration of In (93%) Therefore, it is plausible that these clots correspond to In droplets.
At a N_2/Ar flow ratio higher than 4, no In XRD peaks are observed, which confirms that the thin film is pure InN. The InN thin films are preferentially [0001] out-of-plane oriented.
This deposition series indicates that it's hard to obtain stoichiometric InN thin films in an Ar atmosphere without a high N_2 flow. Guo et al. and Song et al. obtained similar results when measuring the nitrogen concent in InN thin films grown with various N_2/Ar concentrations [8, 9]. According to Natarajan et al., In doesn't react with molecular N_2 at its surface [10]. Additionally,

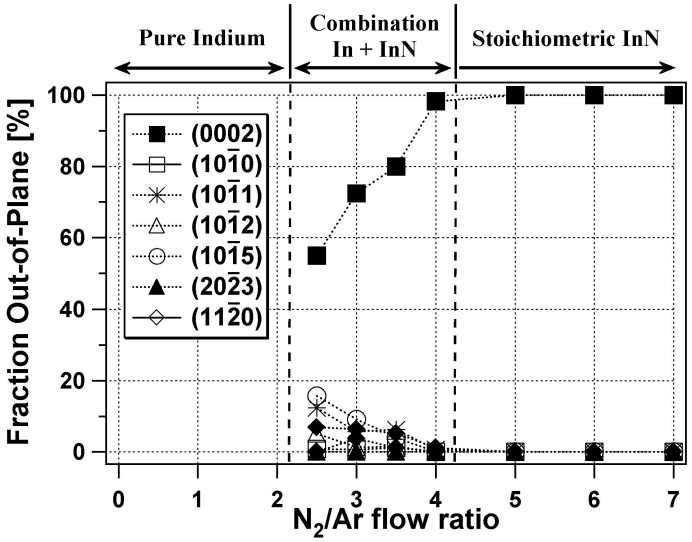

Figure 5.11: The out-of-plane orientation of uniaxially aligned InN as a function of the N_2/Ar flow ratio. For a N_2/Ar flow ratio below 4, also In peaks are observed, but aren't shown here.

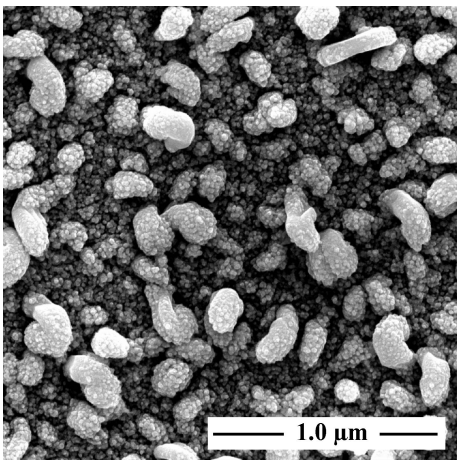

Figure 5.12: SEM plan view image of an In/InN thin film deposited on a non tilted substrate at a N_2/Ar flow ratio of 2.5

dissociative chemisorption does not occur at In surfaces [10]. Hence, only atomic N arriving at a growing In surface can contribute to the growth. There are a few possibilities to dissociate N_2 during sputtering. Firstly, ionized N_2^+ can be accelerated towards the target, and upon impact it may dissociate. Another frequently observed mechanism is a dissociative charge exchange collision whereby

$$N_2^+ + N_2 \rightarrow N^+ + N + N_2 \tag{5.1}$$

In both cases ionized N_2^+ is needed to dissociate N_2. In a glow discharge, N_2 can ionize by an inelastic collision with an energetic electron. However, this has a low probability. The fraction N_2^+ can be increased, when Penning ionization occurs [11]. An excited or ionized rare gas atom which falls back to its ground state during a collision with a N_2 molecule, transfers its energy to N_2. If the energy is high enough, N_2 can be ionized. The Penning ionization process is illustrated in Fig. 5.13. However, in an Ar plasma, the ionization energy of Ar is similar to the ionization

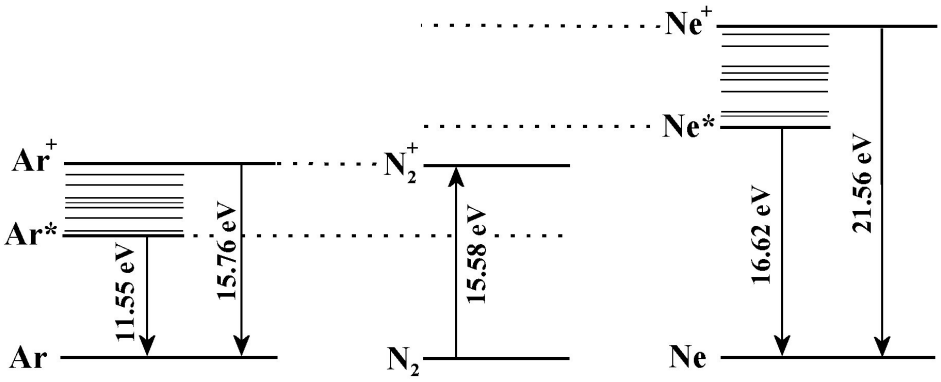

Figure 5.13: Penning ionization. The desexcitation energy of metastable or ionized Ne is sufficient to ionize N_2. However, for Ar, Penning ionization only occur for ionized Ar and is less likely.

energy of N_2, through which Penning ionization will be unlikely. It has been observed by Fan and Newman, that Ar is even disadvantageous for the production of ionized N_2^+ [12]. In contrast, the use of Ne as sputter gas enhances the ionization of N_2. The energy difference between the first metastable state and the ground state of Ne, is much higher than for Ar and is sufficient to ionize nitrogen. The collision reaction is

$$Ne^* + N_2 \rightarrow N_2^+ + Ne + e^- \tag{5.2}$$

By using Ne as sputter gas, the rate of atomic nitrogen ion production is significantly enhanced due to Penning ionization of molecular nitrogen in combination with the dissociative charge exchange collision [11].
Stoichiometric InN thin films were obtained for a N_2/Ne flow rate ratio of 0.5 or higher, which is much lower than for sputtering in an Ar-N_2 ambient. For a ratio below 0.5, there is no glow discharge, which is due to the higher ionization energy of Ne. Fewer secondary electrons have an energy which is high enough (in comparison to those electrons that can ionize Ar or N_2) to sustain the discharge. Alternatively, a RF coil could be used to ionize the nitrogen in the plasma [13]. However, this technique hasn't been used during this work.

5.5.4 Influence of the Substrate on the Growth of Biaxially Aligned Cr

Fig. 5.14 shows the out-of-plane orientation of biaxially aligned Cr thin films deposited on various substrates. The Cr thin films deposited on Ti, Ni, Ta and Hastelloy foil exhibit a preferential [100] out-of-plane orientation. There is a small variation in the fraction of [100] out-of-plane oriented grains. When deposited on alumina, stainless steel or the Fecralloy a large fraction of randomly oriented grains is observed.
For Stainless steel and the FeCr alloy, the lattice parameter coincides with this of Cr. Becau-

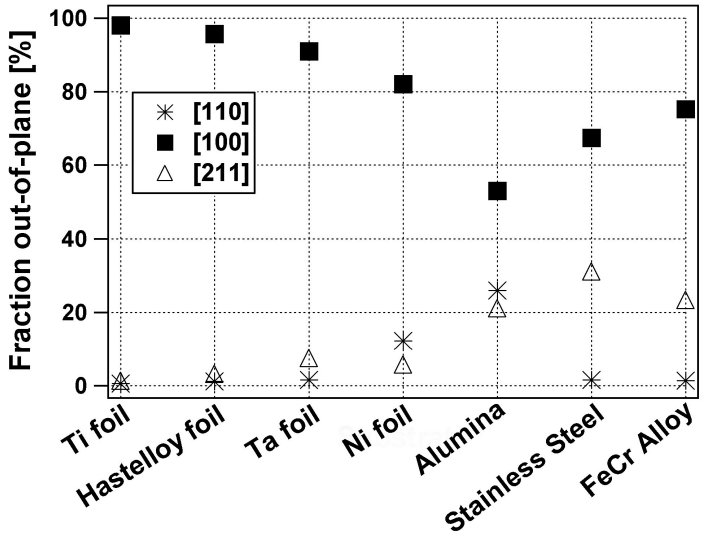

Figure 5.14: The out-of-plane orientation of biaxially aligned Cr thin films deposited on various substrates.

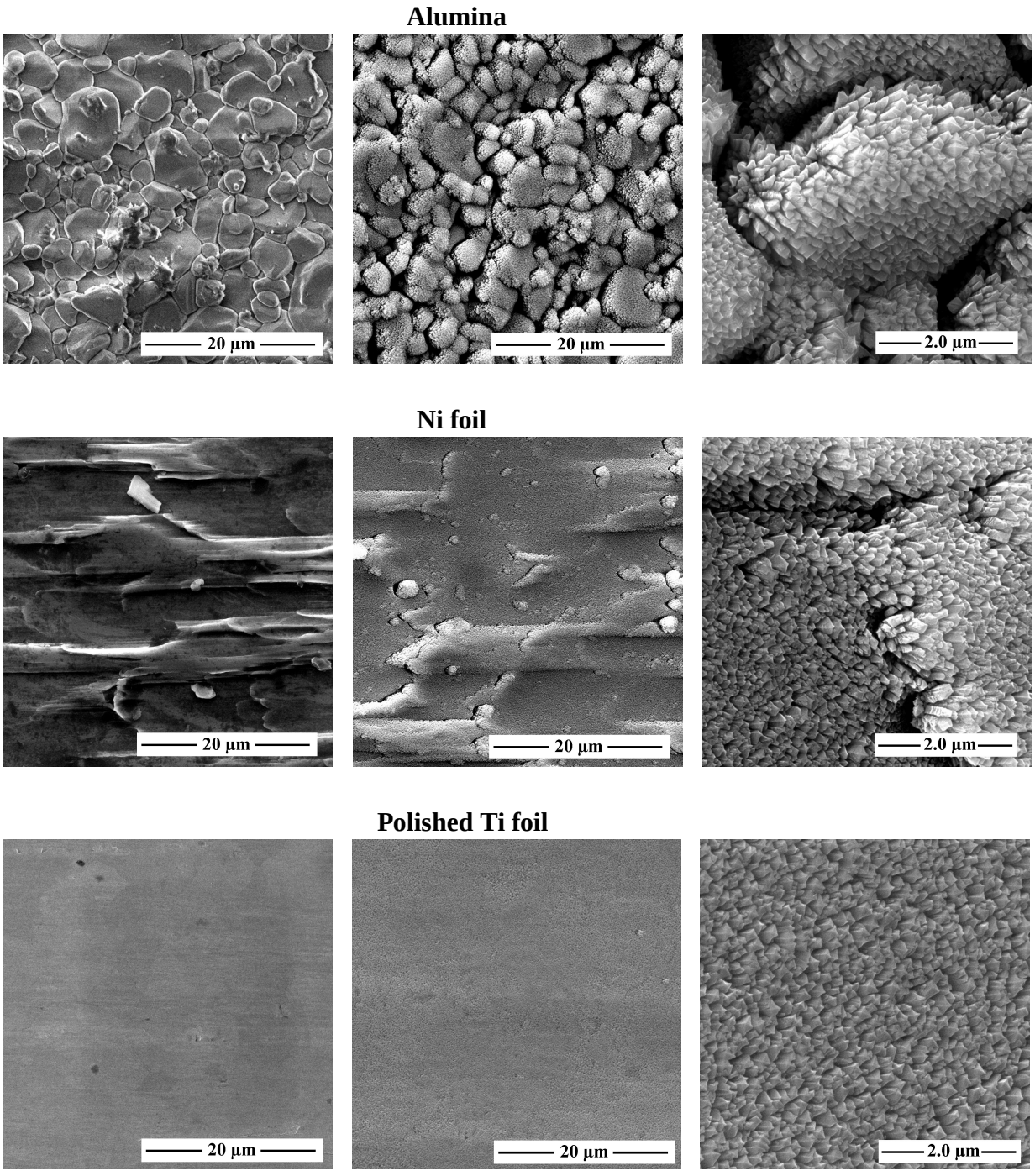

Figure 5.15: (*left*) SEM plan view of three substrates: alumina, Ni foil and polished Ti foil. (*middle - right*) SEM plan view with two different magnifications of Cr thin films deposited on the three substrates.

se the penetration depth of the X-rays is about 3.0 μm for Cr, a considerable contribution of the substrate signal is expected which adds to the Cr signal and no valuable conclusions can be drawn for these substrates.

Fig. 5.15 shows the surface of the various substrates (Alumina, Ni foil, Ta foil) and the surface of the Cr thin film deposited on the same substrate. For the Cr film deposited on alumina, it

is clearly seen that the macroscopic roughness of the substrate is passed onto the Cr thin film roughness (macroscopic roughness means that the length scale of the roughness is much larger than the size of the grains).
These observations are consistent with the proposed model. In section 4.4 it has been discussed that the grains with the geometric fastest growth direction perpendicular to the substrate will overgrow the other grains and determine the out-of-plane orientation. For Cr, the [100] orientation is the geometric fastest growth direction, hence an [100] out-of-plane orientation should be observed. This is observed for the Ti, Ni, Ta and Hastelloy foil. However, when the substrate surface is curved, the grains with the [100] orientation perpendicular to the curved surface will survive. These grains will have a different out-of-plane orientation in comparison with the grains deposited on a non-curved surface. If the substrate contains a lot of curvatures (so a high roughness), there will be a spread on the out-of-plane orientation of the grain. The rougher the surface, the larger the spread. The alumina substrate is composed of macroparticles with a large curvature. As a result, there will be a large spread on the out-of-plane orientation and in XRD a random orientation will be observed. The spread is the smallest for the Ti substrate, which has indeed the smallest roughness.
The roughness will also influence the in-plane orientation, because the orientation of the {110} crystal habit will change when the grains are grown on a curved surface. Consequently, a different capture length will be obtained and the overall in-plane alignment will disappear. Not only for Cr thin films, but also for other biaxially aligned thin films, flat surfaces are needed to obtain biaxially aligned thin films with a good quality.

5.5.5 Influence of the Magnet Configuration

By adjusting the magnet configuration, the plasma density at the position of the substrate will change (Sect. 2.4). A more unbalanced magnet configuration causes an increase in electron and ion density at the substrate. As a result, more charged particles will impinge on the surface of the growing thin film. The mobility of diffusing adparticles will increase, as they dissipate their energy to the growing film.
A comparison between the two magnet configurations has been performed for MgO and InN. For these materials, all the deposition parameters have been optimized for an 1:3 (slightly unbalanced) and 1:9 (strongly unbalanced) magnet configuration. Because the magnet configuration has a direct impact on the adparticle mobility, the optimized values are different for the two magnet configurations.
The best values are obtained for 1:3 magnets. This points out that the adparticle mobility is already quiet high and cutting back the energy delivered by energetic bombardment is beneficial to the growth of biaxially aligned MgO and InN.
It is known for Cr that the diffusion barriers are much lower than for MgO and InN. Therefore it is evident that the mobility should be reduced and 1:3 magnets are used. Experiments with 1:9 magnets never resulted in the growth of an oriented film.

5.6 The Optimized Biaxially Aligned Thin Films

For the various materials, all the depositions parameters have been optimized. Table 5.2 summarizes the optimized deposition conditions for the three materials: MgO, Cr and InN. It should be noticed that some of the values deviate from the optimal values given in the various graphs. This is due to the fact that the optimization of one deposition parameter can compromise the optimized value of the other parameters previously optimized. Therefore, it happened we had to go back to an earlier optimized parameter, to reoptimize it. With these deposition parameters, the MgO, Cr and InN thin film exhibit an [111], [100] and [0001] preferential out-of-plane orientation. Next to this, also the degree of in-plane alignment is optimized. Fig. 5.16 shows the XRD pole figures of the optimized biaxially aligned MgO, Cr and InN thin film. The FWHM of the optimized MgO thin film was 14°, for Cr it was 35° and for InN it was 22°. The higher value for Cr is due to the high affinity of Cr to codeposited contaminants. Because the impurities have a big influence of the atomistic processes on the surface, their influence on the growth of thin films will be pronounced. Chapter 6 is completely devoted to the investigation of the growth of biaxially aligned thin films in the presence of contaminants.

5.7 Conclusions

The growth of biaxially aligned thin films is sensitive to two fundamental parameters: the angular spread of the incoming particles and the energy of the diffusing adparticles. The fraction of out-of-plane oriented grains as well as the degree of in-plane alignment can be optimized by the various deposition parameters. By changing the deposition parameters, the adparticle energy

[2]Because the in-plane alignment improves with increasing inclination angle, an inclination angle of 90° would give the best results. Disadvantageous is that the deposition rate decreases with increasing inclination angle. However, because it is experimentally observed that the degree of in-plane alignment saturates at the higher inclination angles, an angle of 60° is a good compromise between a high deposition rate and an in-plane alignment close to the best obtainable in-plane alignment.

Deposition Parameter	MgO	Cr	InN
Substrate Inclination Angle α	Maximal[2]	Maximal[2]	Maximal[2]
Target-Substrate Distance $d(T-S)$	9 cm	10 cm	9 cm
Working pressure p	0.45 Pa	0.38 Pa	0.25 Pa
Substrate Bias V_{bias}	−15 V	−15 V	−40 V
Discharge Current I_d	0.90 A	0.65 A	0.55 A
Film thickness t	3.0 μm	Maximal	Maximal
Magnet Configuration	1 : 3	1 : 3	1 : 3
Rare gas flow	60 sccm	26 sccm	8 sccm
Reactive gas flow	4 sccm	n/a	36 sccm
Substrate Temperature T_{subst}	floating	floating	floating

Table 5.2: Overview of the optimized value for the several deposition parameters used during the growth of biaxially aligned MgO, Cr and InN

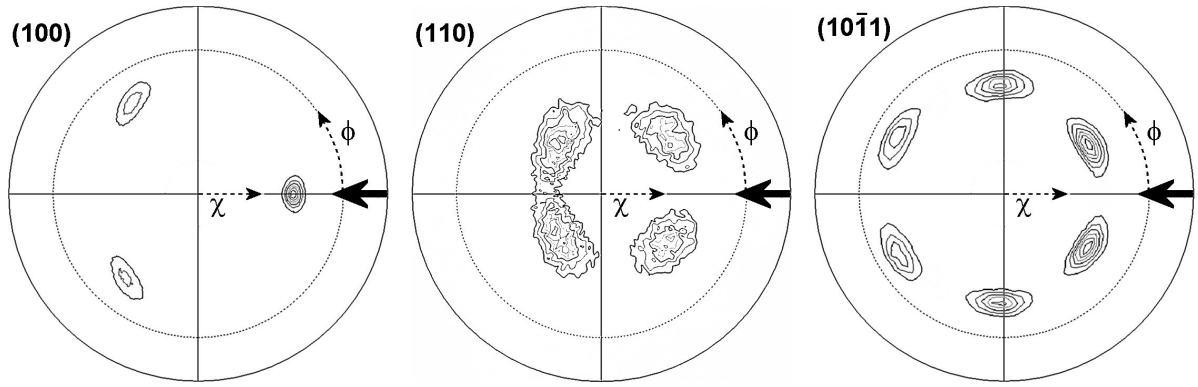

(a) MgO (b) Cr (c) InN

Figure 5.16: XRD pole figures of biaxially aligned (a) MgO thin film, (b) Cr thin film, (c) InN thin films, deposited at optimized deposition conditions.

or the angular spread or both fundamental parameters will alter. Because there is an optimal adparticle mobility, most of the deposition parameters exhibit an optimal value. Quiet often, this optimum is influenced by the need for a minimization of the angular spread.
Because just the energy is so critical, the change of one of the deposition parameter can disorder the optimization of all the other parameters. Therefore, the use of the several deposition parameters should be handled cautiously.

Bibliography

[1] P. Ghekiere, S. Mahieu, G. De Winter, R. De Gryse, D. Depla, Influence of the deposition parameters on the biaxial alignment of MgO grown by unbalanced magnetron sputtering, J. Cryst. Growth 271 (2004) 462–468.

[2] A. Anders, Physics of arcing, and implications to sputter deposition, Thin Solid Films 502 (1–2) (2006) 22–28.

[3] S. D. Ekpe, S. K. Dew, Theoretical and experimental determination of the energy flux during magnetron sputter deposition onto an unbiased substrate, J. Vac. Sci. Technol. A 21 (2) (2003) 476–383.

[4] T. P. Drüsedau, T. Bock, T. M. John, F. Klabunde, W. Eckstein, Energy transfer into the growing film during sputter deposition: An investigation by calorimetric measurements and monte carlo simulations, J. Vac. Sci. Technol. A 17 (5) (1999) 2896–2905.

[5] S. D. Ekpe, S. K. Dew, Investigation of thermal flux to the substrate during sputter deposition of aluminum, J. Vac. Sci. Technol. A 20 (6) (2002) 1877–1885.

[6] D. Depla, G. Buyle, J. Haemers, R. De Gryse, Discharge voltage measurements during magnetron sputtering, Surf. Coat. Technol. 200 (14-15) (2006) 4329–4338.

[7] P. Ghekiere, S. Mahieu, G. De Winter, R. De Gryse, D. Depla, O. I. Lebedev, G. Van Tendeloo, Growth mechanism of biaxially aligned magnesium oxide deposited by unbalanced magnetron sputtering, Solid State Phenom. 105 (2005) 433–438.

[8] Q. Guo, N. Shingai, Y. Mitsuishi, M. Nishio, H. Ogawa, Effects of nitrogen/argon ratio on composition and structure of InN films prepared by r.f. magnetron sputtering, Thin Solid Films 343-344 (1999) 524–527.

[9] P. K. Song, D. Sato, M. Kon, Y. Shigesato, Crystallinity and stoichiometry of InN_x films deposited by reactive dc magnetron sputtering, Vacuum 66 (2002) 373–378.

[10] B. R. Natarajan, A. H. Eltoukhy, J. E. Greene, Mechanisms of reactive sputtering of indium .1. growth of InN in mixed Ar-N2 discharges, Thin Solid Films 69 (1980) 201–216.

[11] A. D. Wilson, J. C. Avelar-Batista, S. J. Dowey, J. Robson, A. Leyland, A. Matthews, K. S. Fancey, Investigation into nitrogen-inert gas interactions in d.c. diode glow discharges, Surf. Coat. Technol. 142-144 (2001) 540–545.

[12] Z. Y. Fan, N. Newman, Precise control of atomic nitrogen production in an electron cyclotron resonance plasma using N_2/noble gas mixtures, Appl. Phys. Lett. 73 (4) (1998) 456–458.

[13] S. J. Patil, D. S. Bodas, A. B. Mandale, S. A. Gangal, Characterization of indium nitride films deposited by activated reactive evaporation process, Thin Solid Films 444 (1) (2003) 52–57.

Chapter 6

Impurity Induced Texture Change in Biaxially Aligned Thin Films

6.1 Introduction

The growth mechanism of biaxially aligned thin films which has been discussed in chapter 4 and 5, does not take into account the incorporation of an impurity species during the growth. However, the codeposition of impurities is a factor which cannot be neglected during the growth of thin films. Firstly, impurities are always present in a vacuum chamber as a residual gas. Secondly, they act directly on the atomistic processes taking place at the surface and have their impact on the fundamental phenomena of structure formation. Therefore the growth mechanism can vary in the presence of impurities.
The influence of impurities was demonstrated during the first deposition series of Cr, which were irreproducible and hard to explain. The answer was found by comparing the base pressures[1] of the various depositions. Cr is a metal and it is known that metals have an affinity to other codeposited elements. After pumping down the system to a base pressure of about 10^{-6} mbar, only residual gases are present in the chamber. Fig. 6.1 shows the residual gases at a base pressure of 10^{-6} mbar as measured by mass spectrometry. Mainly, H_2O, N_2, O_2 and CO_2 are present.
It was observed that the Cr experiments were reproducible only when the base pressure was below $5 \cdot 10^{-6}$ mbar. In order to know the exact influence of the residual gases on the thin films growth, impurities were codeposited during the growth of Cr thin films in a controlled manner. This is discussed in sections 6.2, 6.3 and 6.4. Also the influence of impurities on the growth of biaxially aligned InN thin films and MgO thin film is examined throughly (Sect. 6.5 and Sect. 6.6).

Some definitions

The term impurity is used for any foreign species other than the crystallizing compound. For instance, for MgO thin films, an impurity corresponds to all species different from magnesium,

[1] The base pressure is that pressure which is obtained at the end of the pump down cycle before introducing the sputter gases.

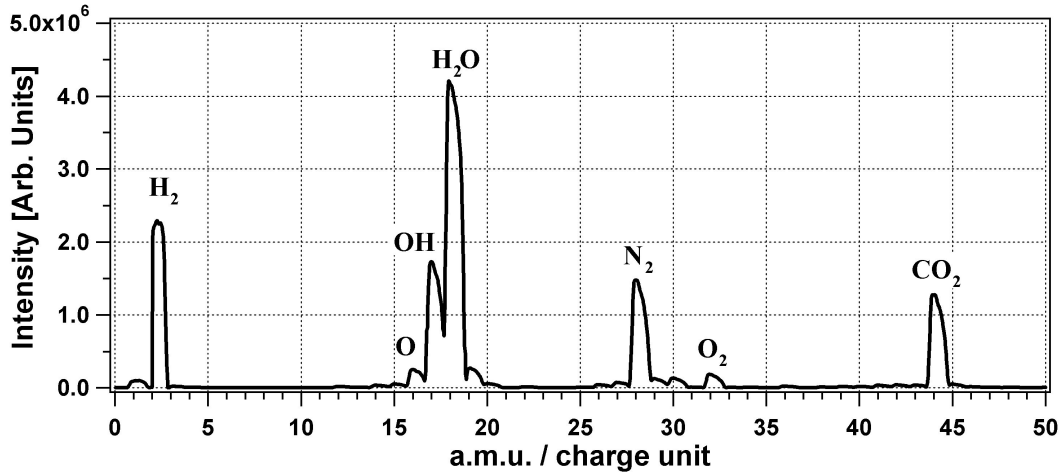

Figure 6.1: Mass scan of the residual gases at a base pressure of 10^{-6} mbar.

oxygen or magnesium oxide. As mentioned in the introduction, this impurity can be incorporated unintentionally during the growth by the presence of residual gases or can be added deliberately during the growth. If the impurity is added deliberately, the impurity is often called an additive. Depending on the interaction with the growing film, an impurity can enhance or obstruct the growth. In general, these impurities are called promoters or inhibitors respectively. Related to a promoter, the term surfactant is used. As the name puts it, surfactants only play a role on the surface. The classical meaning of surfactant is a surface-active agent that reduces the surface free energy [1]. In thin film growth, a surfactant is an agent that controls the growth kinetics. An ideal surfactant smooths the film surface, is not incorporated in the film and can simply be removed after deposition.

To influence the growth of thin films, the solubility of the impurity into the crystal lattice has to be low. If the impurity can dissolve into the lattice, it diffuses from the surface to the bulk and it won't change the growth of the thin film. However, the bulk properties will change. This kind of impurities is known as dopants and are frequently used in the semiconductor industry to change the bandgap structure.

Impurity induced changes of the SZM: a revised Structure Zone Model

In the previous chapters, the classification in zones and the use of the structure zone model have proven to be very useful to describe the growth of polycrystalline thin films. For instance, different mechanisms are responsible for the evolution of the preferential out-of-plane alignment, when the thin film is deposited in a zone T or a zone II. The SZM which has been used, is valid in pure conditions. However, when growing a thin film while codepositing impurities, a change in the SZM can be expected.
In chapter 1 (Sect. 1.6.4), it was already briefly quoted that certain concentrations of impurities cause a shift in the different zones and even some zones may disappear. To understand the growth of biaxially aligned thin films with codeposited impurities, it is essential to understand these changes in the SZM. Therefore, some aspects of the revised structure zone model will be

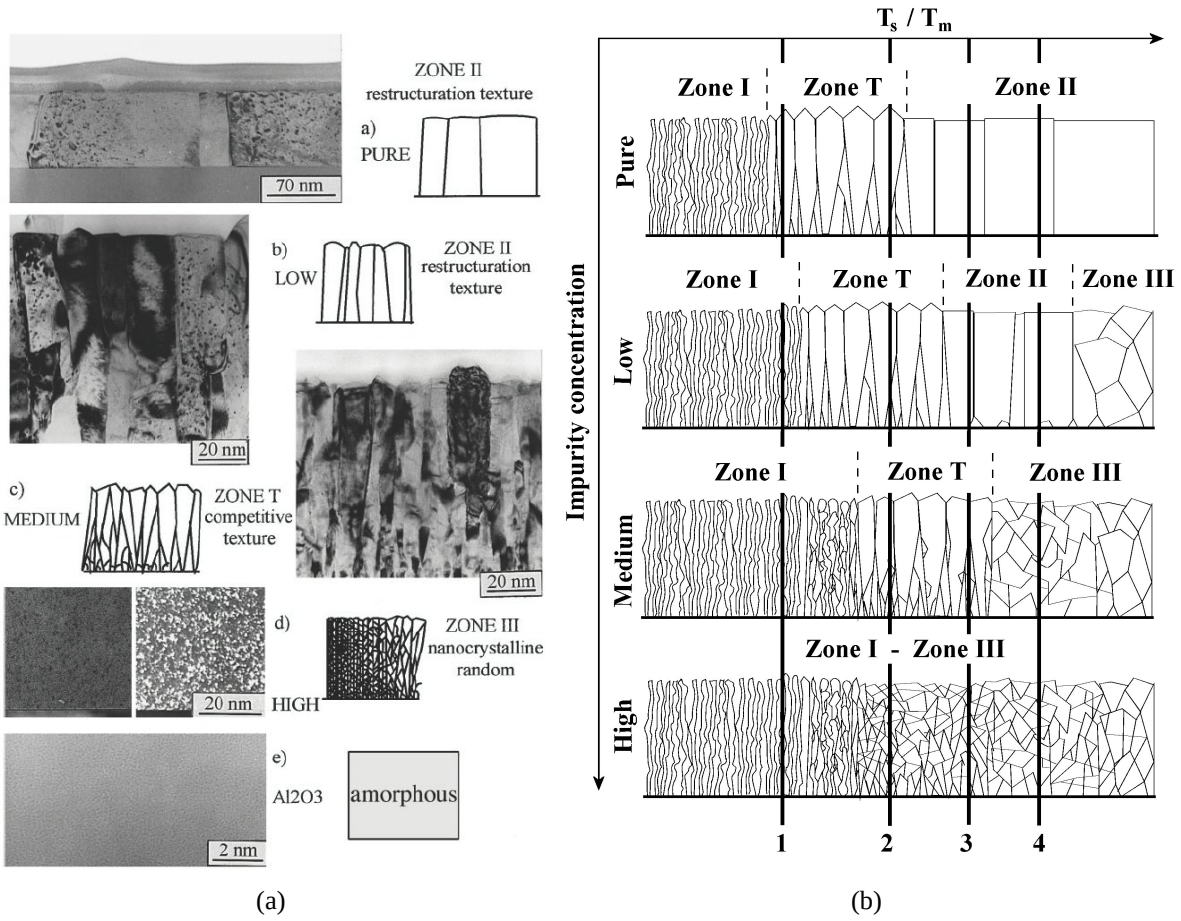

Figure 6.2: (a) Transition from Zone II to zone T to zone III of Al thin films with different concentrations O_2 contamination [3]. (b) revised structure zone model. The various lines show a path that can be followed in the experiments.

repeated briefly.

The revised SZM is published by Barna et al [2, 3]. They examined the growth of polycrystalline Al thin films with the codeposition of O_2, which will act as an inhibitor in the metallic system. Their results are shown in Fig. 6.2(a). Based on these results, a revised structure zone model is developed as shown in Fig. 6.2(b). This revised structure zone model is constructed by discussing the influence of an inhibitor on the fundamental phenomena of structure formation (Sect. 1.6.4). For different impurity concentrations, the change of the zone is discussed, resulting in a shift of the zones to higher homologous temperatures and the disappearance of several zones.

When examining the influence of impurities on the structure evolution of polycrystalline thin films, mostly all deposition parameters are kept constant and only the impurity concentration is varied.[2] Because of the constant deposition parameters, only the influence of O_2 impurities at one specific homologous temperature T_S/T_M is examined. For instance, when in pure conditi-

[2] Due to their low concentration, the influence of the impurities on the deposition parameters is negligible. (e.g. no change in deposition rate or working pressure is expected)

ons a zone II structure is observed, one will look at the change of this zone II structure when adding impurities. The change in structure when codepositing impurities at one specific homologous temperature can be represented by a line on the revised SZM. Depending on the deposition conditions, another homologous temperature will be obtained and hence, another line will be followed. Several of these lines are indicated on the schematic drawing of the revised SZM (Fig. 6.2(b)).
This was also the case in the research of Barna et al. A shift from zone II over zone T to zone III is observed with increasing O_2 impurity concentration. This experiment corresponds to line 3 (Fig.6.2(b)). They explained the observations as follows [3]. In pure conditions, a zone II structure evolves. Because of the low energy barriers of the FCC structured Al, restructurative grain growth will occur at room temperature and broad equiaxed columns will be observed (Sect. 1.6.3). At a low level of oxygen concentration, the restructurative grain growth processes still occur, resulting in equiaxed columns. However, because the oxygen accumulates in the grain boundaries, the mobility of the grain boundaries is limited and smaller columns are observed. At a medium level of oxygen concentration, the growth is limited already at the coalescence stage. The islands which nucleate on the substrate, will have a random crystallographic orientation and keep their random orientation because the oxygen will inhibit restructurative grain growth. However, because oxygen behaves differently on the various Al crystal facets, a growth competition between the different oriented grains can occur, resulting in an evolutionary overgrowth. The structure will correspond to a zone T. At a high level of impurity concentration, the oxygen covers the whole surface and the growth is blocked completely. A globular structure, characteristic for zone III, will evolve.

Depending on the zone in which the polycrystalline thin films are deposited, another line will be followed. This is exactly what we examined in this research. In pure conditions, biaxially aligned thin films are deposited in zone T (Cr, MgO) as well as in zone II (InN). By adding impurities during the growth, a specific path on the revised SZM is examined.
As the noticed changes in the SZM of Al by the addition of O_2 impurities can be explained by fundamental processes, one can assume that this revised SZM proposed by Barna can be generalized and used for other systems. Under these assumptions one can expect the following. Because InN is deposited in zone II, it is reasonable that a similar line is followed as for the Al/O_2 system, at least when the impurity acts as an inhibitor. A transition from zone II over zone T to zone III is expected (line 3). Another path that can be followed is from zone II to zone III directly (line 4).
If an inhibitor is added during the growth of a thin film which has a zone T structure in pure conditions (Cr, MgO), a transition from zone T to zone I is expected (line 1). Another possibility is that the thin film remains in zone T at rather high impurity concentrations, but finally changes to a zone III (line 2).
In case of a promoter, an opposite effect is expected. A different structure zone model should be constructed because the promoter will act differently on the fundamental processes of structure formation. In contrast to the inhibitor, a promoter will cause a shift in zones to a lower homologous temperature.

6.2 Influence of O_2 and N_2 on the Growth of Biaxially Aligned Cr Thin Films

6.2.1 Experimental Setup

The influence of impurities on the growth of Cr thin films is investigated by the deposition of biaxially aligned Cr thin films with varying impurity concentration. Some of the results are reported in [4]. To obtain a controllable concentration of impurities, firstly, the deposition chamber was pumped down to a base pressure below $1 \cdot 10^{-6}$ mbar. For this base pressure, reproducible results were obtained for Cr. Before deposition, a reactive gas which is the impurity during the deposition, is introduced into the chamber via a needle valve. The corresponding partial pressure is used as reference. Both O_2 and N_2 are used as impurity gas, because they are one of the main fragments of the residual gas. Hence, both the influence of O_2 and N_2 on the growth of biaxially aligned Cr is examined. The O_2 and N_2 partial pressure is varied between $1 \cdot 10^{-6}$ mbar and $8 \cdot 10^{-5}$ mbar. During deposition, the corresponding flow is kept constant.
For both deposition series, all deposition parameters are kept constant. The parameters were optimized for the growth of biaxially aligned Cr thin films in pure conditions (see chapter 5). The target-substrate distance is 10 cm, the discharge current is 0.65 A and the substrate bias is −15 V. The Ar flow is 26 sccm resulting in a working pressure of 0.38 Pa. An 1 : 3 magnet configuration is used. Cr thin films are deposited on a tilted and non-tilted substrate. In case of a tilted substrate, the substrate inclination angle is 60°. The substrate is hastelloy. For the TEM analysis, sometimes glass substrates are used. No difference between the various substrates is observed. The layer thickness is about 1000 nm.

6.2.2 Experimental Results

Fig. 6.3(a) shows the preferential out-of-plane alignment of Cr thin films deposited on an inclined substrate as a function of the N_2 partial pressure. Without the intentional addition of nitrogen, here represented by the point at $1.0 \cdot 10^{-6}$ mbar N_2,[3] the Cr thin film exhibits a preferential [100] out-of-plane alignment. The origin of this behaviour has been discussed in chapter 4. By adding a small amount of nitrogen during the deposition ($p(N_2) < 5.0 \cdot 10^{-6}$ mbar), no change in preferential out-of-plane orientation is observed. At a N_2 partial pressure of $7.0 \cdot 10^{-6}$ mbar, the fraction of [100] out-of-plane oriented grains decreases and a change to a preferential [111] out-of-plane orientation is observed. The Cr thin film remains preferential [111] out-of-plane oriented until a N_2 partial pressure of $5.0 \cdot 10^{-5}$ mbar. At a higher N_2 concentration during deposition, the Cr thin film exhibits a random out-of-plane orientation.
A similar deposition series has been carried out with the codeposition of O_2 in stead of N_2. Fig. 6.3(b) shows the preferential out-of-plane orientation of Cr thin film as a function of the O_2 partial pressure. The results are comparable to those with N_2 impurities. Upon the addition of

[3] This has been done because this pressure corresponds to the base pressure at which the deposition is carried out. It should be remarked that the N_2 partial pressure as a part of the residual gases is much lower than $1.0 \cdot 10^{-6}$ mbar. From Fig. 6.1, it is calculated that only 12% of the residual gas is N_2. The other gases are mainly H_2O (33%), H_2 (40%), CO_2 (7%) and O_2 (2%) (The ionization cross sections are taken into account). Hence, at a base pressure of $1.0 \cdot 10^{-6}$ mbar, the N_2 partial pressure is about $0.8 \cdot 10^{-7}$ mbar. Nevertheless, the base pressure is used as upper limit, because the behaviour of the other residual gases is unknown at this point.

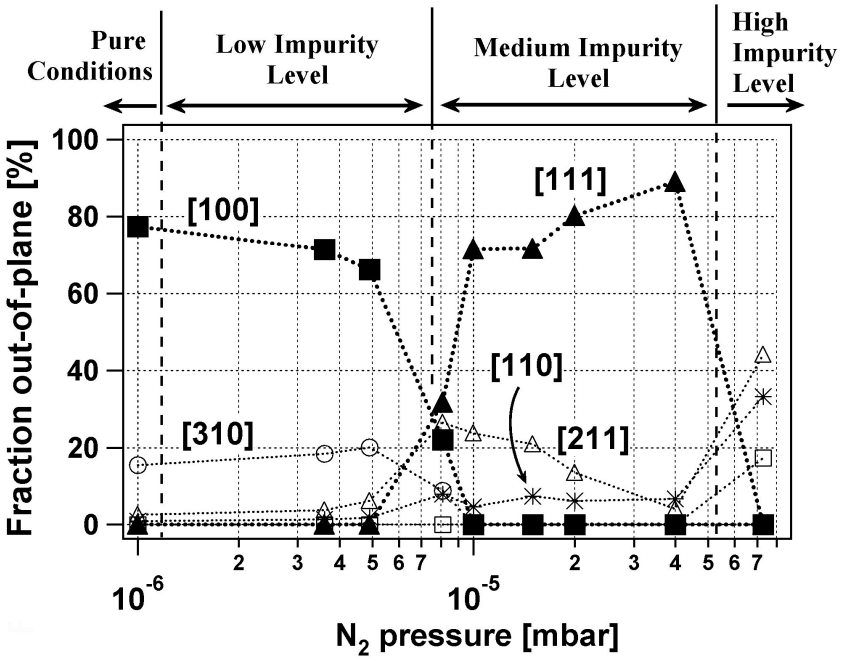

(a) Influence of N_2 on the preferential out-of-plane orientation of Cr thin films

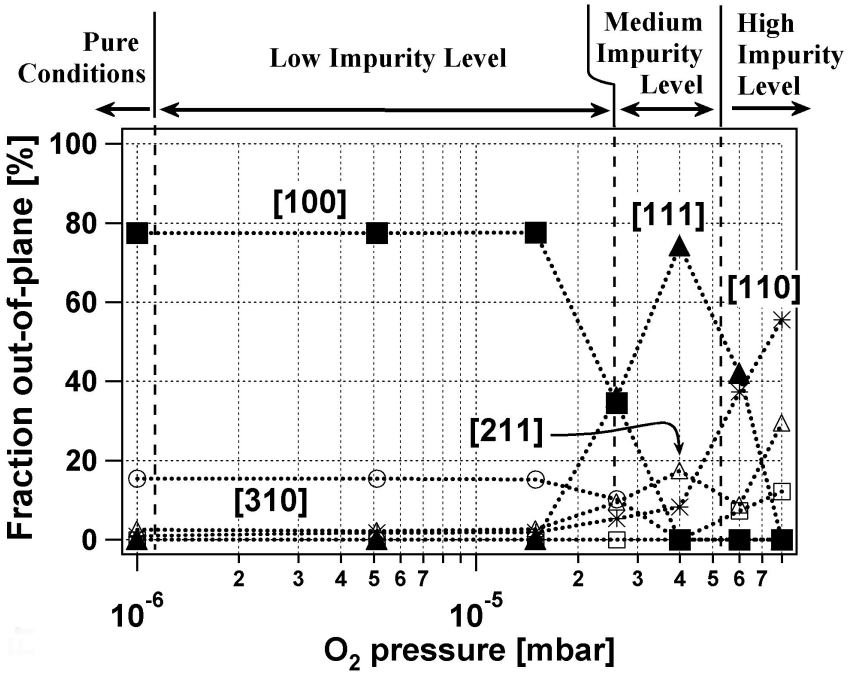

(b) Influence of O_2 on the preferential out-of-plane orientation of Cr thin films

Figure 6.3: The change in preferential out-of-plane orientation of Cr thin films as a function of (a) N_2 partial pressure and (b) O_2 partial pressure. The fraction of out-of-plane orientation is determined by XRD angular scan

a small amount of O_2 ($p(O_2) < 1.5 \cdot 10^{-5}$ mbar), no change in preferential [100] out-of-plane orientation is observed in comparison to the Cr thin film deposited without O_2. Adding more O_2 during the deposition causes a change in preferential out-of-plane orientation from preferential [100] to [111]. At an O_2 partial pressure above $5.0 \cdot 10^{-5}$ mbar, Cr thin film exhibits a random out-of-plane oriented.
The similarity between the results for N_2 and O_2 is striking. Both exhibit the same change in preferential out-of-plane alignment. The only difference is that the change from [100] to [111] occurs at a different partial pressure. In comparison to O_2, the change in out-of-plane alignment of Cr thin films with N_2 occurs at must lower partial pressure. The change to a random out-of-plane orientation does occur at the same partial pressures. Not only the change in out-of-plane orientation, but all the other experimental observations are identical. To avoid an annoying repetition, only the results for N_2 will be presented in this experimental paragraph.

In addition to a change in out-of-plane alignment caused by codeposited impurities, also the in-plane alignment of biaxially aligned Cr thin films changes. Fig. 6.4 shows the XRD pole figures obtained for four different N_2 concentrations. The case without the deliberate addition of impurities (Fig. 6.4(a)) has already been discussed thoroughly in previous chapters. Four distinct poles are observed situated at an angle $\phi = 45° \pm n \cdot 90°$ with respect of to the direction of the incoming vapour flux. The four fold symmetry and the position of the poles at $\chi \approx 45°$ confirm the preferential [100] out-of-plane orientation. This can easily be seen on the corresponding stereographic projection belonging to the XRD pole figure.
Fig. 6.4(b) shows the (110) XRD pole figure of a Cr thin film deposited with a N_2 partial pressure of $3.6 \cdot 10^{-6}$ mbar. For this N_2 partial pressure, no change in preferential out-of-plane alignment is observed with the XRD angular scans. However, the addition of a tiny amount of N_2 causes a change in in-plane alignment. Four distinct poles are observed, but in comparison to the case without impurities, the position of the poles has changed to $\phi = 0° \pm n \cdot 90°$. Because the poles are situated at $\chi \approx 45°$, the [100] out-of-plane alignment is confirmed.
When the Cr thin film is deposited with $1.5 \cdot 10^{-5}$ mbar N_2, a clear in-plane alignment is observed, like visible in the (200) XRD pole figure in Fig. 6.4(c).[4] Three distinct poles are observed at a position $\phi = 0° \pm n \cdot 120°$. Hence, one of the poles is oriented towards the incoming material flux. With this nitrogen concentration, the Cr thin film exhibits a [111] out-of-plane orientation. This is confirmed by the threefold symmetry and position of the poles at an $\chi \approx 50°$, which is close to the angle between the (111) and (200) planes (i.e. 55°).
For a N_2 partial pressure of $7 \cdot 10^{-5}$ mbar N_2, the pole figure has an uniform intensity distribution, indicating a random in-plane alignment (Fig. 6.4(d)). This is not really surprising because for this N_2 concentration, also a random out-of-plane alignment is observed.

Also Cr thin films are deposited on a non-tilted substrate with codeposition of different N_2 impurity concentrations. This series has not been repeated for O_2 because similar results are expected as for N_2. The Cr thin films exhibit only a preferential out-of-plane orientation. Also change in out-of-plane orientation is observed, similar to the deposition series carried out on a tilted substrate. The out-of-plane alignment changes from preferential [100] to preferential [111] out-of-plane alignment with increasing N_2 partial pressure. The change to a [111] out-of-plane

[4] Because the angle between the (111) plane and (110) planes is about 35°, the poles in a (110) pole figure are close to the center and cause an overlap. Therefore an (200) pole figure is measured for the [111] out-of-plane oriented Cr thin films.

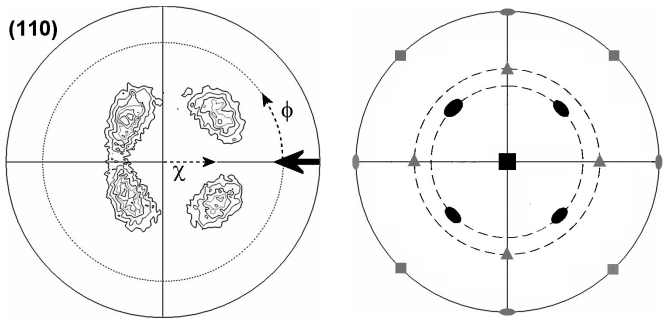

(a) Pure conditions: no deliberate codeposited N_2

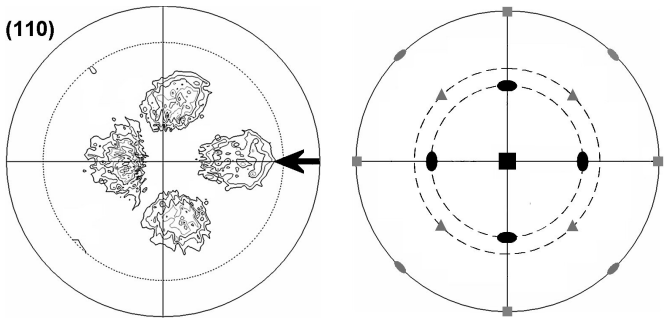

(b) Low Impurity Level: $3.6 \cdot 10^{-6}$ mbar N_2

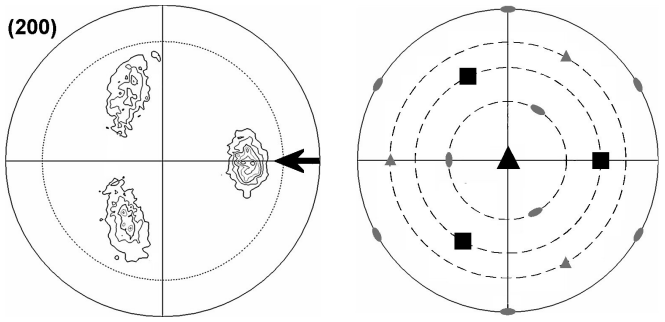

(c) Medium Impurity Level: $1.5 \cdot 10^{-5}$ mbar N_2

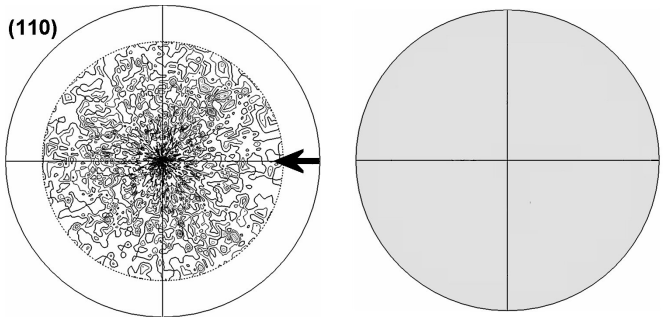

(d) High Impurity Level: $7.3 \cdot 10^{-5}$ mbar N_2

Figure 6.4: (110) and (200) XRD pole figures of biaxially aligned Cr thin films for four different impurity partial pressure (a) none, but the base pressure was about $1.0 \cdot 10^{-6}$ mbar, (b) $3.6 \cdot 10^{-6}$ mbar N_2, (c) $1.5 \cdot 10^{-5}$ mbar N_2, (d) $7.3 \cdot 10^{-5}$ mbar N_2. The direction of the incoming material flux is indicated by the arrow. ϕ is defined as the angle between this direction and direction between pole and centre. The stereographic projections belonging to the pole figures are also shown. The symbols that take into account the crystal symmetry, correspond to the following directions: ■ = [200]; ⬬ = [110]; ▲ = [111]

alignment occurs at about $1.5 \cdot 10^{-5}$ mbar N_2. At the highest partial pressures ($p(N_2) > 1 \cdot 10^{-4}$ mbar) a random orientation is observed. In comparison to the deposition carried out on a tilted substrate, the only difference is the higher N_2 partial pressure at which the texture change occurs. This is probably due to the higher deposition rate. On a tilted substrate, the deposition rate is typically 28 nm/min (Fig. 5.6(b)), while on a non-tilted substrate the deposition rate is typically 35 nm/min. Because of the higher deposition rate on a non-tilted substrate, more N_2 will be needed to obtain the same ratio in arriving N_2 versus arriving Cr adatoms.[5]

Not only the crystallographic texture changes with increasing impurity contamination, also the microstructure changes. The microstructure for the codeposition of both O_2 or N_2 is analyzed. Because the observations are similar, only the results for N_2 are shown. Fig. 6.5 shows the SEM plan views of the Cr thin films at four different N_2 concentration of Cr thin films grown on a non-tilted and tilted substrate. The SEM images of the biaxially aligned films correspond to the pole figures shown in Fig. 6.4.
Without the addition of N_2, both films are composed of grains with a clear faceted structure (Fig. 6.5(a)). In chapter 4, it has been discussed that the grains are limited by an {110} crystal habit. For the Cr thin film deposited on a tilted substrate, the edge of the habit points towards the incoming material flux, indicating a strong in-plane alignment.
When a small amount of N_2 is added during deposition, the Cr thin film still exhibits an [100] out-of-plane orientation. The SEM plan views of such Cr thin films are shown in Fig. 6.5(b). On a non-tilted substrate, the Cr thin film is composed of grains which are limited by a flat surface. Because the surface is parallel to the substrate, the surfaces correspond to the (100) planes. For the biaxially aligned thin films, a terrace-like structure is observed. These terraces are constructed by piling up several (100) planes. This terrace-like structure is schematically shown in Fig. 6.5(b).
Increasing the N_2 partial pressure further, the crystallographic orientation changes to a preferential [111] out-of-plane orientation. The corresponding topography of these Cr thin films is shown in Fig. 6.5(c). On a non-tilted substrate, it is observed that the thin film is composed of grains which are faceted by a crystal habit with a threefold symmetry. This crystal habit corresponds to a tetrahedron which is limited by {100} planes and is schematically shown in Fig. 6.5(c). On a tilted substrate, no uniform crystal habit is observed, but a thin film surface exhibits a scale like structure.
For the highest N_2 partial pressures, i.e. the pressure for which no preferential orientation is observed, SEM plan view shows a cauliflower structure, both for the depositions carried out on a non-tilted and tilted substrate (Fig. 6.5(d)).

Fig. 6.6 shows TEM cross sections of the Cr thin film grown on an inclined substrate for three different N_2 concentrations. Fig. 6.6(a) corresponds to the case where no N_2 is added deliberately. Fig. 6.6(b) corresponds to the case where $3.6 \cdot 10^{-6}$ mbar N_2 is added. For this N_2 partial pressure, the Cr thin film exhibits an [100] out-of-plane orientation and a terrace-like structure. Fig. 6.6(c) corresponds to the case where $1.5 \cdot 10^{-6}$ mbar N_2 is added and for which the Cr thin film has an [111] out-of-plane orientation and a scale like structure.
The TEM cross sections show that the Cr thin film exhibit a columnar structure for the three

[5] The ratio in deposition rate is $35/28 = 1.25$. This is in the same range as the ratio in N_2 partial pressures: $1.5 \cdot 10^{-5}/1.0 \cdot 10^{-5} = 1.5$ (Hereby, the lowest N_2 partial pressure is used for which an [111] out-of-plane alignment is observed.)

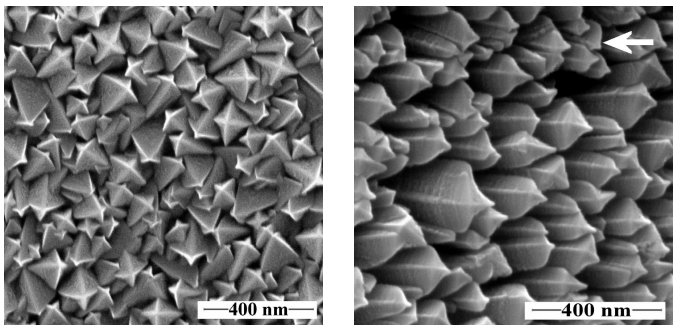

(a) Pure conditions: no N_2 deliberately added

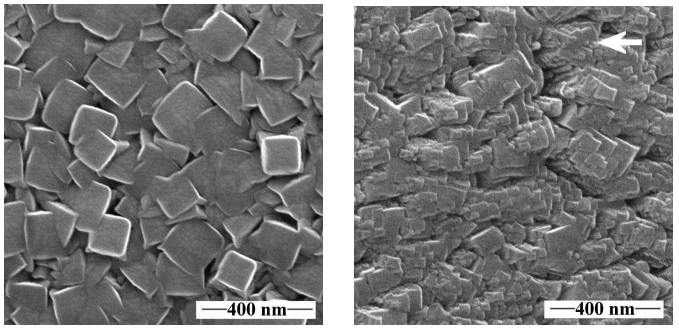

(b) Low Impurity Level

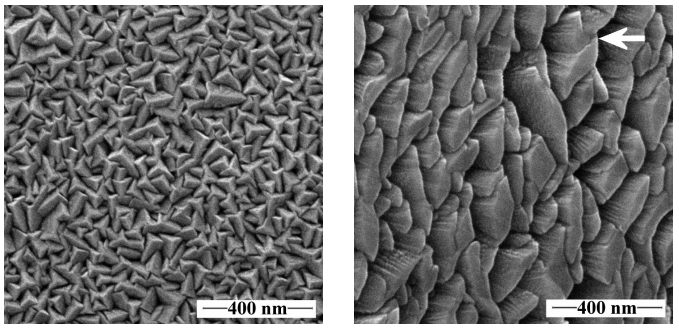

(c) Medium Impurity Level

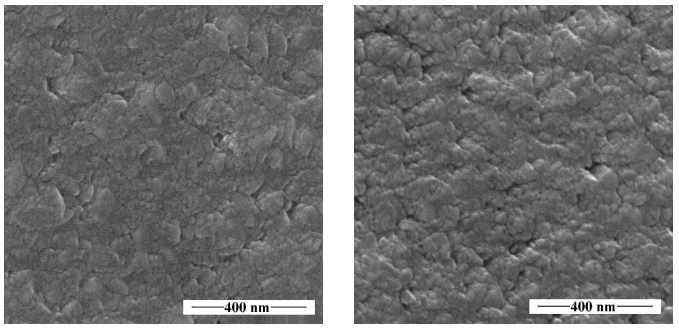

(d) High Impurity Level

Figure 6.5: SEM plan view of Cr thin films deposited at four different levels of N_2 contamination. (*left*) SEM of Cr thin films grown on a non-tilted substrate ; (*middle*) SEM of Cr thin films grown on a tilted substrate ; (*right*) the observed crystal habit. The subdivisions corresponds to Cr thin films deposited with different N_2 concentrations. (*on a non-tilted substrate*): (a) no N_2 deliberately added, (b) $5.0 \cdot 10^{-6}$ mbar N_2, (c) $4.0 \cdot 10^{-5}$ mbar N_2, (d) $2.0 \cdot 10^{-4}$ mbar N_2. (*on a tilted substrate*): (a) no N_2 deliberately added, (b) $3.6 \cdot 10^{-6}$ mbar N_2, (c) $1.5 \cdot 10^{-5}$ mbar N_2, (d) $7.3 \cdot 10^{-5}$ mbar N_2.

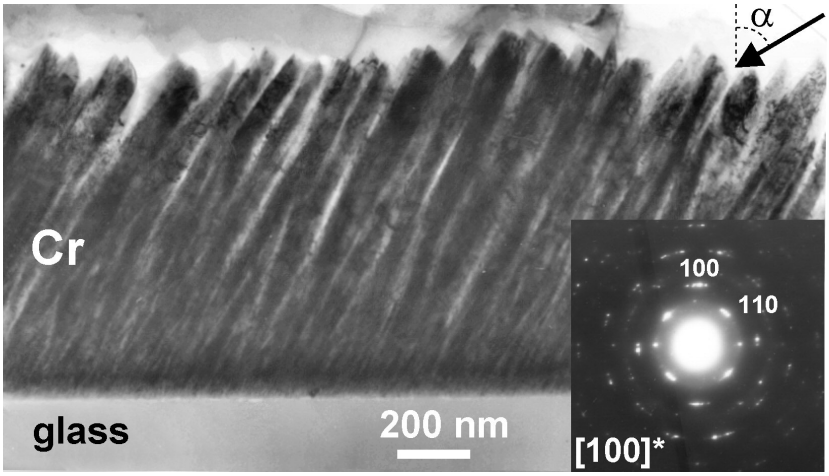

(a) Pure Conditions: no N_2 deliberately added

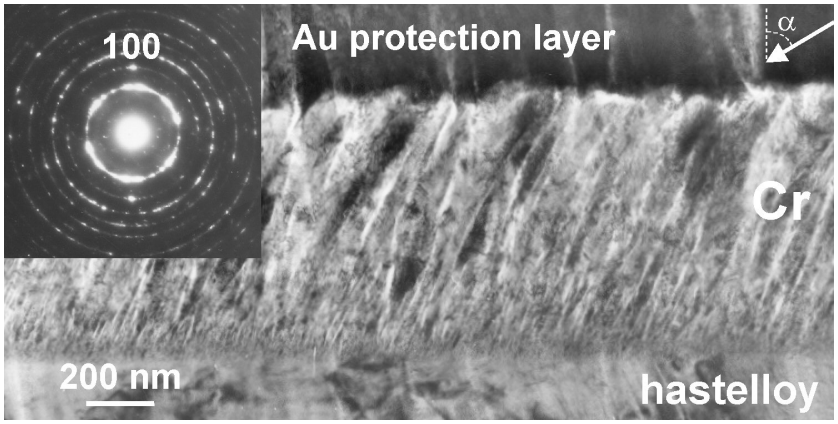

(b) Low Impurity Level: $3.6 \cdot 10^{-6}$ mbar N_2

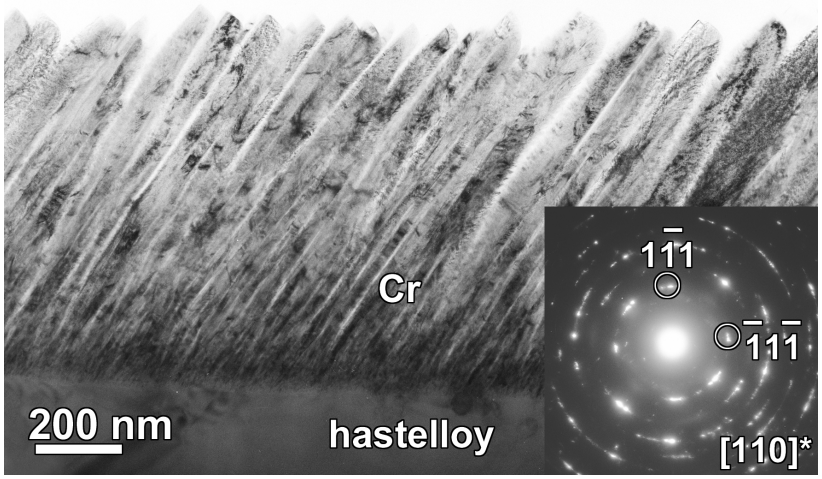

(c) Medium Impurity Level $1.5 \cdot 10^{-5}$ mbar N_2

Figure 6.6: TEM Cross section of biaxially aligned Cr thin films deposited on an inclined substrate. The thin films are growth with various impurity concentrations (a) no N_2 deliberately added; (b) $3.6 \cdot 10^{-6}$ mbar N_2; (c) $1.5 \cdot 10^{-5}$ mbar N_2. The arrow indicates the direction of the incoming material flux.

different N_2 partial pressures. Hereby, the columns are tilted towards the flux. There is no considerable change in columnar tilt between the different Cr thin films. In all thin films, it is observed that small grains nucleate at the substrate. As the growth proceeds, some grains are overgrown by others, resulting in a V-shaped columnar growth. The ED patterns confirm the XRD observations. Without impurities or at a low impurity level, the film is preferentially [100] out-of-plane oriented, while a medium impurity level the Cr thin film is [111] out-of-plane oriented.

In the description of the experimental observation, it becomes clear that the growth of Cr thin films with codeposition of N_2 or O_2 can be subdivided into four classes, depending on the amount of impurity gas added during deposition. These classes are indicated on Fig. 6.3 and mentioned on the other figures. An overview of these classes is given in table 6.1.
In the first class, no impurity gas is added deliberately during deposition. Incorporation of residual gases originating from an $1 \cdot 10^{-6}$ mbar base pressure still occurs. However, because the experimental results are consistent to the proposed model (Chapter 4), it is acceptable that the growth can proceed without being disrupted by impurities. An indication that this isn't completely true and the growth is slightly hindered, will be demonstrate later on. So it is obvious to call this class *Pure Conditions*. In pure conditions, the Cr thin film exhibits an [100] out-of-plane orientation. A strong in-plane alignment is observed with the (110) pole is positioned at an angle $\phi = 45°$ with respect to the incoming material flux. A columnar structure is observed, whereby the top of columns is truncated by an {110} crystal habit.
The second class is referred to as the *Low Impurity Level*. In this class, a small amount of impurities is added during the deposition of Cr thin film. The concentration is too low to cause a change in out-of-plane orientation, hence the Cr thin film has an [100] out-of-plane orientation. However, the in-plane orientation does change. The (110) poles are rotated by 45°, through which one of the poles faces the incoming material flux. Also the microstructure changes and a terrace-like structure is observed. Hereby, the terraces correspond to the (100) planes.
At higher impurity concentrations, the texture changes to an [111] out-of-plane orientation. This third class where an [111] out-of-plane alignment is observed, is called the *Medium Impurity Level*. In this class, also the in-plane alignment changes. Hereby, one of the (200) poles faces the incoming material flux. With the change in crystallographic texture, also the microstructure change. On a non-tilted substrate, grains are faceted by an {100} crystal habit, while on a tilted substrate, a scale like structure is observed.
The fourth class corresponds to the highest impurity concentrations and it is logical to call this class the *High Impurity Level*. In this class, the Cr thin film exhibit a random out-of-plane and in-plane orientation. Additionally, a cauliflower structure is observed.

	Out-of-plane	In-Plane	Faceting	Limit
Influence of N_2 on Cr thin film deposited on a tilted substrate				
Pure	[100]	(110) pole at $\phi = 45°$	{110} crystal habit	p(base) $< 1.0 \cdot 10^{-6}$ mbar
Low	[100]	(110) pole at $\phi = 0°$	(100) terraces	$p(N_2) < 7.0 \cdot 10^{-6}$ mbar
Medium	[111]	(200) pole at $\phi = 0°$	Scale like structure	$p(N_2) < 5.0 \cdot 10^{-5}$ mbar
High	Random	Random	Cauliflower structure	$p(N_2) > 5.0 \cdot 10^{-5}$ mbar
Influence of O_2 on Cr thin film deposited on a tilted substrate				
Pure	[100]	(110) pole at $\phi = 45°$	{110} crystal habit	p(base) $< 1.0 \cdot 10^{-6}$ mbar
Low	[100]	(110) pole at $\phi = 0°$	(100) terraces	$p(O_2) < 2.5 \cdot 10^{-5}$ mbar
Medium	[111]	(200) pole at $\phi = 0°$	Scale like structure	$p(O_2) < 5.0 \cdot 10^{-5}$ mbar
High	Random	Random	Cauliflower structure	$p(O_2) > 5.0 \cdot 10^{-5}$ mbar
Influence of N_2 on Cr thin film deposited on a non-tilted substrate				
Pure	[100]	Random	{110} crystal habit	p(base) $< 1.0 \cdot 10^{-6}$ mbar
Low	[100]	Random	(100) plane	$p(N_2) < 1.5 \cdot 10^{-5}$ mbar
Medium	[111]	Random	{100} crystal habit	$p(N_2) < 1.0 \cdot 10^{-4}$ mbar
High	Random	Random	Cauliflower structure	$p(N_2) > 1.0 \cdot 10^{-4}$ mbar

Table 6.1: Overview of the out-of-plane alignment, in-plane alignment and microstructure of Cr thin films deposited on an inclined substrate with various N_2 and O_2 partial pressures. For N_2, also Cr thin films are deposited on a non-tilted substrate

6.3 Growth Model for Texture Change in Cr Thin Film

The columns of the Cr thin films which are grown at the various impurity concentrations (pure conditions, low and medium impurity level) are V-shaped (Fig. 6.6), which suggests a competitive growth of neighbouring grains, hence an overgrowth mechanism. Additionally, it can be seen on the SEM images (Fig. 6.5), the grains in the Cr thin film grow according to a specific crystal habit. These two observations are characteristic for Zone T growth. At a high impurity level, the random crystallographic orientation and the cauliflower structure indicate a zone III structure.
Hence, the codeposition of N_2 or O_2 during the growth Cr thin films causes a transition from zone T to zone III, whereby the transition occurs at rather high impurity concentrations.
For metals, it is known that the diffusion barriers are much lower than the diffusion barriers of their corresponding oxide or nitride. This implies that O_2 and N_2 will always act as an inhibitor in a metallic system. Because O_2 and N_2 are inhibitors during the growth of Cr thin films, the transition in zones can be defined as a path on the revised structure zone model (Fig. 6.2(b)). Because of the transition from zone T to zone III, it can be concluded that the path corresponding to line 2 is followed when codepositing O_2 or N_2 during the growth of Cr thin films.

Because the Cr thin films exhibit a zone T structure in the first three impurity classes and because a change in microstructure and crystallographic texture is observed, it is likely that O_2 and N_2 affect the growth processes strongly but not enough to interrupt the structure evolution of zone T. As concluded in previous chapters, the structure evolution in zone T depends entirely on the crystal habit. Grains of which the facets of the crystal habit have the largest tilt angle, will have the largest perpendicular growth rate, overgrow the other grains and determine the out-of-plane orientation. Depending on the in-plane orientation of the good out-of-plane oriented grains, some grains capture more diffusing adatoms, hence grow faster, so overgrow the others and determine the in-plane orientation.
If for some reason the crystal habit changes, a different geometric fastest growth direction as well as a different capture length will be obtained. This will result in a change in biaxial alignment. It has been discussed extensively that the crystal habit is formed by facets with the lowest normal growth rate. So, a change in the crystal habit will be due to a change in relative growth rate of the various crystallographic planes.
In our experiments, a change in microstructure is observed with an increasing N_2 or O_2 partial pressure. Hence, in order to clarify the influence of N_2 and O_2 on the growth of Cr thin films, the influence of these impurities on the growth rate of the crystallographic planes has to be investigated.

6.3.1 Impurities and Their Relation to the Growth Rate of Planes

The Effects of Impurities

When impurities are adsorbed on certain crystallographic planes, they will influence the thermodynamic properties as well as the kinetic properties of that plane [5]. With the thermodynamic properties, it is meant that the impurities will change the surface free energy γ of the crystallographic plane. The kinetic properties are related to the growth rate of the various crystallographic planes. Mostly, the impurities will change the growth rate of all crystallographic planes, however the magnitude of its impact will be plane-dependent.

The influence of the impurities on the growth mechanism will also depend on the impurity mobility with respect to the mobility of the diffusing adatoms. If the impurities are mobile, they are able to diffuse on the surface and reach steps or kinks where they can be incorporated. Particularly, these impurities influence the growth rate of the step (or the step progression). If the impurity is immobile (i.e. the impurity mobility is much lower than the step progression), the impurity is considered to be adsorbed on the site of impingement, mostly on a surface terrace.

First consider the case with a low concentration of impurities, i.e. the number of adsorbed impurities is much lower than the number or adsorbed adatoms. When an advancing growth step contacts an impurity, it tends to curl around the impurity [6]. At low impurity concentrations, the immobile impurity will be incapsuled by the growth step and will have a minor influence on the growth rate, hence the thin film growth. Only a change in thermodynamic properties will occur. In case of a mobile impurity, the impurity is rolled with the growth step. As the growth step progresses, more impurities are swept up and the impurity concentration in front of the growth step increases [7]. As the number of impurities gradually increases, nucleation of an impurity phase can occur. This process is illustrated in Fig. 6.7. Most likely, this impurity phase will have a different growth rate. As a result, the step progression will alter. Hence, in case of a low

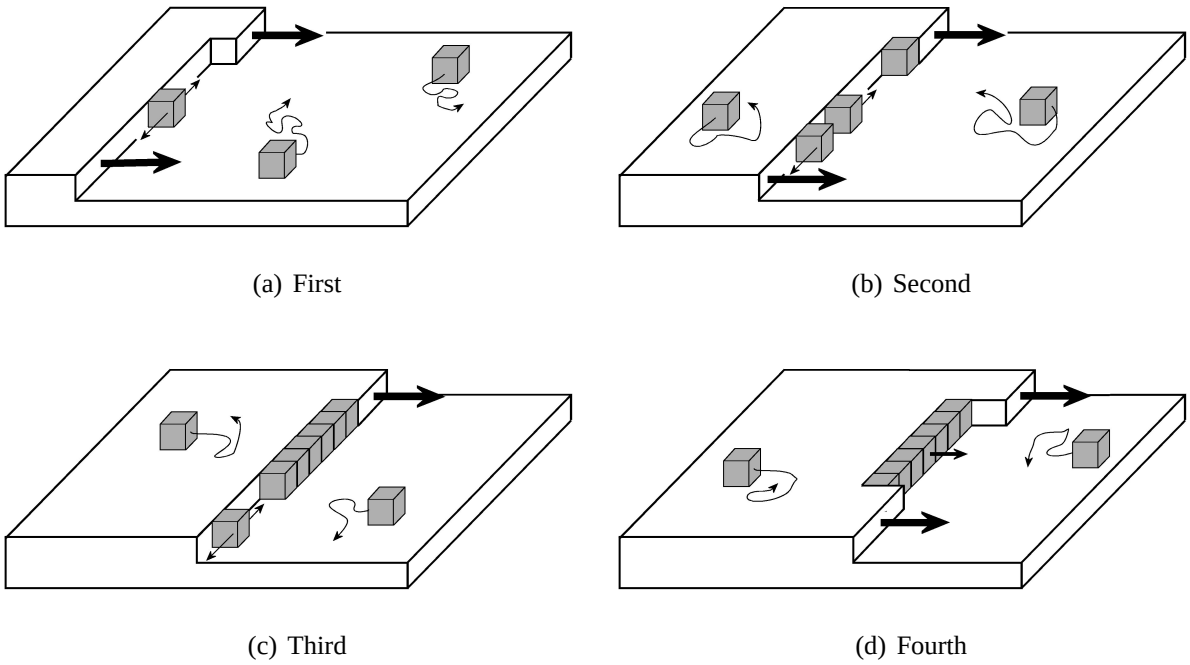

(a) First (b) Second

(c) Third (d) Fourth

Figure 6.7: Growth of a step in presence of mobile impurities. There is a continuous supply of metallic adatoms (not shown) and impurities (black cubes) whereby the impurity concentration is much lower than the concentration of metallic adatoms. Due the incorporation of metallic adatoms at the step, the growth step proceeds. Also, more and more impurities are accumulated at the step edge (b). At a specific critical concentration, an impurity phase may form at the step edge (c). Most likely, the growth rate of the impurity phase will be different from the pure phase, through which a different structure will evolve (d). On the impurity phase, a new pure metallic phase may nucleate.

concentration of mobile impurities, the kinetic properties are mainly affected. For instance, in case of an inhibitor, the impurity will slow down the forward advancement of steps [8, 9, 10, 11].

When the impurity concentration is high, both mobile as immobile impurities will influence the kinetics and modify the step progression. Two phenomena can occur. Firstly, an uniform two dimensional impurity layer may form. Because the condition of the growing surface changes due to the impurity layer, a change in growth rate of the various crystallographic planes will be expected. This 2D layer is also known as a tissue phase. The driving force for the formation of a tissue phase is comparable to the layer-by-layer growth or Frank - Van der Merwe (FM) growth mode (Sect. 1.4.4). If the surface free energy of the impurity (or impurity compound) is lower than the surface free energy of the pure film, it will be more favourable to wet the surface.
Secondly, if no tissue phase is formed, three dimensional clusters could evolve. The clusters interrupt the growth of some parts of the surface, whereas other parts can grow uninterrupted. On the part which grows uninterrupted, impurities can also be present, however their concentration is too low to modify the growth. Due to the difference is in growth rate between the 3D (or volume) impurity phase and the uninterrupted growth surface, hillocks will be formed on the surface which is covered with 3D impurity phases. In addition to a change in growth rate due to a change in step progression, these hillocks will change the growth of a crystallographic plane even more.

It can be concluded that impurities will change the growth of a crystal plane. Because the interaction of the impurity on a crystal plane will depend on the specific crystallographic plane, it is possible that the mutual relative growth rate of the crystallographic planes will diverge. It could occur that in the presence of impurities another crystallographic plane will have the lowest growth rate. Since the crystal habit is determined by facets with the lowest growth rate, the crystal habit of a specific material may change in the presence of impurities. Because of a change in crystal habit (and so morphology), the impurities can lead to a change in crystallographic orientation.

Impurity Concentration in Cr Thin Films

To determine which mechanism influences the growth, the impurity concentration should be known. Therefore, the number of impurities in the deposition system is calculated. In section 6.2.2, the results are discussed in terms of the N_2 and O_2 partial pressure. For example, the transition from a preferential [100] to [111] out-of-plane alignment occurs for N_2 at $7.0 \cdot 10^{-6}$ mbar N_2 and for O_2 at $2.5 \cdot 10^{-5}$ mbar O_2. Using the kinetic theory of gases [12], the impingement rate at which the gas molecules impinge on a surface can be calculated from the partial pressure. An impingement rate of $2.0 \cdot 10^{15}$ atoms N_2/cm^2s and $3.8 \cdot 10^{15}$ O_2/cm^2s is obtained for N_2 and O_2 respectively.
However, not the absolute impurity concentration is of importance, but the relative impurity concentration in proportion to the number of metallic Cr. Typically, a deposition rate of about 28 nm/min is obtained (Fig. 5.6(b)). With this deposition rate, about $4 \cdot 10^{15}$ atoms Cr/cm^2s are adsorbed.[6] Hence, at these pressures, the number of adsorbed Cr adatoms is in the same order of the impurity impingement rate.

[6] Hereby, the porosity of the Cr thin film is not taken into account.

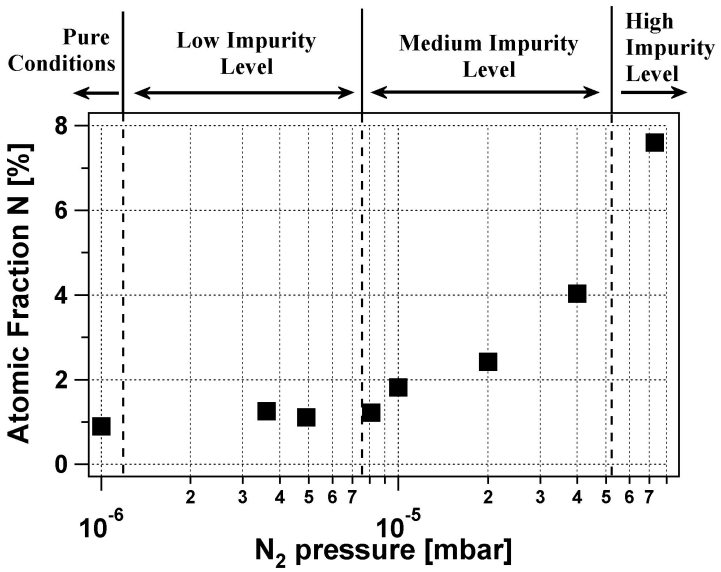

Figure 6.8: The atomic fraction of nitrogen in the Cr thin film as a function of the N_2 partial pressure measured by XPS.

Although a comparable number of impurities impinge on the substrate, it is unlikely that all the impurities will take part in the growth and so influence the growth of the Cr thin film. Therefore, more attention will be paid to the fraction of impurities that is incorporated into the Cr thin film. In the XRD spectra, no chromium oxide nor chromium nitride peaks are observed, which indicates that no crystalline compound is formed. However, XRD isn't sensitive to small concentrations of a crystalline compound. If a small 3D impurity compound or an 2D tissue phase is formed or the impurity compound is amorphous, it will not contribute in a XRD angular scan. Therefore, to obtain information about the impurities concentration in the Cr thin films, XPS measurements are performed.

Fig. 6.8 shows the atomic fraction of nitrogen in the Cr thin film measured by XPS as a function of the N_2 partial pressure during deposition. At a low N_2 partial pressure ($p(N_2) < 7.0 \cdot 10^{-6}$ mbar), no variation of the atomic fraction of nitrogen in the Cr thin film is observed. However, because the observed nitrogen XPS peak is rather small (it can hardly been distinguished from the background) and the XPS equipment has a sensitivity of about 0.5 atomic percent, no exact concentration can be determined.[7] So, no conclusions can be drawn for these N_2 partial pressures, except that the atomic nitrogen concentration is below 2%. This is important because although the impurity concentration is below the XPS detection limit, a major influence on the growth of the Cr thin film is observed.

For partial pressures above $7.0 \cdot 10^{-6}$ mbar, a gradual increase of incorporated nitrogen in the Cr thin film is observed with increasing N_2 partial pressure. At a partial pressure of $1 \cdot 10^{-5}$ mbar N_2, i.e. about the pressure at which the Cr thin film exhibits an [111] out-of-plane orientation, the atomic concentration of nitrogen in the Cr thin film is about 2%. Above $5 \cdot 10^{-5}$ mbar N_2, i.e. the pressure at which a random orientation is observed, the nitrogen atomic concentration is higher

[7] No exact error bars are determined, however an error of 1 atomic percent is reasonable.

than 5%. It can be concluded that only a small fraction of the impinging N_2 is incorporated into the growing Cr thin film. This suggests a low sticking of N_2 on Cr. The sticking coefficient can be calculated from the atomic fraction nitrogen in the Cr thin film and the N_2 impingment rate. The sticking coefficient is about $7 \cdot 10^{-3}$.
XPS measurements for the Cr thin films with codeposited O_2 are also performed, however, no usefull data could be obtained. This is due to a native oxide which is formed on the Cr thin film surface. Although the XPS spectra are measured after sputtering away the first 20 nm to remove this native oxide layer, it was insufficient to remove the native oxide completely. This could also explain the rather low sticking coefficient of nitrogen on Cr. It is possible that after deposition the nitride phase has transformed to a more stable oxide phase (native oxide). As a result, the nitrogen concentration in Cr will be reduced. Hence, the atomic fraction nitrogen measured with XPS will be a lower limit.

With XPS, no crystalline information (crystalline or amorphous) about the impurity or impurity compound in the Cr thin film can be obtained. In order to clarify this, TEM measurements are performed. Fig. 6.9(a) shows the electron diffraction ring pattern of a Cr thin film codeposited with $4.0 \cdot 10^{-5}$ mbar O_2 (i.e. at medium impurity level). The ED pattern is taken from a TEM cross sectional view perpendicular to the incoming vapour flux (this is different from Fig. 6.6). On the ED pattern, several diffraction rings and spots are visible. The corresponding d-values of the several diffraction rings are given in Table 6.2. Some of the d-values are also indicated on the diffraction pattern. When comparing the experimental d-values to the theoretical d-values of Cr, the most intens diffraction spots correspond to the metallic Cr (Fig. 6.9(a)). In addition to the diffraction spots belonging to pure Cr, a lot of other diffraction spots are observed. For example, d_{110} is the highest d-value for pure Cr. All spots which are observed closer to the central spot, have a higher d-value and correspond to another crystalline structure. From Table 6.2 and Fig. 6.9(a), it is obvious that the experimental d-values coincide with the d-values of Cr_2O_3. Hence, it can be concluded that the codeposited O_2 forms a crystalline compound in the Cr thin film. Similar diffraction patterns are obtained at other impurity concentrations. Even in the Cr thin film deposited without deliberately added O_2, weak diffraction spots belonging to a Cr_2O_3 phase can be observed (not shown).

Experiment	Cr		Cr_2O_3	
d [Å]	(hkl)	d [Å]	(hkl)	d [Å]
3.61			(012)	3.6313
2.56			(104)	2.6653
2.47			(110)	2.4797
2.03	(110)	2.0390	(202)	2.0477
1.80			(204)	1.8152
1.67			(116)	1.6724
1.47	(200)	1.4419	(214)	1.4649
1.17			(312)	1.1731

Table 6.2: Measured d-values of the diffraction spots of the ED pattern in Fig. 6.9(a). These values are compared to the values found in literature for Cr and Cr_2O_3.

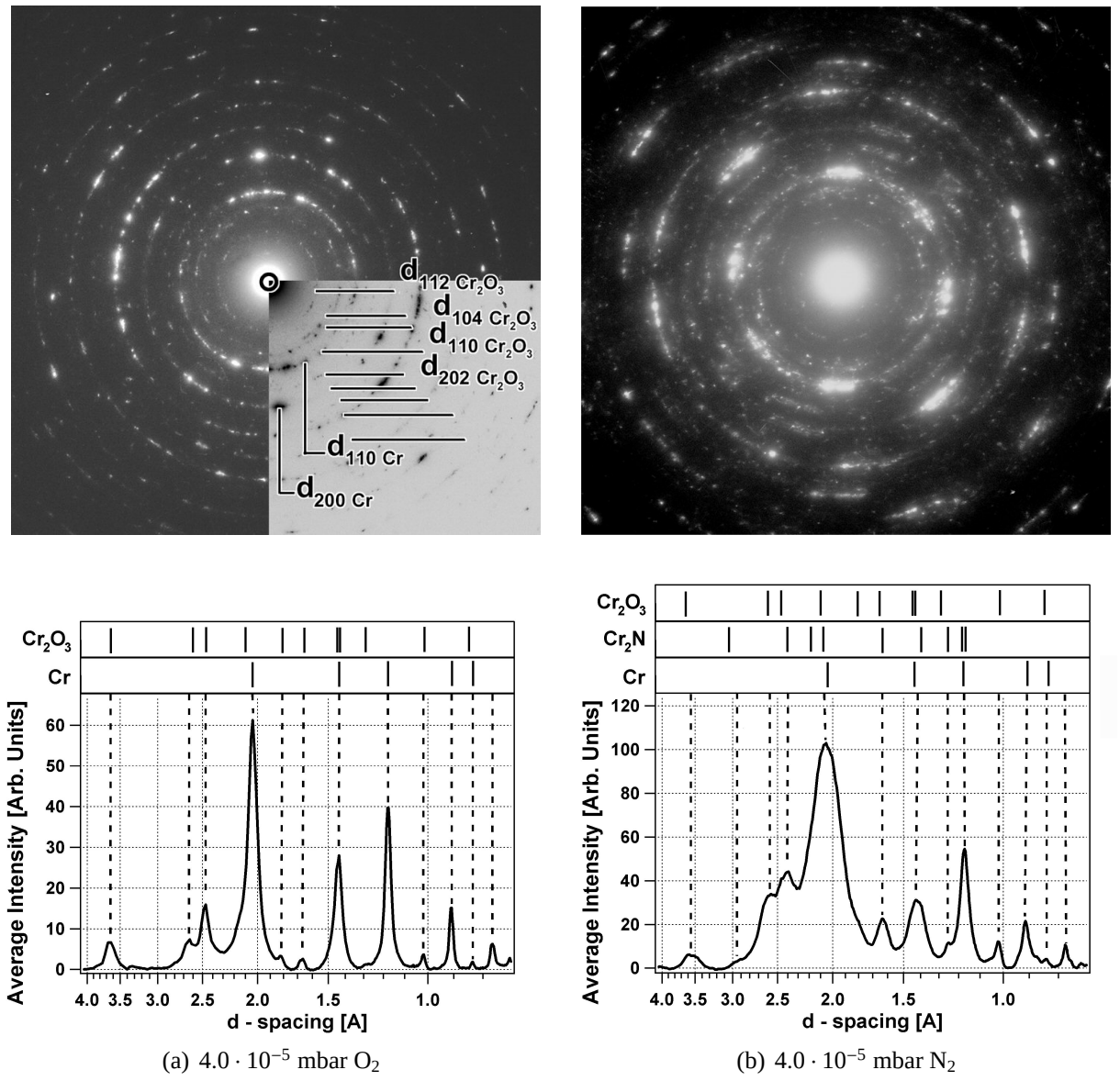

(a) $4.0 \cdot 10^{-5}$ mbar O_2 (b) $4.0 \cdot 10^{-5}$ mbar N_2

Figure 6.9: (*top*) Electron Diffraction pattern of biaxially aligned Cr thin films grown at medium impurity level of (a) O_2 and (b) N_2. Only the most intens peaks are indicated for Cr_2O_3 and Cr_2N. The intensity of the other spots was too low to be observed. (*bottom*) Average intensity over a circle on the electron diffraction pattern as a function of the d-value (i.e. $\sim$ R with R the radius of the circle) [13]. Both patterns show the presence of a crystalline impurity phase.

Also for N_2 codeposition, a lot of diffraction spots are observed in addition to the Cr diffraction spots (Fig. 6.9(b)). The Cr-N phase could be indexed as Cr_2N. In addition to Cr_2N diffraction spots, some spots could be indexed as a Cr_2O_3 phase. This can be attributed to the presence of H_2O during the deposition which originates from the residual gases and/or to the reaction by exposure to the ambient.

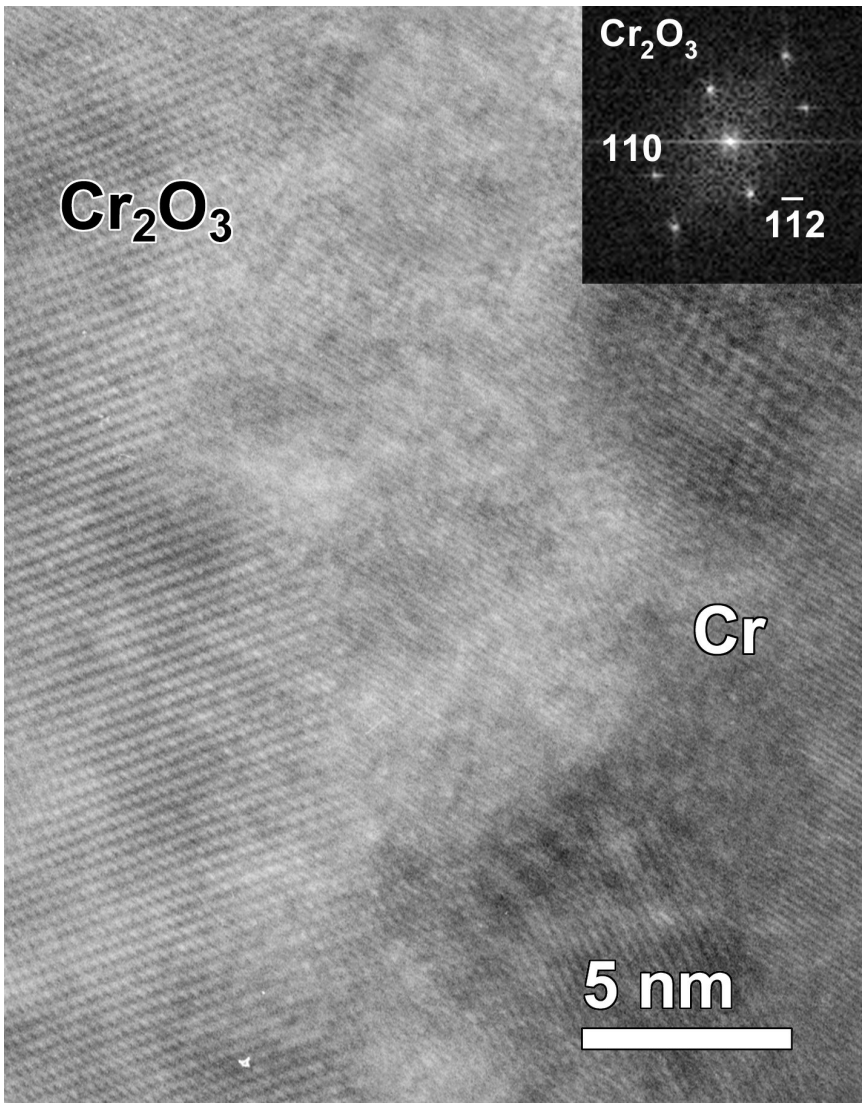

Figure 6.10: High Resolution TEM image of a biaxially aligned Cr thin film grown with $4 \cdot 10^{-5}$ mbar O_2. Two crystalline phases are observed. In the inset, a Fourier transform of the Cr_2O_3 minority phase is shown. The HREM is taken from a TEM cross sectional view.

Impurity Phase

In the subsequent stage, it should be investigated whether a 2D tissue phase or a 3D impurity phase has developed because it is reasonable that the growth mechanism in the presence of an 2D phase or 3D phase is different.
Fig. 6.10 shows a HREM image of a biaxially aligned Cr thin film grown with O_2 impurities at a medium impurity level. The HREM image is obtained from the middle part of the Cr thin film from the TEM cross section. On the image, two crystalline phases can be distinguished. One of the crystalline phases correspond to pure Cr. The other phase corresponds to an uniform Cr_2O_3 lattice, as confirmed by the Fourier transform (inset). This Cr_2O_3 impurity phase is locally observed but throughout the complete film thickness such an impurity phase is found.

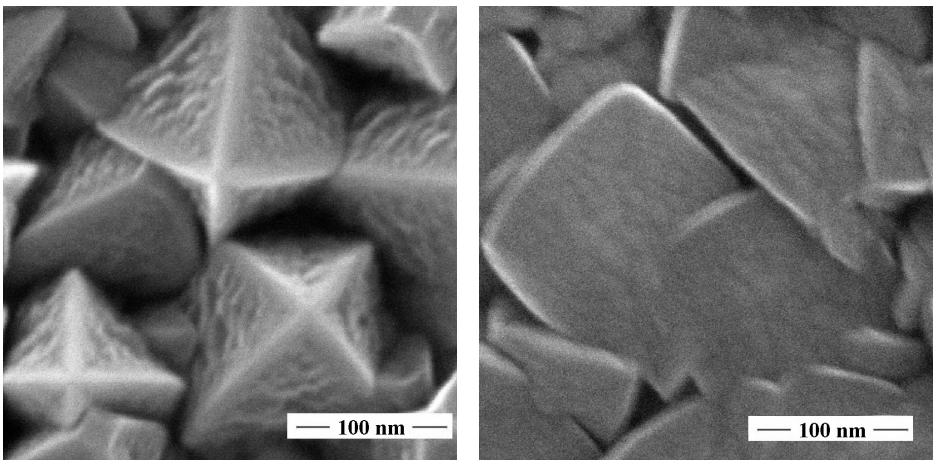

(a) Pure Conditions (b) Low Impurity Level

Figure 6.11: (a) SEM Plan View of an uniaxially aligned Cr thin film deposited in pure conditions. The base pressure was about $1 \cdot 10^{-6}$ mbar. (b) SEM Plan View of an uniaxially aligned Cr thin film deposited at low impurity level ($p(N_2) = 3.6 \cdot 10^{-6}$ mbar N_2)).

Because of the large dimension of the impurity phase (Fig. 6.10) it is reasonable that the impurity phase is three dimensional, rather than a 2D tissue phase. An additional indication of the existence of a 3D impurity phase is the formation of hillocks on the surface of specific crystallographic planes. Here, the impurity itself is not observed, but its influence on the growth. Fig. 6.11(a) shows a close-up of a grain from a Cr thin film deposited in pure conditions. In this class, the grains are faceted by a pyramid which corresponds to an {110} crystal habit. On the (110) planes, the formation of hillocks and irregularities can clearly be observed. As mentioned in paragraph 6.3.1, these hillocks point out the presence of an 3D impurity phase.
This observation indicates that the growth of the Cr thin film is not performed in pure conditions, even though the classification in the pure condition class suggests a pure film. However, in despite of the hillocks, the impurity concentration is too low to cause a change in structure evolution. And that's exactly what the pure condition class means: the impurity concentration is too low to change the structure of the thin film, although impurities are present and locally the growth can be hindered.

Growth Rate of the Crystallographic Planes

The hillocks which are formed on the (110) planes are a clear indication of the impurity incorporation during the growth. With increasing impurity concentration, more 3D impurity phases will be formed resulting in the increase in the number of hillocks. It is not inconceivable that at a specific impurity concentrations, the growth of the pure Cr crystalline phase on the (110) plane is hindered. Because the growth of the (110) planes is hindered, no crystal habit can be formed with {110} planes. Hence, the crystal habit will be determined by the planes with lowest growth rate which are not blocked by impurities.
Because an {100} crystal habit is observed at medium impurity level, we assume that the (100) planes will have the lowest normal growth rate of all the planes that grow without unhindered.

However, no conclusive explanation can be given because it is not possible to apply the reasoning as in pure conditions in which the number of nearest neighbours is calculated (Sect. 4.4.1). Even though the growth of some planes is not interrupted, yet its thermodynamic and kinetic properties will be influenced by the impurities. Furthermore, it is unlikely that these properties change in a similar way for the various planes.

As described above, the different behaviour of the impurities on the various crystallographic planes is at the basis of the change in crystal habit. Firstly, the relative growth rate of the planes will change due to the impurities and secondly, the impurity concentration at which the growth of the planes is hindered is different. Such an anisotropic behaviour is also found in other experiments. For instance, in surface oxidation experiments with Cr single crystals, it is noticed that the (110) surface is more reactive to oxygen than the (100) or (111) crystal faces [14, 15, 16]. Moreover, in the presence of O_2, the (110) surface reconstructs to a faceted structure of which the facets correspond to the less dense packed (100) planes.
Recently, Reichel et al. [17] calculated the interface energy between Cr substrate and a thin chromium oxide layer which is formed on top of Cr. They observed an anisotropy in interaction between differently oriented Cr substrates. The interaction is the strongest on the (110) planes while it's much less on (100) or (111) planes.
Also in this work, a different behaviour of impurities on the various planes of Cr is observed. Fig. 6.11(b) shows a magnification of the surface of some grains of an uniaxially aligned Cr thin film grown with the addition of N_2 at low impurity level. In the description of the experimental results, it has been discussed that the flat surface correspond to the (100) crystallographic planes (Table 6.1). As can be seen in Fig. 6.11(b) no hillocks are observed on the (100) surface. This indicates that no 3D impurity phase is formed on the (100) plane. This contrasts sharply with the (110) planes in pure conditions where the planes are covered with an impurity phase. In despite of the higher N_2 partial pressure during deposition, the growth of the (100) planes is less influenced by N_2 impurities. Because of the similarities between the influence of O_2 and N_2 on the growth of biaxially aligned Cr thin films (Table 6.1), the same behaviour is expected with the codeposition of O_2.

All these experiments point out that the (110) plane is influenced the most by the impurities, but there is no theory to confirm. A possibility is that the probability to incorporate nitrogen or oxygen at its surface can be higher for the (110) plane. This probability depends on the chemical reactivity of the surface and so depends on the number of dangling bonds [18]. For Cr, the (110) plane has the lowest number of dangling bonds (Section 4.4.1) through which the sticking of the impurities on this plane is expected to be low. However, this hypothesis is in contrast to the experimental observations.
Another explanation which is consistent with the experiments, arises from the anisotropy in packing density of the various crystallographic planes. This is proposed by Barna et al. who examined the growth of FCC Al in an O_2 atmosphere [19, 20]. They observed that oxygen penetrates into the crystal lattice of the (100) and (110) planes, but remains on top of the (111) plane. Hence, the impurity remains on top of the crystallographic plane with the highest packing density, which are the (111) plane in a FCC structure. When extrapolating this reasoning to a BCC structure, the impurities should remain on the (110) crystallographic planes, while penetrating into the crystal lattice of the (100) and (111) planes. This can be deduced from table 6.3 which summarizes the packing density of the various crystallographic planes for a FCC and

(hkl)	FCC [Atoms/a^2]	BCC [Atoms/a^2]
(100)	2	1
(110)	$\sqrt{2} \approx 1.414$	$\sqrt{2} \approx 1.414$
(111)	$4/\sqrt{3} \approx 2.309$	$1/\sqrt{3} \approx 0.577$

Table 6.3: The packing density of the (100), (110) and (111) crystallographic planes for a FCC and BCC structure. The packing density is defined as the number of atoms per a^2 where a is the lattice parameter.

BCC structure. If the impurities penetrate into the lattice, the growth on the surface will not be influenced largely. In contrast, when the impurities remain on the surface, an interaction between the impurities and the growing film is expected, changing the growth kinetics. According to our reasoning the impurities remain on the (110) planes, hence the growth will be influenced at first on the (110) plane. A fraction of impurities penetrate into the (100) and (111) plane, hence the growth will be influenced much later on the (100) and (111) planes. However, at higher impurity concentrations, the solubility limit will be reached and the growth of all planes will be hindered. At that point, it is expected that no zone T structure can develop.

6.3.2 Biaxial Alignment in Cr Thin Film Influenced by Impurities

In the previous section, the influence of the impurities on the growth processes is discussed. In this paragraph, the consequences for the structure evolution of the biaxially aligned Cr thin films is explained. The change in biaxial alignment is connected to the change in the growth processes. For this, each impurity class will be discussed separately. In the first three classes, the structure evolution will be based on an overgrowth mechanism because of a zone T growth. Hereby, the growth according to a specific crystal shape will be fundamental. In the discussion, the growth model for biaxially aligned thin films as given in chapter 4 will be used. Due to the similarity between O_2 and N_2, the discussion holds for both impurities and therefore no specification will be made in the discussion.

Pure Conditions

The growth of biaxially aligned thin films has been discussed in chapter 4. Grains grow according to their kinetical growth shape, which is determined by planes with the lowest normal growth rate. Without impurities, it has been discussed that the (110) planes have the lowest normal growth and so an {110} crystal habit will be observed.
Depending on the orientation of the grains, some grains will have a higher perpendicular growth rate. The grains for which the facets of the {110} crystal habit have the highest tilt angle, will have the highest perpendicular growth rate. The highest tilt angle is observed when the grains are [100] out-of-plane oriented. Hence, the [100] out-of-plane oriented grains will have the highest perpendicular growth rate and overgrow the others. As a result, the Cr thin film will exhibit an [100] out-of-plane orientation.
The in-plane orientation is caused by a difference in capture length of differently in-plane oriented grains. Grains which capture the most particles, grow faster than the others and overgrow the neighbouring grains. It has been calculated that grains with the edge of the {110} habit oriented

towards the flux, capture the most particles and overgrow the others. This is in correspondence with the experimental observation made with XRD, SEM and TEM.

Low Impurity Level

At low impurity level, the Cr thin films exhibit a preferential [100] out-of-plane alignment and an in-plane alignment whereby the (110) pole of the XRD pole figure is oriented towards the flux. On a non-tilted substrate, the grains are truncated by an (100) plane which is parallel to the substrate.
In the previous section (Sect. 6.3), it is shown that the growth of the (110) planes is hindered by the impurities before the growth of other crystallographic planes is hindered. Because the deposition is carried in zone T, another crystal habit should evolve, whereby the crystal habit is formed by the unhindered planes with the lowest normal growth rate. A preferential out-of-plane alignment would evolve because of the difference in perpendicular growth rate of differently oriented grains. It has been discussed in chapter 4, the orientation of the grains for which the facets have the highest tilt angle, will have the highest perpendicular growth rate and overgrow the others. However, this is in contrast with our experimental observations. Here, the (100) plane is parallel to the substrate. Hence, it is not obvious why the grains at low impurity level exhibit such a faceting.
In order to understand the structure evolution at low impurity level, the origin of the parallel (100) plane should be examined. Therefore, a Cr thin film is deposited in the transition region between the pure conditions and the low impurity level. Fig. 6.12 shows the SEM plan view of a Cr thin film deposited on a non-tilted substrate with an O_2 partial pressure of $3.0 \cdot 10^{-6}$ mbar. As can be seen, the top of the {110} crystal habit of several grains is cut off and this gives rise to the formation of an (100) plane on the top of the habit. This situation is schematically drawn in Fig. 6.12(b).

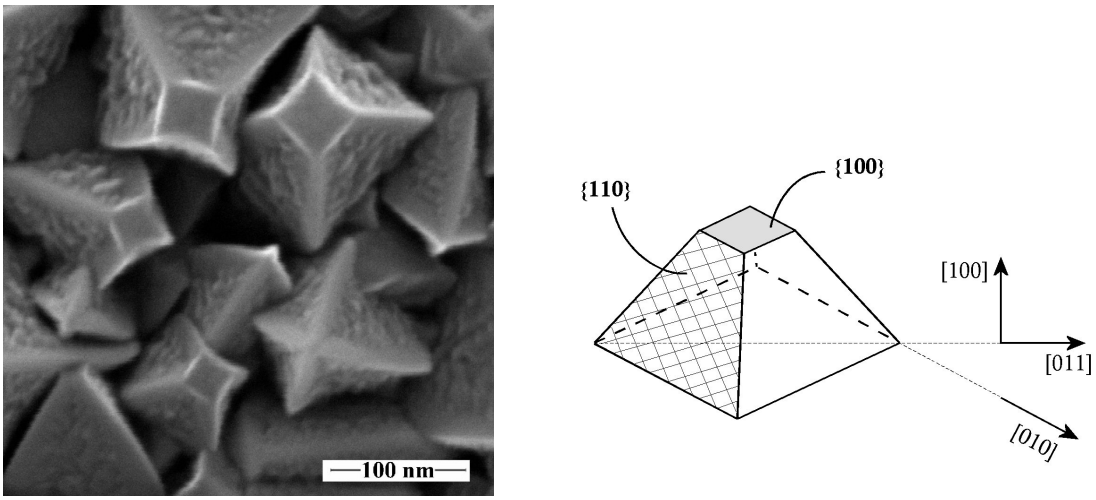

(a) (b)

Figure 6.12: (a) SEM Plan View of an uniaxially aligned Cr thin film, deposited with an O_2 partial pressure of $3.0 \cdot 10^{-6}$ mbar; (b) Schematic drawing of the observed growth shape.

The exact reason for the formation of such a structure is not clear, however, the following mechanism is proposed. Because an {110} crystal habit, or at least a part of it, is visible in the SEM plan view, the impurity concentration is at the initial stages of the growth too low to hinder the growth of the {110} crystal habit. During the growth, more and more impurities accumulate on {110} crystal habit due to continuous supply of impurities. Hereby, the impurity concentration will be the highest at the edges [21]. The growth of the {110} crystal habit can continue until a critical impurity concentration is reached. This point will be reached at first at the top of the crystal habit (three edges). As a result, the growth at the top will be interrupted. As the deposition continues, it is likely that a structure evolves which is less influence by the impurities. It is observed experimentally, that (100) planes will be formed on top of the {110} crystal habit. As long as the deposition proceeds, the surface of the (100) plane will increase because this plane can grow uninterrupted, while the (110) planes are hindered by the impurities. In this way, the complete thin film surface will be covered by (100) planes which are parallel to the substrate (Fig. 6.5(b)).
When the impurity concentration during the growth is increased, the (100) planes will be formed earlier on top of the {110} crystal habit and only grains faceted by (100) planes which are parallel to the substrate will be observed. This is observed experimentally.
Important is that initially an {110} crystal habit must form. If the growth of the (110) planes is hindered at the initial stages of the growth, the (100) would not be parallel to the substrate. Only at the later stages of the growth, the (100) are formed on top of the {110} habit. Hence, initially an out-of-plane alignment will evolve which is characteristic for an {110} crystal habit. This explains the [100] out-of-plane alignment.

On a tilted substrate, several (100) planes pile up and form a terrace-like structure. This microstructure as well as the preferential [100] out-of-plane alignment can be explained in analogy with the growth on a non-tilted substrate.
In addition, an in-plane alignment evolves on a tilted substrate. Because the deposition is carried out in zone T, it is plausible that the model for in-plane alignment is valid for Cr thin films deposited at low impurity level. According to the model, which is described in chapter 4, grains with the highest capture length overgrow the other grains and determine the in-plane alignment. To determine the capture length, the in-plane confinement of the (100) terraces has to be known. However, this confinement is not necessarily the same as for the {110} crystal habit or for truncated pyramid. This is illustrated in Fig. 6.13, which shows the evolution of a single grain grown at low impurity level. Initially, an {110} crystal habit evolve (*a*). In projection (or plan view), this corresponds to a square. Because of the (110) planes, the square is limited by [100] edges. On the top of the {110} crystal habit, an (100) plane will appear whereby the area of this plane will increase during further growth (*b*-*c*). As long as (110) planes are present, the grain in plan view will correspond to a square limited by [100] edges. However, once the grains is limited by a single (100) plane, the in-plane confinement of the grain is unclear because no (110) planes are present (*d*). Now, the confinement will be determined by the growth rate of the various steps. To know this confinement, TEM measurements are used. Fig. 6.14 is a TEM plan view image of a terrace-like grain. The electron diffraction pattern confirms the [100] out-of-plane orientation. From the position of (110) spots, it can be concluded that the {100} terraces are limited by [110] edges, resulting in a square shape. This is different from the case when the grains are limited by an {110} crystal habit. This situation is schematically drawn in Fig. 6.5.

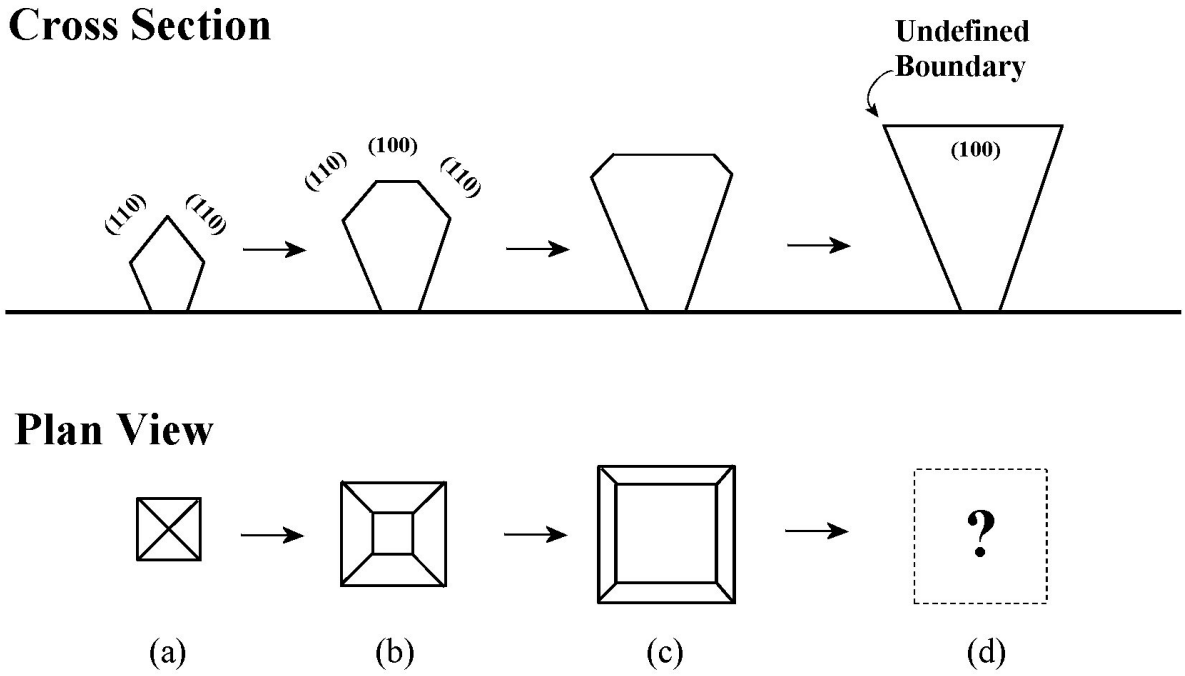

Figure 6.13: Schematic drawing of the evolution of a single grains at low impurity level. Both a cross sectional view and plan view are shown.

The calculations of the capture length of a square limited by [110] edges is similar to those of a square limited by [100] edges (i.e. in pure conditions). This is described in section 4.6.1. The capture length is at its maximum if the edges of the square are oriented towards the direction of the incoming material flux. When the square is limited by [110] edges, the capture length is at its maximum if the [110] steps have an angle of 45° with respect to the incoming material flux. In a pole figure, this would correspond with a (110) pole at $\phi = 45°$ and $\chi = 90°$.[8] This is experimentally confirmed if the measured (110) pole figure is compared to the stereographic projection (Fig. 6.4(b)). Hence, it can be concluded that the structure evolution at low impurity level is understood.

Medium Impurity Level

At a medium impurity concentration, the growth of an {110} crystal will hindered at the initial stages of the growth. Hence, another crystal habit will evolve whereby the crystal habit is composed of planes with the lowest normal growth rate which can grow unhindered. On a non-tilted substrate, the grains are faceted by an {100} crystal habit, probably because the (100) planes have the lowest normal growth rate. This has been discussed in a previous section (Sect. 6.3.1).
At medium impurity level, a change from an [100] to an [111] out-of-plane alignment is observed. Because the Cr thin film has a zone T structure, the evolution of the out-of-plane alignment will be entirely based on the crystal habit. In order to determine the out-of-plane alignment,

[8] $\chi = 90°$ because the [110] egdes are a part of the (100) planes that are parallel to the substrate.

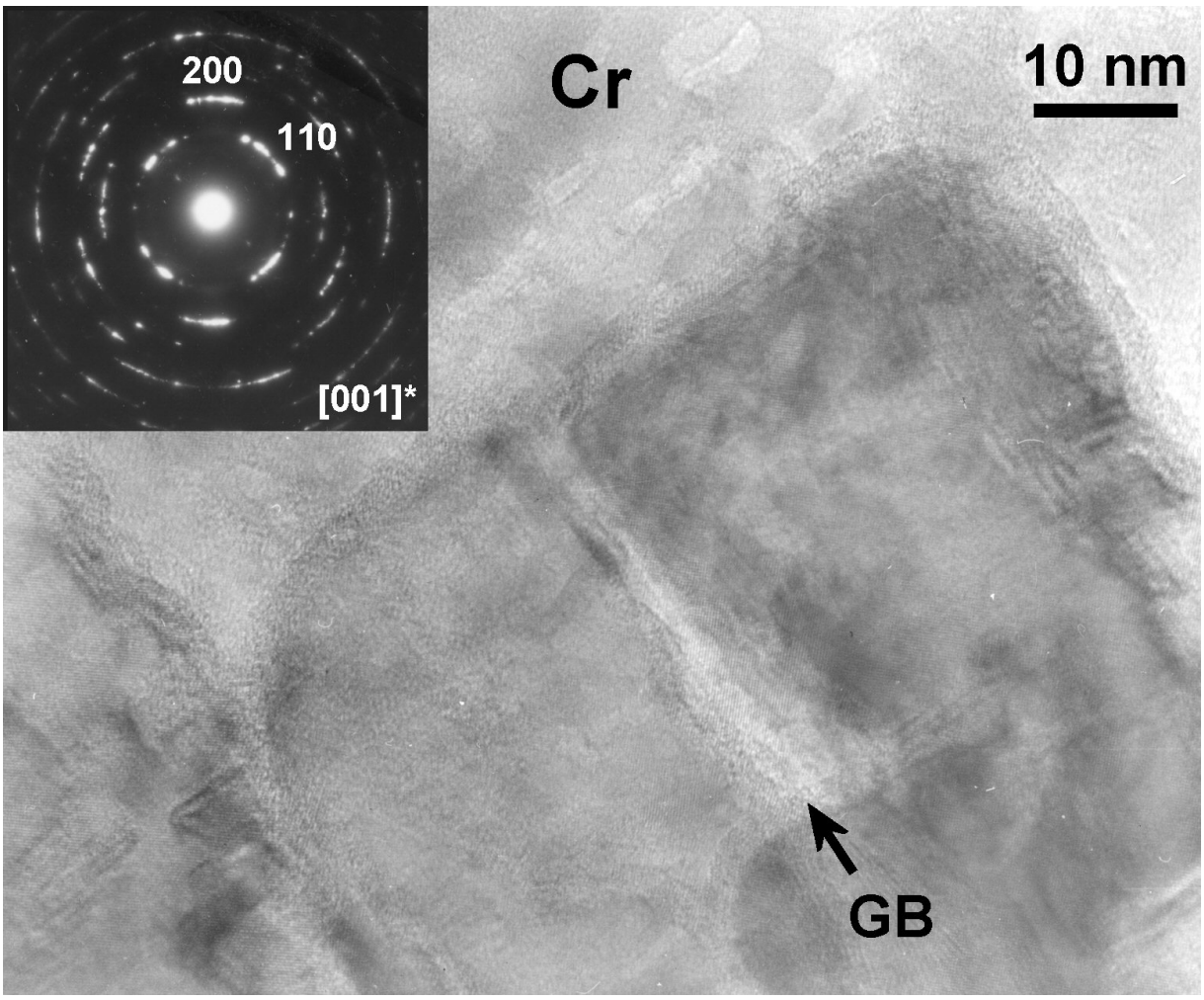

Figure 6.14: TEM plan view of a terrace-like grain of a biaxially aligned Cr thin film grown with O_2 at low impurity level. The ED pattern indicates an [100] out-of-plane orientation. The (100) terraces are limited by [110] steps, which can be deduced from the ED pattern.

the geometric fastest growth direction of the crystal habit should be determined. However, the geometric fastest growth direction of an {100} crystal habit has already been determined before when discussing the out-of-plane alignment of MgO thin films (see chapter 4, section 4.4.2). The geometric fastest growth direction of an {100} crystal habit corresponds to the [111] direction. Hence, the grains with the [111] direction perpendicular to the substrate, will have the highest perpendicular growth rate and overgrow the others. As a result, an [111] out-of-plane alignment should be observed for the Cr thin films deposited at medium impurity level. This is confirmed experimentally (Fig. 6.3).

On a tilted substrate, also an [111] out-of-plane alignment is observed. Because the deposition is carried out on a tilted substrate, additionally an in-plane alignment is observed whereby the (100) pole is oriented towards the flux (Fig. 6.4(c)). The same out-of-plane alignment and in-plane alignment is observed for MgO thin films deposited in pure conditions (Chapter 4). Because the Cr thin film is deposited in zone T, it is expected that the grains are truncated by

an {100} crystal habit. However, the grains of the Cr thin films at medium impurity level are not truncated by a clear crystal habit but a scale-like microstructure is observed experimentally (Fig. 6.5 (c)). This scale like structure can be attributed to a strong columnar bundling effect. This columnar bundling is caused by the shadowing effect [22]. In the shadowed area behind the grain, no atoms can arrive directly from the flux, leaving an empty region behind. Columns perpendicular to the flux are able to group while those along the flux will be separated by voids. The shadowing effect is typically observed in thin film growth with kinetically limited diffusion [23]. In this case, the adatoms cannot diffuse towards the empty regions and compensate the shadowing effect. Due to the impurity compound, it is likely that the Cr adatom mobility will be reduced[9] and the shadowing effect will become important. Additionally, the shadowing effect is more pronounced when the grains are bigger. It is expected that initially there is only a minor influence of shadowing.[10] Therefore, we assume that the columnar bundling occurs after the out-of-plane alignment and in-plane alignment is completed. If this assumption is valid, the out-of-plane and in-plane alignment of Cr thin films deposited at medium impurity level can be explained.

High Impurity Level

Increasing the impurity partial pressure even more, not only the (110) planes will be covered by impurities, but also an impurity phase will be formed on top of the (100) and (111) planes. Further growth will be characterized by repeated nucleation on the impurity phase, resulting in a random crystallographic orientation. A typical cauliflower microstructure evolves (Fig. 6.5(d)). This structure is a typical Zone I - Zone III structure. The size of the grains depends on the rate at which the impurity phase is formed on top, hence the impurity concentration during deposition. At even higher impurity concentration, the formation of a nanocrystalline structure is expected.

6.4 Structure Evolution of Biaxially aligned Cr thin films with codeposited CH_4

N_2 and O_2 have a very similar influence on the growth of biaxially aligned Cr thin films. However, it is likely that another impurity will influence the growth mechanism of biaxially aligned Cr thin films differently because it is expected that a different impurity reacts differently with Cr. In order to verify this, the influence of CH_4 on the growth of biaxially aligned Cr thin films is examined. Because our vacuum system uses a rotation pump to obtain an initial vacuum of 10^{-2} mbar, it is plausible that carboxyl compounds, originating from backstreaming oil, are present in the deposition chamber. Therefore, a simple gaseous molecule with a carbon-hydrogen bond is chosen. Hereby, methane is a logical choice.

[9] Remark that the deposition conditions aren't optimized for the depositions in medium impurity level

[10] It must be stressed that the adparticles are still able to diffuse, however the diffusion distance will be much smaller due to the impurities.

6.4.1 Experimental Setup and Results

To investigate the influence of CH_4 on the growth of biaxially aligned Cr, Cr thin films are deposited with a varying concentration of CH_4. The CH_4 gas is added via a needle valve. The CH_4 partial pressure before deposition varied between $1 \cdot 10^{-6}$ mbar and $4 \cdot 10^{-5}$ mbar. The deposition conditions for the growth of the Cr thin films are identical as in the study of the O_2 and N_2 influence (Sect. 6.2).

Fig. 6.15 shows the preferential out-of-plane alignment of Cr thin films deposited on an inclined substrate as a function of the CH_4 partial pressure. Without the codeposition of CH_4, represented by the point at $1.0 \cdot 10^{-6}$ mbar CH_4, the Cr thin film exhibits a preferential [100] out-of-plane alignment. With the addition of a small concentration of CH_4 ($p(CH_4) < 1.0 \cdot 10^{-5}$ mbar), no change in preferential [100] out-of-plane alignment is observed. At a CH_4 partial pressure above $1.0 \cdot 10^{-5}$ mbar, the Cr thin film exhibits a random out-of-plane orientation.
Because the Cr thin films are deposited on a tilted substrate, also an in-plane alignment is expected. Fig. 6.16 shows the XRD pole figures of Cr thin films deposited with three different CH_4 concentrations. Without the addition of CH_4, four distinct poles are observed at $\phi = 45° \pm n \cdot 90°$ with respect to the direction of the incoming vapour flux. The four fold symmetry and the position of the poles at $\chi \approx 45°$ confirm the preferential [100] out-of-plane orientation. At a CH_4 partial pressure of $4.2 \cdot 10^{-6}$ mbar, a similar XRD pole figure is observed (Fig. 6.16(b)). Hence, no change in in-plane alignment is observed. However, the two fading and mixing poles together with the high background indicate that the degree of in-plane alignment is worse than without the codeposition of CH_4. At a CH_4 partial pressure of $2.0 \cdot 10^{-5}$ mbar, an uniform intensity dis-

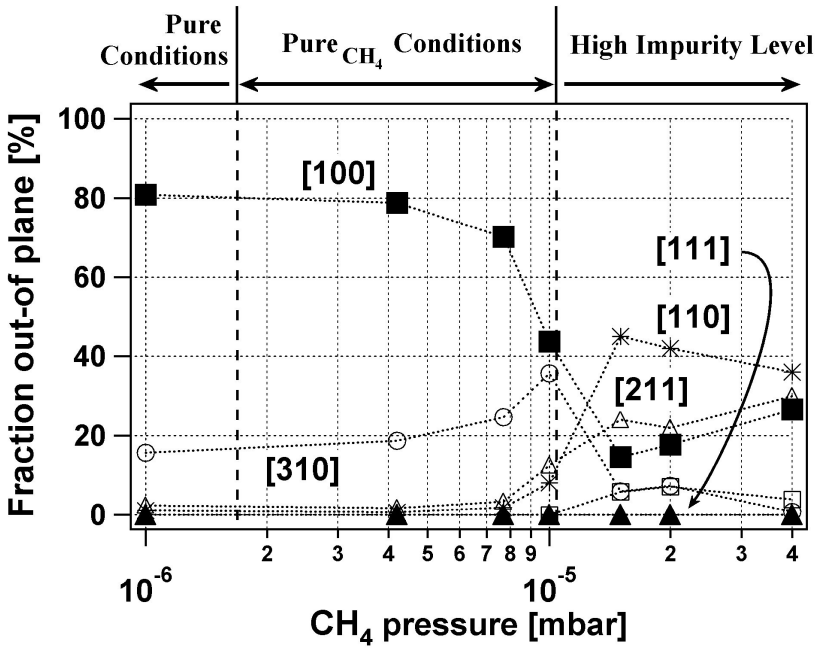

Figure 6.15: The preferential out-of-plane orientation of Cr thin films as a function of the CH_4 partial pressure.

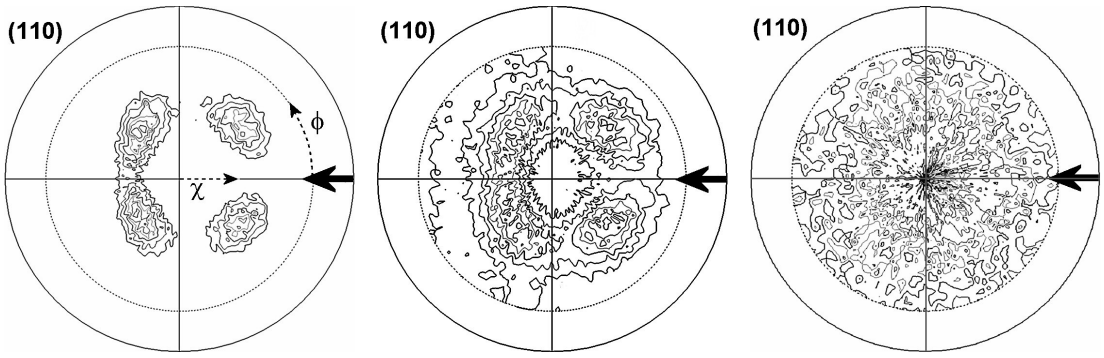

(a) $1.0 \cdot 10^{-6}$ mbar (b) $4.2 \cdot 10^{-6}$ mbar (c) $2.0 \cdot 10^{-5}$ mbar

Figure 6.16: (110) XRD pole figures of biaxially aligned Cr thin films for three different CH_4 partial pressure during deposition (a) none, but the base pressure was about $1.0 \cdot 10^{-6}$ mbar, (b) $4.2 \cdot 10^{-6}$ mbar, (c) $1.5 \cdot 10^{-5}$ mbar. The orthogonal projection of the direction of the incoming material flux is indicated by the arrow. ϕ is defined as the angle between this direction and direction between pole and centre.

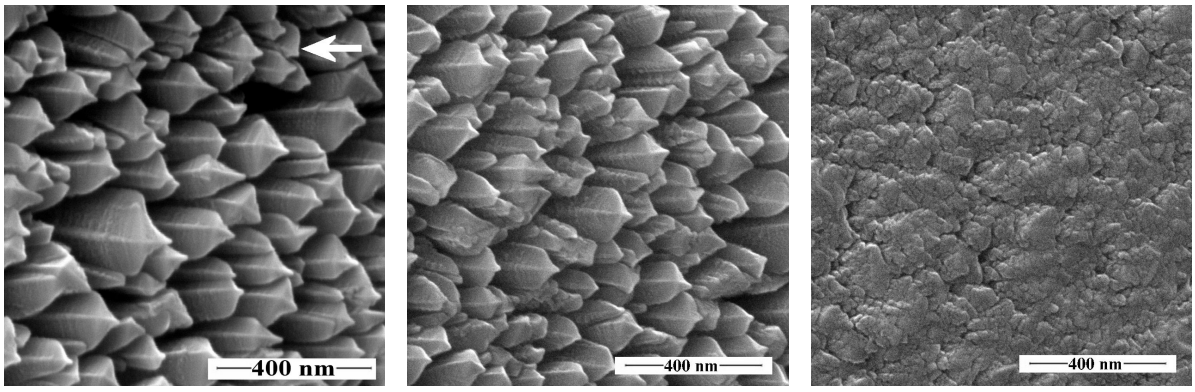

(a) $1.0 \cdot 10^{-6}$ mbar (b) $4.2 \cdot 10^{-6}$ mbar (c) $2.0 \cdot 10^{-5}$ mbar

Figure 6.17: SEM plan view of Cr thin films deposited at three different levels of CH_2 contamination. (a) no CH_4 deliberately added, (b) $4.2 \cdot 10^{-6}$ mbar CH_4, (c) $2.0 \cdot 10^{-5}$ mbar CH_4. The arrow indicates the direction of the incoming material flux.

tribution is observed, indicating a random in-plane and out-of-plane alignment (Fig. 6.16(c)). The microstructure of the Cr thin films with various CH_4 concentrations is analysed with SEM plan views and is shown in Fig. 6.17. Without deliberately added impurities, the grains of the Cr thin films are truncated by a clear {110} crystal habit (see also chapter 4). The edges of the crystal habit of the grains are oriented towards the incoming material flux, which indicates an in-plane alignment. At $4.2 \cdot 10^{-6}$ mbar CH_4, a similar microstructure is observed as without codeposited CH_4. The grains are faceted by an {110} crystal habit and the edge of the crystal habit is oriented towards the incoming material flux. However, small grains without a nice faceted structure are also observed between the other grains. At a CH_4 partial pressure of $2.0 \cdot 10^{-5}$ mbar, a cauliflower structure is observed.

These experimental observations can be subdivided into three different classes, in analogy to the Cr thin films with codeposited N_2 and O_2 (Sect. 6.2). In a first class, the Cr thin film has a prefe-

	Out-of-plane	In-Plane	Faceting	Limit
Pure	[100]	(110) pole at $\phi = 45°$	{110} crystal habit	p(base) < $1.0 \cdot 10^{-6}$ mbar
Pure $_{CH_4}$	[100]	(110) pole at $\phi = 45°$	{110} crystal habit	p(CH_4) < $1.0 \cdot 10^{-5}$ mbar
High	Random	Random	Cauliflower structure	p(CH_4) > $1.0 \cdot 10^{-5}$ mbar

Table 6.4: Overview of the out-of-plane alignment, in-plane alignment and microstructure of Cr thin films deposited with various CH_4 concentrations.

rential [100] out-of-plane orientation and an in-plane alignment with the (110) pole situated at ϕ = 45°. The grains are faceted by an {110} crystal habit. This class is called the *Pure Conditions*. It has been discussed that without the codeposition of impurities, the Cr thin film is deposited in zone T.
The second class is characterised by the codeposition of CH_4 with a partial pressure below $1 \cdot 10^{-5}$ mbar. The Cr thin films in this class exhibit a similar microstructure and crystallographic texture as in the pure conditions. Therefore, this class is called *Pure$_{CH_4}$ Conditions*. However, a worse in-plane alignment and the occurrence of smaller grains suggest a poorer quality of the Cr thin films. Because the Cr thin films are similar to the pure conditions, it is obvious that the Cr thin film is deposited in zone T.
In a third class, the Cr thin film has a random crystallographic orientation and a cauliflower structure. This structure is typical for a zone III structure. In accordance to the investigation with O_2 and N_2, this third class is called the *High Impurity Level*. These three classes are summarized in table 6.4

6.4.2 Discussion

From the experimental observation, it is clear that CH_4 acts complete differently on the growth of biaxially aligned Cr thin films in comparison to O_2 and N_2. For instance, no change in microstructure in zone T nor a change in in-plane alignment is observed while for O_2 and N_2 both are observed. Additionally, for O_2 and N_2 a change to an [111] out-of-plane orientation is observed, while for CH_4 only a transition to a randomly oriented Cr thin film is observed. Furthermore, the transition at which such a zone III structure occurs, is much lower for CH_4 than for O_2 or N_2.
It is concluded that only a transition from zone T to zone III occurs with increasing CH_4 concentration. Similar to for O_2 and N_2, this experiment can be defined as a path on the revised structure zone model (Fig. 6.2(b)). Because no intermediate zone T structures are observed and because the CH_4 partial pressure at which the transition to zone III occurs is much lower than for O_2 and N_2, is likely that the path is different from the path for O_2 and N_2. It is proposed that the growth of Cr thin films with codeposited CH_4 follows the path corresponding to line 1.

There are a few possibilities for the different behaviour of CH_4 on the growth of Cr thin films in comparison to O_2 and N_2, however, none of them is examined into detail. Therefore, the most likely possibilities are just summarized in the following list without further discussion.

- The chemisorption of CH_4 to a Cr surface is more likely in comparison to O_2 or N_2 due to the weaker C-H bond. As a result, the sticking probability of CH_4 to a Cr surface will be higher and the growth of the Cr thin film is hindered more easily.

- CH_4 molecules are much bigger than O_2 or N_2. Therefore, it is likely that CH_4 remains on the surface of all crystallographic planes. Hence, the growth of all crystallographic planes will be hindered by CH_4. Because there is no longer an anisotropy, no change in microstructure (and so crystallographic texture) is expected within zone T. Only at a specific CH_4 concentration, the growth of all planes will be blocked, resulting in a zone III structure.

- CH_4 molecules consist of two elements. At the Cr surface, dissociative chemisorption can occur, resulting in C and H adatoms at the Cr surface. The behaviour of both elements will be different (e.g. different chemical reactivity). Furthermore, C and H can influence the various crystallographic planes differently. As a result, all the crystallographic planes can be hindered.

Giving a conclusive explanation of the structure evolution of Cr thin films with codeposited CH_4 is not the primarily goal of this experiment. What we want to point out in this experiment, is that another impurity will have another influence on the growth of Cr thin films and this has clearly been demonstrated.

6.5 Texture Change in InN caused by Codeposition of O_2

6.5.1 Experimental Observations

It is difficult to grow stoichiometric InN thin films because indium only chemisorbs atomic nitrogen and no molecular N_2 (Sect. 5.5.3). Moreover, the relative low binding energy of InN makes it even harder to grow. In contrast, indium strongly chemisorbes molecular O_2 and the binding energy of In_2O_3 is much higher [24]. As a result, the growth of indium oxide will be preferred to the growth of indium nitride if oxygen is presented.
During the deposition of InN thin films, oxygen is always present in the deposition chamber (as H_2O or O_2). Because indium has a much higher affinity to oxygen than to nitrogen, it is expected that minute concentrations of oxygen are sufficient to modify the growth of InN thin films. To investigate the influence of O_2 to the growth of InN thin films, biaxially aligned InN thin films are deposited with varying O_2 concentrations. For this, the deposition chamber was pumped down to a base pressure below $1 \cdot 10^{-6}$ mbar. Before deposition, O_2 gas is introduced into the chamber via a needle valve. The O_2 partial pressure before deposition is used as reference. The O_2 partial pressure is varied between $1 \cdot 10^{-6}$ mbar O_2 and $3 \cdot 10^{-4}$ mbar O_2. During the deposition, the corresponding gas flow was kept constant.
During this deposition series, all other deposition parameters were kept constant. The target-substrate distance was 9 cm, the discharge current was 0.55 A and the substrate bias was -40 V. Ne gas is used as a sputter gas. The Ne flow was 8 sccm while the N_2 flow was 36 sccm. This resulted in a working pressure of 0.25 Pa. An 1:3 magnet configuration is used. The substrate was stainless steel. For the TEM analysis, Si substrates are used. No difference between the various substrates is observed. The InN thin films have a layer thickness of 1500 nm. These

parameters were optimized for the growth of biaxially aligned InN thin films in pure conditions (see chapter 5).

Fig. 6.18 shows the change in the out-of-plane alignment of biaxially aligned InN thin films as a function of the O_2 partial pressure. Without codeposited O_2, the InN thin film exhibits a preferential [0001] out-of-plane alignment. If the O_2 partial pressure is below $1 \cdot 10^{-5}$ mbar O_2, no change in preferential out-of-plane alignment is observed. At $4.0 \cdot 10^{-5}$ mbar O_2, the out-of-plane alignment changes to a preferential $[20\bar{2}3]_\perp$ out-of-plane alignment. By adding more O_2 during the deposition, the preferential out-of-plane alignment changes again to an [0001] out-of-plane alignment. If the O_2 partial pressure is above $2.0 \cdot 10^{-4}$ mbar O_2, the InN thin film exhibits a random out-of-plane alignment.

When depositing on a tilted substrate, the InN thin films not only exhibit a preferential out-of-plane alignment but also a preferential in-plane alignment. Fig. 6.19 shows the XRD pole figures of biaxially aligned InN grown with various O_2 concentrations. Without the deliberate addition of O_2 (Fig. 6.19(a)), six distinct poles are observed which indicates a strong in-plane alignment. The $(10\bar{1}1)$ poles are situated at $\phi = 30° \pm n{\cdot}60°$ with respect to the incoming material flux. The sixfold symmetry and the position of the poles at approximately $\chi = 60°$, confirm that the InN thin film is [0001] out-of-plane oriented. A similar pole figure is observed when depositing with $7.0 \cdot 10^{-6}$ mbar O_2.
With the codeposition of $4.0 \cdot 10^{-5}$ mbar O_2, four distinct poles are observed (Fig. 6.19(b)). This in-plane alignment is totally different from the sixfold symmetry with the codeposition of O_2. One of the $(10\bar{1}1)$ poles is situated at $\chi = 10°$ away from the incoming material flux. Because

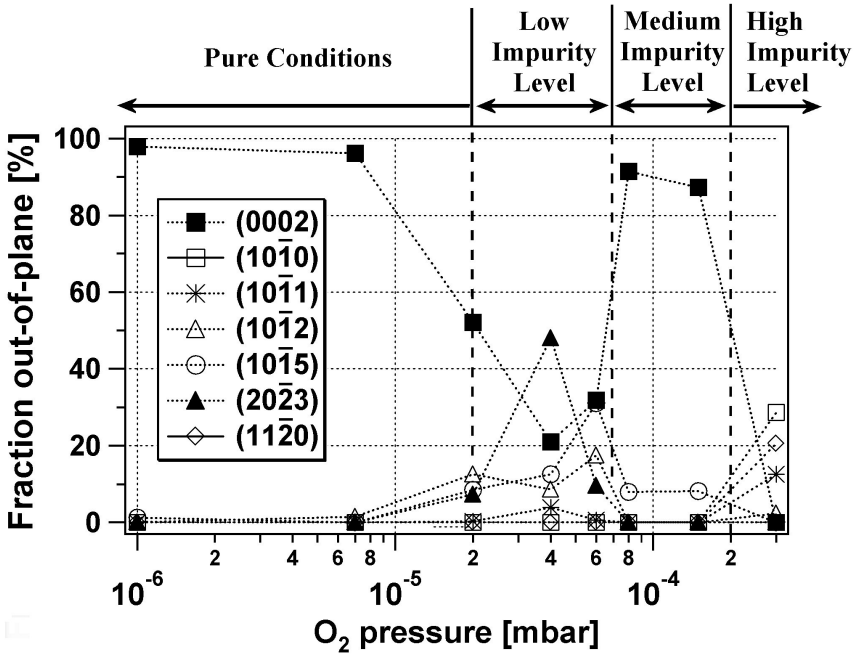

Figure 6.18: The change in preferential out-of-plane orientation of InN thin films as a function of the O_2 partial pressure.

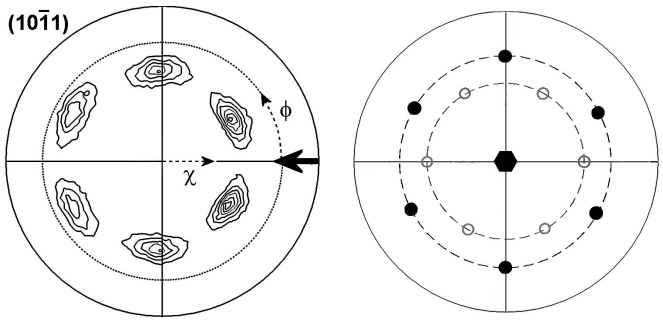

(a) Pure conditions: no deliberate codeposited O_2

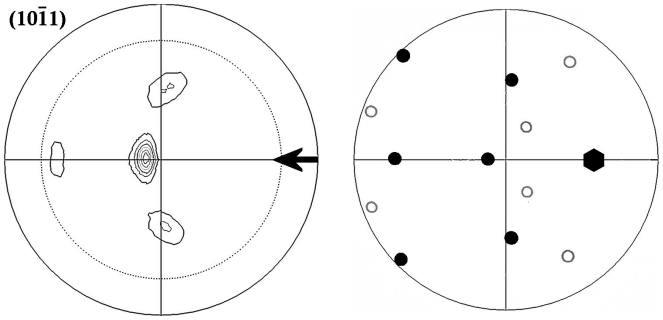

(b) Low Impurity Level: $4.0 \cdot 10^{-5}$ mbar O_2

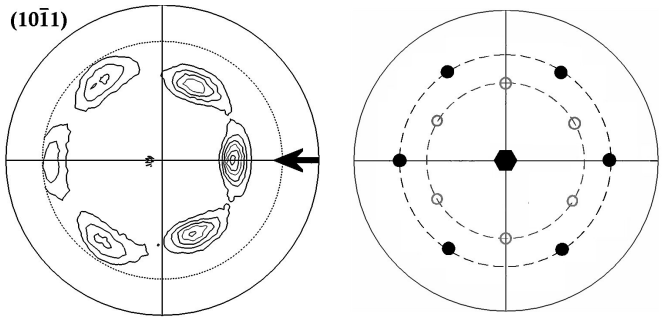

(c) Medium Impurity Level: $8.0 \cdot 10^{-5}$ mbar O_2

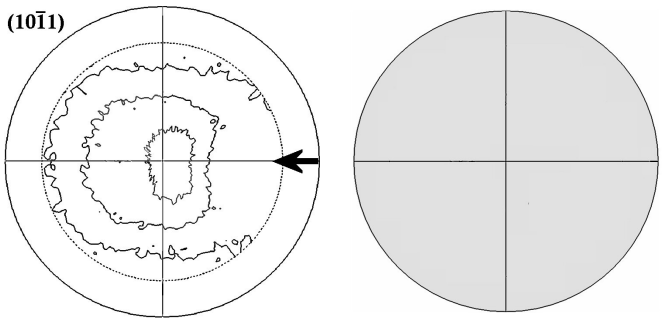

(d) High Impurity Level: $3.0 \cdot 10^{-4}$ mbar O_2

Figure 6.19: (10$\bar{1}$1) XRD pole figures of biaxially aligned InN thin films deposited at three different impurity partial pressure: (a) Pure Conditions; (b) $4 \cdot 10^{-5}$ mbar O_2; (c) $8 \cdot 10^{-5}$ mbar O_2. The orthogonal projection of the direction of the incoming material flux is indicated by the arrow. The stereographic projections belonging to the pole figures are also shown. The symbols which take into account the crystal symmetry, correspond to the following planes: ⬣ = (0001); ● = (10$\bar{1}$1); ○ = (11$\bar{2}$3)

the angle between the $(10\bar{1}1)$ plane and the $(20\bar{2}3)$ plane is 10.63° (App. B), it can be concluded that the InN thin film has a $[20\bar{2}3]_{\perp}$ out-of-plane alignment. This has also been observed with XRD angular scans. The c-axis is 51° inclined towards the incoming material flux. This can be seen on the stereographic projection of Fig. 6.19(b).
If the O_2 partial pressure during deposition was $8.0 \cdot 10^{-5}$ mbar O_2, the in-plane alignment of the InN thin film changes again as can be seen in Fig. 6.19(c). Six distinct poles are observed at χ = 45°. In spite of a small tilt of the [0001] axis, an [0001] out-of-plane alignment is assumed and is consistent to the results of the XRD angular scans. This pole figure resembles to the pole figure of the InN thin film deposited without deliberately added O_2. However, with $8.0 \cdot 10^{-5}$ mbar O_2, the $(10\bar{1}1)$ poles are rotated by 30°and are situated at $\phi = 0° \pm n{\cdot}60°$. Hence, one of the poles is oriented towards the incoming material flux.
At the highest O_2 concentrations ($p(O_2) > 3.0 \cdot 10^{-4}$ mbar), the $(10\bar{1}1)$ XRD pole figure has a broad peak (Fig. 6.19(d)). Because the illumination area is different at different χ angles, it can be reasoned that there is a random intensity distribution. This random intensity distribution indicates a random out-of-plane and a random in-plane alignment.

Also the microstructure of the InN thin films grown with various O_2 impurity concentrations is investigated. Fig. 6.20 shows the SEM plan view of biaxially aligned InN thin films at three different impurity levels of O_2 contamination. Without the O_2 codeposition or if the O_2 partial pressure is $7.0 \cdot 10^{-6}$ mbar O_2, the InN thin film consist of clear faceted grains with a sixfold symmetry (Fig. 6.20(a)). This case has been discussed in detail in chapter 4. It has been reasoned that the grains are truncated by $\{11\bar{2}3\}$ mounds. As can be seen in Fig. 6.20(a), the side of the $\{11\bar{2}3\}$ mound is oriented towards the incoming material flux. This is confirmed by the XRD pole figures. In the stereographic projections of Fig. 6.19(a), it can be seen that one of the $(11\bar{2}3)$ spots is located at $\phi = 0°$, i.e. the angle which corresponds to the direction of the incoming material flux.
At $4.0 \cdot 10^{-5}$ mbar O_2 (i.e. the O_2 partial pressure for which the InN thin film exhibits a $[20\bar{2}3]_{\perp}$ out-of-plane alignment), a saddle roof like structure is observed (Fig. 6.19(b)). The grains are elongated in the direction of the incoming material flux. We were not able to determine the crystal habit univocally.
At $8.0 \cdot 10^{-5}$ mbar O_2, a faceted grains structure is observed. Although it is not very apparent, the grain faceting has a hexagonal symmetry. However, in most cases, the facet which faces the incoming material flux is covered by its two neighbouring facets, through which only five facets are visible. Because the covered facet of all grains is oriented towards the incoming material flux, the in-plane alignment is confirmed. Because in the XRD pole figure (Fig. 6.19(c)), the $(10\bar{1}1)$ pole is oriented towards the incoming material flux, it is suggested that the grains are limited by $\{10\bar{1}n\}$ planes. Like in pure conditions, n can be calculated by measuring the enclosed angle of the pyramid (see further).
The surface of the InN thin film has a cauliflower structure, similar to the cauliflower structure as observed for Cr (not shown here).

The microstructure of the InN thin films is further investigated by TEM cross sections (Fig. 6.21). Without the addition of O_2 during deposition, a clear columnar structure is observed (Fig. 6.21(a)). The columns grow perpendicular to the substrate. The ED pattern confirms the [0001] out-of-plane alignment. The columns are truncated by $\{11\bar{2}3\}$ planes, which could be concluded by measuring the enclosed angle of the columnar top (Chapter 4).

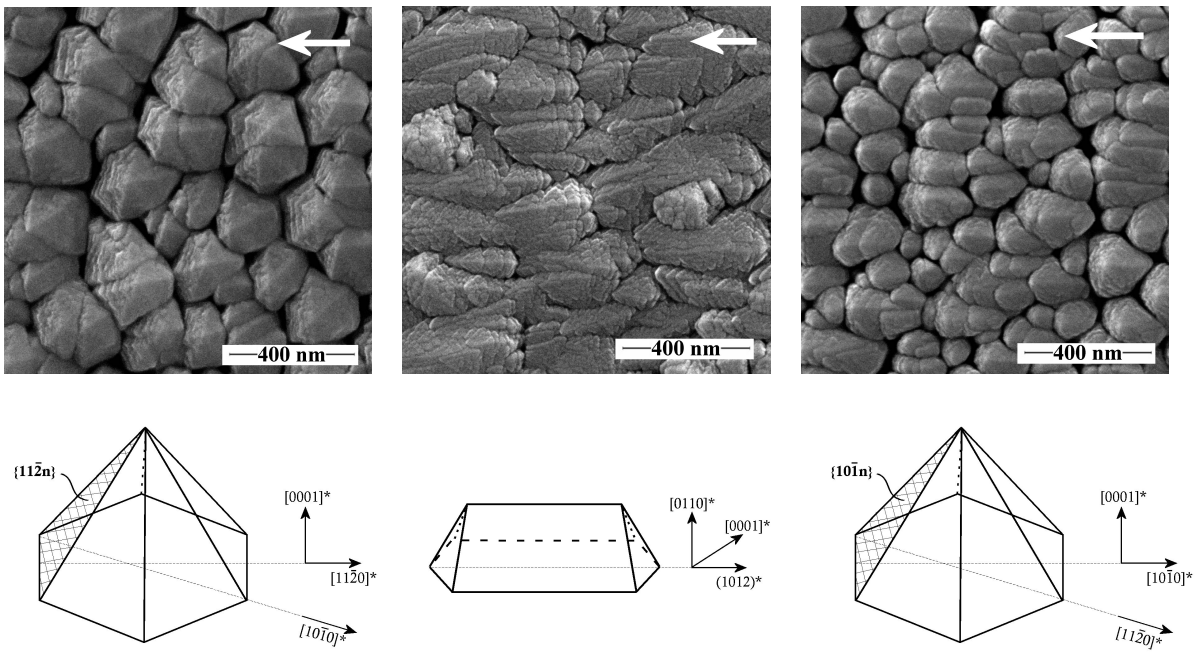

(a) Pure Conditions: No O_2 added (b) Low Impurity Level: $4.0 \cdot 10^{-5}$ mbar O_2 (c) Medium Impurity Level: $8.0 \cdot 10^{-5}$ mbar O_2

Figure 6.20: SEM plan view of biaxially aligned InN thin films deposited on a tilted substrate at three different levels of O_2 contamination: (a) no O_2 deliberately added; (b) $4.0 \cdot 10^{-5}$ mbar O_2; (c) $8.0 \cdot 10^{-5}$ mbar O_2. The direction of the incoming material flux is indicated by an arrow. The observed crystal habit is shown in the schematic drawing below.

Fig. 6.21(b) shows the TEM cross section of an InN thin film with codeposited O_2 impurities ($p(O_2) = 4 \cdot 10^{-5}$ mbar). Detailed anaysis let us conclude that broad columns are observed. There is no tilting of the columns. The ED pattern confirms that the [0001] orientation is tilted by about 50°with respect to the substrate normal. The $(01\bar{1}0)$ planes which deviates slightly from the substrate normal, confirms the earlier observations and the $[20\bar{2}3]_\perp$ out-of-plane orientation. The black regions on the image correspond to pure In regions. These regions are formed during ion milling. Krischok et al. [25] examined the influence of low energetic Ar^+ bombardment on InN. They observed that InN is sensitive to radiation damage. Hereby, N is preferentially sputtered, resulting in an enrichment of In. Due to the low melting temperature, the In aggregates and forms droplets.[11]

The TEM cross section shown in Fig. 6.21(c), corresponds to an InN thin film deposited with $8 \cdot 10^{-5}$ mbar O_2. A voided columnar structure is observed. Hereby, the columns are slightly tilted towards the incoming material flux. At the substrate/film interface, there are a lot of small grains. Only few of them survive during the growth. A V-shape columnar structure is observed. The ED pattern, taken at the InN thin film surface, confirms the [0001] orientation. Because of

[11] We also observed this phenomenon when carrying out XPS measurements. When sputtering the first ten nm to remove an oxide layer, liquid properties are observed locally. When analysing, only pure In is measured.

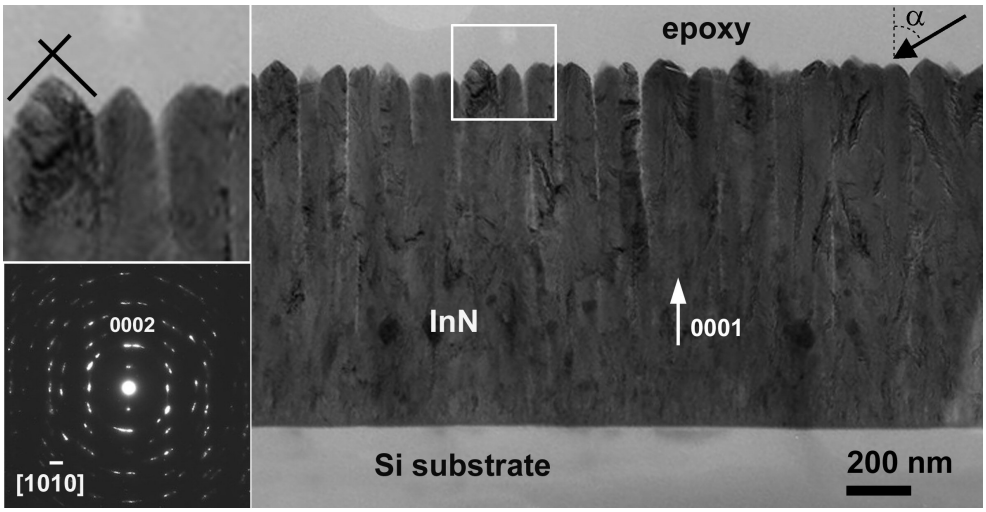

(a) Pure Conditions: No deliberately added O_2

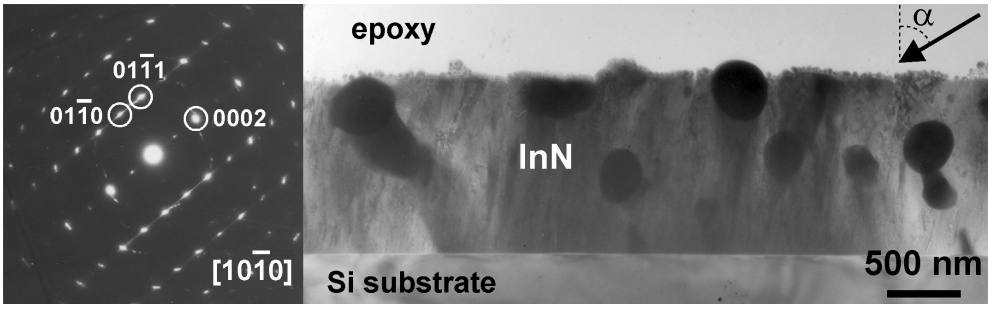

(b) Low Impurity Level: $4.0 \cdot 10^{-5}$ mbar O_2

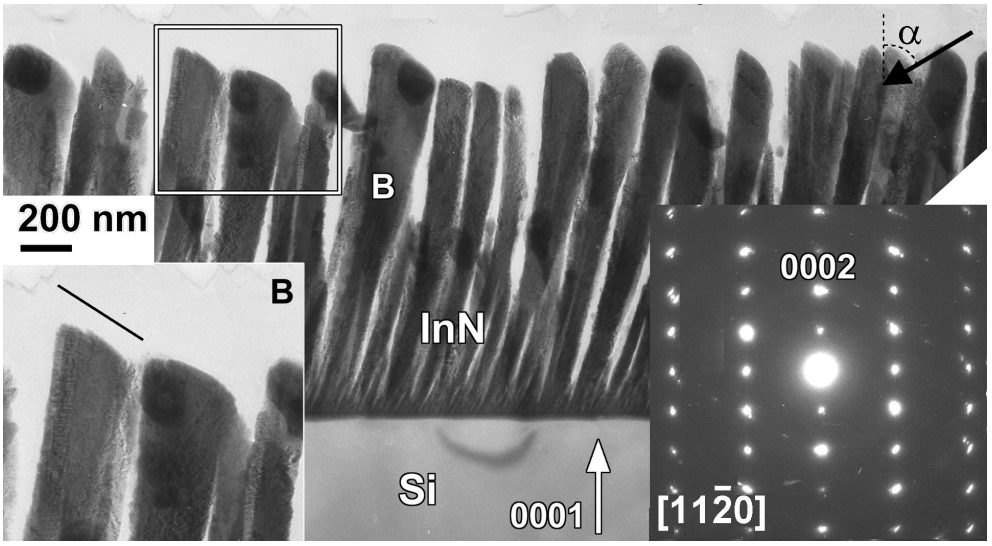

(c) Medium Impurity Level: $8.0 \cdot 10^{-5}$ mbar O_2

Figure 6.21: TEM Cross section of a biaxially aligned InN thin films grown with various O_2 contamination. (a) Pure conditions; (b) $4 \cdot 10^{-5}$ mbar O_2; (c) $8 \cdot 10^{-5}$ mbar O_2. The direction of the incoming material flux is indicated by an arrow. The black spots are pure In regions that were induced by local melt during ion milling.

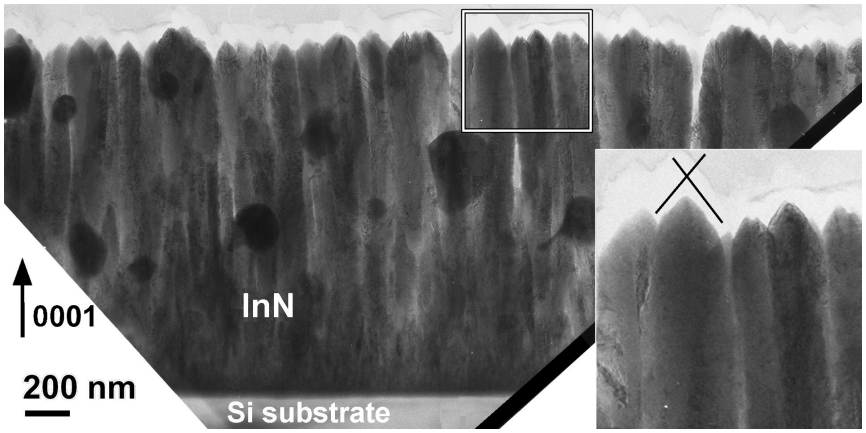

(a) TEM Cross Section

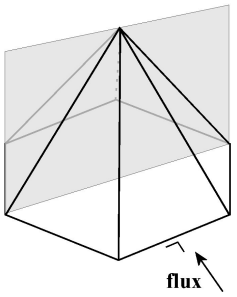

(b) Schematic Drawing

Figure 6.22: (a) TEM Cross Section of biaxially aligned InN thin film deposited with $8.0 \cdot 10^{-5}$ mbar O_2. The cross section is taken perpendicular to the incoming material flux. (b) Schematic drawing of the section taken perpendicular to the incoming material flux. The arrow indicates the orthogonal projection of the direction of the incoming material flux.

the overgrowth mechanism, it is suggested that this film is deposited in zone T conditions.
As mentioned above, the $\{10\bar{1}n\}$ faceting of this film can be determined by measuring the enclosed angle of the columnar top. However, the columnar top is asymmetric and no enclosed angle could be determined. This is probably due to the envelopment of one of the facets by the two neighbouring facets. In the direction perpendicular to the direction of the incoming material flux, no asymmetry is expected. Fig. 6.22(a) shows a TEM cross section of the same InN thin film, but now the cross section is made perpendicular to the incoming material flux. The enclosed angle of the columnar top is about 77°± 6°. Because the cross section is taken perpendicularly, not the angle between the planes, but the angle between the egdes formed by two planes should be compared (Fig. 6.22(b)). From table 6.5, which gives this enclosed angle for the various n, it can be concluded that the grains are limited by $\{10\bar{1}1\}$ planes.

By the analogy with the Cr observations, the influence of O_2 impurities on the growth of biaxially aligned InN can be subdivided into four different classes. In the first class, no O_2 is added delibe-

Habit	Enclosed Angle	Habit	Enclosed Angle
$\{10\bar{1}0\}$	n/a	$\{11\bar{2}0\}$	n/a
$\{10\bar{1}1\}$	74.59°	$\{11\bar{2}1\}$	47.47°
$\{10\bar{1}2\}$	113.43°	$\{11\bar{2}2\}$	82.66°
$\{10\bar{1}3\}$	132.72°	$\{11\bar{2}3\}$	105.67°
$\{10\bar{1}4\}$	143.65°	$\{11\bar{2}4\}$	120.75°

Table 6.5: The enclosed angle of the crystal shape truncated by various crystallographic planes. The angle corresponds to the angle between the egdes formed by two crystallographic planes.

	Out-of-plane	In-Plane	Faceting	Limit
Pure	[0001]	$(10\bar{1}1)$ pole at $\phi = 30°$	$\{11\bar{2}3\}$ mound	$p(O_2) < 2.0 \cdot 10^{-5}$ mbar
Low	$[20\bar{2}3]_\perp$	$(10\bar{1}1)$ pole at $\chi = 10°$	Roof like Structure	$p(O_2) < 7.0 \cdot 10^{-5}$ mbar
Medium	[0001]	$(10\bar{1}1)$ pole at $\phi = 0°$	$\{10\bar{1}1\}$ crystal habit	$p(O_2) < 2.0 \cdot 10^{-4}$ mbar
High	Random	Random	Cauliflower structure	$p(O_2) > 2.0 \cdot 10^{-4}$ mbar

Table 6.6: Overview of the out-of-plane alignment, in-plane alignment and microstructure of InN thin films deposited on an inclined substrate with various O_2 partial pressures.

rately or the impurity concentration is too low to modify the structure evolution ($p(O_2) < 2 \cdot 10^{-5}$ mbar O_2). In this class, the InN thin film exhibits a preferential [0001] out-of-plane orientation and a strong in-plane alignment whereby one of the $(10\bar{1}1)$ poles is situated at $\phi = 30°$. The columns are truncated by $\{11\bar{2}3\}$ mounds. This class is referred to as the *pure conditions*.
The second class is called the *low impurity level*. In this class, the InN thin film exhibits a preferential $[20\bar{2}3]_\perp$ out-of-plane orientation and a clear in-plane orientation. The grains are truncated by roof like structure.
In the third class, the InN thin film has a preferential [0001] out-of-plane orientation and a strong in-plane alignment whereby one of the $(10\bar{1}1)$ poles is situated at $\phi = 0°$. In this class, named the *Medium Impurity Level*, the grains are limited by $\{10\bar{1}1\}$ planes.
In the forth class, the InN thin film has a random in-plane and out-of-plane alignment. Additionally, a cauliflower structure is observed. This class is called the *High Impurity Level*.
The various classes are indicated on Fig. 6.18 and are mentioned on the other figures. An overview of the various classes is given in table 6.6.

6.5.2 Structure Evolution of InN Thin Film with Codeposited O_2

Before discussing the experimental results, it should be known whether oxygen acts as an inhibitor or as a promoter in the growth of InN thin films. It is likely that oxygen is an inhibitor because oxygen has a high affinity to In in comparison to a weak In-N interaction [24]. If O_2 is an inhibitor, the impurity compound will increase the diffusion barriers, decrease the adatom mobility and hinder the fundamental processes of structure formation.
However, information about diffusion barriers of InN or any In-O compound is scarce and to our knowledge no reliable data is found in literature. An approach to obtain information about the diffusion barriers is known as the cohesion approximation [26] and is used frequently for metal systems. In this approach, it is stated that the surface self-diffusion linearly scales with the cohesive energy E_{coh}. For instance, Feibelman [27] found that the energy for a single hop scales as $E_d \sim 1/6 E_{coh}$ for several FCC crystal systems. Because in a compound system, the crystallo-

graphic planes will be terminated by N or O (the supply of reactive particles is much higher than the number of metallic In), the diffusion of the metallic adparticle is decisive. Therefore, this reasoning is extrapolated to the InN thin film. However, the scaling factor will be different.
For InN, the cohesive energy is about 1.5 eV/at, while for In_2O_3, i.e. the In-O compound which is most likely to be formed, the cohesive energy is about 9.6 eV/at. The cohesive energy is calculated from the heat of formation of InN (34 kcal/mol) and In_2O_3 (221 kcal/mol) [24]. Because the cohesive energy of In_2O_3 is much larger than the cohesive energy of InN, it is likely that the diffusion barriers of the In-O compound are much larger than those of InN. As a result, the adatom mobility will be reduced with the presence of oxygen. Hence, it can be concluded that oxygen is an inhibitor in the growth of InN thin films.

The subdivision in four different classes made clear that the addition of an O_2 concentration during the deposition of InN thin films modifies the growth. For the various classes, a different microstructure and crystallographic texture is observed.
In pure conditions, it has been reasoned in chapter 4 that the preferential [0001] out-of-plane orientation originates from an orientation selection at the coalescence stage in order to minimize the surface and interface energy. Because of restructurative grain growth, it was concluded that the InN thin film was deposited in Zone II. At medium impurity level, the TEM cross section indicates that small islands nucleate on the substrate (Fig. 6.21). Only few of them survive during the growth, while the others are overgrown. The columns have a typical V-shaped structure. In addition, the columns are tilted towards the flux and there are large voids between the columns. All these observations are characteristic for a zone T structure. At the high impurity level, a random crystallographic orientation is observed in addition to a cauliflower structure. This observation is typical for a zone III structure. Because of the uncertainties and the incomplete elucidation of the microstructure at the low impurity level, this class will not be used in the further discussion. However, some comments are given at the end, concerning the results for this impurity level.
From these observations, it can be concluded that the addition of O_2 during the growth of InN causes a transition from Zone II to zone T with increasing O_2 concentration. At the highest O_2 concentration the InN thin film changes from a zone T structure to zone III. Because O_2 is an inhibitor, this change in structure can be classified in the revised structure zone model as proposed in sect. 1.6.4. Because all deposition parameters are kept constant, only one path on the revised SZM is examined in this experiment (Fig. 6.2(b)). Owing to the change from zone II over zone T to zone III, it can be concluded that the path corresponding to line 3 of Fig. 6.2(b) is followed for InN with codeposited O_2. Remark that this path is the same as for Al:O system in the experiments of Barna et al. (Sect. 6.1).

Structure Evolution of InN Thin Film at Pure Conditions - Zone II

In pure conditions a Zone II structure is observed. At nucleation, differently oriented grains nucleate on the substrate. However, due to restructurative grain growth, there is an orientation selection during the coalescence stage. The driving force is minimization of the surface and interface energy of the InN thin film. As a result, the [$\bar{0}$001] out-of-plane oriented grains will be favoured. In section 4.5, it has been discussed that {11$\bar{2}$3} mounds are formed on top of the grains because of a high ES barrier. Due to the specific shape of the mounds, there will be an anisotropy

in number of captured adparticles. This anisotropy will depend on the in-plane orientation of the grains and hence an in-plane alignment will evolve.

Structure Evolution of InN Thin Film at Medium Impurity Level - Zone T

When codepositing O_2 during the growth of InN thin films, the oxygen will act as an inhibitor. At a specific impurity concentration, the restructurative grain growth processes will be hindered by the impurity compound. As a result, there will be no orientation selection and the random orientation distribution of the grains at nucleation is preserved. Because it is expected that the oxygen accumulates in the grain boundaries and because the O_2 concentration is too low to cover the surface of the grain, the individual grains are able to grow. These grains are truncated by the specific crystallographic planes. Due to an anisotropy in normal growth rate of the planes, only the planes with the lowest normal growth rate will survive (Remark that the growth rate of the planes will be influenced by O_2). Owing to the crystal faceting, a growth competition between differently out-of-plane oriented grains will occur and a typical zone T structure will evolve.

In chapter 4, the evolution of the out-of-plane and in-plane alignment has been discussed for cubic materials which are deposited in zone T. This model is solely based on the properties of zone T. Because for InN thin films grown at medium impurity level also a zone T structure is observed, it is plausible that the model is also valid in case of InN thin film with codeposited O_2. In zone T, the grains are limited by a crystal habit. According to the model, the crystal habit is due to the geometric fastest growth direction and the capture length of the grains, hence for the out-of-plane alignment and the in-plane alignment respectively. Therefore, it is important to determine the crystal habit. As discussed in paragraph 4.4.1, the facets of the crystal habit corresponds to the planes with the lowest normal growth rate. In pure conditions, it is suggested that the normal growth rate of the plane is inversely proportional to the number of nearest neighbours that the plane offers to diffusing adatoms.
However, in case of codeposited impurities, not only the number of nearest neighbours will determine the normal growth rate of a plane. By analogy with the model for Cr, it is likely that O_2 behaves differently on the various crystallographic planes. As a result, the relative growth rate of the crystallographic planes will change. Moreover, it is possible that some of the planes will be covered by an In-O impurity phase, through which the growth of the plane is completely hindered, while other planes can grow freely. During this thesis work, we were not able to investigate the influence of O_2 on the growth rate of the various crystallographic planes of InN. Consequently, no conclusions can be drawn about the growth rate of the crystallographic planes of InN in presence of O_2.
Taking into account the experimental evidence, it is suggested that the grains of the InN thin film are truncated by an $\{10\bar{1}1\}$ crystal habit at medium impurity level. Hence, for these specific deposition conditions and oxygen concentrations, it is proposed that the $(10\bar{1}1)$ planes have the lowest normal growth rate. In the following discussion, it is assumed that the grains grown in medium impurity level are truncated by an $\{10\bar{1}1\}$ crystal habit.

To determine the out-of-plane orientation, the perpendicular growth rate of the $\{10\bar{1}1\}$ crystal habit should be calculated in all directions. Therefore, consider an $\{10\bar{1}1\}$ crystal habit as defined in Fig. 6.23. A free standing $\{10\bar{1}1\}$ crystal habit corresponds to a hexagonal dipyramid. The orientation of the $\{10\bar{1}1\}$ crystal habit is defined by the angles θ and ω. The substrate plane

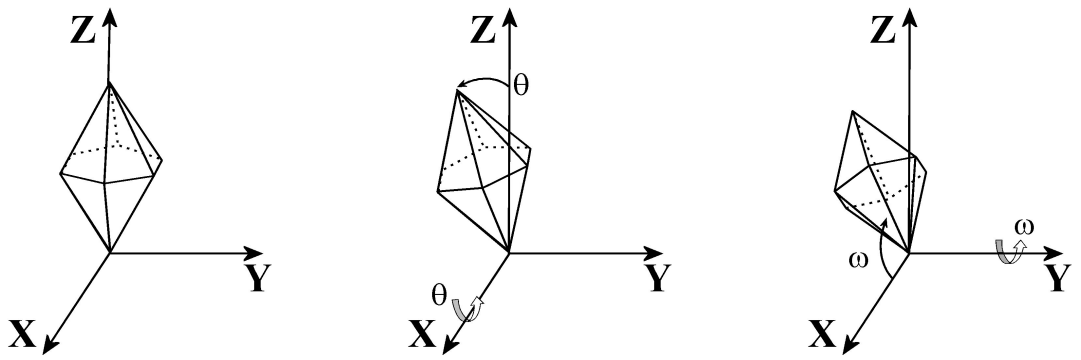

(a) (b) (c)

Figure 6.23: Schematically drawing of a hexagonal dipyramid in a XYZ coordination system. θ is the rotation angle around the X-axis. ω corresponds to the rotation around the Y-axis. The substrate is parallel to the XY plane.

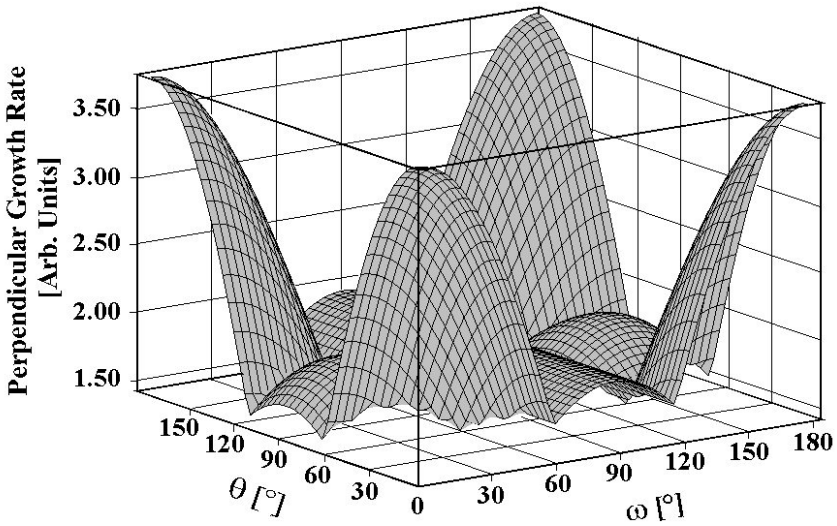

Figure 6.24: Perpendicular growth rate of an $\{10\bar{1}1\}$ crystal habit as a function of its orientation defined by the angle θ and ω

corresponds to the XY-plane. The perpendicular growth rate is calculated from the projection of the crystal habit onto the Z-axis and is plotted in Fig. 6.24.
The perpendicular growth rate is at its maximum for $\omega = \theta = 0°$. This orientation corresponds to the [0001] orientation of the grain. The $\{10\bar{1}1\}$ crystal habit of an [0001] out-of-plane oriented grain, taking into account the substrate, is shown in Fig. 6.20(c)

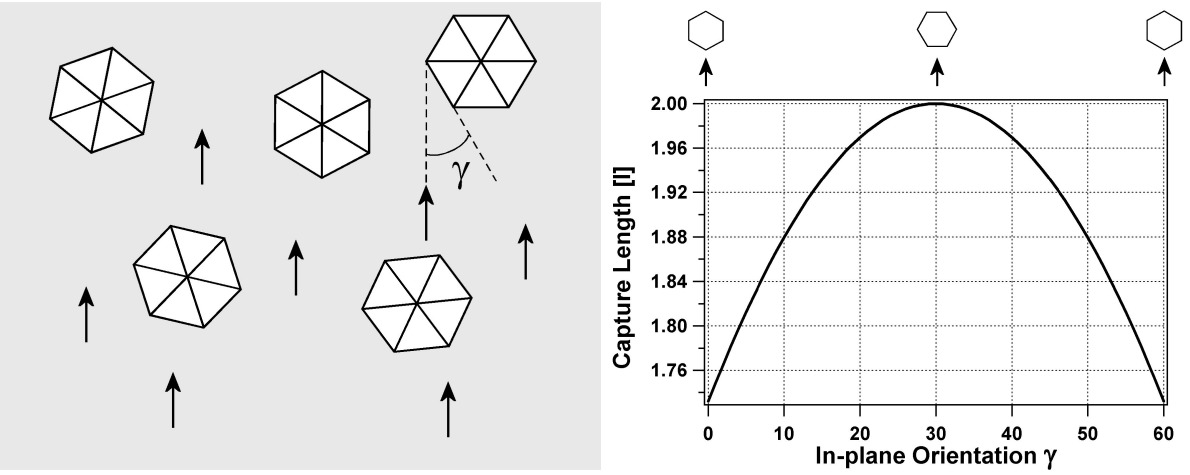

(a) Schematic representation

(b) Capture length

Figure 6.25: (a) Representation of an InN : O thin film surface grown at medium impurity level in Zone T. $\{10\bar{1}1\}$ faceted grains with an [0001] out-of-plane orientation are dispersed on the substrate and are shown in projection as hexagons. γ is the angle between the side of hexagon and the direction of the diffusing adparticles. (b) Capture length of $\{10\bar{1}1\}$ faceted grains with an [0001] out-of-plane orientation as a function of the in-plane orientation of the grain.

Alternatively, the rule of thumbs can be used which states that the geometric fastest growth direction corresponds to the orientation of the grain for which the facets of the crystal habit have the highest tilt angle with respect to the substrate. For an $\{10\bar{1}1\}$ crystal habit, this corresponds to the [0001] direction. As a result, an [0001] out-of-plane orientation should be observed which is confirmed experimentally.

Also the in-plane alignment is agreement with the model. To determine the in-plane orientation, the capture length of the crystal habit should be determined. For an [0001] out-of-plane oriented grain truncated by an $\{10\bar{1}1\}$ crystal habit, the capture length of a hexagon should be calculated. The results are given in Fig. 6.25.
As can be seen, the capture length is at its maximum if the side of the hexagon is oriented towards the flux. This is experimentally observed because one of the poles in the $(10\bar{1}1)$ pole figure is oriented towards the flux. This is also confirmed by SEM plan view, although the side which is oriented towards the flux is enveloped by the two neighbouring facets.
It can be concluded that the structure evolution of InN thin films grown at medium impurity level can be understood by the proposed model, when assuming an $\{10\bar{1}1\}$ crystal habit.

Structure Evolution of InN Thin Film at High Impurity Level - Zone III

At the highest impurity concentration, it is suggested that O_2 forms an impurity phase on the complete surface of the thin film. As a result, the growth will be interrupted repeatedly and globular grains will evolve. There will be no correlation between the orientation of the various grains.

Structure Evolution of InN Thin Film at Low Impurity Level

Based on the results of the other impurity classes, a transition from zone II to zone T is observed with increasing O_2 concentration. Because the low impurity level is in between these classes, it is plausible that the InN thin film at low impurity level exhibits a zone II or a zone T structure. Using the revised SZM (Fig. 6.2(b)), it is unlikely that the InN thin film would be deposited in another zone.
If the InN thin film would have a zone II structure, restructurative grain growth should occur at the coalescence stage. Hence, the planes with the lowest surface energy should be parallel to the substrate. Because a $[20\bar{2}3]_\perp$ out-of-plane alignment is observed, the $(20\bar{2}3)$ planes should have the lowest surface energy. So, if the thin film is deposited in zone II, the addition of O_2 during the growth of InN causes a change in surface free energy of the various crystallographic planes. In this case, the structure evolution should be similar to the structure evolution as described in chapter 4.
If the InN thin film has a zone T structure, the crystallographic texture is determined by the crystal habit of the grains. Because it was not possible to determine the microstructure of the InN thin film univocally, no conclusion could be drawn about the grain faceting. As a result, it was not possible to elucidate the mechanism for the preferential $[20\bar{2}3]_\perp$ out-of-plane alignment and the mechanism for the in-plane alignment if the InN thin film is deposited in zone T.
Because it is no clear in which zone the InN thin film is deposited, no conclusion can be drawn about the structure evolution in this impurity class.

6.6 Growth of Biaxially Aligned MgO with N_2 impurities

6.6.1 Experimental Setup

MgO thin films are deposited by magnetron sputtering on a tilted substrate (α = 55°). Hereby, the target-substrate distance was 10 cm, the discharge current was 0.70 A and the substrate bias was -15 V. The working pressure was 0.45 Pa, obtained by 60 sccm Ar and 3 sccm O_2. The film thickness was 1.5 μm. The magnet configuration was 1:9. The base pressure was about $3 \cdot 10^{-6}$ mbar. With these deposition parameters, the biaxially aligned MgO thin films had a structure as described in chapter 4.
During deposition N_2 gas was added deliberately by a mass flow controller. The N_2 gas flow varied between 0 and 1.0 sccm N_2.

6.6.2 Experimental Results

Fig. 6.26 shows the out-of-plane alignment of a MgO thin film deposited on an inclined substrate as a function of the N_2 gas flow. Without the deliberately added N_2, the MgO thin film exhibits an [111] out-of-plane orientation. By adding N_2 during the growth of the MgO thin film, no change in preferential out-of-plane orientation is observed. The fraction of [111] out-of-plane oriented grains even slightly increases.
Also the in-plane alignment has been determined. Fig. 6.27 shows the XRD pole figures of the MgO thin film deposited without N_2 added (a) and the MgO thin film deposited with 1 sccm N_2 flow (b). The XRD pole figure of the MgO thin film with codeposited N_2 is similar to the pole

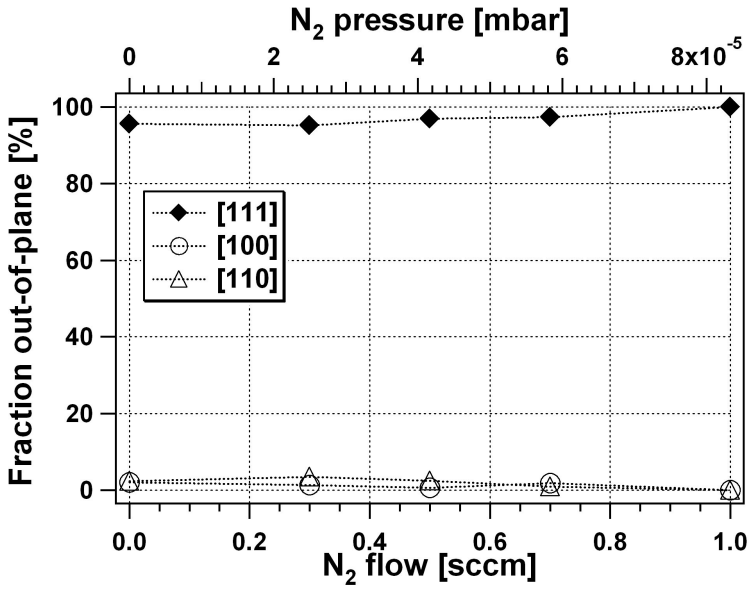

Figure 6.26: The fraction of out-of-plane oriented grains of a MgO thin films as a function of the N_2 gas flow. The fraction of out-of-plane orientation is determined by XRD angular scan

figure in pure conditions. Hence, both films exhibit the same in-plane orientation. From the pole figures, the FWHM is determined and is shown as a function of the N_2 gas flow in Fig. 6.28(a). It is observed that the degree of in-plane alignment improves with increasing N_2 gas flow. Also the pole intensity is plotted as a function of the N_2 gas flow and is shown in Fig. 6.28(b). At 0.7 sccm N_2, the peak intensity doubles with respect to lower N_2 flows.
Also the microstructure of the MgO film with codeposited N_2 has been examined. No difference in microstructure is observed (not shown). For all MgO thin films, a V-shaped columnar structure is observed. The columns are truncated by a {100} crystal habit. The side of the crystal habit points towards the incoming material flux.

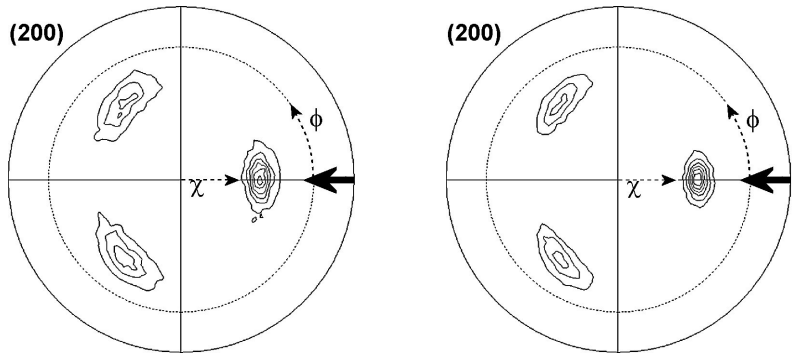

(a) No N_2 deliberately added (b) 1 sccm N_2

Figure 6.27: (200) XRD pole figure of a MgO thin deposited (a) without deliberately added N_2 and (b) with 1 sccm N_2 flow. The arrow indicates the direction of the incoming material flux.

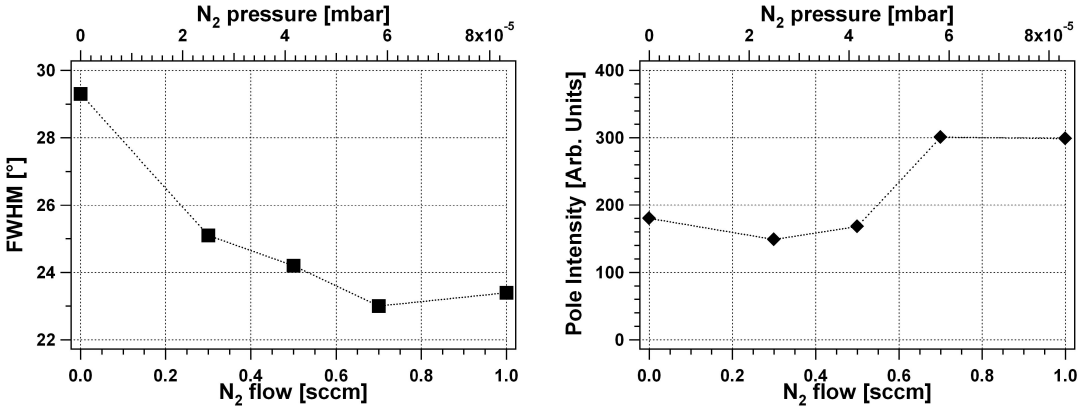

(a) FWHM of the (200) pole

(b) Peak Intensity

Figure 6.28: (a) FWHM of a MgO thin film obtained from the XRD pole figures as a function of the N_2 gas flow added during deposition. (b) The corresponding pole intensity as a function of the N_2 gas flow.

6.6.3 Growth Mechanism

The experimental results indicate that both the preferential out-of-plane alignment and in-plane alignment improve with increasing N_2 flow. In contrast to the Cr and InN thin films, no change in crystallographic texture nor in microstructure is observed with increasing N_2 impurity concentration.
In order to determine the influence of N_2 on the growth of MgO thin films, it should be known whether N_2 acts as an inhibitor or promoter during the growth. It is known that oxygen reacts very strongly with MgO [28]. Additionally, the Mg-O binding is strongly ionic, which causes the diffusion barriers to be high. In contrast to the comprehensive information of MgO properties, no information about the diffusion barriers of any Mg-N compound is found. Similar as in the discussion of InN thin films with codeposited O_2, the cohesion approach is used to get an idea about the diffusion barriers. In this approach, it is stated that the energy barriers scale with the cohesive energy of the material. MgO has a cohesive energy of 40.06 eV, while Mg_3N_2 has a cohesive energy of 3.48 eV [29] (Mg_3N_2 is chosen as impurity compound because it is the only stable nitride of Mg). Because of the large difference in cohesive energy, it is suggested that the diffusion barriers of MgO are much larger than those of Mg_3N_2. Therefore, it is likely that N_2 will act as a promoter during the growth of MgO.

As discussed in chapter 4, MgO thin films are deposited in zone T. Because in zone T, the crystal habit is decisive for the structure evolution of the thin film, the influence of N_2 on the normal growth rate of the various crystallographic planes should be investigated. In section 6.2 it has been discussed for Cr that impurities on a plane with a high packing density tend to remain on that plane, while they penetrate into the other planes. As a result, the plane with the highest packing density will be influenced the most by the impurities. This idea is extrapolated to the growth of MgO thin films with N_2 impurities. Table 6.7 shows the packing density of the various crystallographic planes of MgO. It follows that the (100) planes have the highest packing density. Hence, nitrogen tends to remain on the (100) planes, while it will penetrate into the (110) and (111) planes.

(hkl)	Rocksalt (MgO) [Atoms/a^2]
(100)	**4**
(110)	$\sqrt{2} \cdot 2 \approx 2.828$
(111)	$4/\sqrt{3} \approx 2.309$

Table 6.7: The packing density of the (100), (110) and (111) crystallographic planes for a MgO rocksalt structure. The packing density is defined as the number of atoms per a^2 where a = 4.2 Å is the lattice parameter.

Because the nitrogen remains on top of the (100) planes and because nitrogen is a promoter for the growth of MgO thin films, the growth of the (100) planes will be favoured with respect to the other crystallographic planes. As a result, the growth of an {100} crystal habit will be strengthened. Because the structure evolution is based on an overgrowth mechanism of grains with an {100} crystal habit, the out-of-plane alignment and the in-plane alignment will evolve faster. Because the MgO thin films are deposited with the same thickness, the out-of-plane alignment as well as the in-plane alignment will improve with increasing N_2 gas flow.

Bibliography

[1] Z. Zhang, M. G. Lagally, Atomistic processes in the early stages of thin-film growth, Science 276 (1997) 377–383.

[2] P. B. Barna, M. Adamik, Science and Technology of Thin Films, 1st Edition, World Scientific, 1995, *Chapter: Growth Mechanism of Polycrystalline Thin Films*.

[3] P. B. Barna, M. Adamik, Fundamental structure forming phenomena of polycrystalline films and the structure zone models, Thin Solid Films 317 (1998) 27–33.

[4] S. Mahieu, P. Ghekiere, D. Depla, R. De Gryse, Biaxial alignment in sputter deposited thin films, Thin Solid Films 515 (4) (2006) 1229–1249.

[5] K. Sangwal, Effect of impurities on crystal growth processes, Prog. Crystal Growth and Charact. 32 (1996) 3–43 and references cited therein.

[6] D. T. J. Hurle, Handbook of Crystal Growth. 1a Fundamental, 1st Edition, Elsevier Science, 1993.

[7] V. V. Voronkov, L. N. Rashkovich, Step kinetics in the presence of mobile adsorbed impurities, J. Cryst. Growth 144 (1-2) (1994) 107–115.

[8] J. P. Van der Eerden, H. Müller-Krumbhaar, Dynamic coarsening of crystal surfaces by formation of macrosteps, Phys. Rev. Lett. 57 (19) (1986) 2431–2433.

[9] D. Kandel, J. D. Weeks, Theory of impurity-induced step bunching, Phys. Rev. B 49 (8) (1994) 5554–5564.

[10] D. Kandel, J. D. Weeks, Kinetics of surface steps in the presence of impurities: Patterns and instabilities, Phys. Rev. B 52 (3) (1995) 2154–2164.

[11] J. Krug, New mechanism for impurity-induced step bunching, Europhys. Lett. 60 (5) (2002) 788–794.

[12] M. Ohring, Materials Science of Thin Films, 2nd Edition, Academic Press, San Diego, 2002.

[13] J. Lábár, Consistent indexing of a (set of) SAED pattern(s) with the processdiffraction program, Ultramicroscopy 103 (3) (2005) 237–249.

[14] J. T. Grant, T. W. Haas, Some studies of the Cr(100) and Cr(110) surfaces, Surf. Sci. 17 (1969) 484–485.

[15] P. Michel, C. Jardin, Oxygen adsorption and oxide formation on Cr(100) and Cr(110) surfaces, Surf. Sci. 36 (2) (1973) 478–487.

[16] C. Jardin, P. Michel, Oxydation de la face (111) d'un monocristal de chrome, Surf. Sci. 71 (3) (1978) 575–582.

[17] F. Reichel, L. P. H. Jeurgens, E. J. Mittemeijer, Thermodynamic model of oxide overgrowth on bare metals: Relaxation of growth strain by plastic deformation, Phys. Rev. B 74 (14) (2006) 144103.

[18] P. Hartman, W. Perdok, On the relations between structure and morphology of crystals, Acta Cryst. 8 (1955) 49–52, 521–524, 525–529.

[19] A. Barna, P. B. Barna, G. Radnóczi, F. M. Reicha, L. Tóth, Formation of Aluminium thin films in the presence of Oxygen and Nickel, Phys. Stat. Sol. (a) 55 (1979) 427–435.

[20] P. B. Barna, Impurity effects in the structural development of vacuum deposited thin films, Proc. IX IVC-V ICSS, Madrid (1983) 382–396.

[21] D. Gall, C. S. Shin, T. Spila, M. Oden, M. J. H. Senna, J. E. Greene, I. Petrov, Growth of single-crystal CrN on MgO(001): Effects of low-energy ion-irradiation on surface morphological evolution and physical properties, J. Appl. Phys. 91 (6) (2002) 3589–3597.

[22] L. Abelmann, C. Lodder, Oblique evaporation and surface diffusion, Thin Solid Films 305 (1997) 1–21.

[23] A. G. Dirks, H. J. Leamy, Columnar microstructure in vapor-deposited thin films, Thin Solid Films 47 (3) (1977) 219–233.

[24] A. G. Bhuiyan, A. Hashimoto, A. Yamamoto, Indium nitride (inn): A review on growth, characterization and properties, J. Appl. Phys. 94 (5) (2003) 2779–2808.

[25] S. Krischok, Y. Yanev, O. Balykov, M. Himmerlich, J. A. Schaefer, R. Kosiba, G. Ecke, I. Cimalla, V. Cimalla, O. Ambacher, H. Lu, W. J. Schaff, L. F. Eastman, Investigations of MBE grown InN and the influence of sputtering on the surface composition, Surf. Sci. 556–568 (2) (2004) 849.

[26] S. Y. Davydov, Calculation of the activation energy for surface self-diffusion of transition-metal atoms, Phys. Solid State 41 (1) (1999) 8–10.

[27] P. Feibelman, Scaling of hopping self-diffusion barriers on FCC(100) surfaces with bulk bond energies, Surf. Sci. 423 (1999) 169–174.

[28] V. E. Henrich, P. A. Cox, The Surface Science of Metal Oxides, 1st Edition, Cambridge University Press, 1994.

[29] B. V. Lvov, V. L. Ugolkov, Kinetics and mechanism of free-surface vaporization of groups IIA, IIIA and IVA nitrides analyzed thermogravimetrically by the third-law method, Thermochimica Acta 438 (1-2) (2005) 1–8.

Chapter 7

Extrapolation to other Materials

Polycrystalline MgO, Cr and InN thin films are not the only materials for which a biaxial alignment is observed. Table 7.1 summarizes the materials with a biaxial alignment that are described in literature. These thin films are deposited with various PVD techniques (e-beam evaporation, sputtering, PLD).
For all these references, the biaxial alignment evolves because the adparticles arrive at the substrate with a specific direction different from the substrate normal. Similar to our experiments, this can be done by tilting the substrate [7, 8, 9]. Another possibility to have a directed material incidence, is to move the substrate repetitively through the plasma at regular intervals (i.e. a planetary motion) [6, 10, 11]. The technique for which the oblique incident direction of the material flux causes a biaxial alignment is called Inclined Substrate Deposition (ISD) [7].
Biaxial alignment can also occur when an energetic ion beam is directed towards the growing thin film. This technique is call Ion Beam Assisted Deposition (IBAD). The structure evolution deviates strongly from that of biaxially aligned thin films grown by ISD. The growth is explained in terms of preferential sputtering, ion channeling and anisotropic grain damage [16, 17, 18, 19]. However, it is not the aim of this thesis to examine the growth mechanism of biaxially aligned thin films deposited by IBAD and no further attention is given this technique.

The biaxially aligned thin films that are described in table 7.1, are classified according to their crystallographic structure. In pure conditions, only biaxially aligned thin films with a rocksalt,

Material	Crystal Structure
TiN [1, 2], MgO [3, 4, 5], CrN [6]	Rocksalt
YSZ [7, 8], CeO_2 [9]	Fluorite
Mo [10], Cr [11, 12], Fe [13]	B.C.C.
Al* [14]	F.C.C.
Co* [15]	H.C.P.

Table 7.1: Summary of thin films with a biaxial alignment. The upper part corresponds to biaxially aligned thin films deposited in pure conditions. In the lower part, the biaxial alignment in thin film is only observed with the codeposition of oxygen. These materials are indicated with an asterix.

Crystal System	Structure Type	Materials	Space group
Cubic	F.C.C.	Al, Cu, Ag, Au, Pt, Ni,...	$Fm\bar{3}m$
	B.C.C.	W, Ta, Mo, Nb, V, Cr, Fe,...	$Im\bar{3}m$
	Diamond	C, Si, Ge	$Fm\bar{3}m$
	Rocksalt	MgO, MnO, TiN, CaO,...	$Fm\bar{3}m$
	Fluorite	CeO_2, UO_2, YSZ,...	$Fm\bar{3}m$
	Zinc Blende	α-ZnS, InSb, AlP, BeTe	$F\bar{4}3m$
	Caesium Chloride	CsCl, AuZn, MgTl	$Pm\bar{3}m$
	Spinel	$MgAl_2O_4$	$Fd\bar{3}m$
	Perovskite	$SrTiO_3$, $KTaO_3$, $BaSnO_3$	$Pm\bar{3}m$
Tetragonal	Rutile	TiO_2, SnO_2, WO_2, VO_2	$P4_2/mnm$
Hexagonal	H.C.P	Zn, Co, Mg, Cd, Be, Zr, Ti,...	P6/mmm
	Wurtzite	ZnO, InN, AlN, GaN, β-ZnS	$P6_3mc$
	Graphite	C	$P6_3mc$
Trigonal	Corundum	Al_2O_3, Cr_2O_3, Fe_2O_3	$R\bar{3}c$
	Arsenic	As, Sb, Bi, Hg	$R\bar{3}m$

Table 7.2: Overview of some isostructural groups with specific materials for each groups. Also the space group is indicated.

fluorite or BCC structure are observed. In this work, materials with a wurtzite structure are added to this list. No biaxial alignment is observed for thin films with another structure, at least in pure conditions. With the codeposition of impurities, biaxial aligned thin films are deposited with a FCC and HCP structure. However, the impurity case is left out of consideration at this point.
Table 7.2 gives an overview of a wide range of materials. These materials are categorized in their isostructural groups. As can be seen, there are a lot of different structured materials. In respect to this, a question can be asked: is it possible to grow biaxially aligned thin film of materials with a crystallographic structure other than a rocksalt, fluorite or BCC structure? If so, what are the conditions to satisfy?

To answer this question, we have to go back to the origin of the biaxial alignment. Hereby, two parameters are of importance: the incoming direction of the adparticles with respect to the substrate normal and the mobility of the adparticle on the growing surface (see chapter 4,5).
The direction of the incoming material flux can easily been modified by changing the deposition conditions (for instance by tilting the substrate). This parameter is material independent and hence, it is not of importance in this chapter. Therefore it will not be discussed in detail.
Secondly, the adparticle mobility plays a role in the growth of biaxially aligned thin films. As discussed in chapter 5, the energy of the adparticle must be optimized to grow biaxially aligned thin films. If the adatom mobility is too high or too low, no biaxial alignment will occur.
It had been mentioned that the adatom mobility depends on three key parameters. This is summarized in a flowchart (Fig. 7.1). This flowchart is an expansion of the schematic drawing of Fig. 5.5.

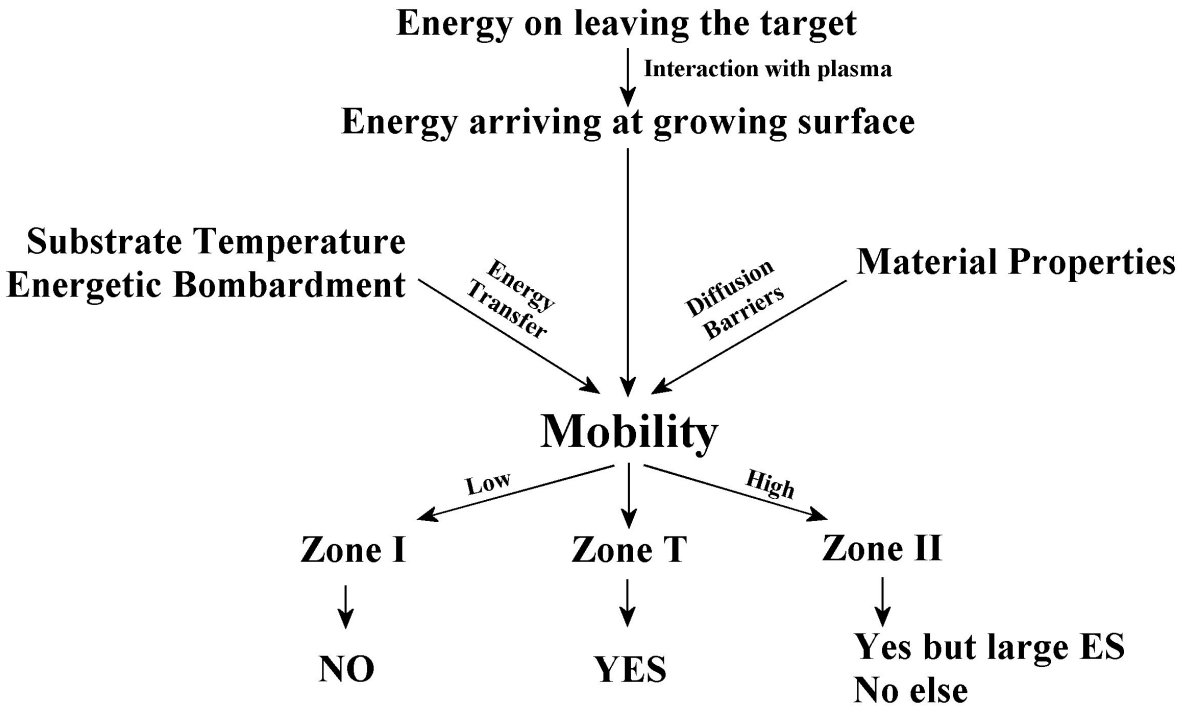

Figure 7.1: Overview of the parameters which influence the mobility and its consequence to evolution of the biaxial alignment

- Firstly, the adparticle mobility depends on its energy at which it arrives at the growing surface. This energy depends on the energy at which the particle is generated and the interaction with the plasma during its transport towards the substrate. In sputter deposition (at normal sputter pressures), the adparticles arrive with an energy of a few eV. In case of e-beam or thermal evaporation, the adparticle energy is assumed to be thermalized (E ~ kT ~ 0.1 eV).

- Secondly, the adparticle mobility depends on the energy transfer between the adparticle and the growing film. With an energetic bombardment or at high substrate temperature, the adparticle will increase its energy and hence, the mobility will increase.

- Thirdly, the mobility of the adparticle depends on the materials properties. For example, if the material has a low activation energy for diffusion (so low diffusion barriers), the mobility of the adparticle will be high.

Depending on the mobility of the adparticle, the thin films will be deposited in different zones (section 1.6). If the adparticle mobility is low and the growth is characterized by a hit-and-stick regime, a typical zone I structure will evolve. In this zone, no preferential orientation will evolve and logically no biaxial alignment will be observed. If the adatoms are able to diffuse on a grain and reach another neighbouring grain, a typical zone T structure will evolve. In this zone, the grains are truncated by a crystal habit. As discussed, this crystal habit will result in the growth of a biaxially aligned thin film in case of an anisotropic material incidence. At the highest mobilities, restructurative grain growth will occur and a zone II will evolve. Broad equiaxed grains

will evolve whereby the plane with lowest surface energy is parallel to the substrate. Because the in-plane boundaries of this plane is no longer defined univocally, no in-plane alignment will be observed. However, if the high Ehrlich-Schwoebel (ES) barrier is high in comparison to the energy of the diffusing adparticle, mound formation can occur. It has been discussed that a biaxial alignment is possible in case of mound formation (chapter 4).

It can be concluded that the adparticle mobility is of importance in order to know whether biaxial alignment can occur. If all deposition conditions are kept constant for the various materials (i.e. the same deposition technique and a comparable energy supply to the diffusing adparticles), than the magnitude of the diffusion barriers is the key parameter which determines the mobility. Thin films of materials with low diffusion barriers will typically exhibit a zone II structure, while thin films of materials with higher diffusion barriers will have a zone T or zone I structure.
Hence, to know whether biaxial alignment is possible for a specific material, it is important to know all diffusion barriers. Only for a few of the isostructural groups, the possibility to grow biaxially aligned thin films will be discussed. For pure metallic thin films with a FCC, BCC and HCP structure, this is discussed into detail. For multicomponent materials, a somewhat different approach is used.

7.1 Pure Metallic Thin Films with a FCC, BCC or HCP Structure

In the first place, the various diffusion barriers should be obtained. However, up to now, there is little data available in literature. Only for a few specific elements (Al, Ag, W, ...), most of the diffusion barriers are known. For most materials, only a small number of energy barriers are known and often, the error bars are large.
Nevertheless, one diffusion barrier is easily to obtain because it can be derived from macroscopical measurements, namely the bulk diffusion. It is plausible that the other diffusion barriers (surface diffusion and grain boundary diffusion) scale with the bulk diffusion. As such, it is reasonable that materials with a low energy barrier for bulk diffusion will have low diffusion barriers for surface diffusion and grain boundary diffusion. Under this assumption, the diffusion barriers of the various materials will be compared.
Before discussing these structures, it should remarked that the ES barriers of metallic films is low. In chapter 1, it had been mentioned that the ES barriers are typically less than 20% of the diffusion barriers. This is rather low. Hence, to obtain a biaxial alignment, the thin film has to be deposited in zone T.
Fig. 7.2 shows the activation energy for bulk diffusion of pure metallic materials as a function of the melting temperature of the material. As can be seen on Fig. 7.2, the activation energy for bulk diffusion of materials with a FCC or HCP structure is lower than 3 eV. In contrast, BCC structured materials have an activation energy above 3 eV. Therefore, it's likely that the diffusion barriers for BCC materials are higher than for FCC and HCP materials.
As can be seen in table 7.1, in pure conditions, only biaxially aligned thin films are observed for BCC structured materials. All these biaxially aligned thin films exhibit a zone T structure. Because for materials with lower diffusion barriers no biaxial alignment is observed, there should a minimal height of the diffusion barriers for which a biaxial alignment is possible. Because no

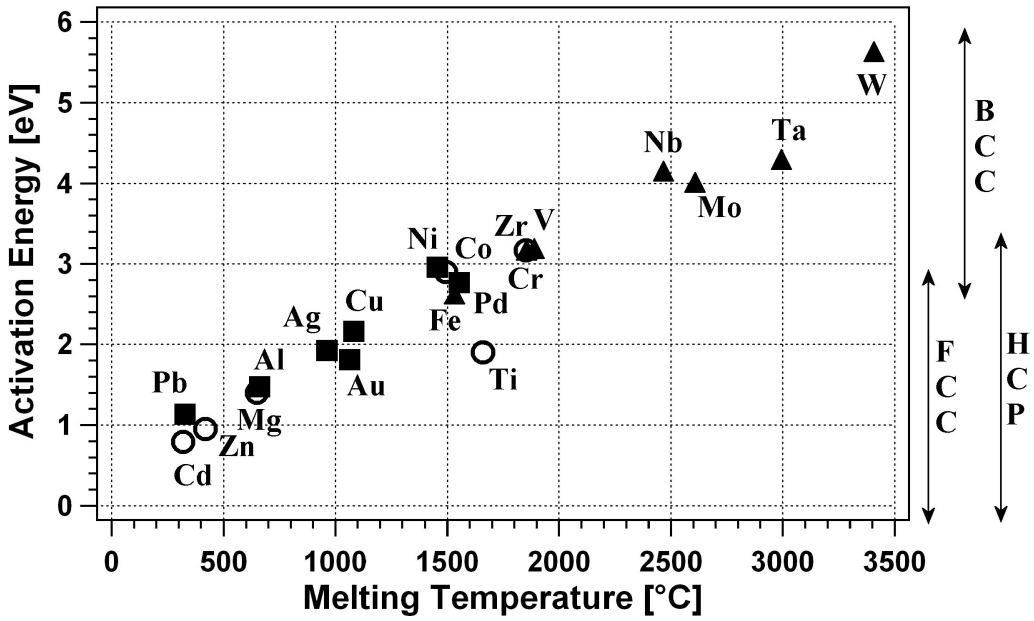

Figure 7.2: Activation energy for bulk diffusion of metallic materials as a function of the melting temperature. The materials are categorized in three structural groups: FCC (■); BCC (▲); HCP (O). The data is obtained from [20, 21, 22, 23, 24]

exact data is available for all diffusion barriers, the activation energy for bulk diffusion is used as a reference. The biaxially thin film with the lowest activation energy for bulk diffusion is Cr. Therefore, an activation energy 3 eV is a lower limit to obtain a zone T growth and hence, a biaxial alignment.

So, for FCC materials, it is expected that the diffusion barriers will be lower than for BCC materials. Therefore, it is likely that a zone II structure will evolve. It is confirmed by Thompson [25] that growth of polycrystalline thin films with a FCC structure is mostly characterized by a zone II growth. For example, sputter deposited Au [26] and Al [27] thin films have a typical zone II structure. However, in sputter deposition, the adparticles arrive with an energy of a few eV. If it turns out that the diffusion barriers are too low, other deposition techniques can be used to reduce to mobility. For example in evaporation, the adparticle energy (E ~ 0.1 eV) is much lower than in sputter deposition. However also with this technique a zone II structure is observed for various FCC structured materials (Au [28]; Ag [29]). To our knowledge, no PVD technique exists whereby the energy of the arriving adparticle is low enough to obtain a zone T structure for these materials. It can be concluded that no biaxial alignment will be possible for most of the FCC materials. Again, if Fig. 7.2 is used as a reference, materials with an activation energy below 2 eV,[1] will exhibit a zone II structure and for these materials no biaxial alignment will be observed.
In-between 2 and 3 eV, no prediction can be made. With some PVD deposition techniques (e.g. evaporation) it should be possible to limit the energy at which the adparticle arrives at the surface,

[1] 2 eV is taken as an upper limit because all FCC materials which have been described here (Al, Ag, Au) have an activation energy below 2 eV.

through which a zone T structure can evolve. For example, Ni and Pd are doubtful. The activation energy for bulk diffusion is comparable to that of Cr (3 eV). Because Cr in deposited in Zone T, it could be possible that Ni or Pd exhibits a zone T structure and consequently a biaxial alignment can occur.
HCP materials have an activation energy for bulk diffusion which is similar to that of FCC materials. If the same reasoning is used as for FCC materials, HCP materials for which the activation energy is below 2 eV, will exhibit a zone II structure and no biaxial alignment will occur. As such, no biaxial alignment is expected for Mg or Zn thin films. Also the HCP materials have also doubtful cases. Two examples are Co and Zr, because their activation energy is close that of Cr (3 eV). For these two materials, it could be possible to grow them in zone T and so a biaxial alignment should be possible.

It is interesting to remark that there is a linear correlation between the activation energy for bulk diffusion and the melting temperature of the material (Fig. 7.2). This used as a rule of thumb for pure metallic systems: if the melting temperature is too low, the diffusion barriers will be low, a zone II structure will evolve and no biaxial alignment will be possible. Hence, the melting temperature can be a fast indicator for the possible growth of biaxially aligned thin films. For example, FCC Ir has a melting temperature of 2410 ^{o}C. This point is not shown on Fig. 7.2 because no data is found in literature. Because of the linear correlation, it is expected that the activation energy for bulk diffusion is about 4 eV. If all the other diffusion barriers scale with the bulk diffusion, than it should be possible to grow biaxially aligned Ir thin films. Once more, don't forget that all diffusion barriers should be known and exceptions on this rule can be expected.

For materials with low diffusion barriers, there is a possibility to grow biaxially aligned thin films. As mentioned in chapter 6, impurities can change the diffusion barriers. If the impurity acts as an inhibitor, the diffusion barriers will be increased and the adparticle mobility will decrease. A change from zone II to zone T is expected. As a result, with the codeposition of impurities, it should be possible to grow biaxially aligned thin films with low diffusion barriers. This is confirmed by two experiments described in literature. Hashimoto et al. [14] grew Al thin film on a tilted substrate with the codeposition of O_2. For specific O_2 concentrations, they observed a biaxial alignment. Itoh et al. [15] deposited biaxially aligned Co thin films with various O_2 concentrations. They also observed a biaxial alignment.

7.2 Biaxial Alignment in Multicomponent Systems

Similar to the metallic thin films, the growth of thin film composed of two or more elements will depend on the diffusion barriers. However, for these films, valuable information about the various diffusion barriers is even more scarce than for metallic systems. Additionally, different diffusion barriers will be expected for the diffusion of the various components, through which the number of barriers multiplies. Because it is a time-consuming task to find some diffusion barriers of the materials and furthermore the few barriers that could be obtained are often questionable, another approach is used to get an idea whether biaxial alignment will be possible. Hereby, the microstructure that is observed in normal deposition conditions (i.e. without substrate heating or a high energetic bombardment) is used as an indicator. If polycrystalline thin films exhibit a zone T structure in normal deposition conditions, than it is likely that those material could be

deposited with a biaxial alignment. If a zone II structure is observed, than it is expected that the diffusion barriers are low. In this case, biaxial alignment will only occur when the energy of the arriving adparticle is reduced or if the ES barrier is high. If a zone I structure is observed or if only at elevated temperature a crystalline thin films are observed, than most probable the diffusion barriers will be high. Biaxial alignment will only occur if the energy of the diffusion particle is increased (e.g. by increasing the substrate temperature).

For all the materials in the various isostructural groups, this reasoning should be applied. This approach is elucidated only for a few isostructural groups. Suggestion whether biaxial alignment can occur or not, will be illustrated using a typical material this group. It is likely that the diffusion barriers of the materials within a specific group are comparable if the melting temperature is about the same. It is plausible that there is a linear correlation between the melting temperature and the diffusion barriers. This is a similar behaviour as for pure metallic materials (Fig. 7.2). However, the slope of this line will probably be different.

Rocksalt Structure

For these materials, biaxially aligned thin films are observed with normal sputter conditions (Table 7.1). A typical zone T structure is observed. It is likely that thin films of other rocksalt structured materials with a comparable melting temperature will also exhibit a zone T structure. Hence, these thin films can be deposited with a biaxial alignment. Indeed, MgO and TiN are two thin films for which a biaxial alignment is observed and both have a comparable melting temperature (2830 ^{o}C and 2930 ^{o}C, respectively). Also CrN thin films are deposited with a biaxial alignment. Because the melting temperature of CrN is 1080 ^{o}C, it is plausible that a biaxial alignment is possible for rocksalt structured materials if the melting temperature ranges between 1000 ^{o}C and 3000 ^{o}C, roughly.

Fluorite Structure

The same reasoning can be applied for materials with a fluorite structure. Thin films with a fluorite structure are grown with a biaxial alignment. Hence, it is likely that fluorite materials with comparable melting temperature as YSZ (2680 ^{o}C) or CeO_2 (2600 ^{o}C) can exhibit a biaxial alignment.
Mahieu [30] observed that the best biaxially aligned YSZ thin films are deposited with a positive substrate bias. With a positive bias, electrons are attracted to the substrate with results in an increased energy supply to the growing film. In contrast, a floating potential is optimal to grow biaxially aligned MgO thin films. This result suggest that the diffusion barriers of YSZ are higher than of MgO.

Corundum

Witthaut [31] mentioned that Al_2O_3 thin films grown by PVD techniques in generally leads to the formation of an amorphous or nanocrystalline phase. This suggests a zone I structure. A stable crystalline phase is only formed if the substrate temperature is above 1000 ^{o}C. Zywitzki [32] pointed out that crystalline Al_2O_3 thin films can be grown at 760 ^{o}C in presence of a high plasma density at the substrate. It can be concluded that only if the energy transfer between the

substrate and the diffusing adparticles is high (e.g. by heating the substrate or by bombardment with energetic particles), a crystalline thin film can be grown. All these observations suggest that the diffusion barriers of Al_2O_3 are high. Hence, a zone T growth will only be possible at high substrate temperatures. However, no polycrystalline Al_2O_3 with a zone T structure are observed in literature. Therefore, it remains doubtful if it's possible to grow biaxial aligned thin films with a corundum structure by PVD techniques.

Wurtzite

As mentioned in chapter 4, InN and more general wurtzite structured materials, have low diffusion barriers. At sputter conditions, the thin film would exhibit a zone II structure. However, typically these materials have a high ES barrier, through which mound formation can occur. In case of mound formation, a biaxial alignment similar as for InN thin films is expected.
Another possibility to obtain a biaxial alignment, is by evaporation. Because the energy of the arriving adparticles is much lower than for sputtering, the adparticle mobility will be lower. Depending on the magnitude of the diffusion barriers, it could be possible that the thin film is deposited in zone T and hence a biaxial alignment can evolve.

Bibliography

[1] S. Mahieu, P. Ghekiere, G. De Winter, R. De Gryse, D. Depla, G. Van Tendeloo, O. I. Lebedev, Biaxially aligned titanium nitride thin films deposited by unbalanced magnetron sputtering, Surf. Coat. Technol. 200 (8) (2004) 2764–2768.

[2] S. Mahieu, P. Ghekiere, G. De Winter, R. De Gryse, D. Depla, G. Van Tendeloo, O. I. Lebedev, Biaxially aligned yttria stabilized zirconia and titanium nitride layers deposited by unbalanced magnetron sputtering, Solid State Phen. 105 (2005) 447–452.

[3] M. Bauer, R. Semerad, H. Kinder, Ybco films on metal substrates with biaxially aligned MgO buffer layers, IEEE Trans. Appl. Supercond. 9 (2) (1999) 1502–1505.

[4] M. P. Chudzik, R. E. Koritala, L. Luo, D. Miller, U. Balachandran, C. R. Kannewurf, Mechanism and processing dependence of biaxial texture development in magnesium oxide thin films grown by inclined-substrate deposition, IEEE Trans. Appl. Supercond. 11 (1) (2001) 3469–3472.

[5] B. Ma, M. Li, Y. A. Jee, R. E. Koritala, B. L. Fisher, U. Balachandran, Inclined-substrate deposition of biaxially textured magnesium oxide thin films for YBCO coated conductors, Physica C 366 (4) (2002) 270–276.

[6] Z. B. Zhao, Z. U. Rek, S. M. Yalisove, J. C. Bilello, Evolution of in-plane texture in reactively sputtered crn films, J. Appl. Phys. 97 (2) (2005) 023525.

[7] K. Hasegawa, Y. Nakamura, T. Izumi, Y. Shiohara, Biaxially aligned YBCO film tapes fabricated by all pulsed laser deposition, Appl. Supercond. 4 (10-11) (1996) 487–493.

[8] S. Mahieu, G. De Winter, D. Depla, R. De Gryse, J. Denul, A model for the development of biaxial alignment in yttria stabilized zirconia layers, deposited by unbalanced magnetron sputtering, Surf. Coat. Techol. 187 (2004) 122–130.

[9] M. Bauer, J. Schwachulla, S. Furtner, P. Berberich, H. Kinder, Deposition of YSZ, CeO_2 and MgO on amorphous and polycrystalline substrates, Inst. Phys. Conf. Ser. 158 (2) (1997) 1077–1080.

[10] O. P. Karpenko, J. C. Bilello, S. M. Yalisove, Combined transmission electron microscopy and x-ray study of the microstructure and texture of sputtered Mo films, J. Appl. Phys. 76 (8) (1994) 4610–4617.

[11] Z. B. Zhao, S. M. Yalisove, Z. U. Rek, J. C. Bilello, Evolution of anisotropic microstructure and residual stress in sputtered Cr films, J. Appl. Phys. 92 (12) (2002) 7183–7192.

[12] G. C. A. M. Janssen, P. F. A. Alkemade, V. G. M. Sivel, S. Y. Grachev, J. D. Kamminga, Anisotropic growth of chromium films during sputter deposition on substrates in planetary motion, J. Vac. Sci. Technol. A 22 (4) (2004) 1773–1777.

[13] K. Okamoto, K. Itoh, Incidence angle dependences of columnar grain structure and texture in obliquely deposited iron films, Jpn. J. Appl. Phys. 44 (3) (2005) 1382–1388.

[14] T. Hashimoto, K. Okamoto, K. Hara, M. Kamiya, H. Fujiwara, Alignment of columnar grains in obliquely deposited aluminum films, Thin Solid Films 182 (1989) 197–207.

[15] K. Itoh, F. Ichikawa, Y. Ishida, K. Okamoto, T. U. T, I. Iguchi, Columnar grain structure in cobalt films deposited obliquely by introducing oxygen during sputtering, J. Magn. Magn. Mater. 248 (1) (2002) 112–120.

[16] R. M. Bradley, J. M. E. Harper, D. A. Smith, Theory of thin-film orientation by ion-bombardment during deposition, J. Appl. Phys. 60 (12) (1989) 4160–4164.

[17] K. G. Ressler, N. Sonnenberg, M. J. Cima, Mechanism of biaxial alignment of oxide thin films during ion-beam-assisted deposition, J. Am. Ceram. Soc. 80 (10) (1997) 2637–2648.

[18] L. Dong, D. J. Srolovitz, Texture development mechanisms in ion beam assisted deposition, J. Appl. Phys. 84 (9) (1998) 5261–5269.

[19] Y. Iijima, M. Hosaka, N. Tanabe, N. Sadakata, T. Saitoh, O. Kohno, Growth structure of yttria-stabilized-zirconia films during off-normal ion-beam-assisted deposition, J. Mater. Res. 13 (11) (1998) 3106–3113.

[20] F. C. Nix, F. E. Jaumot, Self-diffusion in cobalt, Phys. Rev. 82 (1951) 72–74.

[21] S. J. Chen, H. L. Huang, Diffusion activation energies in Face-Centered Cubic metals using the morse potential function, Chin. J. Phys. 19 (4) (1981) 106–112.

[22] G. M. Hood, H. Zou, D. Gupta, R. J. Schultz, α-Zr self-diffusion anisotropy, J. Nucl. Phys. 223 (2) (1995) 122–125.

[23] C. Kittel, Introduction to solid state physics, 7th Edition, John Wiley & Sons, Inc., New York, 1996.

[24] B. B. Panigrahi, M. M. Godkhindi, K. Das, P. G. Mukunda, P. Ramakrishnan, Sintering kinetics of micrometric titanium powder, Mat. Sci. Engin. A 396 (1-2) (2005) 255–262.

[25] C. V. Thompson, Structure evolution during processing of polycrystalline films, Annu. Rev. Mater. Sci. 30 (2000) 159–190.

[26] Y. Jiang, B. Guan, X. L. Xu, Microstructure of Au film prepared by magnetron sputtering deposition, Chin. Phys. Lett. 22 (3) (2005) 730–732.

[27] A. E. Lita, J. E. Sanchez, Effects of grain growth on dynamic surface scaling during the deposition of Al polycrystalline thin films, Phys. Rev. B 61 (11) (2000) 7692–7699.

[28] C. C. Wong, H. I. Smith, C. V. Thompson, Surface-energy-driven secondary grain growth in thin Au films, Appl. Phys. Lett. 48 (5) (1986) 335–337.

[29] M. Adamik, P. Barna, I. Tomov, Texture and grain structure in polycrystalline silver films deposited by partially ionised beam, Vacuum 61 (2001) 251–255.

[30] S. Mahieu, Biaxial alignment in sputter deposited thin films, Ph.D. thesis, Ghent University (2006).

[31] M. Witthaut, R. Cremer, K. Reichert, D. Neuschütz, Preparation of Cr_2O_3-Al_2O_3 solid solutions by reactive magnetron sputtering, Mikrochim. Acta 133 (2000) 191–196.

[32] O. Zywitzki, G. Hoetzsch, F. Fietzke, K. Goedicke, Effect of the substrate temperature on the structure and properties of Al_2O_3 layers reactively deposited by pulsed magnetron sputtering, Surf. Coat. Technol. 82 (1-2) (1996) 169–175.

Summary

In this thesis, the growth of biaxially aligned thin films which are deposited on a tilted substrate by magnetron sputtering, is examined. The aim of this research is to understand the growth mechanism of biaxially aligned thin films and elucidate the fundamental processes that influence the structure evolution.

Aspects of Thin Film Growth

To determine the origin of biaxial alignment in thin films, a fundamental knowledge of thin film growth is essential. Therefore, the first chapter is dedicated to the fundamental aspects of thin film growth.
Particles that are produced by sputtering, can condense on the substrate. Depending on the energy, the particles will be able to diffuse. Because diffusion plays a key role in the growth of thin films, this atomic process is discussed in detail. After this, the various fundamental processes that are decisive for the growth of thin films, being nucleation, crystal growth and restructurative grain growth, will be discussed. Nucleation is the process where diffusing adparticles aggregate and evolve into a stable island. By the incorporation of diffusing adparticles and/or by direct capture from the vapour flux, these islands will grow and evolve into a continuous film (crystal growth). If the energy of the particles in the film is sufficient, restructurative grain growth can occur, through which the thin film growth will modify.
A convenient way to describe the structure evolution of polycrystalline thin films, is the use of the Structure Zone Model (SZM). Initially, the SZM is used to classify the microstructure of thin films as a function of the deposition parameters. This was purely based on experimental observations. However, because there is a correlation between the microstructure and the fundamental growth processes, the SZM can be used to verify which growth process occurs. This resulted in the classification in three zones (zone I, zone T, zone II) as a function of the energy of the adparticles on the surface. Zone I is described by a ballistic model. In zone T, the structure evolution is characterized by an overgrowth processes of neighbouring grains. In zone II, restructurative grain growth determines the structure evolution. Both in zone T as in zone II, the thin film will exhibit a preferential out-of-plane alignment.
Throughout this first chapter, the influence of impurities on the various aspects of thin film growth has briefly been discussed. This resulted in the formulation of a revised structure zone model, which takes into account the presence of minute impurity concentrations. In chapter 6, the revised structure zone model will be discussed in more detail. Additionally, the implication of the

codeposition of impurities on the growth of biaxially aligned thin films will be examined.

Sputter Deposition of Thin Films

In this work, the thin films are deposited by magnetron sputtering. This deposition technique is discussed in chapter 2. Sputtering is a plasma assisted technique which is often used to deposit thin films.
A cathode which contains the source material, is held at a negative potential. As a result, Ar^+ ions are accelerated to the cathode. After impact, a collision cascade can occur in which particles can be ejected from the cathode surface. These sputtered particles travel through the vapour phase towards the substrate where they can condense. Next to the inert Ar gas, a reactive gas can be added during deposition. By doing so, it is possible to deposit a compound from a pure metallic target.

Thin Film Analysis

Chapter 3 describes the techniques to characterize the thin films. The crystallographic orientation is determined by X ray diffraction. The preferential out-of-plane orientation is determined by angular scans, while the degree of in-plane alignment is determined by pole figures. Scanning electron microscopy (SEM) is used to image the surface of the thin film. Transmission electron microscopy (TEM) is also used to analyse to microstructure. The power of TEM is that both information about the microstructure and crystallographic texture can be obtained. Additionally, magnifications to atomic scale are possible. Due to the complexity of sample preparation, only a selected number of thin films is examined by TEM. The chemical composition of the thin film is determined by X ray Photoelectron Spectroscopy.

Growth of Biaxially Aligned Thin Films

Three materials have been examined: MgO, Cr and InN. For these three materials, it was possible to deposit biaxially aligned thin films. The experimental results are presented in chapter 4. A clear difference between the growth of MgO and Cr thin films on the one hand, and InN thin films on the other hand, is observed. For MgO and Cr thin films, the growth is characterized by the overgrowth of neighbouring grains, which indicates a zone T growth. For InN thin films, it has been discussed that an orientation selection occurs at the initial stages of the growth, which is typical for zone II. An in-plane alignment occurs when the substrate is tilted with respect to the incoming material flux. The growth mechanism of biaxially aligned thin films can be broken up into the evolution of the out-of-plane alignment on the one hand, and the evolution of the in-plane alignment on the other hand. For both, a growth model is proposed in chapter 4.

Out-of-plane Alignment: Because MgO and Cr thin films are deposited in zone T and InN thin films are deposited in zone II, the fundamental processes which determine the structure evolution of the thin film will be different in both cases.
In case of zone T growth, the out-of-plane alignment evolves due to an anisotropy in growth rate of neighbouring grains. In zone T, the grains are truncated by a crystal habit. This crystal habit is composed of planes with the lowest normal growth rate. Depending on the orientation of the crystal habit, hence, depending on the crystallographic orientation of the grain, specific grains

will have a higher perpendicular growth rate than others. If the geometric fastest growth direction of the crystal habit of the grain is parallel to the substrate normal, then these grains will have the highest perpendicular growth rate. They will overgrow the others and determine the out-of-plane alignment.
For InN thin films (zone II), orientation selection occurs at the initial stages of the growth. As a result, the total film will aim for the lowest surface and interface energy. The grains of which the plane with lowest surface energy is parallel to the substrate, will be favoured and the corresponding out-of-plane alignment will be observed.

In-plane Alignment In the experiments, an in-plane alignment is observed when tilting the substrate with respect to the incoming material flux. The observations are similar for the three materials, which suggests that the origin of the in-plane alignment has to be similar.
When the substrate is tilted with respect to the incoming material flux, the particles arrive at the substrate with a specific angle. Because of the conservation of momentum, the particle will have a specific diffusion direction. The diffusion direction corresponds to the orthogonal projection of the incoming direction of the particles. If the grains in the polycrystalline thin film are limited by a well-defined shape, then there can be an anisotropy in number of diffusing adparticles that the grain will incorporated. The grains of both MgO and Cr thin films are truncated by a specific crystal habit (typical for zone T). Also the grains of the InN thin film have a well-defined shape because of the mound formation which originates from a high Ehrlich-Schwoebel barrier. Owing to the direction diffusion and the well-defined shape, the number of captured particles will depend on the in-plane orientation of the grain because of a difference in capture length. It is discussed that the grains with the highest capture length, will capture the highest number of diffusing adparticles. As a result, these grains will grow faster and overgrow the other grains. Only grains with a specific in-plane alignment will survive.

Influence of the Deposition Parameters

A lot of deposition parameters can be varied in sputtering. By connecting the deposition parameters to the elementary processes which determine the structure evolution, a detailed description of the growth of biaxially aligned thin films is possible. This is the main topic in chapter 5, which discusses the influence of the deposition parameters on the growth of biaxially aligned thin films. The influence of the deposition parameters can be reduced to two fundamental parameters: the incoming direction of the particles and the energy of the particles on the surface (i.e. the mobility).
To obtain an in-plane alignment, there has to be directional diffusion. When the directional diffusion is more pronounced, the degree of in-plane alignment improves. Often, there is a spread on the incoming direction of the adparticles, through which there will be a spread on the diffusion direction. If the spread is high, the degree of in-plane alignment get worse.
The second parameter which influences the biaxial alignment, is the energy of the diffusing adparticles. The energy of the paricles depends on the energy at which they arrive at the substrate. On its turn, the energy at which the particles arrive at the substrate, depends on the energy when sputtered from the target. Hereby, the energy loss during the transport to the substrate, has to be taken into account. Additionally, there can be an energy transfer between the diffusing adparticles and the film, for example, when the growing film is bombarded with low energetic particles.

Both MgO, Cr and InN thin films must have an optimal energy to have a preferential out-of-plane as well as an in-plane alignment.
By changing the deposition parameters, both fundamental parameters can modify. Consequently, an optimal value is often observed when varying the different deposition parameters.

Impurity Induced Texture Change in Thin Films

Chapter 6 describes the influence of impurities on the growth of biaxially aligned thin films. In previous chapters, it has been assumed that the deposition is carried out in pure conditions. However, a minute concentration of impurities is always codeposited during thin film growth. Because impurities act directly on the atomic processes taking place at the surface, the structure evolution can change and hence, the codeposition of impurities should not be neglected.
To determine the influence of impurities on the growth of biaxially aligned thin films, impurities are added during the deposition in a controlled way. For the various materials, the change in biaxial alignment is investigated as a function of the impurity concentration.
The change in biaxial alignment and microstructure due to the codeposition of O_2 or N_2 during the growth of Cr thin films can be explained by the different behaviour of the impurities on the various crystallographic planes. The growth of the plane which determines the crystal habit in pure conditions, is hindered first by the impurities. Because the growth of the other planes is less influenced, the grains will have a different truncation. Based on the model that is described in chapter 4, the change in biaxial alignment can be explained.
The codeposition of O_2 during the growth of InN thin films causes also a change in biaxial alignment. Furthermore, a change from zone II to zone T is observed. This can be explained by the hindering of the orientation selection by O_2. As a consequence, the thin film will not longer aim for the lowest surface and interface energy. The model for biaxial alignment is still applicable in these conditions.
For MgO thin films, the influence of N_2 on the structure evolution is examined. It has been observed that N_2 promotes the growth of biaxially aligned thin films.
These results indicate that impurities strongly influence the microstructure and the crystallographic orientation. Neglecting the presence of impurities, can cause a misinterpretation of the results and can lead to questionable models.

Extrapolation to Other Materials

In literature, only a few materials with a biaxial alignment are observed. The seventh chapter examines whether it is possible to deposit other materials with a biaxial alignment. The reasoning is based on the model which is developed in chapter 4.
It is discussed that the magnitude of the diffusion barriers determines the possibility and the conditions to grow biaxially aligned thin films. In case the diffusion barriers are low, the energy of the diffusing adparticles should be strongly reduced. In case of high barriers, it is likely that an additional energy supply to the growing film will be needed to grow biaxially aligned thin films.

Samenvatting

Dit proefwerk bestudeert de groei van biaxiaal gealigneerde dunne films die afgezet zijn op een gekanteld substraat door middel van magnetron sputteren. De doelstelling van dit onderzoek is het groeimechanisme van deze biaxiaal gealigneerde dunne films te begrijpen en fundamentele processen die de structuur evolutie beïnvloeden te achterhalen.

Aspecten van de dunne film groei

Om de oorsprong van biaxiale alignatie in dunne films te achterhalen, is een elementaire kennis over de algemene dunne film groei onmisbaar. Daarom wijdt het eerste hoofdstuk zich volledig aan de fundamentele aspecten die de structuur evolutie van de dunne film bepalen.
Deeltjes die gegenereerd zijn door het sputteren, kunnen condenseren op het substraat. Afhankelijk van de energie waarmee de deeltjes toekomen, zullen de deeltjes al dan niet diffunderen. Omdat de diffusie een zeer belangrijke rol speelt in de groei van dunne films, wordt uitgebreid aandacht besteed aan dit atomair proces. Daarna worden stapsgewijs de verschillende processen besproken die een rol spelen in de groei van dunne films zijnde nucleatie, kristalgroei en herstructurerende korrelgroei. Nucleatie is het proces waarbij diffunderende addeeltjes zich kunnen verenigen en uitgroeien tot een stabiel eiland. Door de incorporatie van diffunderende addeeltjes en/of door directe vangst van de deeltjes vanuit de gasfase, zullen deze eilanden groeien en evolueren naar een continue film (kristalgroei). Indien de deeltjes in de film voldoende energie bezitten, kan herstructurerende korrelgroei optreden waardoor de filmgroei zal wijzigen.
Het Structuur Zone Model (SZM) is een handige manier om de structuur evolutie van polykristallijne dunne films te beschrijven. Oorspronkelijk werd de microstructuur van de dunne films geclassificeerd in functie van de depositieparameters. Dit SZM was louter gebaseerd op experimenteel waarnemingen. Omdat er een verband bestaat tussen de microstructuur en de fundamentele groeiprocessen, kan het SZM ook gebruikt worden om na te gaan welke groeiprocessen optreden. Dit leidde tot een onderverdeling in drie zones (zone I, zone T en zone II) in functie van de energie van de deeltjes op het oppervlak. Zone I wordt beschreven door een ballistisch model. In zone T wordt de structuur evolutie gekarakteriseerd door een overgroeiproces van naburige korrels en in zone II is het optreden van herstructurerende korrelgroei bepalend voor de groei van de dunne film. Zowel in zone T als in zone II zal de dunne film een preferentiële uit-het-vlak oriëntatie hebben.
Doorheen dit eerste hoofdstuk is bij elk aspect de mogelijke invloed van onzuiverheden kort aangehaald. Dit resulteerde in het opstellen van een uitgebreid structuur zone model dat naast de

invloed van de energie van de addeeltjes, ook de onzuiverhedenconcentratie tijdens de groei in rekening brengt. In hoofdstuk 6 wordt uitgebreid hierop teruggekomen en wordt er gekeken naar de implicaties van de codepositie van onzuiverheden tijdens de groei van biaxiaal gealigneerde dunne films.

Sputter depositie

In dit onderzoek zijn de dunne films afgezet door middel van magnetron sputteren. Deze depositietechniek wordt toegelicht in hoofdstuk 2. Sputteren is een plasma geassisteerde techniek die veel gebruikt wordt voor het afzetten van deklagen. Een kathode die het bronmateriaal bevat, wordt op een negatieve potentiaal gehouden. Hierdoor worden Ar^+ ionen versneld naar de kathode. Na impact kan er een botsingscascade zijn waarbij deeltjes losgemaakt worden van het kathodeoppervlak. Deze deeltjes bewegen zich in de gasfase naar het substraat waarop ze kunnen condenseren. Naast het draaggas is het mogelijk om een reactief gas toe te voegen tijdens het sputteren. Hierdoor is het mogelijk om een verbinding af te zetten van een puur metallisch target.

Analyse van de dunne films

Hoofdstuk 3 beschrijft de analysetechnieken die gebruikt zijn voor de karakterisatie van de dunne films. De kristallografische oriëntatie van de dunne film is onderzocht aan de hand van X - stralen diffractie. De preferentiële uit-het-vlak alignatie van de dunne film is onderzocht met angulaire scans, terwijl de graad van in-het-vlak alignatie bepaald is aan de hand van poolfiguren. Scanning elektronen microscopie (SEM) is gebruikt om een beeld te verkrijgen van het oppervlak van de dunne film. Transmissie elektronen microscopie (TEM) is eveneens gebruikt voor het analyseren van de microstructuur. De kracht van TEM is dat het zowel informatie over de microstructuur en de kristallografische oriëntatie gegeven wordt. Bovendien zijn vergrotingen mogelijk tot op atomaire schaal. Door de complexiteit van de monsterpreparatie, is TEM analyse gebeurd voor een selectief aantal monsters. De chemische samenstelling is onderzocht met X-stralen foto-elektronen spectroscopie

Groei van biaxiaal gealigneerde dunne films

In dit onderzoek zijn drie materialen onderzocht: MgO, Cr en InN. Voor de drie materialen is het mogelijk dunne films af te zetten met een biaxiale alignatie. De experimentele resultaten worden gepresenteerd in het vierde hoofdstuk. Er is een duidelijk verschil waargenomen in de groei van MgO en Cr dunne films enerzijds en InN dunne films anderzijds. Voor MgO en Cr is de groei gekarakteriseerd door een evolutionaire overgroei van naburige korrels, wat typisch is voor zone T. Voor de InN dunne films is beredeneerd dat er een oriëntatieselectie optreedt in het begin van de dunne film groei, wat wijst op een zone II. Kenmerkend is, dat een in-het-vlak alignatie optreedt, wanneer het substraat gekanteld wordt.
Het groeimechanisme van de biaxiaal gealigneerde dunne films is op te splitsen in het ontstaan van de uit-het-vlak alignatie enerzijds en de in-het-vlak alignatie anderzijds. Voor beide is een groeimodel voorgesteld.

Uit-het-vlak alignatie: Omdat MgO en Cr dunne films afgezet zijn in zone T en InN dunne films afgezet zijn in zone II, zullen andere fundamentele processen een rol spelen in de groei en

zal de structuur evolutie in beide situaties anders zijn.
In het geval van een zone T groei, ontstaat de uit-het-vlak alignatie door de anisotropie in groeisnelheid van naburige korrels. In zone T zijn de korrels begrensd door een kristal habitus. Deze kristal habitus is opgebouwd uit vlakken met de laagste groeisnelheid. Afhankelijk van de oriëntatie van de kristal habitus, en dus afhankelijk van de oriëntatie van de korrel, zullen bepaalde korrels een grotere loodrechte groeisnelheid hebben. Indien de geometrisch snelste groeirichting van de kristal habitus van de korrel evenwijdig is met de substraatnormaal, dan zullen die korrels de snelste groeisnelheid hebben, de andere overgroeien en de uit-het-vlak alignatie bepalen.
Voor InN dunne films (zone II) vind er een oriëntatieselectie plaats. Hierbij zal de totale film streven naar een minimale oppervlakte- en grensvlakenergie. Bijgevolg zullen de korrels waarvan de vlakken met de laagste oppervlakte energie evenwijdig zijn met het substraat bevoordeeld worden en zal een corresponderende uit-het-vlak alignatie waargenomen worden.

In-het-vlak alignatie: Experimenteel is een in-het-vlak alignatie waargenomen wanneer het substraat gekanteld wordt ten opzichte van de inkomende materiaalflux. De waarnemingen zijn gelijkaardig voor de drie materialen. Het ontstaan van de in-het-vlak alignatie moet daarom eenzelfde oorsprong hebben. Wanneer het substraat gekanteld wordt ten opzichte van de materiaalflux, komen de deeltjes onder een bepaalde hoek toe op het substraat. Door het behoud van impuls zullen de deeltjes in een welbepaalde richting diffunderen. De diffusierichting komt overeen met de orthogonale projectie van de invalrichting van de deeltjes. Als de korrels in de polykristallijne film begrensd zijn door een goed gedefinieerde vorm, dan kan er een anisotropie in aantal gevangen deeltjes optreden. De korrels van zowel de MgO als de Cr dunne film zijn begrensd door een welbepaalde kristal habitus (typisch voor zone T). Ook de korrels van de InN dunne film zullen een specifieke begrenzing hebben door de vorming van heuvel die ontstaat door een hoge Ehrlich-Schwoebel barrière. Door de directionele diffusie en de welbepaalde vorm, zal het aantal gevangen deeltjes afhankelijk zijn van de in-het-vlak alignatie van de korrels omdat de vangstlengte verschillend zal zijn. Het is beredeneerd dat de korrels waarvoor de vangstlengte maximaal is, dat deze korrels het meest aantal deeltjes vangen en dus sneller zal groeien dan zijn buren. Hierdoor zullen de trager groeiende korrels overgroeid worden. Het resultaat is dat enkel korrels met een wel bepaalde in-het-vlak alignatie de groei overleven.

Invloed van de depositie parameters

Bij sputter depositie kunnen er veel depositieparameters gevarieerd worden. Door de invloed van de depositieparameters te verbinden met de elementaire processen die de structuur evolutie beïnvloeden, is een gedetailleerd beeld bekomen van de groei van biaxiaal gealigneerde dunne films. Dit was het onderwerp van onderzoek in het vijfde hoofdstuk. Hierin werd de invloed van de depositieparameters op de groei van biaxiaal gealigneerde dunne lagen besproken. De invloed van de depositieparameters op de groei van biaxiaal gealigneerde dunne films was terug te leiden naar twee fundamentele parameters: de invalsrichting van de deeltjes en de energie van de deeltjes op het oppervlak (i.e. de mobiliteit).
Om een in-het-vlak alignatie te verkrijgen, moet er een sterke directionele diffusie zijn. Naarmate de diffusie meer gericht is, zal de graad van in-het-vlak alignatie groter zijn. Vaak zal er een spreiding zijn op de invalsrichting van de addeeltjes, waardoor er een spreiding zal zijn op de diffusierichting. Naarmate de spreiding groter is, zal de graad van in-het-vlak alignatie vermin-

deren.
De tweede parameter die de rol speelt bij de biaxiale alignatie is de energie van de diffunderende deeltjes. De energie van de deeltjes is afhankelijk van de energie waarmee de deeltjes toekomen op het substraat. Op zijn beurt is de energie waarmee de deeltjes toekomen, afhankelijk van de energie waarmee ze gegenereerd zijn. Hierbij moet rekening gehouden worden met het energieverlies tijdens het transport naar het substraat. Bovendien kan er een aanzienlijke energie transfer plaats vinden tussen de diffunderende deeltjes en de film, bijvoorbeeld omdat de film gebombardeerd wordt met laag-energetische deeltjes. Zowel voor MgO, Cr als voor InN dunne films, moet de deeltjes een optimale energie hebben om zowel een preferentiële uit-het-vlak als in-het-vlak alignatie te hebben.
Door de depositieparameters te variëren, worden vaak beide fundamentele parameters veranderd. Dit heeft als resultaat dat een optimale waarde bekomen wordt bij het variëren van de verschillende depositieparameters.

Textuur verandering ten gevolge van codepositie van onzuiverheden

Het zesde hoofdstuk beschrijft de invloed van onzuiverheden op de groei van biaxiaal gealigneerde dunne films. In de vorige hoofdstukken werd er telkens van uit gegaan dat de depositie uitgevoerd is onder optimale, pure, omstandigheden. Het is echter zo dat er altijd een kleine concentratie onzuiverheden mee afgezet wordt tijdens de groei van dunne films. Bovendien mag de codepositie van onzuiverheden niet verwaarloosd worden omdat de onzuiverheden direct inwerken op de atomaire processen die plaats vinden aan het oppervlak, waardoor de structuur evolutie van de dunne film kan wijzigen.
Om de invloed van onzuiverheden op de groei te kennen, werd op een gecontroleerde manier onzuiverheden toegevoegd tijdens de groei van de biaxiaal gealigneerde dunne films. Voor de verschillende materialen is nagegaan hoe de biaxiale alignatie verandert in functie van een stijgende onzuiverhedenconcentratie.
De verandering in biaxiale alignatie en microstructuur ten gevolge van de codepositie van O_2 of N_2 tijdens de groei van Cr dunne films is te verklaren doordat de onzuiverheden de verschillende kristallografische vlakken anders beïnvloeden. De groei van het vlak dat in pure omstandigheden de kristal habitus bepaald, wordt met de codepositie van deze onzuiverheden volledig geblokkeerd. Omdat de groei van de andere vlakken minder gehinderd wordt, zal de korrel een andere begrenzing hebben. Steunend op het model dat ontwikkeld is in hoofdstuk 4, kan de verandering in biaxiale alignatie verklaard worden.
De codepositie van O_2 tijdens de groei van InN dunne films zorgt ook voor een verandering van biaxiale alignatie. Daaraan gekoppeld is een verandering in microstructuur van zone II naar zone T waargenomen. Dit wordt verklaard doordat de oriëntatieselectie aan het begin van de groei verhinderd door O_2. Hierdoor kan de dunne film niet langer streven naar de minimale oppervlakte en grensvlakenergie. De groei zal gekenmerkt worden door de groei volgens een bepaalde kristal habitus. Het model voor biaxiale alignatie blijft toepasbaar in deze omstandigheden.
Voor MgO dunne films is de invloed van N_2 op de structuur evolutie onderzocht. Er is waargenomen dat stikstof de groei van de biaxiale gealigneerde dunne film positief beïnvloedt.
Deze resultaten tonen aan dat onzuiverheden zowel de microstructuur als de kristallografische oriëntatie sterk beïnvloeden. De aanwezigheid van onzuiverheden verwaarlozen, kan tot een verkeerde interpretatie van de resultaten leiden en resulteren in foutieve modellen.

Uitbreiding naar andere materialen

In de literatuur zijn er slechts een beperkt aantal materialen waarvoor een biaxiale alignatie waargenomen is. Het zevende hoofdstuk bekijkt of het mogelijk is om andere materialen met een biaxiale alignatie te groeien. De redenering is gebaseerd op het model dat ontwikkeld is in hoofdstuk 4. Het is geargumenteerd dat de grootte van de diffusiebarrières van de verschillende materialen bepalend zal zijn voor de manier waarop de biaxiale gealigneerde dunne film gegroeid moet worden. In het geval van lage barrières, zal de energie van de diffunderende deeltjes zeer sterk beperkt moeten worden. In het geval van hoge barrières zal het waarschijnlijk zijn dat een extra energietoevoer nodig zal zijn om een biaxiale alignatie te verkrijgen.

Appendix A

Acronyms

BCC Body-Centered Cubic

Cr Chromium

EBSD Electron Backscatter Diffraction

ED Electron Diffraction

EDX Energy Dispersive X-ray analysis

EELS Electron Energy Loss Spectroscopy

ES Ehrlich-Schwoebel

FCC Face-Centered Cubic

FM Frank - Van der Merwe

FWHM Full Width at Half Maximum

HREM High-Resolution Electron Microscopy

IBAD Ion Beam Assisted Deposition

ISD Inclined Substrate Deposition

InN Indium Nitride

JCPDS Joint Committee for Powder Diffraction Standard card

MgO Magnesium Oxide

OES Optical Emission Spectroscopy

PBC Periodic Bond Chains

PVD Physical Vapour Deposition

SEM Scanning Electron Microscopy

STEM Scanning Transmission Electron Microscopy

SK Stranski - Krastanov

SZM Structure Zone Model

TEM Transmission Electron Microscopy

TSK Terrace-Step-Kink

VW Volmer - Weber

XPS X-ray Photoelectron Spectroscopy

XRD X-ray Diffraction

Appendix B

Vector Calculations

B.1 Definitions

B.1.1 General

The scalar product of the vectors $\vec{p}$ and $\vec{q}$ is defined as

$$\vec{p} \cdot \vec{q} = |p|\,|q| \cos\theta \tag{B.1}$$

where θ is the angle between both vectors, $|p| = \sqrt{||\vec{p}||}$, $|q| = \sqrt{||\vec{q}||}$ is the length of both vectors.
The vector product of the vectors $\vec{p}$ and $\vec{q}$ is defined as

$$\vec{p} \times \vec{q} = |p|\,|q| \sin\theta\ \vec{n} \tag{B.2}$$

where $\vec{n}$ is an unit vector perpendicular to $\vec{p}$ and $\vec{q}$ and θ is the angle between both vectors.
A lattice vector $\vec{t}_{[uvw]}$, defining the crystallographic direction [*uvw*], is a linear combination of the base vectors $\vec{a}$, $\vec{b}$, $\vec{c}$ which define the edges of the unit cell.

$$\vec{t}_{[uvw]} = u\vec{a} + v\vec{b} + w\vec{c} \tag{B.3}$$

These base vectors aren't necessarily orthogonal, which is the case in an hexagonal crystal system.
Each crystal system is characterized by a symmetric matrix M, containing the scalar products of the base vectors of the lattice. This matrix M is called the metric tensor.

$$M = \begin{bmatrix} \vec{a}\cdot\vec{a} & \vec{a}\cdot\vec{b} & \vec{a}\cdot\vec{c} \\ \vec{b}\cdot\vec{a} & \vec{b}\cdot\vec{b} & \vec{b}\cdot\vec{c} \\ \vec{c}\cdot\vec{a} & \vec{c}\cdot\vec{b} & \vec{c}\cdot\vec{c} \end{bmatrix} \tag{B.4}$$

Using these notations, the scalar product $\vec{t}_{[u_1v_1w_1]} \cdot \vec{t}_{[u_2v_2w_2]}$ can be expressed as

$$\vec{t}_{[u_1v_1w_1]} \cdot \vec{t}_{[u_2v_2w_2]} = \begin{bmatrix} u_1v_1w_1 \end{bmatrix} \begin{bmatrix} \vec{a}\cdot\vec{a} & \vec{a}\cdot\vec{b} & \vec{a}\cdot\vec{c} \\ \vec{b}\cdot\vec{a} & \vec{b}\cdot\vec{b} & \vec{b}\cdot\vec{c} \\ \vec{c}\cdot\vec{a} & \vec{c}\cdot\vec{b} & \vec{c}\cdot\vec{c} \end{bmatrix} \begin{bmatrix} u_2 \\ v_2 \\ w_2 \end{bmatrix} \tag{B.5}$$

The length of the vector $\vec{t}_{[uvw]}$ is $|\vec{t}_{[uvw]}| = \sqrt{\|\vec{t}_{[uvw]}\|}$ and can be calculated by solving the matrix product. Using Eq. B.1 and Eq. B.5, the angle between $\vec{t}_{[u_1v_1w_1]}$ and $\vec{t}_{[u_2v_2w_2]}$ can be calculated.

B.1.2 Reciprocal space

The recipocal lattice provides an easy way of calculating interplanar angles and spacings. The base vectors in the reciprocal lattice $\vec{a^*}$, $\vec{b^*}$, $\vec{c^*}$ are defined as:

$$\vec{a^*} = \frac{\vec{b}\times\vec{c}}{\vec{a}\cdot(\vec{b}\times\vec{c})} \qquad \vec{b^*} = \frac{\vec{c}\times\vec{a}}{\vec{b}\cdot(\vec{c}\times\vec{a})} \qquad \vec{c^*} = \frac{\vec{a}\times\vec{b}}{\vec{c}\cdot(\vec{a}\times\vec{b})} \tag{B.6}$$

Following this definition, some basic properties of the reciprocal lattice can be derived.

$$\vec{a}\cdot\vec{a^*} = \vec{b}\cdot\vec{b^*} = \vec{c}\cdot\vec{c^*} = 1 \tag{B.7}$$

$$\vec{a}\cdot\vec{b^*} = \vec{a}\cdot\vec{c^*} = \vec{b}\cdot\vec{a^*} = \vec{b}\cdot\vec{c^*} = \vec{c}\cdot\vec{a^*} = \vec{c}\cdot\vec{b^*} = 0 \tag{B.8}$$

A reciprocal lattice vector $\vec{d^*}_{(hkl)}$, is normal to the (hkl) plane and is given by:

$$\vec{d^*}_{(hkl)} = h\vec{a^*} + k\vec{b^*} + l\vec{c^*} \tag{B.9}$$

Similar to the real space, the reciprocal system can be characterized by a symmetric matrix M^*.

$$M = \begin{bmatrix} \vec{a^*}\cdot\vec{a^*} & \vec{a^*}\cdot\vec{b^*} & \vec{a^*}\cdot\vec{c^*} \\ \vec{b^*}\cdot\vec{a^*} & \vec{b^*}\cdot\vec{b^*} & \vec{b^*}\cdot\vec{c^*} \\ \vec{c^*}\cdot\vec{a^*} & \vec{c^*}\cdot\vec{b^*} & \vec{c^*}\cdot\vec{c^*} \end{bmatrix} \tag{B.10}$$

Similar to Eq. B.5 the scalar product of two reciprocal lattice vectors $\vec{d^*}_{(h_1k_1l_1)}$ and $\vec{d^*}_{(h_2k_2l_2)}$ in reciprocal space can be expressed.

$$\vec{d^*}_{(h_1k_1l_1)} \cdot \vec{d^*}_{(h_2k_2l_2)} = \begin{bmatrix} h_1k_1l_1 \end{bmatrix} \begin{bmatrix} \vec{a^*}\cdot\vec{a^*} & \vec{a^*}\cdot\vec{b^*} & \vec{a^*}\cdot\vec{c^*} \\ \vec{b^*}\cdot\vec{a^*} & \vec{b^*}\cdot\vec{b^*} & \vec{b^*}\cdot\vec{c^*} \\ \vec{c^*}\cdot\vec{a^*} & \vec{c^*}\cdot\vec{b^*} & \vec{c^*}\cdot\vec{c^*} \end{bmatrix} \begin{bmatrix} h_2 \\ k_2 \\ l_2 \end{bmatrix} \tag{B.11}$$

The length of the vector $\vec{d^*}_{(hkl)}$ is $|\vec{d^*}_{(hkl)}| = \sqrt{\|\vec{d^*}_{(hkl)}\|}$ and can be calculated by solving the matrix product. Using Eq. B.1 and Eq. B.11, the angle between $\vec{d^*}_{(h_1k_1l_1)}$ and $\vec{d^*}_{(h_2k_2l_2)}$ can be calculated.

B.2 Hexagonal system

The base vectors in a hexagonal system comply with:

$$\begin{cases} a^2 = \|\vec{a}\| = \|\vec{b}\| \neq \|\vec{c}\| = c^2 \\ \alpha = \beta = 90^o \\ \gamma = 120^o \end{cases} \tag{B.12}$$

In a hexagonal system, mostly four indexes are used to denote a direction [uviw] or a plane (hkil), taking into account the symmetry variants. With these notations, the third index doesn't contain additional information, because it is a linear combination of the first two. To calculate angles and distances, this third index isn't used. To simplify the notation, the third index is replaced by a point in this appendix.
By solving the scalar product of the unit vectors the metric tensor in real space and reciprocal space simplifies to

$$M = \begin{bmatrix} a^2 & -\frac{1}{2}a^2 & 0 \\ -\frac{1}{2}a^2 & a^2 & 0 \\ 0 & 0 & c^2 \end{bmatrix} \tag{B.13}$$

$$M^* = \begin{bmatrix} a^{*2} & \frac{1}{2}a^{*2} & 0 \\ \frac{1}{2}a^{*2} & a^{*2} & 0 \\ 0 & 0 & c^{*2} \end{bmatrix} \tag{B.14}$$

B.2.1 Angles between Directions in Real Space

The length of a vector $\vec{t}_{[uv.w]}$ is calculated by solving the matrix product in Eq. B.5:

$$\begin{aligned} \|\vec{t}_{[uv.w]}\| &= \begin{bmatrix} u & v & w \end{bmatrix} \begin{bmatrix} a^2 & -\frac{1}{2}a^2 & 0 \\ -\frac{1}{2}a^2 & a^2 & 0 \\ 0 & 0 & c^2 \end{bmatrix} \begin{bmatrix} u \\ v \\ w \end{bmatrix} \\ &= \left(u^2 - uv + v^2\right) a^2 + w^2 c^2 \end{aligned} \tag{B.15}$$

which yields to

$$|\vec{t}_{[uv.w]}| = \sqrt{\|\vec{t}_{[uv.w]}\|} = \sqrt{\left(u^2 - uv + v^2\right) a^2 + w^2 c^2} \tag{B.16}$$

Analogously, a formula for the scalar product of two different directions can be calculated.

The angle between two directions $\vec{t}_{[u_1v_1.w_1]}$ and $\vec{t}_{[u_2v_2.w_2]}$ can be calculated through the definition of the scalar product (B.1):

$$\cos\theta = \frac{\vec{t}_{[u_1v_1.w_1]} \cdot \vec{t}_{[u_2v_2.w_2]}}{\left|\vec{t}_{[u_1v_1.w_1]}\right| \left|\vec{t}_{[u_2v_2.w_2]}\right|} \tag{B.17}$$

Example The angle between the [11.2] and [10.0] direction in hexagonal InN with a = 3.54 Å and c = 5.693 Å.

$$\begin{aligned}
\vec{t}_{[11.2]} \cdot \vec{t}_{[10.0]} &= \begin{bmatrix} 1 & 1 & 2 \end{bmatrix} \begin{bmatrix} a^2 & -\frac{1}{2}a^2 & 0 \\ -\frac{1}{2}a^2 & a^2 & 0 \\ 0 & 0 & c^2 \end{bmatrix} \begin{bmatrix} 1 \\ 0 \\ 0 \end{bmatrix} \\
&= \begin{bmatrix} 1 & 1 & 2 \end{bmatrix} \begin{bmatrix} a^2 \\ -\frac{1}{2}a^2 \\ 0 \end{bmatrix} \\
&= a^2/2 \\
&= 6.266 \text{ Å}^2 \\
|\vec{t}_{[10.0]}| &= \sqrt{(1^2 - 0 + 0)\, a^2 + 0^2 c^2} = a = 3.54\text{Å} \\
|\vec{t}_{[11.2]}| &= \sqrt{(1^2 - 1 + 1^2)\, a^2 + 2^2 c^2} = \sqrt{a^2 + 4c^2} = 11.924\text{Å} \\
\theta &= \arccos\left(\tfrac{6.266}{3.54 \cdot 11.924}\right) = \arccos(0.1484) = 81.46^{\text{o}}
\end{aligned}$$

B.2.2 Angles between Planes in Reciprocal Space

The angle between two planes can easily be obtained by going to the reciprocal space and using the reciprocal lattice vector $\vec{d}^*_{(hk.l)}$, normal to the (hkl) plane. The length of a vector $\vec{d}^*_{(hk.l)}$ is calculated by solving the matrix product in Eq. B.11:

$$\begin{aligned}
\|\vec{d}^*_{(hk.l)}\| &= \begin{bmatrix} h & k & l \end{bmatrix} \begin{bmatrix} a^{*2} & \frac{1}{2}a^{*2} & 0 \\ \frac{1}{2}a^{*2} & a^{*2} & 0 \\ 0 & 0 & c^{*2} \end{bmatrix} \begin{bmatrix} h \\ k \\ l \end{bmatrix} \\
&= \left(h^2 + hk + k^2\right) a^{*2} + l^2 c^{*2}
\end{aligned} \tag{B.18}$$

Using the basic properties of the reciprocal space, a correlation between length of a base vector in real and reciprocal space can be derived

$$\begin{cases} a = \frac{1}{a^* \cos 30^{\text{o}}} \\ c = \frac{1}{c^*} \end{cases} \tag{B.19}$$

As a result, the length of $|\vec{t}^*_{(hk.l)}|$ is given by:

$$|\vec{d}^*_{(hk.l)}| = \sqrt{\|\vec{d}^*_{(hk.l)}\|} = \sqrt{\frac{4}{3}\left(h^2 + hk + k^2\right)\frac{1}{a^2} + l^2\frac{1}{c^2}} \tag{B.20}$$

The angle between two directions $\vec{d}^*_{(h_1k_1.l_1)}$ and $\vec{d}^*_{(k_2k_2.l_2)}$ can be calculated through the definition of the scalar product (B.1):

$$\cos\theta = \frac{\vec{d}^*_{(h_1k_1.l_1)} \cdot \vec{d}^*_{(h_2k_2.l_2)}}{\left|\vec{d}^*_{(h_1k_1.l_1)}\right| \left|\vec{d}^*_{(h_2k_2.l_2)}\right|} \tag{B.21}$$

Example The angle between the (10.2) and (01.2) planes, which are symmetry variants, in hexagonal InN with a = 3.54 Å and c = 5.693 Å.

$$\begin{aligned}
\vec{d^*}_{(10.2)} \cdot \vec{d^*}_{(01.2)} &= \begin{bmatrix} 1 & 0 & 2 \end{bmatrix} \begin{bmatrix} a^{*2} & \frac{1}{2}a^{*2} & 0 \\ \frac{1}{2}a^{*2} & a^{*2} & 0 \\ 0 & 0 & c^{*2} \end{bmatrix} \begin{bmatrix} 0 \\ 1 \\ 2 \end{bmatrix} \\
&= \begin{bmatrix} 1 & 0 & 2 \end{bmatrix} \begin{bmatrix} \frac{1}{2}a^{*2} \\ a^{*2} \\ 2c^{*2} \end{bmatrix} \\
&= \tfrac{1}{2}a^{*2} + 4c^{*2} \\
&= \tfrac{1}{2}\tfrac{4}{3a^2} + 4\tfrac{1}{c^2} \\
&= 0.1766 \text{ Å}^2 \\
|\vec{d^*}_{(10.2)}| &= \sqrt{\tfrac{4}{3}(1^2 + 0 + 0)\tfrac{1}{a^2} + 2^2\tfrac{1}{c^2}} = \sqrt{\tfrac{4}{3a^2} + 4\tfrac{1}{c^2}} = 0.4794 \text{ Å} \\
|\vec{d^*}_{(01.2)}| &= \sqrt{\tfrac{4}{3}(0 + 1^2 + 0)\tfrac{1}{a^2} + 2^2\tfrac{1}{c^2}} = \sqrt{\tfrac{4}{3a^2} + 4\tfrac{1}{c^2}} = 0.4794 \text{ Å} \\
\theta &= \arccos\left(\tfrac{0.1766}{0.4794 \cdot 0.4794}\right) = \arccos(0.7684) = 39.78^{\text{o}}
\end{aligned}$$

B.2.3 Angle between plane and direction

It is important to remark that in a hexagonal crystal system, the [uv.w] direction is no longer perpendicular to the corresponding (uv.w) crystal plane. Therefore, it's important to know the angle between a direction and its plane.
Through the definition of the scalar product ($\vec{p} \cdot \vec{q} = pq\cos\theta$), the angle θ between the normal vector of the plane $\vec{d^*}_{(hk.l)}$ and a direction $\vec{t}_{[uv.w]}$ can be calculated.

$$\cos\theta = \frac{\vec{t}_{[uv.w]} \cdot \vec{d^*}_{(hk.l)}}{\left|\vec{t}_{[uv.w]}\right| \left|\vec{d^*}_{(hk.l)}\right|} \tag{B.22}$$

where

$$\begin{aligned}
\vec{t}_{[uv.w]} &= u\vec{a} + v\vec{a} + w\vec{c} \\
\vec{d^*}_{(hk.l)} &= h\vec{a^*} + k\vec{a^*} + l\vec{c^*}
\end{aligned} \tag{B.23}$$

and $\vec{a}$, $\vec{c}$ are the unit vectors in the real space and $\vec{a^*}$, $\vec{c^*}$ are the unit vectors in the reciprocal space. Using equation B.23 and the properties $\vec{a} \cdot \vec{a^*} = 1$ and $\vec{a} \cdot \vec{c^*} = 0$, one can calculate

$$\vec{t}_{[uv.w]} \cdot \vec{d^*}_{(hk.l)} = u \cdot h + v \cdot k + w \cdot l \tag{B.24}$$

The length of $\vec{t}_{[uv.w]}$ is given by Eq. B.16

$$\left|\vec{t}_{[uv.w]}\right| = \sqrt{(u^2 - uv + v^2)\,a^2 + w^2c^2}$$

In reciprocal space, the length $\left|\vec{d}^*_{(hk.l)}\right|$ is given by Eq. B.20,

$$\left|\vec{d}^*_{(hk.l)}\right| = \sqrt{\frac{4}{3}\left(h^2 + hk + k^2\right)\frac{1}{a^2} + l^2\frac{1}{c^2}}$$

Finally, the angle between the [uv.w] direction and the (hk.l) plane can be calculated by using the equations above.

Example The angle between the [20.3] direction and the (20.3) plane in hexagonal InN with a = 3.54 Å and c = 5.693 Å.

$$\begin{aligned}
\vec{t}_{[20.3]} \cdot \vec{d}^*_{(20.3)} &= 2 \cdot 2 + 0 \cdot 0 + 3 \cdot 3 = 13 \text{ Å}^2 \\
\left|\vec{t}_{[20.3]}\right| &= \sqrt{(2^2 - 0 + 0)\,a^2 + 3^2 c^2} = \sqrt{4a^2 + 9c^2} = 18.488 \text{ Å} \\
\left|\vec{d}^*_{(20.3)}\right| &= \sqrt{\tfrac{4}{3}\left(2^2 + 0 + 0\right)\tfrac{1}{a^2} + 3^2\tfrac{1}{c^2}} = \sqrt{\tfrac{16}{3a^2} + \tfrac{9}{c^2}} = 0.839 \text{ Å} \\
\theta &= \arccos\left(\tfrac{13}{18.488 \cdot 0.839}\right) = \arccos(0.8384) = 33.02^{\text{o}}
\end{aligned}$$

Appendix C

Capture Length of faceted grains caused by directional diffusion

C.1 [111] out-of-plane oriented grains with an {100} crystal habit - MgO

The projection of an [111] out-of-plane oriented grains with an {100} crystal habit corresponds to an equilateral triangle. This triangle is defined by the points

$$\begin{cases} a = (0,0,0) \\ b = (l,0,0) \\ c = (\frac{1}{2}l, \frac{\sqrt{3}}{2}l, 0) \end{cases}$$

where l is the side length of the triangle (Fig. C.1(a)). Choose the direction of the incoming material flux to be parallel to the X-axis. The in-plane orientation of the grains is selected by rotating the triangle around point a with an angle γ (Fig. C.1(b)). By this, γ is the angle between the incoming material flux and a side of the triangle.
A triangle with given in-plane orientation γ is given by the points

$$\begin{cases} a = (0,0,0) \\ b = (\cos(\gamma)\cdot l, \sin(\gamma)\cdot l, 0) \\ c = (\frac{1}{2}\cos(\gamma)\cdot l - \frac{\sqrt{3}}{2}\sin(\gamma)\cdot l, \frac{\sqrt{3}}{2}\cos(\gamma)\cdot l + \frac{1}{2}\sin(\gamma)\cdot l, 0) \end{cases}$$

Projecting these points to Y-axis yields

$$\begin{cases} a_p = (0,0,0) \\ b_p = (0, \sin(\gamma)\cdot l, 0) \\ c_p = (0, \frac{\sqrt{3}}{2}\cos(\gamma)\cdot l + \frac{1}{2}\sin(\gamma)\cdot l, 0) \end{cases}$$

The capture length is given by length between the two outmost points. If γ is in the region [0°,60°], the capture length is the length between a_p and c_p, while in the region [60°,120°], the capture length is the length between a_p and b_p. Due to the threefold symmetry, the calculation of

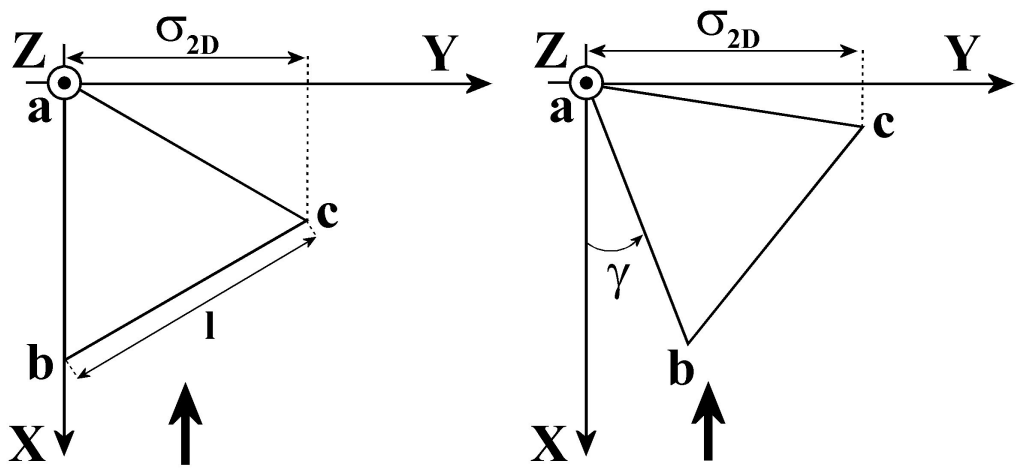

(a) Initial Configuration (b) In-plane Rotated

Figure C.1: Schematical representation of a projected [111] out-of-plane oriented grains with an {100} crystal habit. (a) Initial configuration; (b) Differently in-plane oriented grains with γ the angle between the side of the triangle and the diffusion direction. l is the length of the side of the triangle. The black arrow indicates the diffusion direction

the capture length can be restricted to [0°,120°]. Finally, the capture length is given by

$$\sigma_{\text{2D,MgO}} \begin{cases} \frac{\sqrt{3}}{2}\cos(\gamma)\cdot l + \frac{1}{2}\sin(\gamma)\cdot l & \text{if} \quad \gamma \in [0^{\text{o}}, 60^{\text{o}}] \\ \sin(\gamma)\cdot l & \text{if} \quad \gamma \in [60^{\text{o}}, 120^{\text{o}}] \end{cases}$$

C.2 [100] out-of-plane oriented grains with an {110} crystal habit - Cr

The projection of an [100] out-of-plane oriented grain with an {110} crystal habit corresponds to a square which is determined by its angular points (a,b,c,d). The square is defined in a configuration for which

$$\begin{cases} a = (0,0,0) \\ b = (l,0,0) \\ c = (l,l,0) \\ d = (0,l,0) \end{cases}$$

where l is the side length of the square (Fig. C.2(a)). In this configuration, the diffusion direction is parallel to the Y-axis. The differently in-plane oriented grains are obtained by rotating the square around point a with an angle γ (Fig. C.2(b)). As a result, γ is the angle between the side of the square and the diffusion direction. The square of a differently in-plane oriented grain is

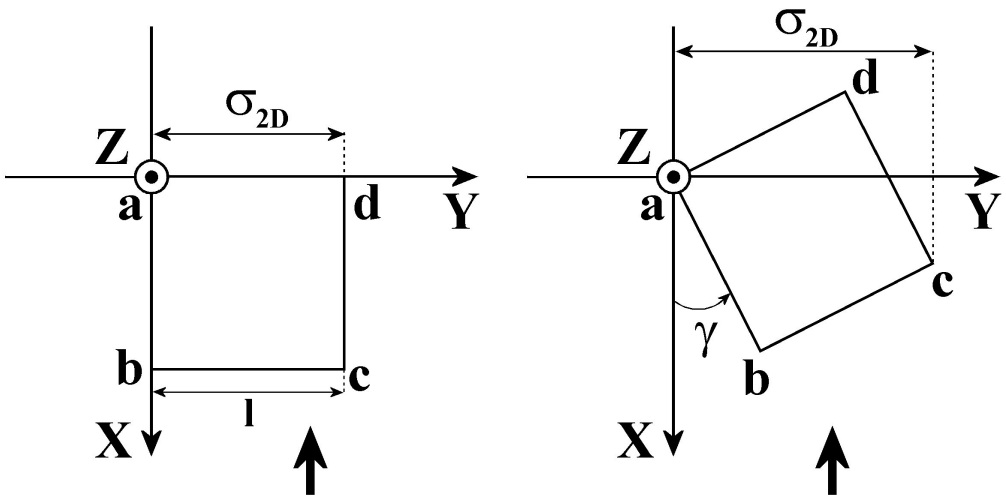

(a) Initial Configuration (b) In-plane Rotated

Figure C.2: Schematical representation of a projected [100] out-of-plane oriented grains with an {110} crystal habit. (a) Initial configuration; (b) Differently in-plane oriented grains with γ the angle between the side of the triangle and the diffusion direction. l is the length of the side of the triangle. The black arrow indicates the diffusion direction

defined by:

$$\begin{cases} a = (0,0,0) \\ b = (\cos(\gamma)\cdot l, \sin(\gamma)\cdot l, 0) \\ c = (\cos(\gamma)\cdot l - \sin(\gamma)\cdot l, \cos(\gamma)\cdot l + \sin(\gamma)\cdot l, 0) \\ d = (-\sin(\gamma)\cdot l, \cos(\gamma)\cdot l, 0) \end{cases}$$

To obtain the capture length of these grains, the grain must be projected on the direction perpendicular to the diffusion direction. Hence, the points (a,b,c,d) must be projected onto the X-axis. This yields

$$\begin{cases} a_p = (0,0,0) \\ b_p = (0, \sin(\gamma)\cdot l, 0) \\ c_p = (0, \cos(\gamma)\cdot l + \sin(\gamma)\cdot l, 0) \\ d_p = (0, \cos(\gamma)\cdot l, 0) \end{cases}$$

Due to the fourfold symmetry, the calculations of the capture length can be restricted to the in-plane orientations for which $\gamma \in [0^o, 90^o]$. In this region, the capture length is the distance between a_p and c_p which is

$$\sigma_{\text{2D,Cr}} = \cos(\gamma)\cdot l + \sin(\gamma)\cdot l$$

C.3 [0001] out-of-plane oriented grains with an {11$\bar{2}$3} crystal habit - InN

The projection of an [0001] out-of-plane oriented grain with an {11$\bar{2}$3} crystal habit is a hexagon, which is confined by six angular points (a,b,c,d,e,f). Define these points in our coordination system (Fig. C.3(a)) as

$$\begin{cases} a = (0, 0, 0) \\ b = (l, 0, 0) \\ c = (\frac{3}{2}l, \frac{\sqrt{3}}{2}l, 0) \\ d = (l, \sqrt{3}l, 0) \\ e = (0, \sqrt{3}, 0) \\ f = (-\frac{1}{2}l, \frac{\sqrt{3}}{2}l, 0) \end{cases}$$

where l is the length of a side of the hexagon. Similar to the previous calculations, the diffusion direction is parallel to the Y-axis. Various in-plane orientations of the hexagon are obtained by rotating the hexagon around point *a* over an angle γ. As a result, γ is the angle between the side

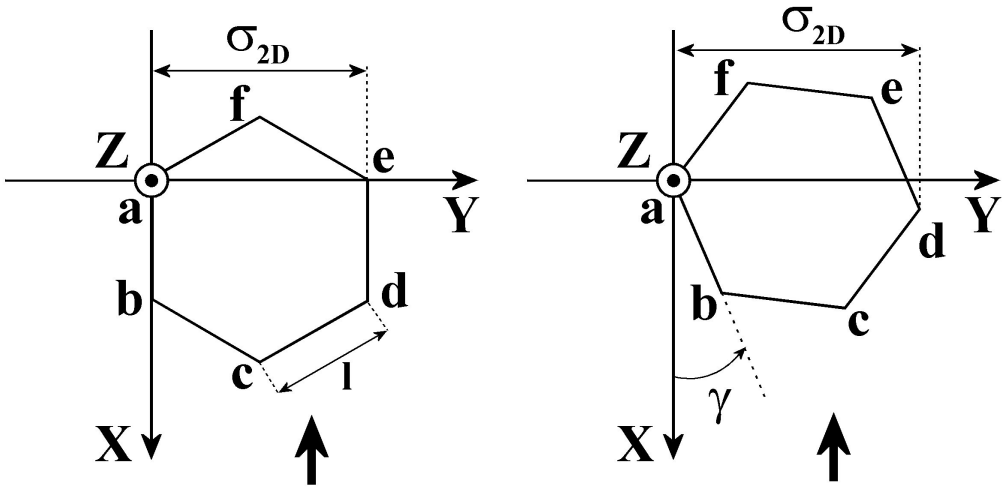

(a) Initial Configuration (b) In-plane Rotated

Figure C.3: Schematical representation of a projected [0001] out-of-plane oriented grains with an {11$\bar{2}$3} crystal habit. (a) Initial configuration; (b) Differently in-plane oriented grains with γ the angle between the side of the triangle and the diffusion direction. *l* is the length of the side of the triangle. The black arrow indicates the diffusion direction

of the hexagon and the diffusion direction. Applying this rotation to the angular points yields

$$\begin{cases} a = (0, 0, 0) \\ b = (\cos(\gamma) \cdot l, \sin(\gamma) \cdot l, 0) \\ c = (\frac{3}{2}\cos(\gamma) \cdot l - \frac{\sqrt{3}}{2}\sin(\gamma) \cdot l, \frac{\sqrt{3}}{2}\cos(\gamma) \cdot l + \frac{3}{2}\sin(\gamma) \cdot l, 0) \\ d = (\cos(\gamma) \cdot l - \sqrt{3}\sin(\gamma) \cdot l, \sqrt{3}\cos(\gamma) \cdot l + \sin(\gamma) \cdot l, 0) \\ e = (-\sqrt{3}\sin(\gamma) \cdot l, \sqrt{3}\cos(\gamma) \cdot l, 0) \\ f = (-\frac{1}{2}\cos(\gamma) \cdot l - \frac{\sqrt{3}}{2}\sin(\gamma) \cdot l, \frac{\sqrt{3}}{2}\cos(\gamma) \cdot l - \frac{1}{2}\sin(\gamma) \cdot l, 0) \end{cases}$$

To obtain the capture length, the hexagon must be projected onto the direction perpendicular to the diffusion direction. Therefore, the angular points of the hexagon are projected onto the X-as. This operation gives

$$\begin{cases} a_p = (0, 0, 0) \\ b_p = (0, \sin(\gamma) \cdot l, 0) \\ c_p = (0, \frac{\sqrt{3}}{2}\cos(\gamma) \cdot l + \frac{3}{2}\sin(\gamma) \cdot l, 0) \\ d_p = (0, \sqrt{3}\cos(\gamma) \cdot l + \sin(\gamma) \cdot l, 0) \\ e_p = (0, \sqrt{3}\cos(\gamma) \cdot l, 0) \\ f_p = (0, \frac{\sqrt{3}}{2}\cos(\gamma) \cdot l - \frac{1}{2}\sin(\gamma) \cdot l, 0) \end{cases}$$

Because of the sixfold symmetry, it is sufficient to calculate the capture length for $\gamma \in [0^o, 60^o]$. With this, the capture length, is the distance between a_p and d_p. A such, the capture length is

$$\sigma_{\text{2D,InN}} = \sin(\gamma) \cdot l + \sqrt{3}\cos(\gamma) \cdot l$$

Appendix D

Capture Area of faceted grains caused by direct capture from the flux

The capture area is defined as the projected area of the crystal habit on the normal plane of the direction of the incoming material flux. To calculate the capture area of the grain as a function of its in-plane orientation and as a function of the substrate inclination angle, three consecutive steps have to be completed. First, the in-plane orientation of the grain must be defined by rotating the crystal habit with an angle γ. Secondly, tilting the substrate is included by changing the direction of the incoming material flux with an angle α and keeping the substrate unaltered, in stead of tilting the substrate. Thirdly, the rotated crystal habit must be projected onto the normal plane perpendicular to the direction of material incidence. The capture area can be calculated from the area of the projected crystal habit.

D.1 [111] out-of-plane oriented grains with an {100} crystal habit - MgO

An [111] out-of-plane oriented grain with an {100} crystal habit corresponds to a tetrahedron and can be defined by four points (*a*,*b*,*c*,*d*):

$$\begin{cases} a = (0,0,0) \\ b = (1,0,0) \\ c = (\frac{1}{2}, \frac{\sqrt{3}}{2}, 0) \\ d = (\frac{1}{2}, \frac{\sqrt{3}}{6}, \frac{1}{\sqrt{6}}) \end{cases}$$

where the length |*ab*| is put on par with 1. The tetrahedron is shown in Fig. D.1. In this coordination system, the direction of material incidence is parallel to the Z-axis.
A specific in-plane orientation is selected by rotating the tetrahedron with an angle γ around

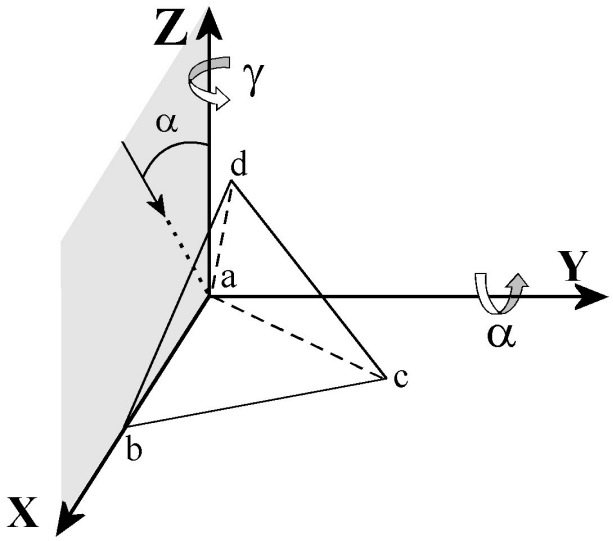

Figure D.1: Initial setup for the calculations of the capture area of an {100} faceted grain with an [111] out-of-plane orientation. The length of |ab| is put on par with 1. More specification are summarized in the text.

point *a*. Applying this rotation to the tetrahedron yields:

$$\begin{cases} a_r = (0,0,0) \\ b_r = (\cos(\gamma), \sin(\gamma), 0) \\ c_r = (\frac{1}{2}\cos(\gamma) - \frac{\sqrt{3}}{2}\sin(\gamma), \frac{\sqrt{3}}{2}\cos(\gamma) + \frac{1}{2}\sin(\gamma), 0) \\ d_r = (\frac{1}{2}\cos(\gamma) - \frac{\sqrt{3}}{6}\sin(\gamma), \frac{\sqrt{3}}{6}\cos(\gamma) + \frac{1}{2}\sin(\gamma), \frac{1}{\sqrt{6}}) \end{cases}$$

In a second step, the direction of material incidence is inclined in the XZ-plane with an angle α. With this, the plane normal to this direction, which initially corresponds to the XY-plane, is constructed by rotating the XY-plane with an angle α around the Y-axis. Projecting the rotated {100} crystal habit onto the normal plane converts the points into:

$$\begin{cases} a_p = (0,0,0) \\ b_p = (\cos(\gamma)\cos(\alpha)^2, \sin(\gamma), -\cos(\gamma)\cos(\alpha)\sin(\alpha)) \\ c_p = (\frac{1}{2}\cos(\alpha)^2(\cos(\gamma) - \sqrt{3}\sin(\gamma)), \frac{\sqrt{3}}{2}\cos(\gamma) + \frac{1}{2}\sin(\gamma), \frac{1}{2}\cos(\alpha)\sin(\alpha)(\sqrt{3}\sin(\gamma) - \cos(\gamma)) \\ d_p = (\frac{1}{6}\cos(\alpha)(3\cos(\gamma)\cos(\alpha) - \sqrt{3}\sin(\gamma)\cos(\alpha) - \sqrt{6}\sin(\alpha)), \frac{\sqrt{3}}{6}\cos(\gamma) + \frac{1}{2}\sin(\gamma), \\ \qquad -\frac{1}{6}\sin(\alpha)(3\cos(\gamma)\cos(\alpha) - \sqrt{3}\sin(\gamma)\cos(\alpha) - \sqrt{6}\sin(\alpha))) \end{cases}$$

The capture area of the various facets is calculated by taking the area of the corresponding projected facet. For instance, the capture area σ of the facet formed by the points (*a*,*b*,*d*) corresponds to the area of the triangle limited by the points (a_p,b_p,d_p). This yields:

$$\sigma_{\text{3D,abd}} = \frac{\sqrt{3}}{12}\left|\sqrt{2}\sin(\gamma)\sin(\alpha) + \cos(\alpha)\right|$$

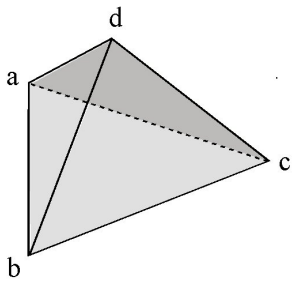

Figure D.2: By summing the capture area of the various facets, the projected area of the facets formed by (*a*,*c*,*d*) is counted twice.

$$\sigma_{3D,bcd} = \left| \frac{\sqrt{3}}{12}\cos(\alpha) + \frac{\sqrt{2}}{8}\cos(\gamma)\sin(\alpha) - \frac{\sqrt{6}}{24}\sin(\gamma)\sin(\alpha) \right|$$

$$\sigma_{3D,acd} = \left| \frac{\sqrt{3}}{12}\cos(\alpha) - \frac{\sqrt{2}}{8}\cos(\gamma)\sin(\alpha) - \frac{\sqrt{6}}{24}\sin(\gamma)\sin(\alpha) \right|$$

The total capture area is the sum of the areas of the three projected facets. However, for specific orientations and inclination angles, some of the facets are shadowed by the others, like in Fig. D.2. This causes an overlap of the different projected areas. The area without overlap, corresponds to the area of the base plane formed by (a_p,b_p,c_p). By adding the area of the base plane to the sum of the three areas, the total capture area is counted twice. Therefore, the total area is given by [1]:

$$\sigma_{3D,MgO} = \frac{1}{2}\left(\sigma_{3D,acd} + \sigma_{3D,acd} + \sigma_{3D,acd} + \sigma_{3D,abc}\right)$$

where $\sigma_{3D,abc} = \left|\frac{\sqrt{3}}{4}\cos(\alpha)\right|$

D.2 [100] out-of-plane oriented grains with an {110} crystal habit - Cr

An [100] out-of-plane oriented grain with an {110} crystal habit corresponds to a pyramid and can be defined by five points (*a*,*b*,*c*,*d*,*e*) where *begin*

$$\begin{cases} a = (0,0,0) \\ b = (1,0,0) \\ c = (1,1,0) \\ d = (0,1,0) \\ e = (\frac{1}{2},\frac{1}{2},\frac{1}{2}) \end{cases}$$

[1] This formula is valid for $\gamma \in [0°,360°]$ and $\alpha \in [0°,360°]$. One can get around this reasoning adding restriction to γ and α.

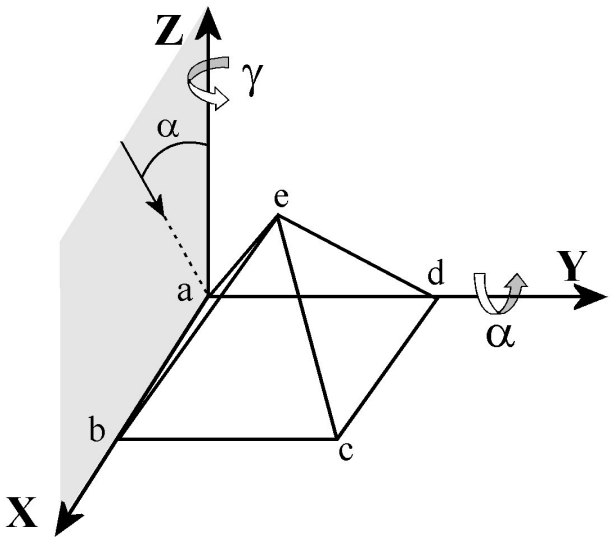

Figure D.3: Initial setup for the calculations of the capture area of an {110} faceted grain with an [100] out-of-plane orientation. The length of |ab| is put on par with 1. More specification are summarized in the text.

This is shown in Fig. D.3. In this coordination system, the direction of material incidence is parallel to the Z-axis.
A specific in-plane orientation is selected by rotating the pyramid with an angle γ around point a. Applying this rotation to the pyramid yields:

$$\begin{cases} a_r = (0,0,0) \\ b_r = (\cos(\gamma), \sin(\gamma), 0) \\ c_r = (\cos(\gamma) - \sin(\gamma), \cos(\gamma) + \sin(\gamma), 0) \\ d_r = (-\sin(\gamma), \cos(\gamma), 0) \\ e_r = (\frac{1}{2}(\cos(\gamma) - \sin(\gamma)), \frac{1}{2}(\cos(\gamma) + \sin(\gamma)), \frac{1}{2}) \end{cases}$$

The direction of material incidence is inclined in the XZ-plane with an angle α. With this, the plane normal to this direction, which initially corresponds to the XY-plane, is constructed by rotating the XY-plane with an angle α around the Y-axis. Projecting the rotated {110} crystal habit onto the normal plane converts the points into:

$$\begin{cases} a_p = (0,0,0) \\ b_p = (\cos(\gamma)\cos(\alpha)^2, \sin(\gamma), -\cos(\gamma)\cos(\alpha)\sin(\alpha)) \\ c_p = (\cos(\alpha)^2(\cos(\gamma) - \sin(\gamma)), \cos(\gamma) + \sin(\gamma), \cos(\alpha)\sin(\alpha)(\sin(\gamma) - \cos(\gamma)) \\ d_p = (-\sin(\gamma)\cos(\alpha)^2, \cos(\gamma), \sin(\gamma)\cos(\alpha)\sin(\alpha)) \\ e_p = (\frac{1}{2}\cos(\alpha)(\cos(\gamma)\cos(\alpha) - \sin(\gamma)\cos(\alpha) - \sin(\alpha)), \frac{1}{2}(\cos(\gamma) + \sin(\gamma)), \\ \qquad -\frac{1}{2}\sin(\alpha)(\cos(\gamma)\cos(\alpha) - \sin(\gamma)\cos(\alpha) - \sin(\alpha))) \end{cases}$$

The capture area of the various facets is calculated by taking the area of the corresponding projected facet. This yields:

$$\sigma_{3D,abe} = \frac{1}{4}\,|\sin(\gamma)\sin(\alpha) + \cos(\alpha)|$$

$$\sigma_{3D,bce} = \frac{1}{4}\,|\cos(\gamma)\sin(\alpha) + \cos(\alpha)|$$

$$\sigma_{3D,cde} = \frac{1}{4}\,|-\sin(\gamma)\sin(\alpha) + \cos(\alpha)|$$

$$\sigma_{3D,ade} = \frac{1}{4}\,|\sin(\gamma)\sin(\alpha) - \cos(\alpha)|$$

The total capture area is calculated from the sum of the areas of the four projected facets. Taking into account the overlap of the different projected areas, the total capture length is given by

$$\sigma_{3D,Cr} = \frac{1}{2}\left(\sigma_{3D,abe} + \sigma_{3D,bce} + \sigma_{3D,cde} + \sigma_{3D,ade} + \sigma_{3D,abcd}\right)$$

where $\sigma_{3D,abcd} = |\cos(\alpha)|$ corresponds to the area of the base plane.

D.3 [0001] out-of-plane oriented grains with an $\{11\bar{2}3\}$ crystal habit - InN

An [0001] out-of-plane oriented grain with an $\{11\bar{2}3\}$ crystal habit corresponds to a hexagonal pyramid and can be defined by seven points (*a*,*b*,*c*,*d*,*e*). These points are given by:

$$\begin{cases} a = (0,0,0) \\ b = (1,0,0) \\ c = (\frac{3}{2}, \frac{\sqrt{3}}{2}, 0) \\ d = (1, \sqrt{3}, 0) \\ e = (0, \sqrt{3}, 0) \\ f = (-\frac{1}{2}, \frac{\sqrt{3}}{2}, 0) \\ g = (\frac{1}{2}, \frac{\sqrt{3}}{2}, \tan(\theta)) \end{cases}$$

where θ is the angle between the $(11\bar{2}3)$ plane and the basal plane ($\theta = 46.99°$). The $\{11\bar{2}3\}$ crystal habit is shown in Fig. D.4. In this coordination system, the direction of material incidence is parallel to the Z-axis.
A specific in-plane orientation is selected by rotating the hexagonal pyramid with an angle γ

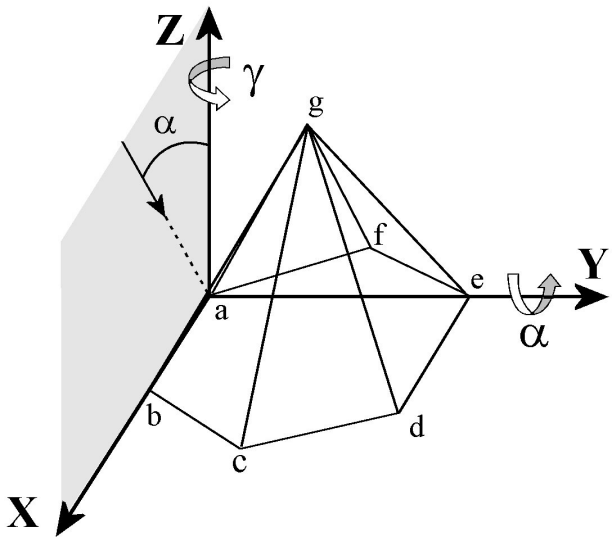

Figure D.4: Initial setup for the calculations of the capture area of an $\{11\bar{2}3\}$ faceted grain with an [0001] out-of-plane orientation. The length of |ab| is put on par with 1. More specification are summarized in the text.

around point *a*. Applying this rotation to the hexagonal pyramid yields:

$$\begin{cases} a_r = (0,0,0) \\ b_r = (\cos(\gamma), \sin(\gamma), 0) \\ c_r = (\frac{3}{2}\cos(\gamma) - \frac{\sqrt{3}}{2}\sin(\gamma), \frac{\sqrt{3}}{2}\cos(\gamma) + \frac{3}{2}\sin(\gamma), 0) \\ d_r = (\cos(\gamma) - \sqrt{3}\sin(\gamma), \sqrt{3}\cos(\gamma) + \sin(\gamma), 0) \\ e_r = (-\sqrt{3}\sin(\gamma), \sqrt{3}\cos(\gamma), 0) \\ f_r = (-\frac{1}{2}\cos(\gamma) - \frac{\sqrt{3}}{2}\sin(\gamma), \frac{\sqrt{3}}{2}\cos(\gamma) - \frac{1}{2}\sin(\gamma), 0) \\ g_r = (\frac{1}{2}\cos(\gamma) - \frac{\sqrt{3}}{2}\sin(\gamma), \frac{\sqrt{3}}{2}\cos(\gamma) + \frac{1}{2}\sin(\gamma), \tan(\theta)) \end{cases}$$

To obtain the capture area, the crystal habit must be projected onto the plane perpendicular to direction of the incoming material flux. The direction of material incidence is inclined in the XZ-plane with an angle α. With this, the plane normal to this direction, which initially corresponds to the XY-plane, is constructed by rotating the XY-plane with an angle α around the Y-axis.

Projecting the rotated {110} crystal habit onto the normal plane converts the points into:

$$\begin{cases} a_p = (0,0,0) \\ b_p = (\cos(\gamma)\cos(\alpha)^2, \sin(\gamma), -\cos(\alpha)\sin(\alpha)\cos(\gamma)) \\ c_p = (\frac{1}{2}\cos(\alpha)^2(3\cos(\gamma) - \sqrt{3}\sin(\gamma)), \frac{\sqrt{3}}{2}\cos(\gamma) + \frac{3}{2}\sin(\gamma), \frac{1}{2}\cos(\alpha)\sin(\alpha)(-3\cos(\gamma) + \sqrt{3}\sin(\gamma))) \\ d_p = (-\cos(\alpha)^2(-\cos(\gamma) + \sqrt{3}\sin(\gamma)), (\sqrt{3}\cos(\gamma) + \sin(\gamma)), \cos(\alpha)\sin(\alpha)(-\cos(\gamma) + \sqrt{3}\sin(\gamma))) \\ e_p = (-\sqrt{3}\sin(\gamma)\cos(\alpha)^2, \sqrt{3}\cos(\gamma), \sqrt{3}\cos(\alpha)\sin(\alpha)\cos(\gamma)) \\ f_p = (-\frac{1}{2}\cos(\alpha)^2(\cos(\gamma) + \sqrt{3}\sin(\gamma)), \frac{\sqrt{3}}{2}\cos(\gamma) - \frac{1}{2}\sin(\gamma), \frac{1}{2}\cos(\alpha)\sin(\alpha)(\cos(\gamma) + \sqrt{3}\sin(\gamma))) \\ g_p = (\frac{1}{2}\cos(\alpha)\left(\cos(\alpha)\cos(\gamma) - \sqrt{3}\cos(\alpha)\sin(\gamma) - 2\sin(\alpha)\tan(\theta)\right), \frac{1}{2}(\sqrt{3}\cos(\gamma) + \sin(\gamma)), \\ \qquad -\frac{1}{2}\sin(\alpha)\left(\cos(\alpha)\cos(\gamma) - \sqrt{3}\cos(\alpha)\sin(\gamma) - 2\sin(\alpha)\tan(\theta)\right)) \end{cases}$$

The capture area of the various facets is calculated by taking the area of the corresponding projected facet. This yields:

$$\sigma_{3D,abg} = \frac{1}{4}\left|2\sin(\gamma)\sin(\alpha)\tan(\theta) + \sqrt{3}\cos(\alpha)\right|$$

$$\sigma_{3D,bcg} = \frac{1}{4}\left|\sqrt{3}\cos(\gamma)\sin(\alpha)\tan(\theta) + \sin(\gamma)\sin(\alpha)\tan(\theta) + \sqrt{3}\cos(\alpha)\right|$$

$$\sigma_{3D,cdg} = \frac{1}{4}\left|\sqrt{3}\cos(\gamma)\sin(\alpha)\tan(\theta) - \sin(\gamma)\sin(\alpha)\tan(\theta) + \sqrt{3}\cos(\alpha)\right|$$

$$\sigma_{3D,deg} = \frac{1}{4}\left|2\sin(\gamma)\sin(\alpha)\tan(\theta) - \sqrt{3}\cos(\alpha)\right|$$

$$\sigma_{3D,efg} = \frac{1}{4}\left|\sqrt{3}\cos(\gamma)\sin(\alpha)\tan(\theta) + \sin(\gamma)\sin(\alpha)\tan(\theta) - \sqrt{3}\cos(\alpha)\right|$$

$$\sigma_{3D,afg} = \frac{1}{4}\left|\sqrt{3}\cos(\gamma)\sin(\alpha)\tan(\theta) - \sin(\gamma)\sin(\alpha)\tan(\theta) - \sqrt{3}\cos(\alpha)\right|$$

The total capture area is calculated from the sum of the areas of the six projected facets. Taking into account the overlap of the different projected areas, the total capture length is given by

$$\sigma_{3D,InN} = \frac{1}{2}\left(\sigma_{3D,abg} + \sigma_{3D,bcg} + \sigma_{3D,cdg} + \sigma_{3D,deg} + \sigma_{3D,efg} + \sigma_{3D,afg} + \sigma_{3D,abcdef}\right)$$

where $\sigma_{3D,abcdef} = \left|\frac{3\sqrt{3}}{2}\cos(\alpha)\right|$ corresponds to the area of the base plane.

Appendix E

Parameter Overview

- These parameters aren't optimized. After optimization of one parameters, this parameter has been used to continue the next series.
- Mention that some parameters aren't summarized. This is due to the fact that these parameters doesn't change during the deposition series: substrate temperature, substrate and sputtergas

Influence of the Target-Substrate distance

	α	I_d	V_{bias}	p	Sputter gas flow	Reactive gas flow	t	Magnets
MgO	55°	0.70 A	0 V	0.45 Pa	60 sccm Ar	3 sccm O_2	1.0 μm	1 : 9
Cr	60°	0.60 A	−15 V	0.40 Pa	26 sccm Ar	n/a	1.0 μm	1 : 3
InN	60°	0.55 A	−40 V	0.25 Pa	35 sccm Ne	35 sccm N_2	1.5 μm	1 : 3

Influence of the Working Pressure

	α	$d(T-S)$	I_d	V_{bias}	Sputter gas flow	Reactive gas flow	t	Magnets
MgO	55°	10 cm	0.70 A	0 V	60 sccm Ar (1)	3 sccm O_2 (1)	1.0 μm	1 : 9
Cr	60°	11 cm	0.65 A	−15 V	26 sccm Ar (1)	n/a	1.0 μm	1 : 3
InN	60°	9 cm	0.55 A	−40 V	(2)	(2)	1.5 μm	1 : 3

(1) The pressure is adjusted by changing the pumping speed.
(2) The pressure is adjusted by changing the Ne and N_2 flow. The Ne to N_2 ratio was 1:1 and was kept constant.

Influence of the Substrate Bias

	α	$d(T-S)$	I_d	p	Sputter gas flow	Reactive gas flow	t	Magnets
MgO	55°	10 cm	0.70 A	0.45 Pa	60 sccm Ar	3 sccm O_2	1.0 μm	1 : 9
Cr	60°	11 cm	0.65 A	0.40 Pa	26 sccm Ar	n/a	1.0 μm	1 : 3
InN	60°	10 cm	0.35 A	0.40 Pa	46 sccm Ne	46 sccm N_2	2.0 μm	1 : 3

Influence of the Discharge Current

	α	$d(T-S)$	V_{bias}	p	Sputter gas flow	Reactive gas flow	t	Magnets
MgO	55°	10 cm	0 V	0.45 Pa	60 sccm Ar	3 sccm O_2	1.0 μm	1 : 9
Cr	60°	11 cm	−15 V	0.40 Pa	26 sccm Ar	n/a	1.0 μm	1 : 3
InN	60°	9 cm	−40 V	0.40 Pa	35 sccm Ne	35 sccm N_2	2.0 μm	1 : 3

Influence of the reactive gas flow

	α	$d(T-S)$	I_d	V_{bias}	p	Sputter gas flow	t	Magnets
MgO	55°	10 cm	0.65 A	floating	0.45 Pa	60 sccm Ar	1.0 μm	1 : 9

Influence of the Sputter Gas

	α	$d(T-S)$	I_d	V_{bias}	p	t	Magnets
InN	0°	10 cm	0.40 A	−20 V	0.30 Pa	2.0 μm	1 : 3

Influence of the Substrate

	α	$d(T-S)$	I_d	V_{bias}	p	Sputter gas flow	t	Magnets
Cr	60°	11 cm	0.65 A	−15 V	0.40 Pa	46 sccm Ar	1.0 μm	1 : 3

Appendix F

Publication List

International Journals with Reading Committee

P. Ghekiere, S. Mahieu, G. De Winter, R. De Gryse, D. Depla, Influence of the deposition parameters on the biaxial alignment of MgO grown by unbalanced magnetron sputtering, J. Cryst. Growth 271 (3-4) (2004) 462-468.

S. Mahieu, P. Ghekiere, G. De Winter, S. Heirwegh, D. Depla, R. De Gryse, O.I. Lebedev, G. Van Tendeloo, Mechanism of preferential orientation in sputter deposited titanium nitride and yttria stabilized zirconia layers, J. Crys. Growth 279 (1-2) (2005) 100-109.

S. Mahieu, P. Ghekiere, G. De Winter, D. Depla, R. De Gryse, O.I. Lebedev, G. Van Tendeloo, Influence of the Ar/O_2 ratio on the growth and biaxial alignment of yttria stabilized zirconia layers during reactive unbalanced magnetron sputtering, Thin solid films 484 (1-2) (2005) 18-25.

P. Ghekiere, S. Mahieu, G. De Winter, R. De Gryse, D. Depla, O.I. Lebedev, G. Van Tendeloo, Growth mechanism of biaxially aligned magnesium oxide deposited by unbalanced magnetron sputtering, Solid State Phenomena 105 (2005) 433-438.

S. Mahieu, P. Ghekiere, G. De Winter, R. De Gryse, D. Depla, O.I. Lebedev, G. Van Tendeloo, Biaxially aligned Yttria Stabilized Zirconia and Titanium Nitride layers deposited by unbalanced magnetron sputtering, Solid state phenomena 105 (2005) 447-452.

P. Ghekiere, S. Mahieu, G. De Winter, R. De Gryse, D. Depla, Scanning electron microscopy study of the growth mechanism of biaxially aligned magnesium oxide layers, Thin Solid Films 493 (1-2) (2005) 129-134.

S. Mahieu, P. Ghekiere, G. De Winter, D. Depla, R. De Gryse, G. Van Tendeloo, O.I. Lebedev, Biaxially aligned Titanium Nitride thin films deposited by unbalanced magnetron sputtering, Surf. Coat. Technol. 200 (8) (2006) 2764-2768.

S. Mahieu, G. Buyle, D. Depla, S. Heirwegh, P. Ghekiere, R. De Gryse, Monte Carlo simulation of the transport of atoms in DC magnetron sputtering.” Nucl. Instr. Meth. B 243 (2) (2006) 313-319.

S. Mahieu, P. Ghekiere, D. Depla, R. De Gryse, O.I. Lebedev, G. Van Tendeloo, Mechanism of in-plane alignment in magnetron sputtered biaxially aligned yttria stanilized zirconia, J. Cryst.

Growth 290 (1) (2006) 272-279.

P. Ghekiere, S. Mahieu, R. De Gryse, D. Depla, Structure evolution of the biaxial alignment in sputter-deposited MgO and Cr, Thin Solid Films 515 (2) (2006) 485-488.

S. Mahieu, G. Buyle, P. Ghekiere, S. Heirwegh, R. De Gryse, D. Depla, Mechanism of biaxial alignment in thin films, deposited by magnetron sputtering, Thin Solid Films 515 (2) (2006) 416-420.

S. Mahieu, P. Ghekiere, D. Depla, R. De Gryse, Biaxial alignment in sputter deposited thin films, Thin Solid Films 515 (4) (2006) 1229-1249 (review).

Journals without Reading Committee

S. Mahieu, G. De Winter, P. Ghekiere, D. Depla, R. De Gryse, J. Denul, Biaxially aligned YSZ layers deposited by unbalanced magnetron sputtering: a model, Belvac 20 (1) (2004) 6-16.

P. Ghekiere, S. Mahieu, G. De Winter, R. De Gryse, D. Depla, Growth and optimization of biaxially aligned MgO deposited by unbalanced magnetron sputtering, Belvac 21 (1) (2005) 5-16.

S. Mahieu, G. Buyle, D. Depla, S. Heirwegh, P. Ghekiere, R. De Gryse, Transport of DC sputtered atoms: a Monte Carlo simulation, Belvac 21 (2) (2005) 11-20.

Contributed Lectures on International Conferences and Symposia

S. Mahieu, P. Ghekiere, G. De Winter, O.I. Lebedev, D. Depla, R. De Gryse : ”Mechanism of preferential orientation in thin films deposited by unbalanced magnetron sputtering”, Reactive Sputter Processes and Related Phenomena III, 9 - 10 December 2004, Ghent.

P. Ghekiere, S. Mahieu, D. Depla, R. De Gryse : ”Structure evolution of the biaxial alignment in sputter deposited MgO and Cr”, 13th International Congress on Thin Films (ICTF 13) 19 - 23 June 2005, Stockholm.

S. Mahieu, P. Ghekiere, S. Heirwegh, R. De Gryse, D. Depla : ”Mechanism of biaxial alignment in thin films deposited by magnetron sputtering”, 13th International Congress on Thin Films (ICTF 13) 19 - 23 June 2005, Stockholm.

P. Ghekiere, S. Mahieu, D. Depla, R. De Gryse : ”Impurity Induced Texture Change in Cr”, Reactive Sputter Deposition 2005, Conference organised by Nevac, Belvac and TU Delft, 8 - 9 December 2005, Delft.

S. Mahieu (i), P. Ghekiere, D. Depla, R. De Gryse : ”Mechanism of Biaxial Alignment in Thin Films”, Reactive Sputter Deposition 2005, Conference organised by Nevac, Belvac and TU Delft, 8 - 9 December 2005, Delft.

P. Ghekiere, S. Mahieu, D. Depla, R. De Gryse : ”Impurity Induced Texture Change in Cr”, 48th

IUVSTA Workshop on the Influence of Trace Elements on the Nucleation and Growth of Thin Films 26 - 31 August 2006, Budapest.

S. Mahieu (i), R. De Gryse, P. Ghekiere, D. Depla : ”Influence of adspecies flux on texture and structure evolution of biaxially aligned thin films”, 48th IUVSTA Workshop on the Influence of Trace Elements on the Nucleation and Growth of Thin Films 26 - 31 August 2006, Budapest.

P. Ghekiere (i), S. Mahieu, D. Depla, R. De Gryse : ”Structure Evolution of Biaxially Aligned Thin Films”, Reactive Sputter Deposition 2006, Conference organised by Belvac and Nevac, 30 November - 1 December 2006, Ghent.

Poster Presentations at International Conferences and Symposia

P. Ghekiere, S. Mahieu, G. De Winter, R. De Gryse, D. Depla : ”Mechanism of biaxially aligned MgO grown by unbalanced magnetron sputtering”, 16th International Vacuum Conference (IVC 16) 28 June - 2 July, 2004, Venice.

S. Mahieu, P. Ghekiere, G. De Winter, R. De Gryse, D. Depla : ”Reactive sputter deposition of biaxially aligned TiN by unbalanced magnetron sputtering”, 16th International Vacuum Conference (IVC 16) 28 June - 2 July, 2004, Venice.

P. Ghekiere, S. Mahieu, G. De Winter, O.I. Lebedev, R. De Gryse, D. Depla : ”Growth mechanism of biaxially aligned Magnesium Oxide deposited by unbalanced magnetron sputtering”, 2nd International Conference on Texture and Anisotropy of Polycrystals (ITAP) 7 - 9 July, 2004, Metz.

S. Mahieu, P. Ghekiere, G. De Winter, R. De Gryse, D. Depla, O.I. Lebedev : ”Biaxially aligned YSZ and TiN layers deposited by unbalanced magnetron sputtering”, 2nd International Conference on Texture and Anisotropy of Polycrystals (ITAP) 7 - 9 July, 2004, Metz.

S. Heirwegh, S. Mahieu, P. Ghekiere, D. Depla, R. De Gryse : ”Reactive Sputter Deposition of aluminium oxide: influence of target erosion”, , Reactive Sputter Deposition 2005, Conference organised by Nevac, Belvac and TU Delft, 8 - 9 December 2005, Delft.